



HAL
open science

Exploration de surfaces d'énergie potentielle par modélisation moléculaire en chimie organique

Anouk Siri

► **To cite this version:**

Anouk Siri. Exploration de surfaces d'énergie potentielle par modélisation moléculaire en chimie organique. Chimie théorique et/ou physique. Aix-Marseille Université, 2015. tel-01406769

HAL Id: tel-01406769

<https://hal.science/tel-01406769>

Submitted on 1 Dec 2016

HAL is a multi-disciplinary open access archive for the deposit and dissemination of scientific research documents, whether they are published or not. The documents may come from teaching and research institutions in France or abroad, or from public or private research centers.

L'archive ouverte pluridisciplinaire **HAL**, est destinée au dépôt et à la diffusion de documents scientifiques de niveau recherche, publiés ou non, émanant des établissements d'enseignement et de recherche français ou étrangers, des laboratoires publics ou privés.

Habilitation à Diriger les Recherches

Exploration de surfaces d'énergie potentielle par modélisation moléculaire en chimie organique

Université d'Aix-Marseille

UMR 7273 - Institut de Chimie Radicalaire

Dr. Anouk Gaudel-Siri

2 avril 2015

Pr. Roberto Lazzaroni (Université de Mons-Hainaut), Rapporteur
Pr. Carlo Adamo (Ecole Nationale Supérieure de Chimie de Paris), Rapporteur
Pr. Serge Antonczak (Université de Nice), Rapporteur
Dr. Patrick Trouillas (Université de Limoges), Examineur
Dr. Jean-Luc Parrain (Université d'Aix-Marseille), Examineur
Pr. Nicolas Ferré (Université d'Aix-Marseille), Examineur

Table des matières

<i>Première Partie : Curriculum Vitae détaillé</i>	7
<i>Deuxième Partie : Activités de Recherche</i>	17
1 Introduction	17
1.1 Les multiples facettes de la modélisation moléculaire	17
1.2 Points stationnaires d'une surface d'énergie potentielle	18
2 La mécanique moléculaire : principe et applications	19
2.1 Principe et objectifs	19
2.2 Champ de force de Mécanique Moléculaire	19
2.2.1 Expression de l'énergie stérique	19
2.2.2 Paramètres et fonctions utilisés en mécanique moléculaire	20
2.2.3 Paramétrisation de champ de force	23
2.3 Application à l'analyse conformationnelle des N-oxy-pyrrolidines	24
3 La dynamique moléculaire : principe et applications	47
3.1 Introduction	47
3.2 Déroulement d'une simulation de dynamique moléculaire	48
3.2.1 Configuration initiale	48
3.2.2 Equilibration	48
3.2.3 Phase de production et calcul de propriétés	51
3.3 Application à l'étude de nanocomposites à base de Montmorillonite	52
4 La chimie quantique : méthodes et applications	67
4.1 Méthodes quantiques : survol des différentes approches théoriques	67
4.1.1 Approximation de Born-Oppenheimer	67
4.1.2 Approximation orbitale	67
4.1.3 Déterminant de Slater	67
4.1.4 Application aux molécules : méthode LCAO	67
4.1.5 Méthode Hartree-Fock - Principe variationnel	67
4.1.6 UHF/RHF et contamination de spin	68
4.1.7 Méthodes semi-empiriques	68
4.1.8 Problème de la corrélation électronique	68
4.1.9 Corrélation statique : méthodes des perturbations post-HF, méthodes multi-références (CI, CAS)	68
4.1.10 Corrélation dynamique	69
4.1.11 Approche par DFT	69
4.2 Application à la réactivité des N-alcoxyamines	70
4.3 Application à la réactivité des énediynes	95
4.4 Application à l'organocatalyse	115
5 Conclusions et perspectives	133
5.1 Réactivité des espèces radicalaires	133
5.1.1 Etude théorique de la décomposition des adduits de spin de radicaux oxygénés	133
5.1.2 Etude théorique de la fragmentation des radicaux en spectrométrie de masse	135
5.2 Etude d'espèces radicalaires par dynamique moléculaire	136
5.3 Etude de la réactivité de systèmes complexes	146

Première Partie
Curriculum Vitae détaillé

Anouk GAUDEL-SIRI

Maître de Conférences, Université d'Aix-Marseille

Née le 15 janvier 1971 à Nancy (44 ans) Nationalité française, mariée, 2 enfants

Lotissement Cosimo, 219 ter av. F. Mitterrand, Les Cadeneaux, 13170 Les Pennes Mirabeau

Tel : 04 91 28 28 19 Fax : 04 91 28 91 87 @ : anouk.siri@univ-amu.fr

Lycée Périer, Marseille

— 1989 : Baccalauréat C, mention « Bien »

Lycée Thiers, Marseille

— 1989-1990 : CPGE Vêto

Université de Provence, Aix-Marseille I

— 1990-1991 : DEUG « Sciences de la Nature et de la Vie », mention « Bien »

— 1991-1992 : Licence de Chimie-Physique, mention « Bien »

— 1992-1993 : Maîtrise de Chimie-Physique, mention « Bien » (2e/50)

Stage (1 mois)

au laboratoire SREP sous la direction du Dr. D. Siri « Mécanique moléculaire, modélisation et analyse conformationnelle du myo-inositol-hexakis(phosphate) »

Stage industriel (6 semaines)

dans la société ATS, Les Milles (13), sous la direction de Mr. Gavelle « Caractérisation mécanique de différents types de polyéthylènes sous forme de films »

Université de la Méditerranée, Aix-Marseille II

— 1993-1994 : DESS Informatique Double Compétence, mention « Bien » (8e/30)

Stage (3 mois)

au laboratoire SREP sous la direction du Dr. D. Siri « Elaboration d'une interface X Window pour le programme de modélisation moléculaire GenMol »

Université d'Aix-Marseille III

Université d'Aix-Marseille III

— 1994-1995 : DEA Synthèse et Modélisation de Molécules Bioactives, mention « Très Bien » (2e/30)

Stage (5 mois)

au laboratoire SREP sous la direction du Dr. D. Siri « Etude par mécanique moléculaire de cycles N-oxy-pyrrolidiniques dans une cage de solvant à l'aide du logiciel GenMol »

— 1995-1999 : Doctorat en Chimie-Physique de l'Université d'Aix-Marseille III, au laboratoire "Structure et Réactivité des Espèces Paramagnétiques", UMR 6517 Directeurs de thèse : Pr. P.Tordo/Dr. D. Siri Sujet de recherche : « Contribution à la modélisation des nitroxydes et des N-alcoxyamines : structure, rôle en polymérisation radicalaire contrôlée »

Thèse soutenue à Marseille le 30 juin 1999 devant le jury composé de : Dr. G. Pèpe, Dr. J.-F. Pierson, Pr. M. Roche, Pr. A. Rockenbauer, Pr. B. Silvi, Pr. P. Tordo.

Mention « Très Honorable avec les Félicitations du Jury »

ATOFINA

— 2000 : stage post-doctoral au laboratoire Chimie Théorique et Modélisation Moléculaire de l'UMR 6517, en collaboration avec le laboratoire SREP de l'UMR 6517

Sujet de recherche : « Etude du contrôle de la polymérisation radicalaire par les nitroxydes à l'aide de différentes techniques de modélisation »

Université de Mons-Hainaut, Mons (Belgique)

— 2001 : stage post-doctoral au Service Chimie des Matériaux Nouveaux, Laboratoire de Photonique et Electronique Moléculaires du Pr. R. Lazzaroni

Sujet de recherche : « Modélisation par Dynamique Moléculaire de Nanocomposites Montmorillonite/poly(ϵ -caprolactone) »

Université d'Aix-Marseille III

— sept. 2001-2007 : Maître de Conférences (titulaire le 01/09/2002) dans l'équipe « Réactivité en Synthèse Organique » Poste MCF n° 0310 Section CNU n° 32

— 2008-2010 : Maître de Conférences dans l'équipe « Chimie Théorique et Mécanismes », Institut des Sciences Moléculaires de Marseille

— 2011-2012 : Maître de Conférences dans l'équipe « Chimie Théorique », Laboratoire Chimie Provence

Université d'Aix-Marseille

Depuis 2012 : Maître de Conférences dans l'équipe « Chimie Théorique », Institut de Chimie Radicalaire (ICR - UMR 7273)

Responsabilités

— 2006-2013 Présidente suppléante des jurys L2S3 Physique-Chimie et L2S4 Physique-Chimie

— 2008-2009 Enseignant référent en L1SPC

— 2009-2011 Participation à l'orientation active de l'Admission Post-bac

— Depuis fév. 2012 Codirection administrative du Centre Régional de Compétences en Modélisation Moléculaire

— Depuis 2012 Membre élu du conseil de laboratoire de l'Institut de Chimie Radicalaire

Autres activités scientifiques

— 2003 Membre du comité d'organisation de la XVI^e Réunion de la SFC-PACA (Faculté St-Jérôme, Marseille)

— 2004 Membre du comité d'organisation de l'EUCO-CC5 (La Londe-les-Maures)

— 2010 Membre du comité d'organisation de la 3^e Journée de l'iSm2 (Faculté St-Jérôme, Marseille)

— 2012 Membre du comité d'organisation du RCTF (Site St-Charles, Marseille)

Activités Pédagogiques

En licence comme en master j'ai participé à différents enseignements, dans le domaine de la chimie-physique et de la chimie théorique sur les sites de Saint-Jérôme (Marseille) et de Montperrin (Aix-en-Provence).

1. TD d'atomistique/Structure de la matière (L1 Physique-Chimie et Biologie)
2. Encadrement de projet découverte du monde scientifique : « A la découverte d'une molécule » (L1 Physique-Chimie)
3. Cours/TD/TP de méthodologie scientifique (L1 Physique-Chimie) en présentiel et en télé-enseignement
4. TP de chimie informatique (L1 Maths-Informatique)
5. Cours/TD de cinétique chimique (L1, L2 Physique-Chimie, L2 Maths-Physique-Chimie-Informatique)
6. TP de chimie générale (L2 Physique-Chimie)
7. Cours/TD/TP d'initiation à la modélisation moléculaire (L2 Maths-Informatique)
8. TD de chimie quantique (L2, L3 Physique-Chimie)
9. Cours de stéréochimie (MST Chimie Fine)
10. TP de chimie quantique (M1 Chimie)
11. Cours/TP de modélisation moléculaire (M1,M2 Chimie, parcours « Chimie Informatique, Spectrométries, Analyse »)
12. Cours de dynamique moléculaire (M2 Chimie, parcours « Chimie Informatique, Spectrométries, Analyse »)

En 2010, j'ai commencé la création du cours de cinétique chimique (L2) sur la plateforme pédagogique Moodle de l'université Paul Cézanne. Depuis la rentrée universitaire 2011, le cours est mis à la disposition des étudiants de L2. En 2012, le cours a migré sur la plateforme pédagogique de l'université d'Aix-Marseille (AMeTICE) où il est mis à jour chaque année.

En 2014, j'ai repris le télé-enseignement des cours/TD/TP de méthodologie scientifique (L1 Physique-Chimie).

Activités d'encadrement

- Sept. 2002-juin 2004 Lycia Fournier, doctorat en chimie organique (co-encadrement avec Pr. Jean-Marc Pons) Titre de la thèse : « Etude expérimentale et théorique de la translactonisation de β -lactones. Applications en synthèse totale de produits naturels
- Mars-juin 2004 Chaouki Lakhdar, stage de M2 de chimie parcours « Chimie informatique, Spectrométries, Analyse » Titre du stage : « Chimiosélectivité de la Réaction de Diels-Alder »
- Nov. 2009-Oct. 2010 Pramod Akula Bala, stage post-doctoral (ANR blanc Novopioïdes) Titre du stage : « Etude des interactions protéine/ligand par docking et dynamique moléculaire. Application au récepteur A1 de l'adénosine et au récepteur opioïde μ »
- Juin-juil. 2010 Aude Giard, stage technicien de l'Ecole Centrale de Marseille (2 mois) Titre du stage : « Addition de Michaël organocatalysée : Etude théorique de l'effet de substituant sur la stéréosélectivité »
- Nov. 2011-oct. 2012 Diana Cheshmedzhieva, stage post-doctoral (ANR blanc Oereka) Titre du stage : « Etude théorique du mécanisme de la réaction de Michael organocatalysée de β -cétamides sur des carbonyles α,β -insaturés »
- Depuis nov. 2012 Sergiu Lescic, doctorat en chimie informatique et théorique (co-encadrement avec Pr. Didier Siri) Titre de la thèse : « Etude théorique du mécanisme de décomposition des adduits de spin de radicaux oxygénés »

Synthèse des travaux scientifiques

Au cours de ces douze années, au sein de différentes équipes successives, j'ai approfondi mes connaissances concernant des méthodes variées de modélisation moléculaire, basées sur la mécanique classique (mécanique moléculaire et dynamique moléculaire) ou la chimie quantique (méthodes semi-empiriques, *ab initio* ou basées sur la fonctionnelle de la densité). J'ai appliqué ces diverses méthodes à l'exploration de surfaces d'énergie potentielle, dans le cadre d'études de réactivité ou d'analyse conformationnelle. J'ai utilisé ces techniques dans le cadre de projets proposés par différentes équipes d'expérimentateurs, en essayant d'utiliser la technique de modélisation la plus adaptée à chaque cas. J'ai ainsi pu avoir des collaborations très enrichissantes avec de nombreuses équipes d'expérimentateurs au sein de mon unité de recherche.

Les méthodes de la chimie quantique m'ont permis d'étudier la réactivité à l'état fondamental de systèmes organiques variés, aussi bien à couche fermée que radicalaires. En fonction des sujets de recherche et de la taille du système, le choix de la méthode la plus adaptée pour résoudre le problème posé est une étape primordiale. Ces travaux ont fait l'objet de treize publications et sont présentés dans la deuxième partie de ce manuscrit.

Au cours de ces années de recherche, je me suis également spécialisée en mécanique moléculaire et dynamique moléculaire. Dans ces modèles, les atomes sont représentés par des sphères dures et les liaisons par des ressorts, les électrons ne sont pas représentés explicitement, ce qui rend impossible toute étude de réactivité (rupture et formation de liaisons). Par contre, ces modèles permettent d'explorer la surface d'énergie potentielle de systèmes de grande taille, d'effectuer de l'analyse conformationnelle, de calculer des propriétés moyennées sur la durée des simulation. Ces travaux ont fait l'objet de quatre publications et sont également présentés dans la première partie de ce manuscrit.

Publications

1. A. Quintard, D. Cheshmedzhieva, M. del Mar Sanchez Duque, A. Gaudel-Siri, J.-V. Naubron, Y. Génisson, J.-C. Plaquevent, X. Bugaut, J. Rodriguez, T. Constantieux « Origin of the enantioselectivity in organocatalytic Michael additions of β -ketoamides to α,β -unsaturated carbonyls : a combined experimental, spectroscopic and theoretical mechanistic study » *Chem. Eur. J.* **2015**, *21*, 778-790. doi : 10.1002/chem.201404481
2. D. Bardelang, G. Casano, F. Poulhes, H. Karoui, J. Filippini, A. Rockenbauer, R. Rosas, V. Monnier, D. Siri, A. Gaudel-Siri, O. Ouari, P. Tordo « Spin exchange monitoring of the strong positive homotropic allosteric binding of a tetradical by a synthetic receptor in water » *J. Am. Chem. Soc.* **2014**, *136*, 17570-17577. doi : 10.1021/ja509586k
3. A. Gaudel-Siri, D. Campolo, S. Mondal, M. Nechab, D. Siri, M.P. Bertrand « Theoretical study to explain how chirality is stored and evolves throughout the radical cascade rearrangement of enyne-allenes » *J. Org. Chem.* **2014**, *79*, 9086-9093. doi : 10.1021/jo501450k
4. G. Audran, P. Brémond, S.R.A. Marque, A. Gaudel-Siri, D. Siri, M. Santelli « Theoretical modelling of the epoxidation of vinylallenes to give cyclopentenones » *Tet. Lett.* **2013**, 6607-6610.
5. J.-P. Reboul, P. Verhaeghe, D. Siri, A. Gaudel-Siri, C. Castera-Ducros, A. Dumètre, S. Hutter, N. Azas, P. Rathelot, P. Vanelle, A. Iliadis « Synthesis and antiplasmodial receptor independent 4D-QSAR study in 4-aryl-2-trichloromethylquinazoline series » *Curr. Chem. Biol.* **2013**, 139-150.
6. D. Campolo, A. Gaudel-Siri, S. Mondal, D. Siri, E. Besson, N. Vanthuyne, M. Nechab, M.P. Bertrand « Mechanistic Investigation of Ene-diyne Connected Amino Esters Rearrangement. Theoretical Rationale for the Exclusive Preference for 1,6- or 1,5-Hydrogen Atom Transfer Depending on the Substrate. A Potential Route to Chiral Naphtho-Azepines » *J. Org. Chem.* **2012**, *77*, 2773-2783. doi : 10.1021/jo202580y
7. M. del Mar Sanchez Duque, O. Baslé, N. Isambert, A. Gaudel-Siri, Y. Génisson, J.-C. Plaquevent, J. Rodriguez, T. Constantieux « A cooperative participation of the amido group in the organocatalytic construction of all-carbon quaternary stereocenters by Michael addition with β -ketoamides » *Org. Lett.* **2011**, *13*, 3296-3299. doi : 10.1021/ol200924e

8. M. Lansalot, Y. Guillaneuf, B. Luneau, S. Acerbis, P.-E. Dufils, A. Gaudel-Siri, D. Gignes, S. R. A. Marque, P. Tordo, D. Bertin « A Step Towards High-Molecular-Weight Living/Controlled Polystyrene Using SG1-Mediated Polymerization » *Macromol React. Eng.* **2010**, *4*, 403-414.
9. S.C. Mathew, Y. By, A. Berthault, M.-A. Virolleaud, L. Carrega, G. Chouraqui, L. Commeiras, J. Condo, M. Attolini, A. Gaudel-Siri, J. Ruf, J. Rodriguez, J.-L. Parrain, R. Guieu « Expeditious synthesis and biological evaluation of new C-6 1,2,3-triazole adenosine derivatives A1 receptor antagonists or agonists » *Org. Biomol. Chem.* **2010**, *8*, 3874-3881. doi : 10.1039/c0ob00017e
10. Hamadouche, M.; Gaudel-Siri, A.; Pons, J.-M.; El Abed, D. «Reactive Stability of a Series of 1,2,3-Triazolines. Theoretical Study of Substituent Effects» *J. Mol. Struct. (Theochem)* **2010**, 33-37. doi :10.1016/j.theochem.2010.06.019
11. S. C. Mathew, N. Ghosh, Y. By, A. Berthault, M.-A. Virolleaud, L. Carrega, G. Chouraqui, L. Commeiras, J. Condo, M. Attolini, A. Gaudel-Siri, J. Ruf, J.-L. Parrain, J. Rodriguez, and R. Guieu. « Design, Synthesis and Biological evaluation of a bivalent μ opiate and adenosine A1 receptor antagonist » *Bioorg. Med. Chem. Lett.* **2009**, *19*, 6736-6739. doi :10.1016/j.bmcl.2009.09.112
12. Ghobsi, A.; Hacini, S.; Wavrin, L.; Gaudel-Siri, A.; Corbère, A.; Nicolas, C.; Bonne, D.; Viala, J.; Rodriguez, J. "Palladium-Catalysed Isomerisation of 2-Vinylidenehydrofurans into 1,3-Dienes and some Aspects of their Reactivity", *Eur. J. Org. Chem.* **2008**, *26*, 4446-4453. doi : 10.1002/ejoc.200800517
13. Gignes, D.; Gaudel-Siri, A.; Marque, S.R.A.; Bertin, D.; Tordo, P.; Astolfi, P.; Greci, L.; Rizzoli, C. "Alkoxyamines of Stable Aromatic Nitroxides : N-OC Bond vs NO-C Bond Homolysis", *Helv. Chim. Acta* **2006**, *89*, 2312-2326. doi : 10.1002/hlca.200690215
14. Gaudel-Siri, A.; Siri, D.; Tordo, P. "Homolysis of N-Alkoxyamines. A Computational Study", *ChemPhysChem* **2006**, *7*, 430-438. doi : 10.1002/cphc.200500308.
15. Gaudel-Siri, A.; Pons, J.-M.; Piétri, N.; Tamburelli-Couturier, I.; Aycard, J.-P. "The Reaction of Trimethylsilylketene with HCl : Mechanistic Study", *Int. J. Quantum Chem.* **2006**, *106*, 719-726. doi : 10.1002/qua.20836
16. Pietri, N.; Gaudel-Siri, A.; Couturier-Tamburelli, I.; Pons, J.-M.; Aycard, J.-P. "Breaking of Ketene Bonds during HCl Addition to Trimethylsilylketene" *J. Phys. Chem. A* **2005**, *109*, 2120-2126. doi : 10.1021/jp044862o
17. Gardebien, F.; Gaudel-Siri, A.; Brédas, J.-L.; Lazzaroni, R. "Molecular Dynamics Simulations of Intercalated Poly(ϵ -caprolactone)-Montmorillonite Clay Nanocomposites", *J. Phys. Chem. B* **2004**, *108*, 10678-10686. doi :10.1021/jp0493069
18. Gaudel-Siri, A.; Brocorens, P.; Siri, D.; Gardebien, F.; Brédas, J.-L.; Lazzaroni, R. "Molecular Dynamics Study of ϵ -Caprolactone Intercalated in Wyoming Sodium Montmorillonite", *Langmuir* **2003**, *19*, 8287-8291. doi :10.1021/la034491n
19. Rockenbauer, A.; Gaudel-Siri, A.; Siri, D.; Berchadsky, Y.; Le Moigne, F.; Olive, G.; Tordo, P. "Large phosphorus hyperfine coupling as a sensitive tool for studying molecular dynamics : ESR and molecular mechanics study of ring interconversion in cis-2,5-diphosphoryl-2,5-dimethylpyrrolidin-1-oxyl radical", *J. Phys. Chem. A* **2003**, *107*, 3851-3857. doi :10.1021/jp0213351
20. Fournier, L.; Gaudel-Siri A.; Kocienski, P.J.; Pons, J.-M. "The β -Lactone Route to β -Hydroxy or α,β -Unsaturated γ - and δ -Lactones. Syntheses of (\pm)-Massoialactone and (\pm)-Prelactone B", *Synlett.* **2003**, *1*, 107-111 et 584. doi :10.1055/s-2003-36222
21. Siri, D.; Gaudel-Siri, A.; Pons, J.-M.; Liotard, D.; Rajzmann, M. "Reaction mechanism studies made simple using simulated annealing. Potential energy surface exploration", *J. Mol. Struct. (Theochem)* **2002**, *588*, 71-78. doi :10.1016/S0166-1280(02)00133-1
22. Siri, D.; Gaudel-Siri, A.; Tordo, P. "Conformational analysis by molecular mechanics of five-membered rings : application to nitroxides", *J. Mol. Struct. (Theochem)* **2002**, *582*, 171-185. doi :10.1016/S0166-1280(01)00773-4
23. Tordo, P.; Le Mercier, C.; Gaudel, A.; Siri, D.; Marque, S.; Martschke, R.; Fischer, H. "Characteristics of phosphonylated nitroxides and alkoxyamines used in controlled/"living" radical

polymerization" Book of Abstracts, 218th ACS National Meeting, New Orleans, Aug. 22-26 1999, American Chemical Society Ed., Washington, DC.

24. Le Mercier, C. ; Gaudel, A. ; Siri, D. ; Tordo, P. ; Marque, S. ; Martschke, R. ; Fischer, H. "Characteristics of phosphonylated nitroxides and alkoxyamines used in controlled/"living" radical polymerizations", *Polym. Prepr. (Am. Chem. Soc., Div. Polym. Chem.)* **1999**, *40*, 313-314.

Communications orales

- juin 2012 7^e Rencontres de Chimie Organique (RCOM7) (Marseille) Cheshmedzhieva D., Gaudel-Siri A., Constantieux T. « Theoretical investigations on the mechanism of the organocatalyzed Michael addition with β -ketoamides »
- déc. 2009 6^e Journée Biologie, Chimie, Physique (Marseille) Akula Bala, P. ; Gaudel-Siri, A. « Etude théorique des interactions protéine-ligand : Application aux récepteurs A1 de l'adénosine et opioïde μ »
- juin 2004 5th European Conference on Computational Chemistry (EUCCO-CC5) (La Londe-les-Maures) Gaudel-Siri, A. ; Pons, J.-M. ; Piétri, N. ; Tamburelli-Couturier, I. ; Aycard, J.-P. "The Reaction of Trimethylsilylketene with HCl : a Mechanistic Study"
- oct. 2003 4^e Symposium Sigma Aldrich des Jeunes Chimistes (SAJEC 2003) (Arcachon) Fournier, L. ; Gaudel-Siri, A. ; Kocienski, P.J. ; Pons, J.-M. « Formation de δ -lactones α,β -insaturées par translactonisation. Etude théorique et synthèses de la (-)-Massoialactone et de la Goniotalamine »
- avr. 2003 16^e Réunion de la SFC-PACA (Marseille) Fournier, L. ; Gaudel-Siri, A. ; Kocienski, P. ; Pons, J.-M. « Nouvelle méthode de formation du motif δ -lactone. Application à la synthèse de produits naturels »
- mai 2001 12^e Réunion du Groupe de Graphisme et de Modélisation Moléculaire (GGMM) (Nîmes) Gaudel, A. ; Brocorens, P. ; Dubois, P. ; Brédas, J.-L. ; Lazzaroni, R. "Molecular modeling of poly(ϵ -caprolactone)/montmorillonite nanocomposites"
- mars 2000 Réunion de la SFC (Avignon) Le Mercier, C. ; Acerbis, S. ; Gignes, D. ; Gaudel, A. ; Siri, D. ; Le Moigne, F. ; Bertin, D. ; Tordo, P. « Design de nouveaux nitroxydes et de nouvelles alkoxyamines pour l'élaboration de polymères vivants »
- août 1999 218th ACS National Meeting (New Orleans, USA) Tordo, P. ; Le Mercier, C. ; Gaudel, A. ; Siri, D. ; Marque, S. ; Martschke, R. ; Fischer, H. "Characteristics of phosphonylated nitroxides and alkoxyamines used in controlled / "living" radical polymerizations"

Communications par affiches

- juin 2014 8^e Rencontres de Chimie Organique (RCOM8) (Marseille) Lescic S., Siri, D., Gaudel-Siri A. « Mechanism of decomposition of peroxy spin-adducts : a theoretical study »
- juil. 2013 18th European Symposium on Organic Chemistry (ESOC) (Marseille) Hamadouche M., Gaudel-Siri A., Pons J.-M., El Abed D. « Synthesis of triazolines and degradation to amidines. Theoretical study »
- juil. 2012 XIII^e Rencontre des Chimistes Théoriciens Francophones (RCTF) (Marseille) Cheshmedzhieva D., Gaudel-Siri A., Constantieux T. « Theoretical investigations on the mechanism of the organocatalyzed Michael addition with β -ketoamides »
- avr. 2012 6^e Journées Franco-Italiennes de Chimies (Marseille) Campolo D., Gaudel-Siri A., Mondal S., Perfetti P., Maury J., Besson E., Siri D., Vanthuyne N. Nechab M., and Bertrand M.P. « Memory of Chirality in Cascade Rearrangement of Eneidyne : Mechanistic Study »
- sept. 2011 6th Conference on Synthesis, Properties and Implications of Nitroxides (SPIN 2011) (Marseille) A. Gaudel-Siri, F. Ferré N. Siri, D. « Theoretical Investigations on the Decomposition of Peroxy Spin Adducts of 5,5-dimethyl-1-pyrroline-N-oxide (DMPO)»
- mai 2010 6^e Rencontres de Chimie Organique (RCOM6) (Marseille) A. Gaudel-Siri, F. Liéby-Muller, T. Constantieux, J. Rodriguez « Etude Théorique du Mécanisme de Synthèse « one-pot » de Benzimidazole en présence de tamis moléculaire »

- avril 2009 21^e Journée de la Chimie SFC-PACA (Marseille) Hamadouche, M. ; Pons, J.-M. ; Bressy, C. ; Gaudel-Siri, A. ; El Abed, D. « Synthèse de D2(1,2,3)-triazolines : Activation par les micro-ondes et étude théorique »
- mai 2007 20^e Réunion de la SFC-PACA (Avignon) Hamadouche, M. ; Pons, J.-M. ; Bressy, C. ; Gaudel-Siri, A. ; El Abed, D. « Réactivité des énamines vis-à-vis des azides organiques »
- sept. 2004 9^e Rencontre des Chimistes Théoriciens Francophones (RCTF) (Pau) Gaudel-Siri, A. ; Fournier, L. ; Pons, J.-M. « Influence de la Substitution sur la Réaction de Translactonisation β -Lactones/ γ -, δ -, ϵ -Lactones »
- sept. 2004 Journées de Chimie Organique (JCO 2004) (Palaiseau) Lakhdar, C. ; Gaudel-Siri, A. ; Rodriguez, J. « Chimiosélectivité de la Réaction de Diels-Alder dans des Systèmes Polyéniques Fonctionnalisés »
- juil. 2004 40th International Symposium on Macromolecules (IUPAC-MACRO 2004) (Paris) Gaudel-Siri, A. ; Siri, D. ; Tordo, P. « Strengthening of the NO-C Bond in N-Alkoxyamines. A NBO Study »
- mai 2004 3^e Rencontres de Chimie Organique (RCOM3) (Marseille, France) Lakhdar, C. ; Gaudel-Siri, A. ; Rodriguez, J. « Chimiosélectivité de la Réaction de Diels-Alder » L. Fournier, A. Gaudel-Siri, P. Kocienski et J.-M. Pons « Translactonisation. Etude théorique et applications en synthèse totale »
- avr. 2004 2^e Journées de Chimie France-Canada (Nice) L. Fournier, A. Gaudel-Siri, P. Kocienski et J.-M. Pons « Translactonisation. Etude théorique et applications en synthèse totale »
- mai 2003 13^e Colloque du Groupe de Graphisme et de Modélisation Moléculaire (GGMM) (Cahors, France) Gaudel-Siri, A. ; Raponi, E. ; Pons, J.-M. « Importance du Contrôle par Chélation dans l'Observation d'Alcoxyoxétènes Instables » Siri, D. ; Gaudel-Siri, A. ; Reboul, J.-P. « Etude QSAR-3D de Psychotropes Tricycliques »
- sept. 2002 8^e Rencontre des Chimistes Théoriciens Français (RCTF) (Strasbourg) Gaudel-Siri, A. ; Pons, J.-M. ; Piétri, N. ; Couturier-Tamburelli, I. ; Aycard, J.-P. « Etude de la réaction entre le triméthylsilylcétène et HCl »
- avril 2002 2^e Rencontres de Chimie Organique (RCOM) (Marseille, France) Fournier, L. ; Gaudel-Siri, A. ; Kocienski, P. ; Pons, J.-M. « Preparation of β -hydroxy and α,β -unsaturated δ -lactones : synthesis and molecular modeling. Total synthesis of (\pm)-Prelactone B and (\pm)-Massoialactone »
- mai 2001 12^e Réunion du Groupe de Graphisme et de Modélisation Moléculaire (GGMM) (Nîmes) Siri, D. ; Gaudel, A. ; Pons, J.-M. ; Rajzmann, M. « Reaction mechanism studies made simple using simulated annealing. Potential energy surface exploration »
- août 2000 6th International Symposium on Spin-Trapping (Marseille) Gaudel, A. ; Siri, D. ; Tordo, P. « Chemical exchange and anomeric effect in oxygen radical spin adducts : a molecular mechanics study »
- sept. 1999 25^e Congresso Chimici Teorici di Espression Latina (Naples, Italie) Rajzmann, M. ; Gaudel, A. ; Siri, D. « Application du recuit simulé à l'étude des mécanismes réactionnels »
- mai 1999 11^e Réunion du Groupe de Graphisme et de Modélisation Moléculaire (GGMM) (Dardilly) Siri, D. ; Gaudel, A. ; Tordo, P. « Conformational analysis by molecular mechanics of five-membered cyclic nitroxyl radicals ; comparison with ESR experimental data »
- mai 1997 10^e Réunion du Groupe Graphique Moléculaire (GGM) (Dourdan) - Gaudel, A. ; Siri, D. ; Tordo, P. « Intérêt des radicaux nitroxy pour le contrôle de la polymérisation radicalaire. Calculs semi-empiriques » - Gaudel, A. ; Siri, D. ; Pèpe, G. ; Tordo, P. « Analyse conformationnelle par mécanique moléculaire (GenMol) d'une famille de cycles N-oxy pyrrolidiniques »

Deuxième Partie

Activités de Recherche

1 Introduction

1.1 Les multiples facettes de la modélisation moléculaire

La modélisation moléculaire ou chimie computationnelle consiste à représenter des édifices chimiques à l'échelle atomique et moléculaire afin d'étudier, expliquer, prévoir leur comportement et/ou leur réactivité.¹ Dans cet objectif, une grande panoplie de modèles théoriques sont à notre disposition et, le choix du modèle théorique le plus adapté au problème à résoudre représente la première étape de tout projet d'étude en modélisation moléculaire. Ces modèles nous permettent d'explorer une surface d'énergie potentielle (SEP) et de nous focaliser sur certains de ses points critiques.

Quelle que soit la technique de modélisation moléculaire utilisée, nous travaillons sur des modèles et pas sur des molécules réelles. La qualité des résultats dépend directement de la qualité du modèle utilisé.

- Pour déterminer un profil réactionnel, nous avons un grand choix de méthodes quantiques à notre disposition. Laquelle choisir ?
 1. Le système reste-t-il dans son état fondamental ?
 2. Le système est-il à couche ouverte ou fermée ? Quelle est sa multiplicité de spin ?
 3. Quelle est la taille du système ? Dix atomes, 50 atomes, 200 atomes ?
 4. Quelle est la précision recherchée ? De l'ordre du qualitatif ou une enthalpie de formation avec une précision semblable aux données expérimentales ?
 5. Les interactions à longue distance ont-elles une grande importance dans la description du système ?
 6. Quelle est la puissance de calcul disponible ?

Suivant la réponse à ces questions (la liste n'est pas exhaustive), notre choix se portera sur la méthode quantique la plus adaptée.

- L'analyse conformationnelle d'une molécule comportant un nombre réduit de degrés de liberté peut être réalisée en mécanique moléculaire, avec le champ de force approprié. Les différents conformères peuvent être mis en évidence (minima de la SEP) avec leurs énergies relatives ainsi que leurs proportions selon la loi de Boltzmann. Cependant, la taille des molécules ou la complexité du système chimique, donc le nombre de degrés de libertés, rendent impossible l'utilisation de la mécanique moléculaire : molécules biologiques, molécules solvatées, complexes, ... Dans ce cas, il devient indispensable de recourir à la dynamique moléculaire qui permet d'explorer de façon rapide et efficace la SEP du système et de tenir compte des multiples minima locaux dans le calcul des propriétés.

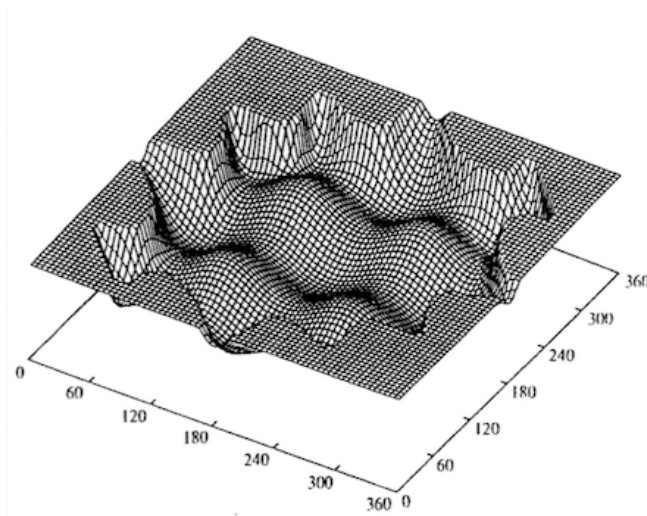
Pour effectuer une analyse conformationnelle, nous avons un grand choix de champs de force et de logiciels à notre disposition. Le(s)quel(s) choisir ?

1. Un champ de force spécifique a-t-il été développé pour le système étudié ?
2. Le système comporte-t-il plusieurs catégories de molécules (solvant, soluté, molécule organique, molécule biologique, ...) et un champ de force spécifique doit-il être attribué à chaque catégorie ?
3. Le champ de force est-il valable dans le domaine de température et/ou de pression de l'étude ?
4. Les interactions non-covalentes ont-elles une grande importance dans la description du système (liaisons hydrogène, espèces chargées, ...) ?

Suivant la réponse à ces questions (la liste n'est pas exhaustive), notre choix se portera sur le champ de force le plus adapté.

1. a) Leach, A. *Molecular modelling, principles and applications*, Longman, 1998. b) Jensen, F. *Introduction to computational chemistry*, Wiley, 1999.

FIGURE 1.1 – Exemple de surface d'énergie potentielle présentant des minima, des maxima et des point-selles.



1.2 Points stationnaires d'une surface d'énergie potentielle

D'une part, nous nous intéressons aux minima de la SEP qui représentent des états stables du système. D'autre part, en réactivité, nous souhaitons connaître la structure et l'énergie des états de transition correspondant aux transformations chimiques étudiées. A l'aide de toutes ces données, nous pouvons calculer l'énergie d'activation et l'énergie de réaction. Ces différents points stationnaires de la SEP ont des caractéristiques particulières qui permettent de les localiser à l'aide d'algorithmes de minimisation de l'énergie ou du gradient de l'énergie.

Pour tout point stationnaire, les composantes du vecteur gradient (dérivées premières de l'énergie par rapport aux coordonnées) sont nulles. Le signe des éléments de la matrice H (dérivées secondes de l'énergie par rapport aux coordonnées) renseigne alors sur la nature du point stationnaire. Plusieurs cas sont possibles (Figure 1.1) :

- 1) Tous les éléments diagonaux de H sont positifs : c'est un minimum
- 2) Tous les éléments diagonaux de H sont négatifs : c'est un maximum
- 3) Tous les éléments diagonaux de H sont positifs sauf un : c'est un point-selle d'indice 1
- 4) Tous les éléments diagonaux de H sont positifs sauf n : c'est un point-selle d'indice n.

Pour trouver un minimum sur la SEP en minimisant la fonction énergie potentielle multidimensionnelle, on part d'un point quelconque de la SEP et on utilise des méthodes numériques qui modifient progressivement les coordonnées atomiques du système de telle sorte que l'énergie potentielle diminue jusqu'à ce que le minimum le plus proche du point de départ soit atteint. Les méthodes numériques développées pour trouver les minima du système sont basées sur le principe suivant : il suffit de calculer les composantes du vecteur gradient (dérivées premières partielles de l'énergie par rapport à chacune des coordonnées atomiques) et de trouver les points de l'hypersurface où ces dérivées sont nulles. Il existe deux types de méthodes : les unes utilisent uniquement le vecteur gradient qui indique la pente de l'hypersurface (méthode de la plus grande pente ou du gradient conjugué par exemple), les autres utilisent à la fois le vecteur gradient et la matrice H (méthodes de type Newton-Raphson). D'une manière générale, on calcule la direction du vecteur gradient et on se déplace sur la SEP suivant cette direction ou une direction recalculée, plus efficace.

La localisation d'un état de transition est plus délicate : c'est un point-selle d'indice 1. Les composantes du vecteur gradient sont nulles puisque c'est un point stationnaire mais on ne peut pas le situer en minimisant l'énergie. En se plaçant dans une géométrie proche de celle de l'état de transition et en minimisant le gradient, on peut localiser l'état de transition après un premier calcul de H. D'autres méthodes peuvent être utilisées, telles que la méthode de la chaîne, où une série de structures sont générées entre celle des réactifs et celle des produits. Ces structures forment une chaîne qui est ensuite relaxée afin qu'elle passe par un point-selle, l'état de transition recherché.

2 La mécanique moléculaire : principe et applications

2.1 Principe et objectifs

La mécanique moléculaire est une méthode empirique basée sur un modèle mécanique dans lequel les atomes sont assimilés à des sphères dures non-interpénétrables de masse donnée, tandis que les liaisons et les angles de valence sont assimilés à des ressorts. L'idée d'assimiler une molécule à un modèle mécanique est due à Andrews (1930). Cette méthode n'a pu réellement se développer qu'à partir des années 60 grâce à l'apparition des premiers ordinateurs (Wiberg, 1965). Par mécanique moléculaire, on peut calculer la structure et l'énergie potentielle d'un composé moléculaire. L'énergie potentielle calculée en mécanique moléculaire est nommée énergie stérique, exprimée en $kJ.mol^{-1}$ ou $kcal.mol^{-1}$. L'énergie stérique de la molécule est directement liée à la position des atomes dans l'espace et sera exprimée sous la forme d'une somme de contributions dépendant de chaque coordonnée interne. On peut ainsi chercher la géométrie la plus stable d'une molécule (par optimisation de géométrie) en minimisant son énergie stérique. On peut aussi comparer l'énergie de différentes conformations d'une molécule pour déterminer le conformère le plus stable en faisant ainsi son analyse conformationnelle. Si on compare deux conformères ou deux isomères, plus l'énergie stérique est basse, moins il y a de tension dans la molécule. La géométrie à l'équilibre d'une molécule est ainsi obtenue automatiquement en la relaxant vers son minimum d'énergie. Cependant, l'analyse conformationnelle exhaustive d'une molécule devient rapidement impossible. Par exemple, soient 50 liaisons simples pour lesquelles on ne prend en compte que les conformations décalées (on a donc 3^{50} conformations à calculer). Si on considère 1s pour la minimisation de chaque conformation, il faudra 3^{50} secondes soit 2.10^{16} années !!

2.2 Champ de force de Mécanique Moléculaire

2.2.1 Expression de l'énergie stérique

L'énergie stérique (V_{MM}) est constituée d'une somme de termes sans limitation en nombre. Le nombre de termes dépend directement du champ de force utilisé. En général, dans l'étude de molécules, l'expression minimale est la suivante : $V_{MM} = V_l + V_\theta + V_\phi + V_d$ où

- V_l est la somme de toutes les énergies correspondant à l'élongation de toutes les liaisons par rapport à une valeur de référence : énergie d'élongation des liaisons ou de stretching
- V_θ est la somme de toutes les énergies correspondant à la déformation de tous les angles de valence par rapport à une valeur de référence : énergie de déformation des angles de valence ou de bending
- V_ϕ est la somme de toutes les énergies correspondant à la déformation de tous les angles de torsion par rapport à une valeur de référence : énergie de torsion
- V_d est la somme de toutes les énergies d'interaction entre atomes non-liés. Les atomes non-liés sont séparés par au moins trois liaisons.

Ces énergies sont déterminées par des fonctions et des paramètres constituant le champ de force. Une fois l'énergie stérique calculée pour une géométrie initiale, l'objectif de la mécanique moléculaire est de la minimiser afin d'obtenir une géométrie optimisée de la molécule dans le champ de force utilisé. La mécanique moléculaire étant une méthode empirique, les paramètres utilisés n'ont aucune signification physique précise. Ce sont simplement des valeurs qui permettent de retrouver par le calcul les géométries expérimentales d'un certain nombre de molécules pour lesquelles le champ de force est développé. Les paramètres sont donc transférables d'une molécule à une autre, une fois définis

les paramètres pour chaque type d'atome. Cependant, beaucoup de paramètres sont nécessaires pour traiter un large échantillon de fonctions chimiques.

2.2.2 Paramètres et fonctions utilisés en mécanique moléculaire

Le champ de force est l'ensemble des paramètres et des fonctions utilisés pour le calcul de l'énergie stérique. Il existe un grand nombre de champs de force, développés par des chercheurs et commercialisés ou disponibles gracieusement. C'est N.L. Allinger qui a développé le premier logiciel de calcul par mécanique moléculaire (MM1, 1973). Cette première ébauche appliquée aux alcanes a été suivie de plusieurs versions améliorées traitant les hétéroatomes : MM2 (1977), MM3 (1989) et MM4 (2003). Depuis cette époque, de nombreux champs de force ont été développés, soit dans l'objectif de la modélisation de systèmes chimiques variés, soit dans l'optique de traiter spécifiquement une famille de composés. On peut citer par exemple UFF¹ parmi les premiers. Plusieurs champs de force ont été développés pour la simulation de molécules biologiques (ADN, ARN, protéines, ...) et de leur interaction avec le solvant ou des ligands (petites molécules organiques). On peut citer par exemple Amber/GAFF,² CHARMM,³... Différents champs de force sont également disponibles pour représenter les molécules d'eau dans le traitement de molécules solvatées (TIP3P, TIP4P, ...).⁴ Les fonctions peuvent varier en expression et en nombre d'un champ de force à l'autre ; néanmoins, on retrouve dans chaque champ de force les principales fonctions décrites ci-dessous.

a) Liaisons et angles de valence

— Stretching et bending

Nous savons que les liaisons tendent vers une longueur naturelle dépendant de la nature des atomes impliqués. Il en est de même pour les angles de valence. C'est la raison pour laquelle ils sont représentés par des ressorts en mécanique moléculaire. Un ressort a une longueur naturelle où son énergie potentielle est minimale ; en cas d'élongation ou de compression, l'énergie potentielle du ressort augmente. La fonction énergie potentielle est alors une parabole (potentiel harmonique de la loi de Hooke). Dans le cas de faibles déformations des liaisons et des angles de valence comme les vibrations, on peut également appliquer la loi de Hooke : $V_l = \frac{1}{2}k_l(l - l_0)^2$ et $V_\theta = \frac{1}{2}k_\theta(\theta - \theta_0)^2$ où k est une constante de force et l_0 , θ_0 des valeurs de référence. La parabole est centrée sur la valeur de référence. Le potentiel de Morse n'est pas utilisé dans la majorité des logiciels de Mécanique Moléculaire car c'est une fonction exponentielle ($V_l = D_e[1 - \exp(-a(l - l_e))]^2$) où D_e représente l'énergie de liaison) qu'on préfère remplacer par une fonction puissance pour accélérer les calculs (Figure 2.1). Pour se rapprocher de la fonction de Morse, un développement limité de V_l et V_θ est possible avec des termes d'ordre 2, 3, etc mais le terme cubique entraîne une aberration à longue distance et ne doit être pris en compte que proche du minimum.

— Out-of-plane bending

En présence d'un atome central C, hybridé sp^2 et entouré de 3 voisins (A, B, O), on sait que l'arrangement des atomes doit être trigonal. Or, en mécanique moléculaire, on ne dispose pas d'électrons π conduisant obligatoirement à une structure plane. On doit alors faire appel à deux fonctions dans le calcul de l'énergie stérique : une fonction décrivant la modification des angles de valence dans le plan (bending) et une fonction décrivant la modification des angles de valence dans un plan perpendiculaire (out-of-plane bending) (Tableau 2.1). P étant la projection de C dans le plan (ABO), l'énergie de déformation des angles de valence est la somme des contributions dans le plan et hors du plan.

Les termes $V_{\theta, out-of-plane} = \frac{1}{2}k_\theta(\theta - \theta_0)^2$ auront un paramètre θ_0 égal à 0 et une constante de force relativement élevée de façon à contraindre le système à la planéité.

— Termes croisés

1. a) Rappé, A. K. ; Casewit, C. J. ; Colwell, K. S. ; Goddard, W. A., III ; Skiff, W. M. J. Am. Chem. Soc. 1992, 114, 10024. (b) Casewit, C. J. ; Colwell, K. S. ; Rappé, A. K. J. Am. Chem. Soc. 1992, 114, 10035. (b) Casewit, C. J. ; Colwell, K. S. ; Rappé, A. K. J. Am. Chem. Soc. 1992, 114, 10046.

2. a) Wang, J., Wolf, R. M. ; Caldwell, J. W. ; Kollman, P. A. ; Case, D. A. J. Comput. Chem. 2004, 25, 1157-1174. b) Wang, J., Wang, W., Kollman P. A. ; Case, D. A. J. Mol. Graph. Model. 2006, 25, 247260.

3. B.R. Brooks, R.E. Bruccoleri, B.D. Olafson, D.J. States, S. Swaminathan, Ma. Karplus, J. Comput. Chem 1983, 4, 187-217.

4. Jorgensen, W. L. ; Chandrasekhar, J. ; Madura, J. D. ; Impey, R. W. ; Klein, M. L. J. Chem. Phys 1983, 79, 926-935.

FIGURE 2.1 – Potentiel harmonique (ronds blancs) comparé au potentiel de Morse (ronds noirs) correspondant à l'évolution de l'énergie de liaison en fonction de la distance interatomique r .

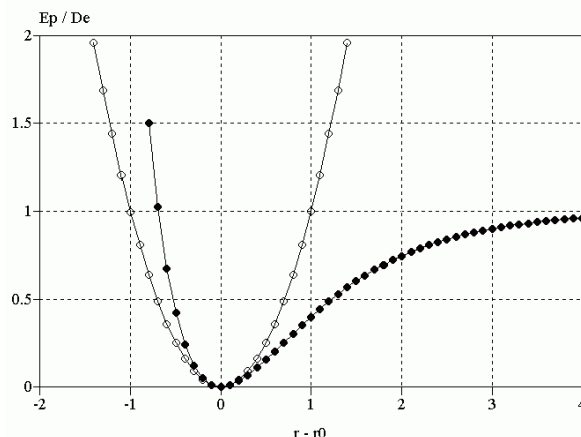


TABLE 2.1 – Composantes dans le plan et hors du plan pour le bending et le out-of-plane bending.

Angle	Composantes dans le plan	Composantes hors du plan
$\theta(ACB)$	$\theta(APB)$	$\theta(COP)$
$\theta(ACO)$	$\theta(APO)$	$\theta(CAP)$
$\theta(BCO)$	$\theta(BPO)$	$\theta(CBP)$

Dans certains champs de force sont ajoutés des termes croisés afin d'affiner les interactions entre stretching, bending, torsion. En effet, quand un angle de valence est anormalement faible, les longueurs de liaison associées sont anormalement grandes. Pour rendre compte de ce phénomène expérimental, on ajoute par exemple la contribution suivante de stretch-bend :

$$V_{l,\theta} = \frac{1}{2} k_{l,\theta} (l_1 - l_{1,0} + l_2 l_{2,0}) (\theta_{12} - \theta_{12,0}).$$

b) Interactions entre atomes non-liés

Le stretching et le bending sont insuffisants pour rendre compte des géométries moléculaires. En effet, si l'on considère deux conformations du pentane (1 : zig-zag plan, 2 : repliée et éclipsée), leurs termes de stretching et de bending ont à peu près la même valeur puisque les longueurs de liaisons et les angles de valence sont proches de leur valeur idéale. Or, la géométrie 1 est beaucoup plus basse en énergie que la géométrie 2 où sont présentes des interactions entre atomes non-liés (atomes d'hydrogène).

Les atomes non-liés sont séparés par au moins trois liaisons : on distingue ainsi les interactions 1-4, 1-5, ...

La fonction utilisée en mécanique moléculaire pour décrire les interactions entre atomes non-liés est dérivée des potentiels d'interaction entre atomes à l'état gazeux (Figure 2.2) : c'est le modèle de van der Waals. La forme générale du potentiel de van der Waals est obtenue par la somme de deux termes correspondant à une faible attraction à longue distance et une forte répulsion à courte distance. En fonction de la nature des atomes considérés, la fonction est caractérisée par la distance σ où elle s'annule, la profondeur du puits ϵ et la pente de la partie répulsive (dureté). La forme la plus générale pour traiter l'interaction entre atomes non-liés est le potentiel de Lennard-Jones 12-6 : $V_{LJ} = 4\epsilon[(\frac{\sigma}{r})^{12} - (\frac{\sigma}{r})^6]$. Il s'écrit également sous la forme : $V_{LJ} = \epsilon[(\frac{r_0}{r})^{12} - 2(\frac{r_0}{r})^6]$ où r_0 correspond au minimum de la fonction. Le potentiel de Lennard-Jones est une approximation du potentiel de van der Waals. L'exposant de la partie attractive est choisi en accord avec les interactions à longue distance entre molécules non-polaires (forces de dispersion). La forme de la partie répulsive n'a pas de réelle justification physique. Elle devrait dépendre exponentiellement de la distance mais le terme de répulsion utilisé est plus pratique à calculer : $r^{12} = r^{6*2}$. D'autres exposants sont utilisés suivant les champs de force (r^9, r^{10}, \dots). Le potentiel de Lennard-Jones offre une grande souplesse grâce à ses

FIGURE 2.2 – Evolution de l'énergie potentielle du dimère de l'argon en fonction de la distance interatomique R .

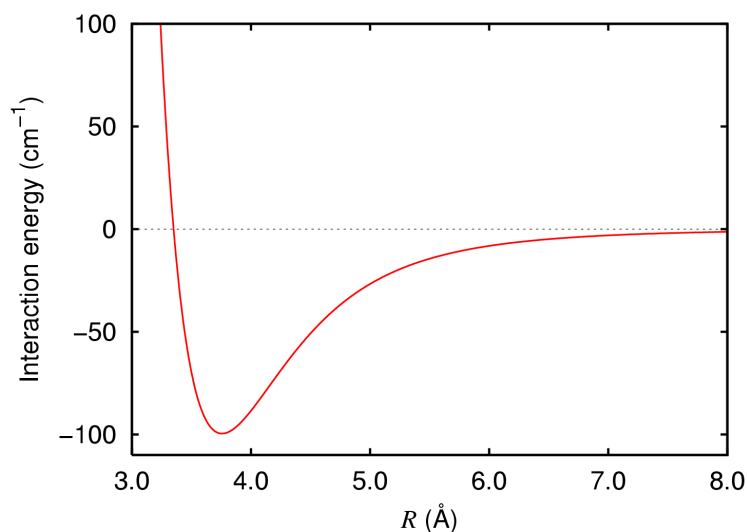
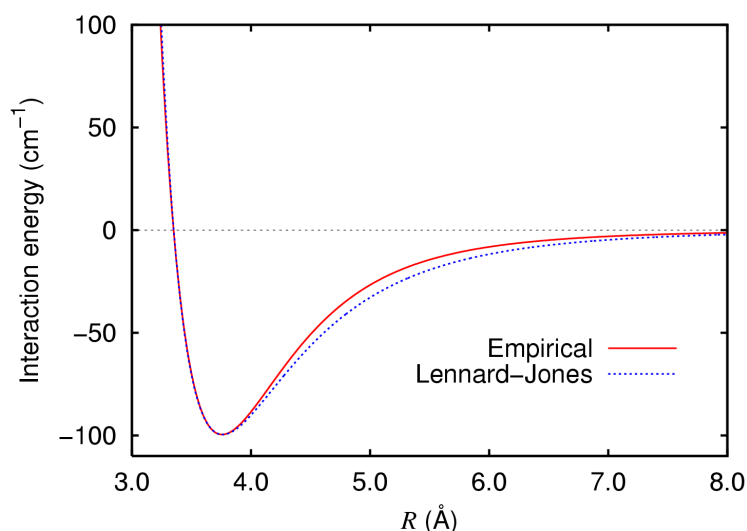


FIGURE 2.3 – Comparaison du potentiel du dimère d'argon et du potentiel de Lennard-Jones paramétré pour l'argon.



paramètres ϵ et σ ajustables à chaque paire d'atomes et rend parfaitement compte des interactions entre atomes non-liés (Figure 2.3).

c) Energie de torsion

Plusieurs essais ont été tentés pour concevoir des champs de force utilisant uniquement le stretching, le bending et les interactions de van der Waals en variant les paramètres et les fonctions. A chaque fois, on a été confronté au même problème : on n'observe pas de différence d'énergie stérique entre la conformation décalée et le conformation éclipsée de l'éthane. Un terme représentant la variation d'énergie lors de la rotation autour d'une liaison (torsion) doit donc être introduit. La fonction ne peut pas être semblable à celle utilisée pour le stretching et le bending car on est en présence de grands déplacements (360°) pour lesquels l'approximation harmonique n'est pas utilisable et la fonction doit être périodique. Habituellement, on utilise une série de Fourier limitée aux trois premiers termes : $V_\phi = \frac{1}{2}[V_1(1 + \cos\phi) + V_2(1 - \cos(2\phi)) + V_3(1 + \cos(3\phi))]$. Les termes en V_1 et en V_3 déstabilisent les formes éclipsées par rapport aux formes décalées. Ils sont donc importants pour les atomes de type sp^3 . Le terme en V_2 déstabilise les formes ayant un angle de torsion à 90° au profit des formes ayant un angle

de torsion de 0° ou 180°. Il est donc important pour décrire correctement un arrangement plan des atomes.

d) Energie électrostatique

Tant que les molécules étudiées sont des alcanes, les interactions électrostatiques sont négligeables. Dès qu'on étudie des molécules comportant un ou plusieurs hétéroatomes, les interactions électrostatiques jouent un rôle très important dans la stabilisation relative des conformations. L'énergie électrostatique est en général calculée en attribuant des charges ponctuelles q_i aux atomes et en calculant :

$$E_{elec} = \frac{1}{D} \sum_i \sum_j \frac{q_i q_j}{r_{ij}}$$

La constante D correspond à la constante diélectrique du milieu et est prise entre 1 et 4 dans la plupart des champs de force. Tout le problème réside dans l'attribution des charges atomiques car ce ne sont pas des observables, mesurables expérimentalement. Dans un nombre croissant de champs de force, les charges atomiques proviennent de calculs quantiques effectués sur des molécules modèles. Le problème est alors déplacé sur le choix de la méthode quantique de calcul des charges : Mulliken, calcul à partir du potentiel électrostatique (CHelp,⁵ CHelpG,⁶ RESP,⁷ ...) ? D'autres méthodes existent, en particulier la méthode de J. Gasteiger et M. Marsili⁸ qui calcule les charges atomiques simplement à partir de la table de connexion de chaque atome. En partant de la charge formelle (0, 1, -1, ...) de chaque atome de la molécule, c'est une méthode itérative dans laquelle les atomes les moins électronégatifs transfèrent de la charge négative vers les atomes les plus électronégatifs. L'avantage de cette méthode est qu'elle est très rapide (quatre à cinq itérations) pour calculer la distribution des charges de grosses molécules.

e) Liaison hydrogène

La présence d'hétéroatomes dans une molécule peut entraîner la formation d'une liaison hydrogène $XH\cdots Y$. Le traitement de ce type d'interaction est indispensable dans l'étude de molécules biologiques par exemple (ADN, ARN, protéines, ...), où la conformation la plus stable de la molécule est en grande partie liée à la présence de liaisons hydrogène. Beaucoup de champs de force ne tiennent pas compte explicitement des liaisons hydrogène qui sont alors englobées dans les interactions électrostatiques et de van der Waals. Certains champs de force remplacent le potentiel de Lennard-Jones 6-12 entre les atomes impliqués dans une liaison hydrogène (H et Y) par un potentiel de Lennard-Jones 12-10 plus attracteur : $V_{lH} = \frac{A}{r_{HY}^{12}} - \frac{B}{r_{HY}^{10}}$. D'autres champs de force complètent cette expression afin de tenir compte non seulement de la distance $Y\cdots H$ mais aussi du caractère directionnel des liaisons hydrogène : $V_{lH} = \left(\frac{C}{r_{HY}^6} - \frac{D}{r_{HY}^4} \right) \cos^4 \theta_{XHY}$.

2.2.3 Paramétrisation de champ de force

A chaque élément du tableau périodique dans un état d'hybridation donné correspond un type dans les logiciels de mécanique moléculaire. Pour chacun de ces types d'atomes, sont définis les paramètres de stretching, de bending, de torsion, de van der Waals, de charges, etc, en fonction des types d'atomes auxquels il est lié. La qualité d'un champ de force de Mécanique Moléculaire, c'est-à-dire la précision et la fiabilité de ses résultats, dépend des fonctions de potentiel et surtout de l'ensemble de ces paramètres. Deux champs de force différents utilisant en général des fonctions de potentiel différentes, il est hasardeux de transférer les paramètres d'un champ de force à l'autre en espérant que cela donne des résultats corrects sans ajustement. Ainsi, lors de l'élaboration d'un nouveau champ de force, la paramétrisation est une tâche difficile qui demande du temps et beaucoup de tests sur différentes familles de molécules de structure connue. Rien que l'ajout de paramètres à un champ de force existant pour traiter une nouvelle famille peut être long et fastidieux car tous les paramètres sont interdépendants. Les paramètres de stretching et de bending sont assez faciles à optimiser (une petite variation de paramètres entraîne

5. L. E. Chirlian, M. M. Francl, J. Comp. Chem. 1987, 8, 894-905.

6. C. M. Breneman, K. B. Wiberg, J. Comp. Chem. 1990, 11, 361-73.

7. C.I. Bayly, P. Cieplak, W.D. Cornell, P.A. Kollman, J. Phys. Chem. 1993, 97, 10269-10280.

8. J. Gasteiger, M. Marsili, Tetrahedron 1980, 36, 3219-3228

une variation importante de la valeur de la fonction), contrairement aux paramètres dits « mous » des interactions de non-liaison et de torsion. Dans les champs de force de première génération, le choix des paramètres provenait exclusivement de données expérimentales (diffraction des rayons X, spectroscopie infrarouge,...) mais, dans les champs de force de seconde génération, on utilise des données expérimentales et des résultats de calculs de Mécanique Quantique (pour les charges et les constantes de force par exemple). L'optimisation des paramètres d'un champ de force peut se faire manuellement par essais-erreurs en commençant par les paramètres mous : énergie de van der Waals puis énergie électrostatique et enfin énergie de torsion (barrières de torsion, énergies relatives des conformères). Les paramètres de bending puis de stretching sont alors optimisés. On peut également choisir une méthode automatique par la technique des moindres carrés. L'avantage apparent est que cette méthode optimise précisément et mécaniquement tous les paramètres sans intervention manuelle, mais elle présente deux inconvénients. Le temps de calcul requis est souvent très long et la méthode des moindres carrés ne peut optimiser que des paramètres x_i ayant la même unité : $erreur = \sum (valeur_{calc} - valeur_{exp})^2$. On est donc amené à utiliser une méthode des moindres carrés pondérée pour tenir compte des différentes unités des paramètres (Å, kJ.mol⁻¹.Å⁻¹, degrés, ...) et des propriétés calculées. D'autre part, la méthode des moindres carrés s'utilise pour des fonctions qui varient linéairement en fonction des paramètres à optimiser et ce n'est pas le cas des fonctions de potentiel de Mécanique Moléculaire (paraboles, fonctions de Morse, fonctions périodiques). L'optimisation des paramètres se fait donc de façon itérative jusqu'à la convergence des paramètres : $erreur(\vec{x} + \delta\vec{x}) = erreur(\vec{x}) + Z\delta\vec{x}$ où \vec{x} représente l'ensemble des paramètres de l'étape 1, $\delta\vec{x}$ est la modification apportée à l'ensemble des paramètres conduisant à l'étape suivante de l'optimisation, et Z est la matrice des dérivées partielles de chaque propriété par rapport à chaque paramètre.

2.3 Application à l'analyse conformationnelle des N-oxy-pyrrolidines

L'analyse conformationnelles des cycles N-oxy-pyrrolidiniques a été menée à l'aide du logiciel GenMol que nous avons modifié afin de traiter :

- la fonction nitroxyle
- la pseudorotation des cycles à cinq chaînons (méthode développée par D. Cremer et J.A. Pople)
- la fonction peroxydique
- l'effet anomère

Ces travaux ont fait l'objet de deux publications et trois communications par affiche.



ELSEVIER

Journal of Molecular Structure (Theochem) 582 (2002) 171–185

THEO
CHEM

www.elsevier.com/locate/theochem

Conformational analysis of five-membered rings by molecular mechanics: application to nitroxides

Didier Siri^{a,*}, Anouk Gaudel-Siri^a, Paul Tordo^b

^aLaboratoire de Chimie Théorique et Modélisation Moléculaire, UMR-CNRS 6517, Université de Provence, Case D42, 13397 Marseille Cedex 20, France

^bLaboratoire Structure et Réactivité des Espèces Paramagnétiques, UMR-CNRS 6517, Université de Provence, Case 521, 13397 Marseille Cedex 20, France

Received 30 July 2001; accepted 6 November 2001

Abstract

We report here a method to perform the conformational analysis of five-membered rings. This method is based on the Cremer and Pople description and it has been implemented in the GenMol software. After testing our method on a series of five-membered rings, we used it to study the behavior of pyrrolidine-*N*-oxy radicals. These calculations allowed us to calculate ESR β -hyperfine coupling constants (β -hfcc) and to compare them with experimental ones. This approach can be used to assist the design of new nitroxide targets with desired properties. © 2002 Elsevier Science B.V. All rights reserved.

Keywords: Molecular mechanics; Pseudorotation surface; Five-membered rings; Nitroxides; ESR

1. Introduction

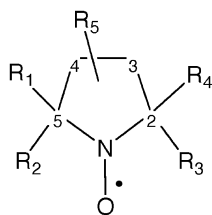
Many aminoxyl radicals (nitroxides) are stable species under ordinary conditions and are widely used in spin-labeling and spin-trapping experiments [1–3]. This stability has allowed to determine some structural parameters of nitroxides by X-ray crystallographic methods [4–10]. Moreover, a large number of stable or persistent five-membered ring aminoxyl radicals (Scheme 1) have been characterized by ESR spectroscopy [11,12]. The ESR parameters of aminoxyl radicals depend directly on the geometry of the favored conformers, and molecular mechanics is helpful to determine these geometries.

In the literature, a lot of simple aminoxyl radicals have been studied with high level quantum mechanics methods, essentially to estimate their equilibrium geometry and spin densities, but few molecular mechanics works have dealt with aminoxyl radicals [13–17] and often consist of force field parametrizations.

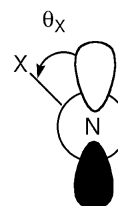
On the other hand, five-membered rings are very flexible molecules and their out of plane motion has been widely studied by quantum mechanics methods [18–21]. The ring conformations are usually described by the mean of two models based on either intracyclic dihedral angles [22,23] or displacements perpendicular to an invariant mean plane [24–27]. Molecular dynamic simulations have been carried out only on cyclopentane [28,29] but some conformational analyses by molecular mechanics of various five-membered ring compounds of biological interest

* Corresponding author. Tel.: +33-4912-884-14; fax: +33-4919-885-12.

E-mail address: siri@dexter.u-3mrs.fr (D. Siri).



Scheme 1.



Scheme 2.

were reported [30–33]. The main advantage of molecular mechanics methods is the short requested time of calculation that allows the conformational study of large molecules.

In a precedent paper [15], we described the results of a molecular mechanics modeling of five-membered aminoxyl radicals using both GenMol [34] and MM2 [35]. The GenMol parameters of the aminoxyl moiety have been refined and two automatic procedures of quantitative conformational analysis of five-membered rings have been implemented in GenMol. In the present study, we report the results concerning various five-membered ring molecules and especially pyrrolidine-*N*-oxyl radicals. Rockenbauer et al. have developed a semi-classical approach based on the fitting of ESR parameters measured at different temperatures [36,37] and their approach was applied to study the geometry of pyrrolidine-*N*-oxyl radicals. In this study, the results of the two methods will be compared.

2. Method

The available experimental data for pyrrolidine-*N*-oxyl radicals are the ESR hyperfine coupling constants (hfcc) between the unpaired electron and the atoms with a non-zero nuclear spin. The TOMER (2,5,5-trimethyl-5-diethoxyphosphoryl-pyrrolidine-1-oxyl) ESR spectrum is reported on Fig. 1. The six main lines result from the coupling with the ^{14}N ($a_{\text{N}} = 13.7$ G) and ^{31}P ($a_{\text{P}} = 50.0$ G) nuclei and are accompanied of satellite lines due to a ^{13}C coupling.

For any GenMol calculated conformation, the β -hfcc are obtained from the Heller–McConnell relation [38]: $a_{\text{X}} = B_{\text{X}} \cos^2 \theta_{\text{X}}$ where θ_{X} is the dihedral angle of the X substituent with the nitrogen p_z orbital (Scheme 2): $B_{\text{P}} = 58.3$ G, $B_{\text{C}} = 9.6$ G [39]. For a set of conformers in Boltzmann proportions, the Boltzmann weighted β -hfcc were calculated and directly compared to the experimental ones.

In order to perform a quantitative conformational analysis of puckered five-membered rings, the method

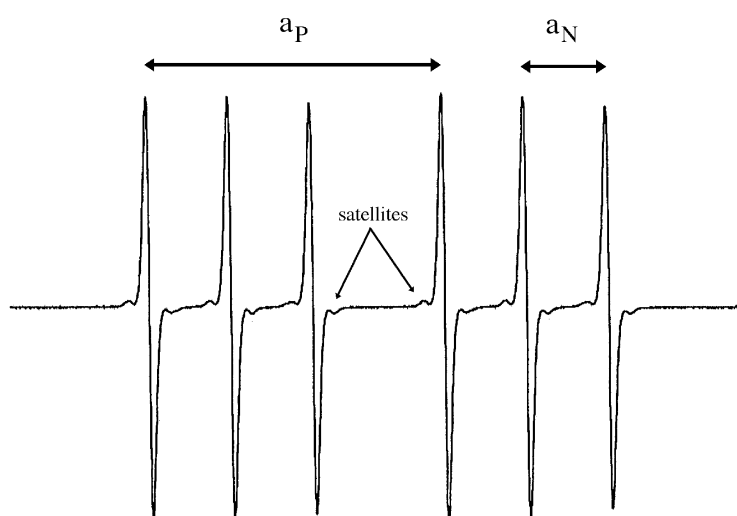
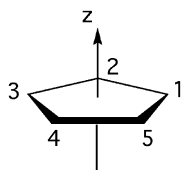


Fig. 1. ESR spectrum of TOMER recorded in benzene at room temperature.



Scheme 3. Invariant mean plane and z direction of the pseudorotational displacement.

developed by Cremer and Pople [24–26] has been implemented in GenMol, in the same way as did French and Tran [27] for furanose rings with MMP2(85). This method is based on the definition of a mean plane that is invariant during the pseudorotation. For any conformation of the ring, the z_j coordinate of the j th atom of the ring measures its displacement out of the mean plane (Scheme 3) and is written (Eq. 1):

$$z_j = \sqrt{\frac{2}{5}} q \cos\left(\frac{4\pi(j-1)}{5} + \varphi\right) \quad \varphi \in [0; 2\pi] \quad (1)$$

$q \in [0.3; 0.5 \text{ \AA}]$ for most of the five-membered rings where q represents the puckering amplitude of the ring and φ describes the ring conformation (Fig. 2). The z_j displacements are normalized so that $\sum_{j=1}^5 z_j^2 = q^2$ and the ring may adopt an infinity of conformations when φ varies from 0 to 360° . Pure twist (T) and envelope (E) conformations are spaced by 18° . In cyclopentane, two conformations at φ and $\varphi + \pi$ are symmetric toward the planar ring and this interconversion may occur by inversion (through the planar form) or pseudorotation. However, the barrier to planarity is usually higher than the pseudorotational barrier, if the latter exists.

With any value of the puckering amplitude q and of the pseudorotation angle ϑ , the corresponding conformation of a five-membered ring may be automatically built by GenMol as follows:

(a) The molecule is placed in the coordinate system defined in Scheme 4:

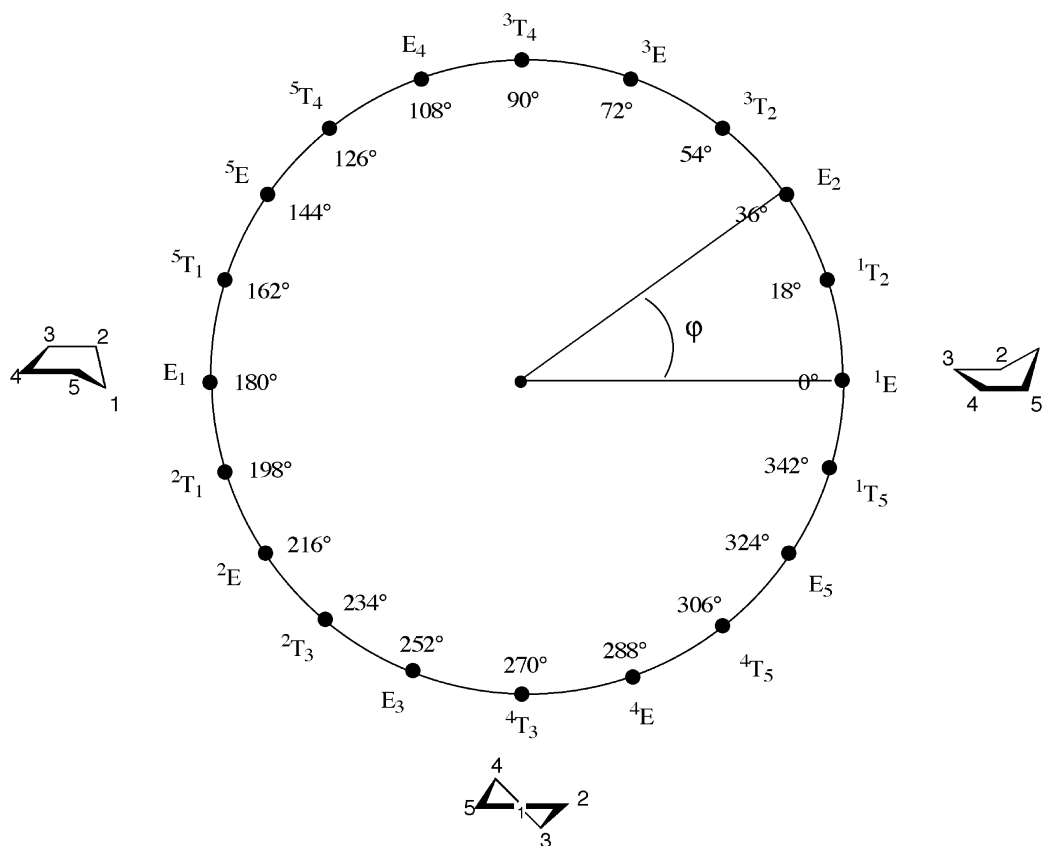
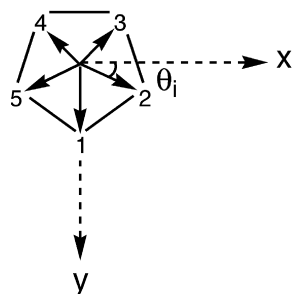


Fig. 2. Usual representation of the pseudorotation of five-membered rings.



Scheme 4. Definition of the coordinate system.

the origin is at the five-membered ring geometric center.

the Oxy plane is defined by the ring mean plane.
the Oy axis goes through the projection of the first atom of the ring in the ring mean plane.

$$\theta_i = \frac{2\pi(i-1)}{5} \text{ for } i = 1, \dots, 5$$

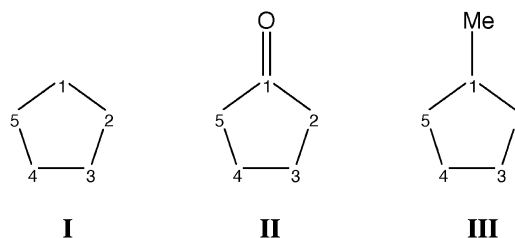
$$\vec{O}_x = \sum_{i=1}^5 \vec{i} \cdot \cos \theta_i \quad \vec{O}_y = \sum_{i=1}^5 \vec{i} \cdot \sin \theta_i$$

where \vec{i} is the vector corresponding to the i th atom

$$\vec{O}_z = \vec{O}_x \wedge \vec{O}_y$$

(b) For each couple (q, φ) , the z coordinate of each ring atom is modified according to Eq. (1)

(c) Then, each substituent bound to each ring atom i undergoes the movement of the atom i .



Scheme 5. I: Cyclopentane, II: Cyclopentanone, III: Methyl-cyclopentane.

(d) Finally, the obtained conformation is optimized by steric energy minimisation.

Two automatic conformational analysis procedures have been implemented in GenMol:

The first procedure is exhaustive: φ varies from 0 to 359° with a step of one degree and q varies from 0 to 1 Å with a step of 0.1 Å. A pseudo-rotational surface including 3960 conformations is constructed and the GenMol values of the pseudo-rotational and ring planarity barriers are obtained.

A potential energy curve is extracted from this surface if for each value of φ , we consider only the most stable conformation. It is interesting to note that this potential energy curve takes into account the

Table 1
GenMol force field parameters

Stretching parameters			
Bond type	r_0 (Å)	k_r (mdyn Å ⁻¹)	
C=O	1.208	10.8	
C(sp ³)-C(sp ³)	1.523	4.4	
C(sp ²)-C(sp ³)	1.497	4.4	
Bending parameters			
Bond angle	θ_0 (deg)	k_θ (mdyn Å rad ⁻²)	
C(sp ³)-C(sp ³)-C(sp ³)	108.0	0.45	
C(sp ³)-C(sp ²)-C(sp ³)	116.6	0.40	
C(sp ³)-C(sp ²)=O	122.5	0.46	
Torsional constants			
Torsion angle	V_1 (kJ mol ⁻¹)	V_2 (kJ mol ⁻¹)	V_3 (kJ mol ⁻¹)
C(sp ³)-C(sp ³)-C(sp ³)-C(sp ³)	0.200	0.270	0.093
C(sp ³)-C(sp ³)-C(sp ³)-C(sp ²)	0.170	0.270	0.093
C(sp ³)-C(sp ³)-C(sp ²)=O	-0.300	1.200	-0.350

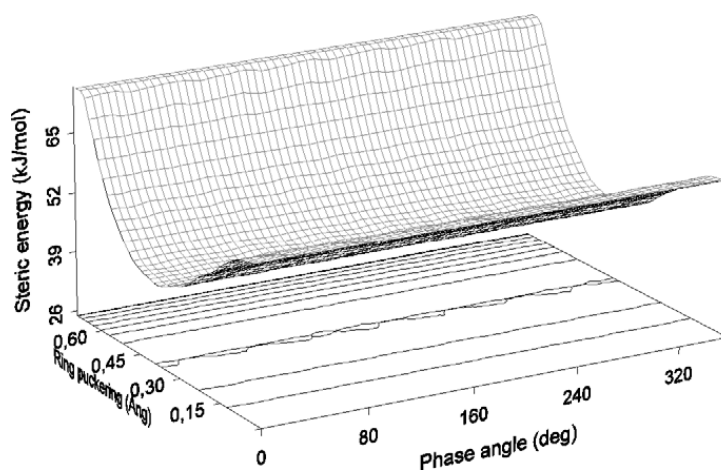


Fig. 3. Pseudorotational surface of cyclopentane. Two contour lines are 6.5 kJ mol^{-1} apart. For clarity, all surfaces are zoomed on the minima.

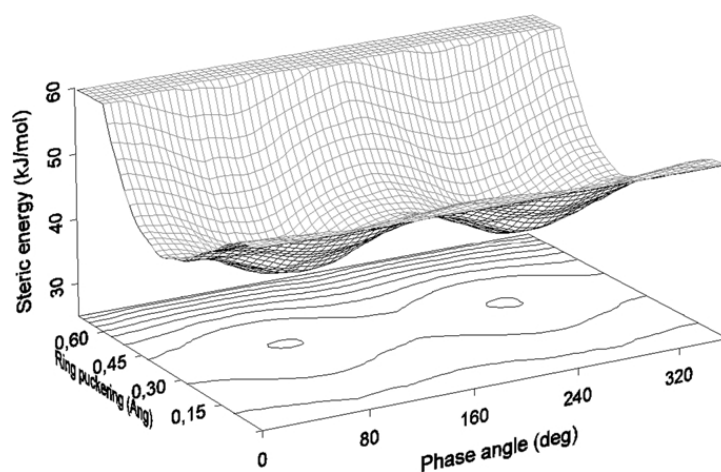


Fig. 4. Pseudorotational surface of cyclopentanone. Two contour lines are 6.7 kJ mol^{-1} apart.

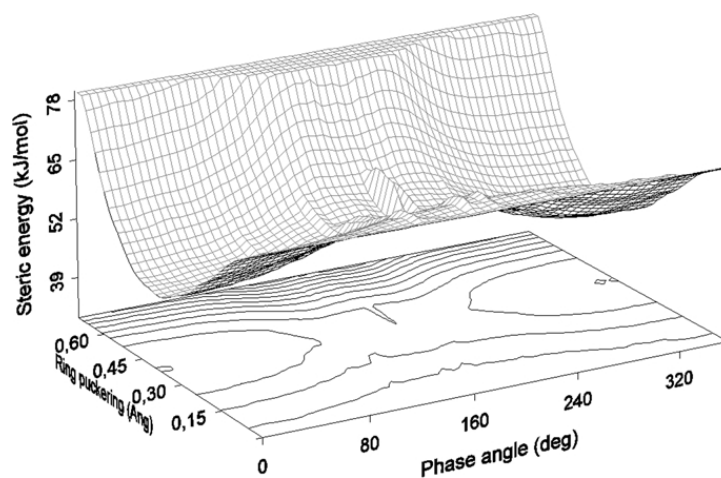


Fig. 5. Pseudorotational surface of methyl-cyclopentane. Two contour lines are 6.6 kJ mol^{-1} apart.

Table 2
Barriers to planarity for **I**, **II** and **III** (Scheme 5)

	GenMol barrier (kJ mol ⁻¹)	MM2 barrier [45] (kJ mol ⁻¹)	Experimental barrier (kJ mol ⁻¹)
I	17.2	19.6	21.6 [41]
II	15.5	13.3	16.7 [44]
III	21.9	–	–

variation of q during the pseudorotation. In the case of pyrrolidine-*N*-oxyl radicals, this pseudopotential function was compared with the pseudorotational potential according to the Rockenbauer's approach [36,37].

The second procedure is a simplification of the first one and it will be explained in the last section.

During this full conformational analysis of the ring conformations, the orientation of the substituents was fixed. In the case of asymmetric substituents like the diethoxyphosphoryl moiety, a preliminary study was done, in which we started from several staggered orientations of the substituents. For each orientation, a rough conformational analysis was carried out: we started from the 10 pure twist and 10 pure envelope conformations and minimized the steric energy to find the most stable conformers lying in a chosen energy range. Only the substituent orientation that gave the less constrained conformers was kept for the full conformational analysis.

3. Results

3.1. Conformational analysis of uncrowded five-membered rings

At first, we tested our full conformational analysis

Table 3
Contributions to the steric energy of the major conformers

	Steric energy ^a (kJ mol ⁻¹)				
	E_{vdW}	$E_{\text{electrostatic}}$	$E_{\text{stretching}}$	E_{bending}	E_{torsion}
I	-0.7	-0.2	0.1	3.6	-19.7
II	0.1	0.2	0.9	5.2	-20.6
III	-3.3	-0.2	-0.3	2.2	-20.5

^a Relative the planar conformation.

procedure with three simple five-membered rings for which experimental data about the pseudorotation were published (Scheme 5). GenMol force field parameters used for these calculations are reported in Table 1. Cyclopentane **I** is the smallest one and represents the basic test of the force field, cyclopentanone **II** is a model of pyrrolidine-*N*-oxyl radicals because of the planarity of the carbonyl function. At last, the

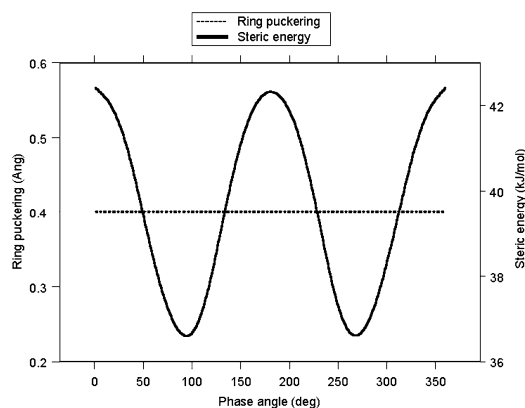


Fig. 6. Variation of the steric energy and of the puckering amplitude for **II** on the pseudorotational pathway. For each value of φ , only the conformation with the lowest steric energy is considered.

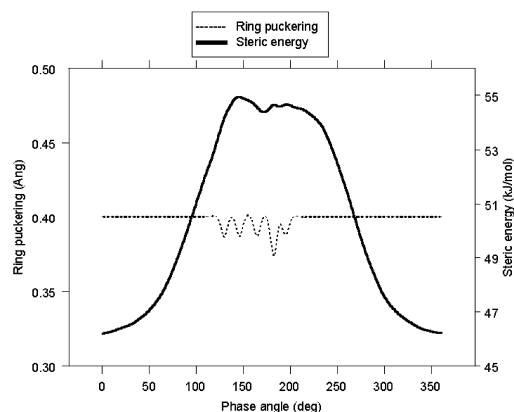


Fig. 7. Variation of the steric energy and of the puckering amplitude for **III** on the pseudorotational pathway. For each value of φ , only the conformation with the lowest steric energy is considered.

Table 4
Calculated pseudorotational barriers

	q (Å)	Minimum		Maximum		Barrier (kJ mol ⁻¹)
		Steric energy (kJ mol ⁻¹)	Location	Steric energy (kJ mol ⁻¹)	Location	
I	0.4	42.3	–	–	–	0
II	0.4	36.6	³ T ₄ , ⁴ T ₃	42.0	¹ E, E ₁	5.4 ^a
III	0.3–0.4	46.2	¹ E	58.7	² T ₁ / ² E ⁵ E/ ⁵ T ₁	12.5

^a Experimental barrier: 16.2 kJ mol⁻¹ for the ground state and 7.2 kJ mol⁻¹ for the excited S¹ state [44].

preferred conformers of methyl-cyclopentane **III** must have the methyl substituent in equatorial position [19]. The pseudorotational surfaces are reported on Figs. 3–5.

The calculated barriers to planarity are slightly underestimated but the relative values were in agreement with the number of eclipsed bonds in the planar form: cyclopentanone < cyclopentane < methyl-cyclopentane (Table 2). Moreover, the calculated (1.1) and experimental (1.3) barrier height ratio **I/III** were in good agreement.

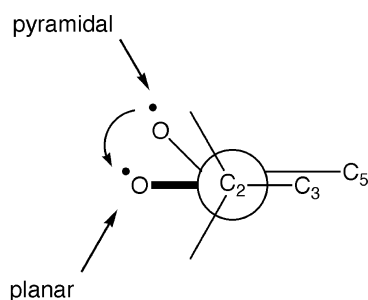
In the planar form, the major part of the steric energy represents the torsional strain of the intracyclic dihedral angles and was thus quite constant in the three cases (Table 3). As expected, the van der Waals interactions and the torsional energy decreased when the ring puckers and the bending energy increased because the intracyclic bond angles get away from the ideal value of 109°.

According to Fig. 3, the free pseudorotation of **I** is well reproduced. The pseudorotation occurs at a constant value of q (0.4 Å), in agreement with the experimental estimated value [40–43] (0.43–0.48 Å). For **II** and **III**, the pseudorotational pathway curves are reported on Figs. 6 and 7. For **II**, two symmetric wells are centered on ³T₄ and ⁴T₃ twist forms with a planar carbonyl function, but the ³E, E₃, ⁴E, E₄ forms are not very higher in energy (less than 2 kJ mol⁻¹). In case **III**, two symmetric conformations with the methyl substituent in axial position represent the maxima on the pseudorotational pathway. There is a slight oscillation of the puckering amplitude around the pseudorotation barrier but it may be attributed to the precision limit of the calculations. The global minimum well is very flat around the ¹E conformer, as provided by ¹H NMR investigations [19].

However, according to recent experimental data

Table 5
GenMol force field parameters for pyrrolidine-*N*-oxyl radicals

Stretching parameters			
Bond type	r_0 (Å)	k_r (mdyn Å ⁻¹)	
N–O [•]	1.2222	5.90	
N–C(sp ³)	1.4700	3.52	
Bending parameters			
Bond angle	θ_0 (deg)	k_r (mdyn Å rad ⁻²)	
C(sp ³)–N–C(sp ³)	112.0	0.70	
N–C(sp ³)–C(sp ³)	103.0	0.40	
C(sp ³)–N–O [•]	120.0	0.56	
Torsional constants			
Torsion angle	V_1 (kJ mol ⁻¹)	V_2 (kJ mol ⁻¹)	V_3 (kJ mol ⁻¹)
C(sp ³)–C(sp ³)–N–O [•]	0	0	0
C(sp ³)–C(sp ³)–C(sp ³)–N	0	0	0

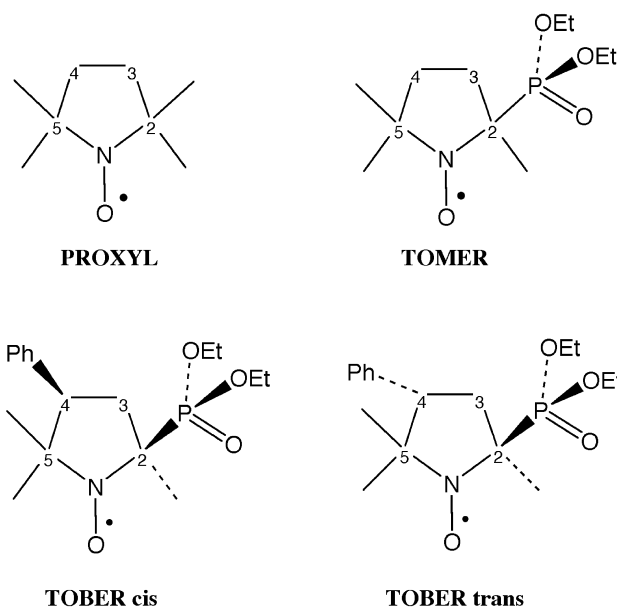


Scheme 6. Torsional angles around the aminoxyl function in pyrrolidine-*N*-oxyl radicals.

about **II** [44], GenMol pseudorotational barriers seem to be underestimated (Table 4). In summary, GenMol provides a fast conformational analysis of five-membered rings with conformers in good agreement with the experimental data: only the quantitative estimations of the pseudorotational barriers disagree with experimental data but the comparison of the barrier heights provides informations about the steric hindrance in the various tested five-membered rings. However, if the preferred conformations are governed by pure electronic factors like in the unsubstituted pyrrolidine [21], molecular mechanics methods are not appropriate or a specific parametrization of the force field must be considered (e.g. anomeric effect).

3.2. Pyrrolidine-*N*-oxyl radicals

Force field parameters for pyrrolidine-*N*-oxyl radicals are summarized in Table 5. It is not necessary to introduce improper torsional parameters for pyrrolidine-*N*-oxyl radicals because the aminoxyl function is assumed to be planar [13,46] in five-membered rings (Scheme 6). If we consider some structural parameters of PROXYL (2,2,5,5-tetramethyl-pyrrolidine-*N*-oxyl)



Scheme 7. PROXYL: 2,2,5,5-tetramethyl-pyrrolidine-*N*-oxyl, TOMER: 2,5,5-trimethyl-2-diethoxyphosphoryl-pyrrolidine-*N*-oxyl, TOBER: 2,5,5-trimethyl-2-diethoxyphosphoryl-4-phenyl-pyrrolidine-*N*-oxyl.

(Scheme 7), GenMol geometry was in good agreement with the experimental data and the results obtained with different methods (Table 6). Starting from the 20 pure conformations, a brief conformational analysis was carried out on TOMER [15,16] (2,5,5-trimethyl-2-diethoxyphosphoryl-pyrrolidine-*N*-oxyl) and the two diastereoisomers of TOBER [15,16] (2,5,5-trimethyl-2-diethoxyphosphoryl-4-phenyl-pyrrolidine-*N*-oxyl) to determine the best orientation of the diethoxyphosphoryl moiety. The full automatic procedure was then applied to the four stable pyrrolidine-*N*-oxyl radicals represented on Scheme 7.

The analysis of the pseudorotational surfaces clearly shows two major conformers for PROXYL

Table 6

Comparison of some structural parameters of PROXYL. PM3 calculations were performed with AMPAC 6.55 [48] and DFT calculations with GAUSSIAN94 [49]

	Exp [55]	GenMol	MM2(88)	PM3 [47]	B3LYP/6-31G*
N–O (Å)	1.272(3)	1.274	1.317	1.242	1.276
C–N (Å)	1.484(3)	1.496	1.486	1.524	1.490
θ (CNC) (deg.)	118.9	115.1	114.8	111.2	115.5

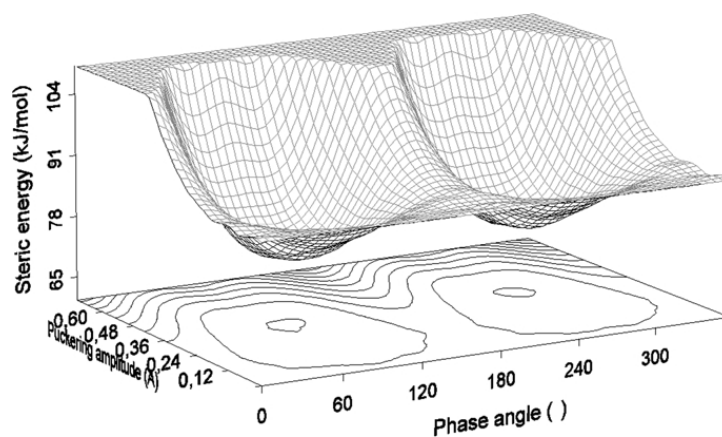


Fig. 8. Pseudorotational surface of PROXYL. Two contour lines are 13.0 kJ mol^{-1} apart.

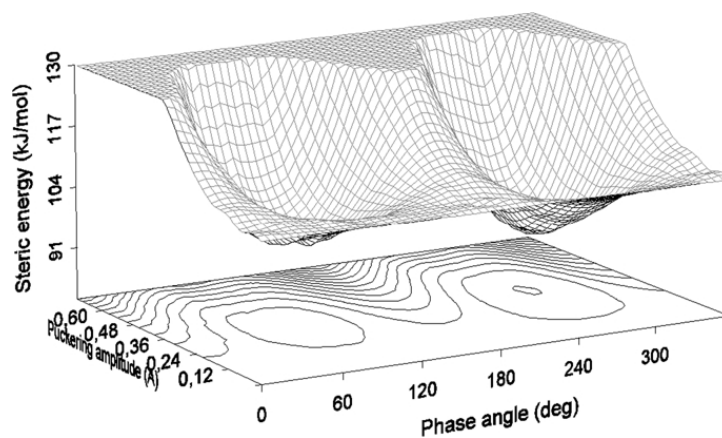


Fig. 9. Pseudorotational surface of TOMER. Two contour lines are 11.0 kJ mol^{-1} apart.

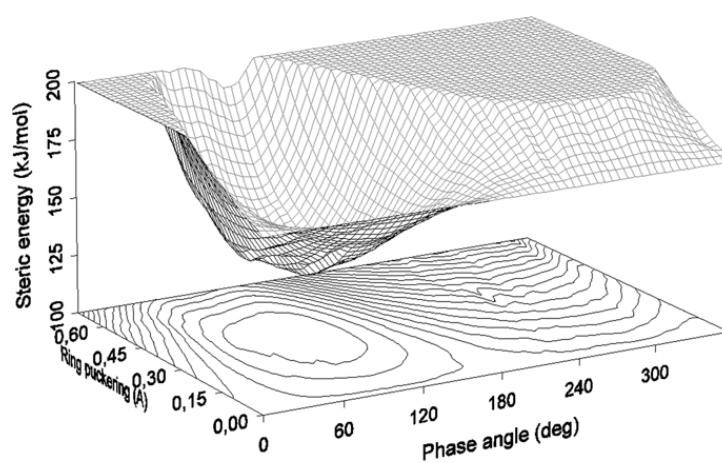


Fig. 10. Pseudorotational surface of TOBER *cis*. Two contour lines are 13.3 kJ mol^{-1} apart.

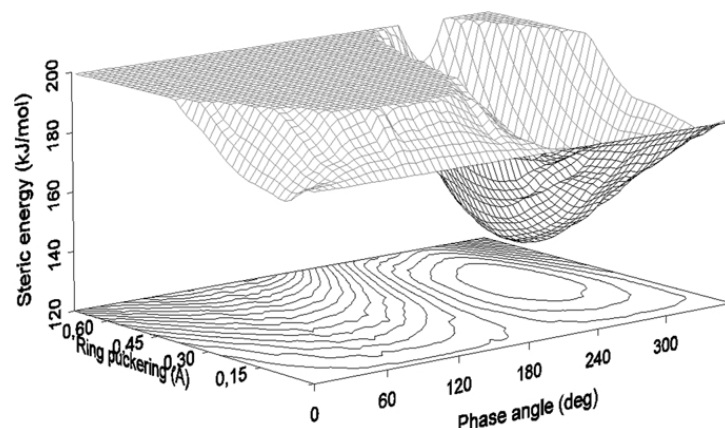


Fig. 11. Pseudorotational surface of TOBER *trans*. Two contour lines are 13.4 kJ mol^{-1} apart.

and TOMER and a single conformer for each diastereoisomer of TOBER (Figs. 8–11). The symmetry of PROXYL is well reproduced since we have two equivalent wells, and the phosphorylated compounds have characteristic features. The results are easier to interpret on Figs. 12 and 13, showing the pseudorotational pathway. For PROXYL and TOMER, the chemical exchange occurs between two twist conformers (3T_4 and 4T_3) and the pseudorotational barrier heights are 14 and 16 kJ mol^{-1} , respectively. In fact, according to the variation of the puckering amplitude (Figs. 12 and 13), this is not a pseudorotation anymore but a pseudoinversion or an inversion due to the four β -substituents on C_2 and C_5 .

The diethoxyphosphoryl moiety of TOMER is in a

pseudoaxial position whereas it is a bulky substituent. This preferential orientation is attributed to a stabilizing anomeric effect [50–53] between the electronegative dialkylphosphoryl group [54] and the aminoxyl function (Scheme 8).

In the case of TOBER, there is neither pseudorotation nor inversion (Figs. 10 and 11) because of the phenyl substituent on C_4 , which is blocked in an equatorial position and prevents any conformational exchange (the calculated barriers are 43 and 48 kJ mol^{-1} for TOBER *cis* and TOBER *trans*, respectively). In TOBER *trans*, there is a synergy between two stabilizing effects (equatorial phenyl and anomeric effect) whereas these two interactions are *opposite* in TOBER *cis* (equatorial phenyl or

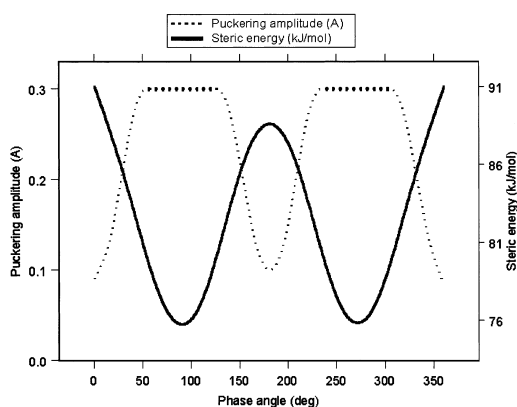


Fig. 12. Variation of the steric energy and of the puckering amplitude for PROXYL on the pseudorotational pathway. For each value of φ , only the conformation with the lowest steric energy is considered.

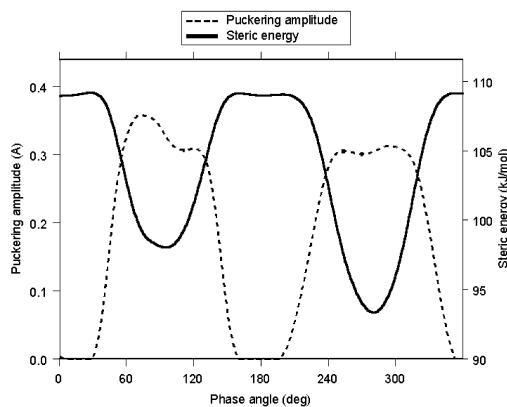
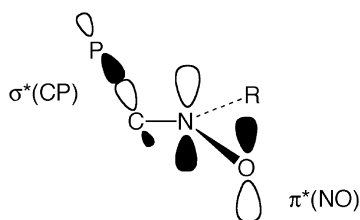


Fig. 13. Variation of the steric energy and of the puckering amplitude for TOMER on the pseudorotational pathway. For each value of φ , only the conformation with the lowest steric energy is considered.



Scheme 8. Anomeric interaction between the nitroxyl π system and the σ^* (CP) bond.

anomeric effect). As expected, the steric interaction dominates and leads to a final conformation with a pseudoequatorial phosphorus.

It is interesting to note that TOBER *cis* and TOBER *trans* of the phosphorus coupling are almost independent of the temperature ($a_p = -5.8 \times 10^{-3} T + 53.06$). This trend is in agreement with the existence of a largely major conformer for these radicals. However, for the TOMER, the variation of a_p is significant ($a_p = -19.6 \times 10^{-3} T + 50.57$), in agree-

ment with the existence of a rapid exchange between two conformers with different a_p values.

3.3. Comparison of the two pseudorotational potentials

A semi-classical approach based on the simulation of ESR spectra at different temperatures has been developed [36,37]. From the experimental β -hfcc and temperature coefficients, a pseudopotential is established:

$$V(\varphi) = \frac{V_1}{2}(1 - \cos(\varphi - \varphi_1)) + \frac{V_2}{2}(1 - \cos 2(\varphi - \varphi_2))$$

where V_1 , V_2 , φ_1 and φ_2 parameters are adjusted to reproduce the experimental data. The pseudopotential allows to determine the nature of the conformers (relative energies and Boltzmann proportions) and the pseudorotational barrier. The variation of the

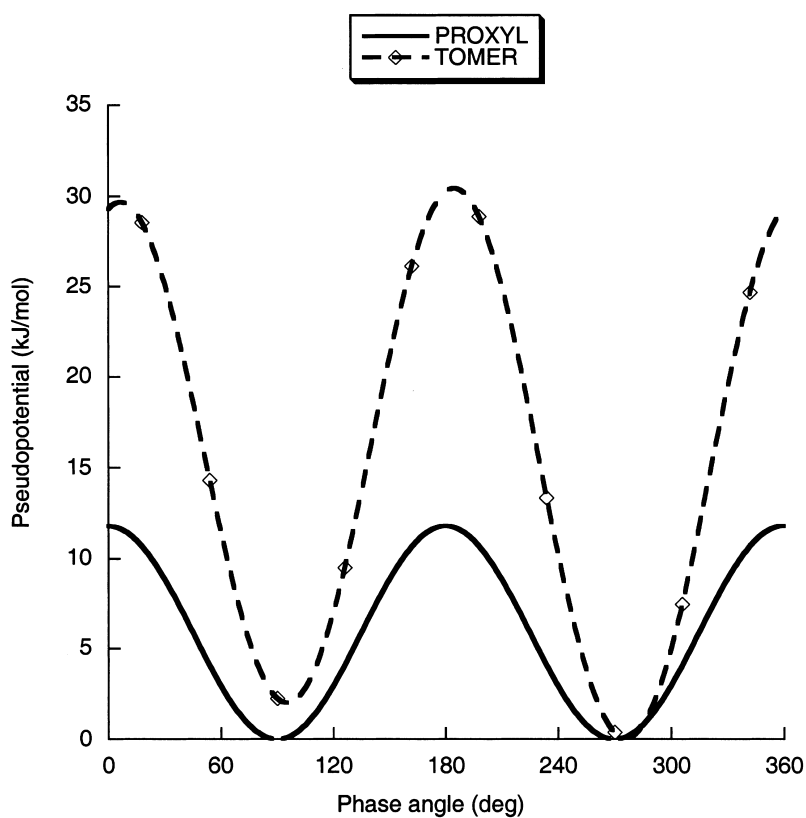


Fig. 14. Pseudopotential for PROXYL [36,37] and TOMER [15,16].

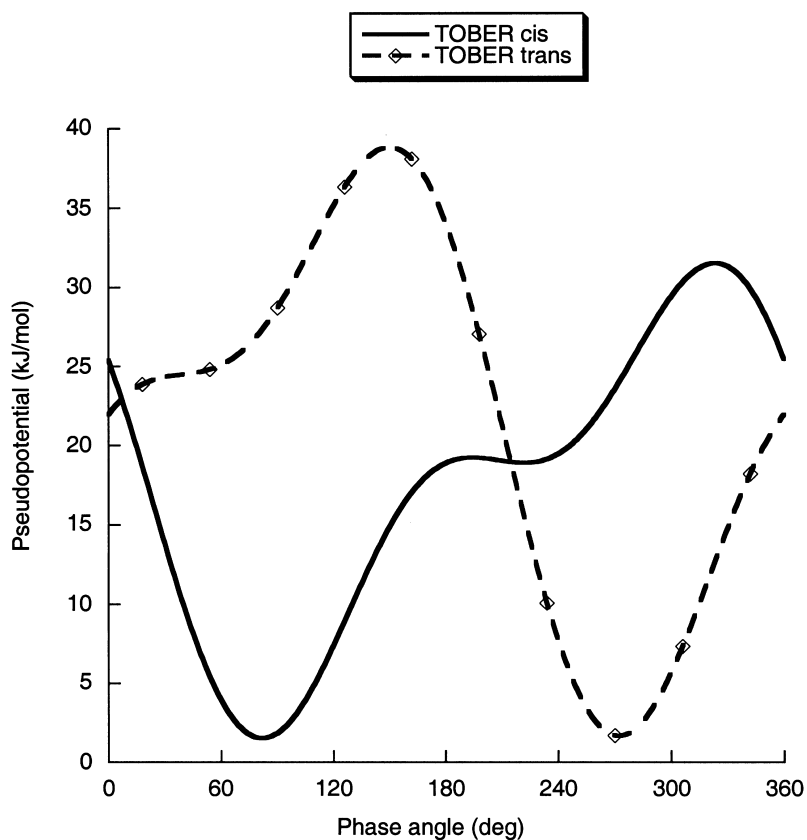


Fig. 15. Pseudopotential for the two diastereoisomers of TOBER [15,16].

Table 7

Comparison of the energetic values resulting from the two studies and the positions of the critical points obtained by the two methods

	GenMol		Rockenbauer [36,37]	
	Barrier (kJ mol ⁻¹)	Gap between minima (kJ mol ⁻¹)	Barrier (kJ mol ⁻¹)	Gap between minima (kJ mol ⁻¹)
PROXYL	14	0	11.8	0
TOMER	16	4	30.2	2
TOBER <i>cis</i>	43	–	30	–
TOBER <i>trans</i>	48	–	37.2	–

	GenMol				Rockenbauer [36,37]			
	Minima		Maxima		Minima		Maxima	
	φ_1 (deg)	φ_2 (deg)	φ_3 (deg)	φ_4 (deg)	φ_1 (deg)	φ_2 (deg)	φ_3 (deg)	φ_4 (deg)
PROXYL	88	273	3	180	90	270	0	180
TOMER	94	282	(-16;45) ^a	(147–209) ^a	95	276	7	185
TOBER <i>cis</i>	100	–	(-178;21) ^a	–	82	–	324	–
TOBER <i>trans</i>	–	291	–	(14–201) ^a	–	272	–	150

^a Range of the phase angle for which the planar form is the lowest conformation.

Table 8
 β -hfcc of PROXYL calculated by integration on the whole pseudorotational curve

	GenMol	Exp [36,37]
$\langle a_{\beta_1} \rangle$ (G)	7.1	7.3
$\langle a_{\beta_2} \rangle$ (G)	7.0	7.0
$\langle a_{\beta_3} \rangle$ (G)	7.1	7.6
$\langle a_{\beta_4} \rangle$ (G)	7.1	6.8
Mean value (G)	7.1	6.9

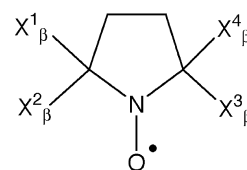
puckering during the pseudorotation is neglected. The Boltzmann weighted β -hfcc are calculated according to:

$$\langle a_X \rangle = \frac{\sum_i B^i \cos^2 \theta_i \cdot \exp(-V_i/kT)}{\sum_i \exp(-V_i/kT)}$$

where V_i is the pseudopotential value for the i th conformation.

This method has been applied to the four pyrrolidine-*N*-oxyl radicals (Figs. 14 and 15) and the results were compared to the molecular mechanics study.

Both methods provided similar results (Figs. 10–15



Scheme 9.

and Table 7). For PROXYL, the minima positions are very close and the two calculated barriers were in good agreement. For TOMER, the minima are located around the same positions but we found a large difference between the barrier values. Unlike the Rockenbauer's approach, our molecular mechanics method takes into account the variation of the puckering amplitude during the ring motion. For the maximum value of the steric energy, we found that the puckering amplitude value was close to zero (planar conformation) (Fig. 13). With both methods, we found a unique minimum for each diastereoisomer of TOBER (Figs. 10, 11 and 15). The minima positions of each diastereoisomer are close: 100 vs. 82° for TOBER *cis* and 291 vs. 272° for TOBER *trans* (Table 7). The GenMol barrier values are overestimated. Nevertheless, the GenMol (1.1) and the Rockerbauer's (1.2) barrier height ratio (*trans/cis*) are in good agreement.

Table 9
 β -hfcc of the phosphorylated pyrrolidine-*N*-oxyl radicals calculated by integration on the whole pseudorotational curve

	TOMER		TOBER <i>cis</i>		TOBER <i>trans</i>	
	GenMol	Exp [39]	GenMol	Exp [39]	GenMol	Exp [39]
$\langle a_{\beta_1} \rangle$ (G)	7.2	7.2	4.3	3.0	9.5	8.1
$\langle a_{\beta_2} \rangle$ (G)	5.6	5.6	9.1	9.3	3.5	5.2
$\langle a_{\beta_3} \rangle$ (G)	7.2	5.0	7.5	8.6	8.3	4.1
$\langle a_{\beta_4} \rangle$ (G)	45.1	50.2	42.0	36.4	38.0	53.0

Table 10
 Conformers resulting from the simplified conformational analysis

	Conformer 1				Conformer 2			
	Type	E_{steric} (kJ mol ⁻¹)	φ (deg.)	q (Å)	Type	E_{steric} (kJ mol ⁻¹)	φ (deg.)	q (Å)
PROXYL	⁴ T ₃	74	269	0.34	³ T ₄	74	84	0.34
TOMER	⁴ T ₃	87	267	0.34	³ T ₄	93	99	0.33
TOBER <i>cis</i>	³ T ₄	114	92	0.33	–	–	–	–
TOBER <i>trans</i>	⁴ T ₃	109	276	0.33	–	–	–	–

Table 11
 β -hfcc of PROXYL calculated from 3T_4 and 4T_3 conformers

	GenMol	Exp [36,37]
$\langle a_{\beta_1} \rangle$ (G)	7.3	7.3
$\langle a_{\beta_2} \rangle$ (G)	6.9	7.0
$\langle a_{\beta_3} \rangle$ (G)	7.5	7.6
$\langle a_{\beta_4} \rangle$ (G)	6.9	6.8
Mean value (G)	7.2	6.9

3.4. Hyperfine coupling constant calculation

From the pseudorotational curves (Figs. 12 and 13), we calculated the Boltzmann weighted β -hfcc of each β - X^k nucleus with non zero spin (Scheme 9) according to: $\langle a_X \rangle = \sum_{i=1}^{360} p_i a_{X_i}$ and compared them to the experimental values (Tables 8 and 9). For PROXYL, GenMol provided a good estimation of the β -hfcc, however, the values obtained for the β -phosphorylated nitroxides were not in agreement with experimental data (Table 9). As it will be shown in the next section, GenMol calculations were satisfying to determine the minima on the pseudorotational path. However, the pseudorotational barriers were underestimated thus suggesting that the weight of some conformations is overestimated to calculate the β -hfcc. To check this point, we decided to calculate the β -hfcc considering only two conformers for PROXYL and TOMER and one conformer for each diastereoisomer of TOBER.

3.5. Simplified conformational analysis

The 20 ideal conformations ($\varphi = 0, 18, 36, \dots, 342^\circ$) with an arbitrary puckering amplitude $q = 0.4 \text{ \AA}$ are automatically built by the GenMol software. Each conformation is then fully optimized and classified (${}^3T_4, {}^3E, \dots$). After removing the redundancies, the β -

hfcc calculations were done on the most stable conformers only (Table 10).

The β -hfcc calculated from one (for TOBER *cis* and *trans*) or two (for TOMER and PROXYL) conformers are in much better agreement with the experimental values (Tables 11 and 12). These results confirm that the problem encountered with the β -hfcc calculated from the 360 conformations was due to underestimated pseudorotational barriers.

4. Conclusion

GenMol appeared to be a useful tool for the conformational analysis of five-membered rings. Compared to earlier studies, we considered the variation of the ring puckering during the pseudorotation. A dramatic variation of the puckering amplitude during the ring motion of highly substituted pyrrolidine-*N*-oxyl radicals has been established, leading to a pseudoinversion or an inversion rather than a true pseudorotation. When a phenyl substituent is fixed on the carbon 3 of the ring, because of strong steric interactions, only one major conformer exists. Compared with the results obtained by the pseudopotential method, GenMol failed to give a good quantitative estimation of barrier heights for the pseudorotation of some five-membered rings. However, the relative values give a qualitative idea of the steric strain variation during the pseudorotation and (or) the inversion.

The main advantage of this molecular mechanics approach is its predictive character since it allows to design new nitroxides with a desired conformational behavior and a characteristic ESR spectrum.

The conformations of pyrrolidine-*N*-oxyl radicals are essentially governed by steric interactions and molecular mechanics is a fast and efficient method to model such interactions. Moreover, the simplified conformational

Table 12
 β -hfcc calculated from either two rapidly exchanging conformers (TOMER) or a single conformer (TOBER *cis*, TOBER *trans*)

	TOMER		TOBER <i>cis</i>		TOBER <i>trans</i>	
	GenMol	Exp [39]	GenMol	Exp [39]	GenMol	Exp [39]
$\langle a_{\beta_1} \rangle$ (G)	8.3	7.2	5.4	3.0	8.8	8.1
$\langle a_{\beta_2} \rangle$ (G)	6.1	5.6	8.7	9.3	5.2	5.2
$\langle a_{\beta_3} \rangle$ (G)	5.8	5.0	8.5	8.6	6.3	4.1
$\langle a_{\beta_4} \rangle$ (G)	52.5	50.2	36.8	36.4	50.1	53.0

analysis limited to the most stable conformers, turned out to be more efficient than the calculation over the full pseudorotational surface. It may be thus applied to five-membered rings bearing many bulky substituents without a huge increase of the calculation time.

References

- [1] L.D. Berliner (Ed.), Spin Labelling, Theory and Applications, vol. 1, Academic Press, New York, 1976.
- [2] L.D. Berliner (Ed.), Spin Labelling, Theory and Applications, vol. 2, Academic Press, New York, 1979.
- [3] N. Kocherginsky, H.M. Swartz, Nitroxide Spin Labels, CRC Press, Boca Raton, 1995.
- [4] B. Chion, A. Capiomont, J. Lajz rowicz, Acta Cryst. B 28 (1972) 618.
- [5] T.A. Olszak, M.J. Grabowski, K. Gwozdziński, Acta Cryst. C 49 (1993) 1722.
- [6] T.A. Olszak, P.H. Sobczynski, A. Brzozowski, M.J. Grabowski, K. Gwozdziński, Acta Cryst. C 51 (1995) 121.
- [7] R. Benassi, F. Taddei, L. Greci, L. Marchetti, G.D. Andreotti, G. Bocelli, P. Sgarabotto, J. Chem. Soc., Perkin Trans. 2 (1980) 786.
- [8] J.C.A. Boeyens, G.J. Kruger, Acta Cryst. B 26 (1970) 668.
- [9] A. Grand, P. Rey, Acta Cryst. B 35 (1979) 2149.
- [10] W. Turley, F.P. Boer, Acta Cryst. B 28 (1972) 1641.
- [11] A.R. Forrester, in: H. Fisher, K.H. Hellwege (Eds.), Landolt–B rnstein Magnetic Properties of Free Radicals, Landolt–B rnstein Magnetic Properties of Free Radicals 1979, pp. 386–442 Part C1.
- [12] A.R. Forrester, in: H. Fisher, K.H. Hellwege (Eds.), Landolt–B rnstein Magnetic Properties of Free Radicals, vol. 17, Springer, Berlin, 1989, pp. 126–187.
- [13] V. Barone, A. Bencini, M. Cossi, A. Di Matteo, M. Mattesini, F. Totti, J. Am. Chem. Soc. 120 (1998) 7069.
- [14] K. Sakakibara, H. Kawamura, T. Nagata, J. Ren, M. Hirota, K. Shimazaki, T. Chuman, Bull. Chem. Soc. Jpn 67 (1994) 2768.
- [15] F. Vila, P. Tordo, D. Siri, G. P pe, Free Rad. Res. Commun. 19 (1993) S17–S22.
- [16] A. Mercier, Y. Berchadsky, D. Badrudin, S. Pietri, P. Tordo, Tetrahedron Lett. 32 (1991) 2125.
- [17] J.M. Tronchet, A. Ricca, F. Barbalat-Rey, M. Geoffroy, Carbohydr. Res. 214 (1991) 235.
- [18] D. Cremer, J.A. Pople, J. Am. Chem. Soc. 97 (1975) 1358.
- [19] D. Cremer, J.S. Binkley, J.A. Pople, J. Am. Chem. Soc. 98 (1976) 6836.
- [20] E. Cortez, J. Laane, J. Mol. Struct. 346 (1995) 41.
- [21] L. Carballeira, I. P rez-Juste, J. Chem. Soc. Perkin Trans. 2 (1998) 1339.
- [22] C. Altona, M. Sundaralingam, J. Am. Chem. Soc. 94 (1972) 8205.
- [23] H.J. Geise, C. Altona, C. Romers, Tetrahedron Lett. 15 (1967) 1383.
- [24] D. Cremer, J.A. Pople, J. Am. Chem. Soc. 97 (1975) 1354.
- [25] H. Essen, D. Cremer, Acta Cryst. B 40 (1984) 418.
- [26] D. Cremer, J. Phys. Chem. 94 (1990) 5502.
- [27] A.D. French, V. Tran, Biopolymers 29 (1990) 1599.
- [28] W.D. Cornell, M.P. Ha, Y. Sun, P.A. Kollman, J. Comput. Chem. 17 (1996) 1541.
- [29] W. Cui, F. Li, N.L. Allinger, J. Am. Chem. Soc. 115 (1993) 2943.
- [30] M.T. Gordon, T.L. Lowary, C.M. Hadad, J. Am. Chem. Soc. 121 (1999) 9682.
- [31] J. Gruza, J. Koca, S. P rez, A. Imberty, J. Mol. Struct. (Theochem) 424 (1998) 269.
- [32] S. P rez, A. Imberty, S.B. Engelsen, J. Gruza, K. Mazeau, J. Jimenez-Barbero, A. Poveda, J.-F. Espinosa, B.P. van Eyck, G. Johnson, A.D. French, M.L. Kouwijzer, P.D.J. Grootenuis, A. Bernardi, L. Raimondi, H. Senderowitz, V. Durier, G. Vergoten, K. Rasmussen, Carbohydr. Res. 314 (1998) 141.
- [33] J. Raap, J.H. van Boom, H.C. van Lieshout, C.A.G. Haasnoot, J. Am. Chem. Soc. 110 (1988) 2736.
- [34] G. P pe, D. Siri, Stud. Phys. Theor. Chem. 11 (1990) 411.
- [35] N.L. Allinger, J. Am. Chem. Soc. 99 (1977) S8127.
- [36] A. Rockenbauer, M. Gy r, O. Hankovszky, K. Hideg, in: M.C.R. Symons (Ed.), Electron Spin Resonance, vol. 11A, The Royal Society of Chemistry, Cambridge (UK), 1988, p. 145.
- [37] A. Rockenbauer, L. Korecz, K. Hideg, J. Chem. Soc., Perkin Trans. 2 (1993) 2149.
- [38] C. Heller, H.M. Mac Connell, J. Chem. Phys. 32 (1960) 1535.
- [39] L. Dembrowski, J.-P. Finet, C. Fr jaille, F. Le Moigne, R. Maurin, A. Mercier, P. Pages, P. Stipa, P. Tordo, Free Rad. Res. Commun. 19 (1993) S23.
- [40] J.E. Kilpatrick, K. Pitzer, R. Spitzer, J. Am. Chem. Soc. 69 (1947) 2483.
- [41] J.R. Durig, D.W. Wertz, J. Chem. Phys. 49 (1968) 2118.
- [42] L.A. Carreira, G.J. Jiang, W. Person, J.N. Willis, J. Chem. Phys. 56 (1972) 1440.
- [43] L.E. Bauman, J. Laane, J. Phys. Chem. 92 (1988) 1040.
- [44] J. Choo, J. Laane, J. Chem. Phys. 101 (1994) 2772.
- [45] R.L. Rosas, C. Cooper, J. Laane, J. Phys. Chem. 94 (1990) 1830.
- [46] I. Komaromi, J.M.J. Tronchet, J. Phys. Chem. 99 (1995) 10213.
- [47] J.J.P. Stewart, J. Comput. Chem. 10 (1989) 209.
- [48] Ampac 6.55,  1998 Semichem, Inc., PO BOX 1649, Shawnee, KS 66222.
- [49] M.J. Frisch, G.W. Trucks, H.B. Schlegel, P.M.W. Gill, B.G. Johnson, M.A. Robb, J.R. Cheeseman, T. Keith, G.A. Petersson, J.A. Montgomery, K. Raghavachari, M.A. Al-Laham, V.G. Zakrzewski, J.V. Ortiz, J.B. Foresman, J. Ciolowski, B.B. Stefanov, A. Nanayakkara, M. Challacimbe, C.Y. Peng, P. Y. Ayala, W. Chen, M.W. Wong, J.L. Andres, E.S. Replogle, R. Gomperts, R.L. Martin, D.J. Fox, J.S. Binkley, D.J. Defrees, J. Baker, J.P. Stewart, M. Head-Gordon, C. Gonzalez, J.A. Pople, GAUSSIAN94, Gaussian Inc., Pittsburgh, 1995.
- [50] E. Juaristi, G. Cuevas, Tetrahedron 48 (1992) 5019.
- [51] V.G.S. Box, Heterocycles 31 (1990) 1157.
- [52] P. Deslongchamps, Stereoelectronic Effects in Organic Chemistry, Pergamon Press, Oxford, 1983, pp. 4–53.
- [53] U. Salzner, J. Org. Chem. 60 (1995) 986.
- [54] J. Katzhendler, I. Ringel, R. Karaman, H. Zaher, E. Breuer, J. Chem. Soc., Perkin Trans. 2 (1997) 341–349.
- [55] F.H. Allen, O. Kennard, 3D search and research using the Cambridge structural database, Chem. Des. Autom. News 8 (1993) 31.

Large Phosphorus Hyperfine Coupling as a Sensitive Tool for Studying Molecular Dynamics: ESR and Molecular Mechanics Studies of Ring Interconversion in the *cis*-2,5-Diphosphoryl-2,5-dimethyl-pyrrolidinoxyl Radical

Antal Rockenbauer,[†] Anouk Gaudel-Siri,[‡] Didier Siri,[‡] Yves Berchadsky,[§] François Le Moigne,[§] Gilles Olive,[§] and Paul Tordo^{*,§}

Chemical Research Center, Institute of Chemistry H-1075 Budapest, Pusztaszeri 59, Hungary, Laboratoire de Chimie Théorique et Modélisation Moléculaire, UMR 6517, CNRS-Universités d'Aix-Marseille I et III, Case D42, 13397 Marseille, Cédex 20, France, and Laboratoire Structure et Réactivité des Espèces Paramagnétiques, UMR 6517, CNRS-Universités d'Aix-Marseille I et III, Case 521, 13397 Marseille, Cédex 20, France

Received: June 5, 2002; In Final Form: January 20, 2003

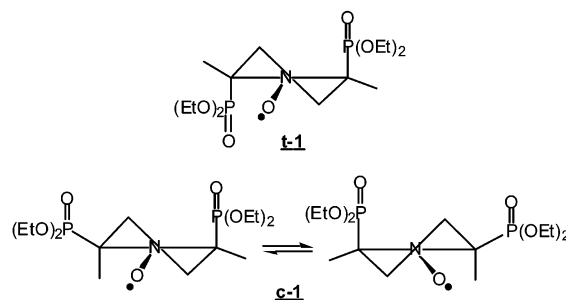
ESR spectra of *cis*- and *trans*- β -diphosphorylated pyrrolidine-*N*-oxyl radicals, **c-1** and **t-1**, were studied in liquid and frozen solution. The expected 1:2:1 triplet (a_P (2)) of the 1:1:1 triplet (a_N) was observed for **t-1**; however, for **c-1**, the inner lines of the 1:2:1 triplet showed a dramatic broadening characteristic of chemical exchange between two equivalent conformations. Owing to the large difference in the hyperfine splitting constants (hfsc) of the exchanging phosphorus ($\Delta a_P \approx 21$ G), the coalescence temperature was unusually high (193 K, in *n*-pentane), and the potential barrier for ring interconversion (10.5 kJ mol⁻¹) was easily obtained from the temperature dependence of the exchange rate. This value was in very good agreement with the value obtained for an empirical pseudorotational potential (11 kJ mol⁻¹) that was adjusted to fit the temperature dependence of the phosphorus hfsc. For **c-1**, molecular mechanics calculations gave similar characteristics for the pseudorotational potential and indicated the existence of two identical minima with distorted geometries lying between ³T₄ and ³E or ⁴T₃ and E₃. For **t-1**, only the ³T₄ conformer was found to be significantly populated. Frozen solution spectra showed that the phosphorus hfsc anisotropy is higher when the C–P bond is pseudoaxial; this result can be explained by a geometry-dependent delocalization of the unpaired electron into the phosphorus 3p orbitals.

Introduction

Because of the biological importance of various five-membered rings such as those of ribose rings in nucleic acids¹ and proline residues in peptides and proteins,² there is still considerable interest in determining the conformational states of five-membered rings. Pyrrolidine-*N*-oxyl radicals (Scheme 1) form an important class of five-membered ring radicals. If their dismutation is prevented by the absence of hydrogens on the α carbons, then most of these radicals are chemically stable, and different approaches have been developed to investigate their conformational behavior.^{3,4}

The conformers of five-membered rings can be close to either envelope (E) or twist (T) geometries (Figure 1). Conversion among the various conformers is usually thought to occur through pseudorotation. Spectroscopic techniques often fail to give reliable information on the heights and positions of barriers to interconversion, except for few simple molecules when the microwave technique is applicable.⁵ As compared to six-membered rings containing six σ bonds (sp³ carbon or nitrogen atoms) where energetically well-separated (ΔG^0 is ca. 20 kJ mol⁻¹) and slowly interconverting (the interconversion fre-

SCHEME 1



quency is less than 5×10^8 s⁻¹ below room temperature) conformers exist,⁶ the analogous five-membered rings are rather flexible, and interconversion is fast. (ΔG^0 does not exceed 10 kJ mol⁻¹, and the interconversion frequency is larger than 7×10^9 s⁻¹ above 200 K.^{7,8a}) This difference is evident in ESR spectroscopy studies where line-width alternation due to chemical exchange is often observed in the spectra of radicals centered on a six-membered ring. However, for the five-membered ring analogues, such phenomena were detected only in a few cases using the low-temperature matrix technique.⁸ For five-membered ring radicals, the lack of line-width alternation is caused by the complete averaging of coupling constants due to the fast pseudorotation.

Line broadening resulting from chemical exchange depends on the square of the differences in the coupling constants for

* Corresponding author. E-mail: tordo@srepir1.univ-mrs.fr. Tel: 33 4 91 632 851.

[†] Institute of Chemistry.

[‡] Laboratoire de Chimie Théorique et Modélisation Moléculaire, CNRS-Universités d'Aix-Marseille I et III.

[§] Laboratoire Structure et Réactivité des Espèces Paramagnétiques, CNRS-Universités d'Aix-Marseille I et III.

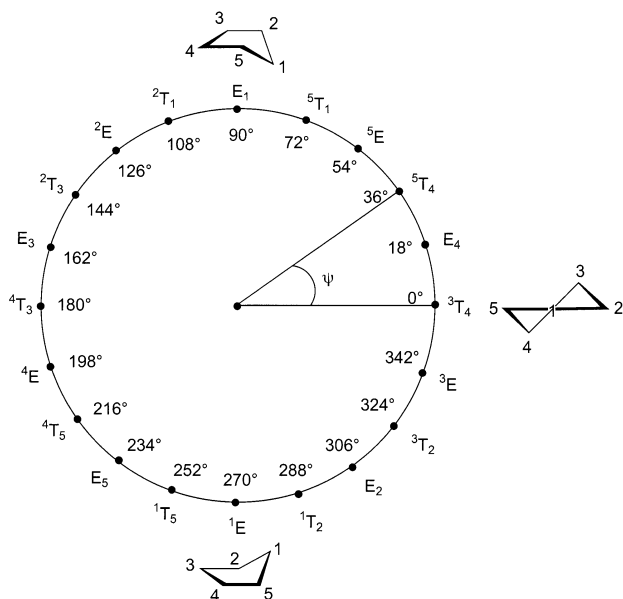


Figure 1. Usual representation of the pseudorotation of five-membered rings.

interconverting sites, and since β -phosphorus couplings are typically two or three times larger than the respective β -hydrogen couplings, the presence of a β - ^{31}P atom in a free radical should enhance the chance to observe chemical exchange.

In our earlier studies, dramatic line-broadening effects were indeed observed on the ESR spectra of peroxy radical adducts of 2-diethoxyphosphoryl-2-methyl-3,4-dihydro-2H-pyrrole-1-oxide (DEPMPO)^{9a,b} as well as on those of geminal diphosphoryl-substituted pyrrolidinoxyl radicals.^{9c} Interconversion between conformers with different ring geometries resulting from hindered rotation around the O—OR bond in the first case or the C—P bond in the second case^{9c} can explain the observed line broadening. However, in both cases, the barrier for ring inversion does not represent the major contribution to the total barrier for interconversion, and thus the rate of ring inversion is not available from ESR experiments.

Because of the preference of the pyrrolidinoxyl radicals for $^3\text{T}_4$ and $^4\text{T}_3$ twist conformations³ and the preference of the diethoxyphosphoryl group for axial geometry,^{3c} no ring interconversion was observed for *trans*-2,5-diethoxy-phosphoryl-2,5-dimethyl-pyrrolidinoxyl nitroxide **t-1** (Scheme 1, Figure 2). However, for *cis*-2,5-diethoxyphosphoryl-2,5-dimethyl-pyrrolidinoxyl nitroxide **c-1** (Scheme 1), one phosphoryl substituent occupies the preferred axial geometry, and the second is forced to the less stable equatorial orientation. As a consequence, a double minimum is expected in the pseudorotational itinerary of the pyrrolidinoxyl ring.

In the present paper, we give a complete analysis of the ESR spectra of **c-1** recorded over a large temperature range. To obtain reliable calculated data, liquid and frozen solution spectra were simulated by an automatic parameter-fitting procedure.¹⁰ The study of the influence of temperature on the interconversion rate yielded the thermodynamic parameters of the process. We also considered the influence of solvent molecules on the chemical exchange. Moreover, in frozen solution, where different ring geometries can be fixed by solvation, we examined the possibility of phase transition due to molecular rearrangements in the coordination sphere.

Finally, to have a complete description of the pseudorotational itinerary, conformational analysis of **t-1** and **c-1** was performed

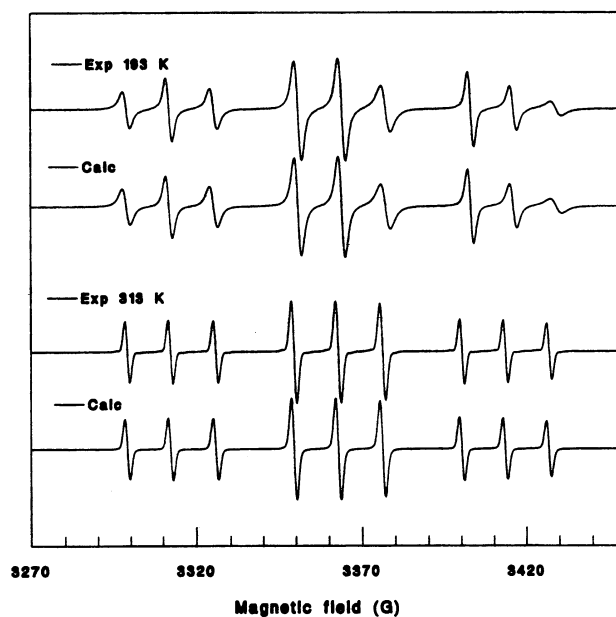


Figure 2. Experimental and calculated ESR spectra for **t-1**: 193 K (top) and 313 K (bottom).

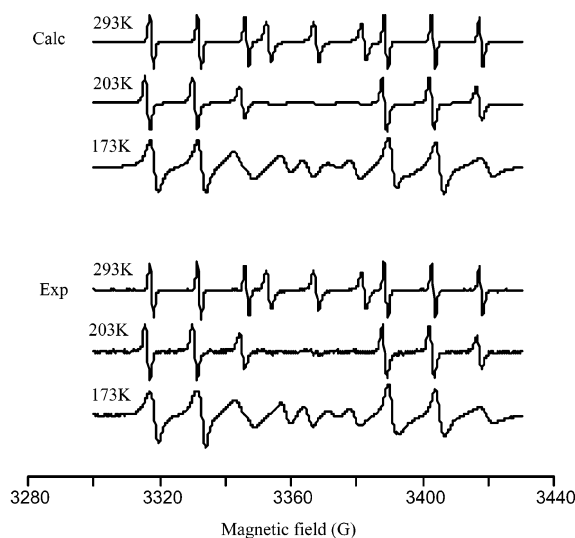


Figure 3. Experimental and calculated ESR spectra for **c-1** at different temperatures.

using molecular mechanics calculations. In this approach, the influence of rotation around the C—P bonds was considered.

Results and Discussion

ESR Spectra. The ESR spectrum of **t-1** consisted of a large 1:2:1 triplet due to coupling with two equivalent phosphorus nuclei, each line being further split into the 1:1:1 triplet of ^{14}N . As shown in Figure 2, no chemical exchange was observed in the temperature range between 193 and 313 K.^{9c}

At elevated temperature, the ESR spectra of **t-1** and **c-1** are similar. However, for the *cis* isomer, the inner lines of the 1:2:1 triplet showed a dramatic broadening that is characteristic of a chemical exchange (Figure 3). A decrease in the temperature increased the broadening of the inner lines, whereas lines in the wings remained sharp. Inner and outer lines had nearly identical amplitudes at 253 K, and coalescence was achieved at 193 K. Below this temperature, new lines evolved in the center of the spectrum, indicating the presence of frozen conformers.

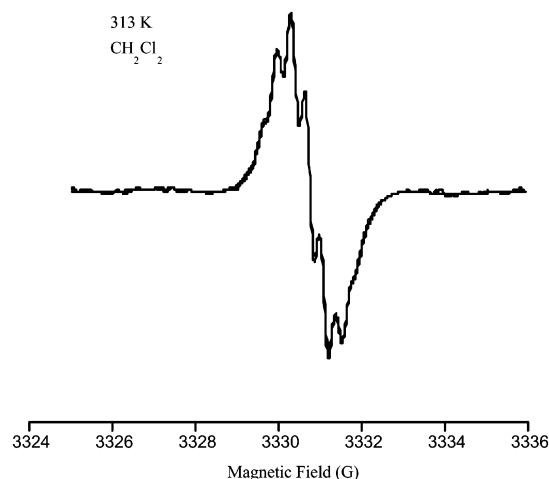


Figure 4. Experimental and calculated central line of the low-field nitrogen triplet for **c-1** showing the resolution of long-range couplings.

Below 133 K, anisotropic frozen solution spectra can be detected; further cooling to 103 K increased the line width. All of these spectral changes were reversible.

Significant solvent effects were also observed; better spectrum resolution was found in CH_2Cl_2 and benzene, where long-range proton couplings give a further multiplet structure. Simulations optimizing the square deviation between experimental and calculated spectra showed that eight hydrogens (six from the two methyl groups and two from the methylene groups) build up the multiplet structure (Figure 4).

Computer Simulations for Liquid Solution. For all ESR spectra of β -phosphorylated pyrrolidinoxyl radicals, the relative amplitudes of nitrogen triplet lines are different for the different quantum numbers of the phosphorus nuclei. This dependence can be described by two further relaxation parameters β' and γ' , and the line widths were computed from the equation $\Delta H_{MM} = \alpha + \beta M + \gamma M^2 + \beta' M' + \gamma' MM'$, where M and M' represent the magnetic quantum numbers of nitrogen and phosphorus, respectively. The terms $\beta' M'$ and $\gamma' MM'$ are a consequence of the large anisotropy of the phosphorus hyperfine interaction. The ESR spectra were calculated with the automatic fitting procedure in which alternative algorithms were applied to achieve convergence in the least-squares process.¹⁰ Between 333 and 143 K, the spectra of **c-1** were calculated by assuming a chemical exchange between two symmetric conformers. Ten parameters were adjusted, namely, the g factor, a_N , a_P^A , a_P^B , the exchange rate $k = 1/\tau$ as well as the five relaxation parameters α , β , γ , β' , and γ' . At elevated temperature, the parameter fitting cannot give a reliable difference between a_P^A and a_P^B (Δa_P), which makes the determination of the exchange rate less precise. To obtain confident results in the high-temperature region, Δa_P was fixed at a value determined from spectra recorded below the coalescence temperature, and a nine-parameter fit was carried out. When they were resolved, long-range proton couplings and ^{13}C satellite lines were also simulated. The values of the adjusted hfsc and their temperature coefficients are listed in Table 1.

An Arrhenius plot of the exchange time showed good linearity (Figure 5), though above 303 K the exchange rate showed significant acceleration. The Arrhenius parameters in the low-temperature region are $E_a = 10.5 \text{ kJ mol}^{-1}$ and $k = 2.5 \times 10^{11} \text{ s}^{-1}$ for $1/T = 0$.

Computer Simulations for Frozen Solution. Since the inclusion of rhombic parameters did not improve the quality of the fit significantly, the frozen solution spectra were simulated assuming axially symmetric g , a_N , a_P^A , and a_P^B tensors. For

TABLE 1: Experimental and Calculated ESR Parameters for c-1 and t-1

	c-1					
	hfsc (G)		temp coeff (mG deg ⁻¹)		potential constants (kJ mol ⁻¹)	
	simulated	computed ^c	measured	computed ^c	V_1	V_2
a_N	14.06 ^a		1.9 ^a		8.5	15.0
a_P^A	46.97 ^a	46.67	-11.2 ^a	-10.5		
a_P^B	25.80 ^a	25.63	-0.6 ^a	0.2		
a_{Me}	0.36 ^b					
$a_{\text{H(CH}_2)}$	0.28 ^b					
	t-1					
	hfsc (G)		temp coeff (mG deg ⁻¹)		potential constants (kJ mol ⁻¹)	
	simulated ^d	computed ^c	measured ^d	computed ^c	V_1	V_2
a_N	13.20				8.7	22.7
a_P	50.97	51.28	-11.2	-11.3		
a_{Me}	0.52					
$a_{\text{H(CH}_2)}$	0.30					
$a_{\text{H(CH}_2)}$	0.17 ^c					

^a In pentane. ^b In CH_2Cl_2 . ^c Computed by the semiempirical approach. In CH_2Cl_2 $a_N = 14.5 \text{ G}$, $a_P^A = 45.2 \text{ G}$, $a_P^B = 27.16 \text{ G}$, and ^{13}C couplings are 6.4 and 5.4 G. ^d In toluene.

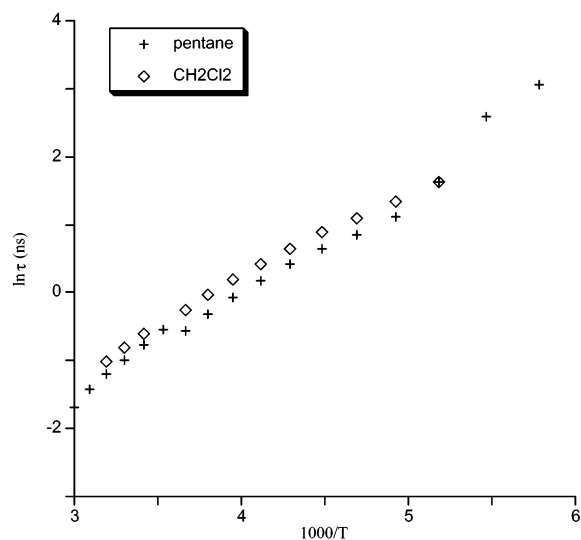


Figure 5. Arrhenius plot of the exchange time for **c-1**.

strain broadening, $\Delta H_{ii} = [\alpha_{ii} + \beta M + \gamma M^2]^{1/2}$, where $i = x, y$, or z ,^{10c} was taken in account by an axially symmetric α tensor, and β and γ were considered to be isotropic. Line shape was computed as a mixture of Lorentzian and Gaussian components. Altogether, 13 parameters were adjusted, and good agreement was observed between calculated and experimental spectra (Figure 6).

The average of the principal values of hyperfine tensors (Table 2) was rather close to the isotropic constants determined in liquid solution (Table 1).

The frozen-solution spectra showed significant ^{31}P anisotropy: for the axial phosphorus, the parallel component is larger than the perpendicular one by 8.8 G, whereas the opposite and a smaller difference (1.7 G) was observed for the equatorial phosphorus. The same trend was also observed by Chachaty et al.¹¹ for mono β -phosphorylated nitroxide radicals: when the isotropic ^{31}P hfsc was large ($a_P = 58\text{--}60 \text{ G}$), the parallel component exceeded the perpendicular one by 7–8 G, whereas the difference was significantly smaller (4 G) when a_P was less than 40 G. This anisotropy cannot be explained by a direct

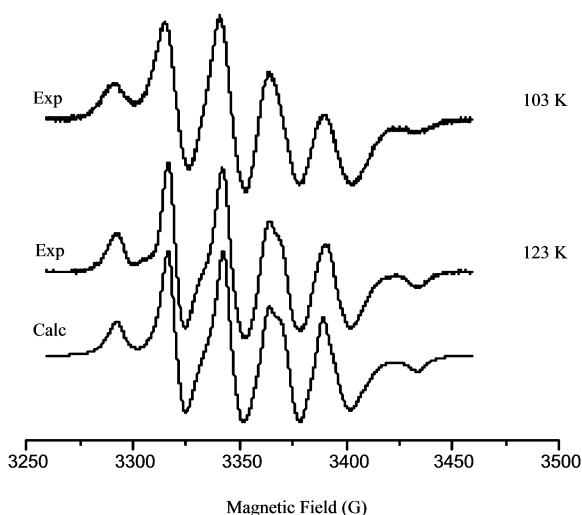


Figure 6. Experimental and calculated ESR spectra for **c-1** recorded in frozen *n*-pentane.

TABLE 2: g and hfsc Tensors for **c-1 in Frozen *n*-Pentane**

temp (K)	123	103
$g_{ }$	2.00221	2.00244
g_{\perp}	2.00761	2.00757
$a_{N }$ (G)	30.8	29.6
$a_{N\perp}$ (G)	5.0	7.0
$a_{P }^A$ (G)	24.0	26.5
$a_{P\perp}^A$ (G)	25.7	25.5
$a_{P }^B$ (G)	55.1	56.0
$a_{P\perp}^B$ (G)	46.3	42.3

dipolar interaction between the π unpaired electron and the ^{31}P nuclei. For a N–P distance of around 2.7×10^{-8} cm, the anisotropy should be smaller than 1 G. The large ^{31}P anisotropy could result from hyperconjugation between the singly occupied molecular orbital (SOMO) and the C–P bonds. Contrary to the case of the C–H bond, where spin density is transferred only to the 1s AO of hydrogen, the C–P bond spin density is transferred both to 3s and 3p AOs of phosphorus. As a consequence, the same Heller–McConnell¹²-type angular dependence should exist both for the isotropic and anisotropic hyperfine interactions; furthermore, the local symmetry axis for dipolar interaction should be parallel to the C–P bond. For the axial C–P bond, the dihedral angle is small, and the local symmetry axis is close to the principal direction of the unpaired electron density; therefore, $a_{||}(\text{P})$ is large. However, for the equatorial C–P bond, the local symmetry axis is almost perpendicular to the principal direction of the unpaired electron density, leading to larger $a_{\perp}(\text{P})$.

There is a significant difference between the frozen-solution spectra recorded at 133 and 103 K. At 133 K, the line shape is mainly Lorentzian (79% character), and at 103 K, it becomes mainly Gaussian (93% character). This trend can be explained by residual motion above 103 K.

Relaxation and Solvent Effects. The exchange rate also exhibited significant solvent dependence; it was somewhat larger in CH_2Cl_2 . (The slope in the Arrhenius plot was the same, but its position was shifted.) This indicates complex formation between CH_2Cl_2 molecules and nitroxide radicals. The relaxation parameters for the nitrogen triplet ($\alpha + \beta M + \gamma M^2$) showed different behavior: although α was significantly larger in *n*-pentane, the β and γ parameters were slightly larger in CH_2Cl_2 . The enhancement of α can be caused by a stronger spin–spin exchange in *n*-pentane that is due to the more frequent

molecular encounters in a less viscous medium, whereas the increase in β and γ can be rationalized by a slower rotation in CH_2Cl_2 that is due to complex formation. The phosphorus relaxation given by β' and γ' was rather significant at low temperature, which indicates significant hyperfine anisotropy for β -phosphorus contrary to the case of β -hydrogen splitting. The presence of phosphorus relaxation was less clear for **c-1**, where chemical exchange is also present; however, for **t-1**, strongly different amplitude ratios were observed for the three nitrogen triplets. The sharpest lines were the central line and the first line in the low-field triplet and the high-field triplet, respectively.

Semiempirical Approach to the Pseudorotation of the Pyrrolidinoyl Ring. We previously developed an ESR method utilizing the temperature dependence of β - ^{13}C hfsc that gives quantitative information about the pseudorotation of pyrrolidinoyl rings.³ We assumed the following potential function

$$V = -\frac{1}{2}V_1[1 + \cos(\psi - \psi_1)] - \frac{1}{2}V_2[\cos(2(\psi - \psi_2))] \quad (1)$$

where ψ is the pseudorotation phase with a value set to zero for conformation ${}^3\text{T}_4$ (Figure 1). Because of the symmetry of **c-1**, $\psi_1 = \pi/2$, and $\psi_2 = 0$, and for a fixed puckering angle φ_0 (assumed to be ca. 40° from X-ray data¹³), all torsion angles and dihedral angles can be computed as a function of ψ .¹⁴ We verified that the puckering angle affects the hfsc only slightly, thus its value is not critical within a wide range (between 30 and 45°).

The torsion angles are

$$\varphi_j = \varphi_0 \cos\left[\psi + \frac{4\pi}{5}(j-1)\right]$$

where the torsion angle is denoted by φ_j instead of the more conventional notation using four indices as $\varphi_{j-2, j-1, j+1, j+2}$. The dihedral angles of substituents on the C-2 and C-5 carbons are $\theta_2 = \pi/6 \pm \varphi_4$ and $\theta_5 = \pi/6 \pm \varphi_3$, respectively, where \pm refers to the methyl or phosphoryl substituents.

The phosphorus coupling a_P was obtained from the simplified Heller–McConnell relation, $a_P = 58 \cos^2(\theta)$.¹⁵ The mean value of $\cos^2(\theta)$ can be calculated by using the Boltzmann populations (eq 2) where the integration is carried out on the whole pseudorotational itinerary.

$$\langle \cos^2(\theta) \rangle = \frac{\int_0^{2\pi} \cos^2(\theta(\psi)) \exp\left(\frac{-V(\psi)}{kT}\right) d\psi}{\int_0^{2\pi} \exp\left(\frac{-V(\psi)}{kT}\right) d\psi} \quad (2)$$

In the presence of chemical exchange, the two interconverting sites can be represented by two potential wells separated by the potential barriers with pseudorotational phases ψ' and ψ'' . Between these barriers, the rate of pseudo-oscillation around each minimum is still fast, whereas the chemical exchange is slowed by the hindrance of barriers. When $\langle \cos^2(\theta) \rangle$ is calculated from eq 2 for sites A and B, the integration limits are replaced

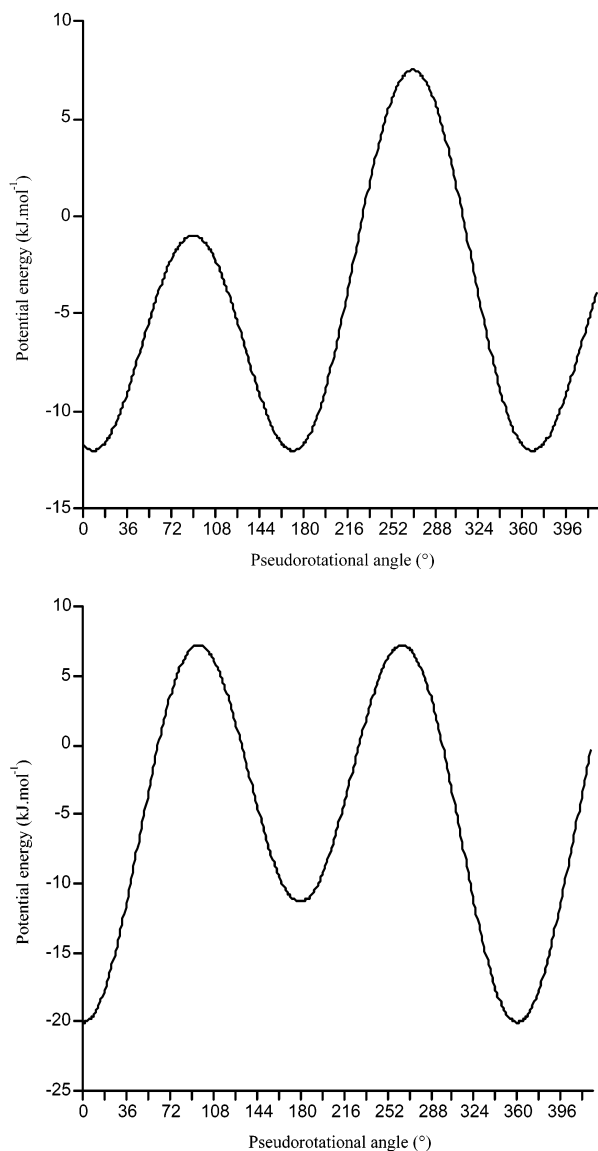


Figure 7. Empirical potential curve obtained according to eq 1 (left: **c-1**, right: **t-1**).

by $[\psi', \psi'']$ and $[\psi'', \psi']$, respectively:

$$\langle \cos^2(\theta) \rangle_A = \frac{\int_{\psi'}^{\psi''} \cos^2(\theta(\psi)) \exp\left(\frac{-V(\psi)}{kT}\right) d\psi}{\int_{\psi'}^{\psi''} \exp\left(\frac{-V(\psi)}{kT}\right) d\psi} \quad (3a)$$

$$\langle \cos^2(\theta) \rangle_B = \frac{\int_{\psi''}^{\psi'} \cos^2(\theta(\psi)) \exp\left(\frac{-V(\psi)}{kT}\right) d\psi}{\int_{\psi''}^{\psi'} \exp\left(\frac{-V(\psi)}{kT}\right) d\psi} \quad (3b)$$

The rather large effective moment of inertia of the ring allows us to use a classical approach to describe the pseudorotation. Because of the symmetry of **c-1**, the potential minima should have identical energy, whereas the barriers can be different. On the contrary, for **t-1**, the barrier heights are identical, but the energy minima are different, allowing only a single populated conformer (Figure 7).

According to eq 1, the phosphorus hfsc depends on only two parameters, V_1 and V_2 . Equations 1–3 allow us to determine

both the hfsc and their temperature coefficients. Nonlinear least-squares iteration was used to find the V_1 and V_2 values giving the best agreement between experimental and calculated data (see Table 1). Altogether, four experimental data points—two hfsc and two temperature coefficients—were used to determine V_1 and V_2 . The good agreement obtained for all data indicated the consistency of the applied model. Computations yielded potential amplitudes of $V_1 = 8.5 \text{ kJ mol}^{-1}$ and $V_2 = 15 \text{ kJ mol}^{-1}$, whereas the positions of potential minima are $\psi_A = 8.3^\circ$ and $\psi_B = 171.7^\circ$, respectively. The phases of the minima indicate that the ground conformers have intermediate geometry between 3T_4 and 3E or 4T_3 and 4E . Note that the molecular symmetry defines only the positions of the potential maxima, but the positions of the minima are not defined! The potential barriers separating potential wells are found to be 11.0 and 19.6 kJ mol^{-1} . The smaller value is remarkably close to the barrier of 10.5 kJ mol^{-1} that was obtained from the Arrhenius plot (Figure 5) of the exchange rate in the low-temperature region, and it also agrees with the potential barrier determined by the analysis of ${}^{13}\text{C}$ hfsc for the 2,2,5,5-tetramethyl-pyrrolidine-1-oxyl radical.³

The Arrhenius curve showed an increased slope at high temperature. This increase can be explained by an alternative route of ring inversion: a puckering vibration through the planar structure. According to microwave spectroscopy,⁵ the barrier of this inversion process is rather high, but because of the large entropy of this motion, it can be faster than the pseudorotation at elevated temperature. (Note that in the course of inversion pseudorotational motion requires a series of well-defined molecular geometries, whereas any two puckered conformations could be directly interconverted via the planar ring geometry.)

As a comparison, the same analysis was carried out for **t-1**. In this case, the two energy minima have exact 3T_4 and 4T_3 geometries, but the former has significantly larger energy (8.7 kJ mol^{-1} , see Table 1). For this reason, only one conformer is populated, and no chemical exchange can occur.

Conformational Analysis by Molecular Mechanics. The results obtained from the above semiempirical approach have been compared with the results derived from molecular mechanics calculations. For this purpose, we used GenMol software¹⁶ that includes the parameters for an aminoxyl moiety.^{4,17} Moreover, the method developed by Cremer and Pople¹⁸ has been implemented in GenMol for a quantitative conformational analysis of five-membered rings.⁴ This method is based on the definition of a mean plane, which is invariant during the pseudorotation. For any conformation of the ring, the z_j coordinate of the j th atom of the ring measures its distance to the mean plane and is written

$$z_j = \sqrt{\frac{2}{5}} q \sin\left(\frac{4\pi(j-1)}{5} + \psi\right) \quad \psi \in [0; 2\pi]$$

$$q \in [0.3; 0.5](10^{-8} \text{ cm})$$

for most of the five-membered rings

With any values of the puckering amplitude q and pseudorotation angle ψ , the corresponding conformation of a five-membered ring can be automatically built by GenMol. The same kind of strategy was used by French and Tran¹⁹ to analyze the fructofuranose conformations with the MMP2(85) program.

For **t-1** and **c-1**, the 20 ideal-ring conformers (10 envelopes and 10 twists) equally spaced by 18° on the pseudorotation circle were generated (Figure 1). Around each C–P bond, three staggered rotamers a, g–, and g+ were considered (Scheme 2). Therefore, for each envelope or twist conformer, 9 ideal

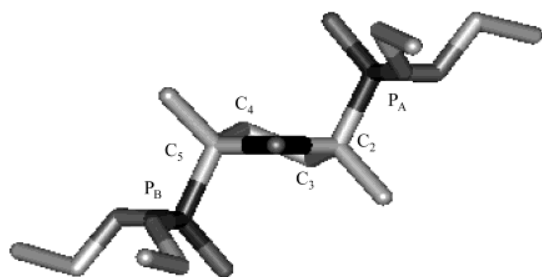


Figure 8. Preferred geometry of **t-1** obtained from molecular mechanics.

SCHEME 2: g⁺, g⁻, and a Orientations of the Diethoxyphosphoryl Groups

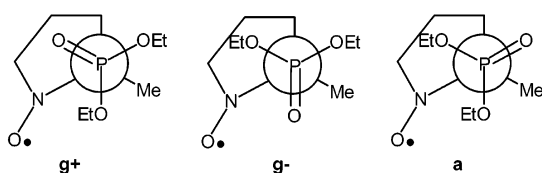


TABLE 3: Results of the Preliminary Conformational Analysis of t-1

	$E_{\text{steric}}(^4T_3)$ (kJ mol ⁻¹)	population (273 K) (%)	q (10 ⁻⁸ cm)	ψ (deg)	a_P^A (G)	a_P^B (G)
g-g-	84	42.8	0.37	177	53.6	52.2
aa	90	3.0	0.36	178	52.8	52.2
g+g+	93	0.8	0.36	177	52.3	51.2
ag-	86	17.7	0.35	174	54.6	50.8
g-a	86	17.7	0.36	184	50.8	54.4
g-g+	88	7.3	0.37	180	52.0	52.9
g+g-	88	7.3	0.36	182	52.2	52.7
ag+	91	2.0	0.36	178	52.3	51.9
g+a	92	1.3	0.35	177	52.7	51.4
mean values			0.36	178	52.9	52.4

rotamers (aa, ag+, ag-, g+a, g-a, g+g+, g+g-, g-g+, g-g-) must be considered, and for either **t-1** or **c-1**, 180 conformations were generated. These conformations were then optimized in the GenMol force field up to the convergence limit of 0.005 kJ mol⁻¹ using the following procedure.

Each conformation was built with an arbitrary puckering amplitude (0.4 10⁻⁸ cm), and the geometry of the ethoxyl chains was first optimized by a local conformational analysis (the remaining atoms being fixed). Then, the geometry optimization of the whole molecule was performed. For **t-1** and **c-1**, the energy minima that were found correspond to ³T₄ and ⁴T₃ conformers, and the energy maxima, to ¹E and E₁ conformers.

Conformational Analysis for t-1. The analysis showed that the orientation of the diethoxyphosphoryl substituents can only

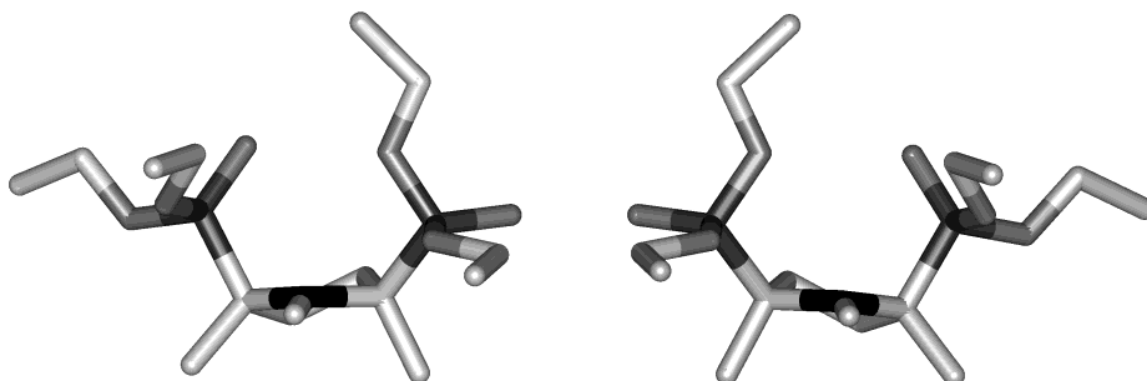


Figure 9. ag-⁴T₃ and g+a/³T₄ symmetric conformers of **c-1**.

TABLE 4: Results of the Conformational Analysis of c-1^a

	minimum 1 (⁴ T ₃ or E ₃)			minimum 2 (³ T ₄ or E ₄)		
	E_{steric} (kJ mol ⁻¹)	q (10 ⁻⁸ cm)	ψ (deg)	E_{steric} (kJ mol ⁻¹)	q (10 ⁻⁸ cm)	ψ (deg)
aa	89	0.37	173	89	0.37	6
g+g-	91	0.36	173	91	0.36	8
g-g+	92	0.36	181	92	0.36	-2
g+g+	<i>94</i>	<i>0.35</i>	<i>165</i>	<i>90</i>	<i>0.36</i>	2
g-g-	90	0.36	179	94	0.36	14
ag-	88	0.36	174	92	0.35	-1
g+a	92	0.35	180	88	0.36	6
ag+	96	0.37	175	88	0.36	6
g-a	88	0.36	173	96	0.37	5
mean values			174.5			5.2

^a Envelopes are in italics.

slightly change the geometry of ground ³T₄ and ⁴T₃ conformers. For each kind of rotamer, the ⁴T₃ conformer with pseudoaxial phosphorus atoms was largely favored. We obtained a value of $\langle\psi\rangle = 178^\circ$, which is close to the value calculated by the semiempirical approach ($\langle\psi\rangle = 180^\circ$). The energy difference between the ⁴T₃ and ³T₄ conformers was found to be around 10 kJ mol⁻¹, in good agreement with the value obtained by the analysis of ³¹P hfsc (8.7 kJ mol⁻¹, see Table 1). The results of the calculations for the ⁴T₃ rotamers are shown in Table 3. For the most favored rotamer (g-g-), the ethoxyl fragments are as far as possible from the ring to reduce steric interactions (Figure 8).

Conformational Analysis for c-1. As already mentioned, the conformational study gave two potential wells around the ³T₄ and ⁴T₃ conformations. However, for the nine rotamers, the phase minima were shifted, suggesting an intermediate geometry between ⁴T₃ and E₃ ($\langle\psi\rangle = 174.5^\circ$) or ³T₄ and E₄ ($\langle\psi\rangle = 5.2^\circ$), respectively (Table 4). Molecular mechanics calculations are then in agreement with the results of the above semiempirical model ($\psi = 171.8$ and 8.3° respectively). The type of rotamer can influence the energy minima up to 8 kJ mol⁻¹. According to C_v symmetry, the aa, g+g- and g-g+ rotamers of the ³T₄ and ⁴T₃ conformers are mirror images (Figure 9), whereas for the rotamer pairs (g+g+, g-g-), (ag-, g+a) and (ag+, g-a) the symmetry exists if one of the rotamers is combined with ³T₄ and the other, with ⁴T₃ (ag-/⁴T₃ ↔ g+a/³T₄).

The interconversion between the symmetric ³T₄ and ⁴T₃ conformers can take place either through inversion via a planar ring or by the pseudorotational process. In both cases, the molecular geometry should change through intricate geared motions including ring distortion, rotation around the C-P bonds, and reorientation of the ethoxyl chains.

To calculate the potential barrier, the nine E₁ rotamers and the nine ¹E rotamers were built with an initial puckering

amplitude of 0.3×10^{-8} cm. Starting from these 18 initial rotamers, the puckering amplitude was then systematically varied between 0 and 0.7×10^{-8} cm, and the most stable E_1 and 1E conformations were determined. Mainly because of steric repulsion between the axially oriented phosphoryl groups, we found that the 1E conformers had larger energy. Computations suggested that for the most stable E_1 geometry the ring was almost planar ($q = 0.11 \times 10^{-8}$ cm) and the energy was 25 kJ mol $^{-1}$ higher than the energy of the most favored 3T_4 or 4T_3 conformer. Hence, molecular mechanics yields for the exchange process a significantly larger barrier than that derived from the temperature dependence of either the interconversion rate (10.5 kJ mol $^{-1}$) or the phosphorus hfsc (11.1 kJ mol $^{-1}$).

Conclusions

The temperature dependence of the ESR spectrum for *cis*- and *trans*-2,5-diphosphoryl-2,5-dimethyl-pyrrolidinoxyl radicals **c-1** and **t-1**, respectively, was studied over a large temperature range. For **t-1**, line-width changes can be explained by the expected relaxation processes. However, for **c-1**, dramatic changes in the hyperfine pattern were observed and attributed to an interconversion between two symmetric conformations separated by a potential barrier. The large difference in the two phosphorus hfsc ($\Delta A_p \approx 21$ G) accounts for the unusually large alternating line broadening observed at high temperature. In the low-temperature region, the temperature dependence of the interconversion rate gives a potential barrier of 10.5 kJ mol $^{-1}$. At elevated temperature, an acceleration of the exchange rate shows that interconversion could also take place by alternative routes. Although at low temperature the major process is a pseudorotation with a small energy barrier and a small entropy value, at high temperature, a puckering vibration through the planar structure could be predominant, where both the barrier and the entropy are larger. The significant decrease of the exchange rate observed in methylene chloride could result from complexation.

Apart from the "dynamic" phenomenon of chemical exchange, the population averaging of conformers in the pseudo-rotational itinerary was also studied via the phosphorus couplings and their temperature coefficients. This analysis yielded a 11.1 kJ mol $^{-1}$ potential barrier for pseudorotation, which was in a remarkably good agreement with the value derived from the dynamic model. Computation suggests that the pseudorotation has two minima with geometry that corresponds to an "intermediate" structure between conformers 3T_4 and 3E as well as between conformers 4T_3 and E_3 .

Molecular mechanics computations were in a good agreement with the semiempirical potential derived from ESR data. Both for **t-1** and **c-1** the major characteristics of the potential function are well reproduced, even though the value of the potential barrier is overestimated by a factor of 2. Rotation around the C–P bonds can significantly affect the size of the potential barrier but cannot modify the geometries of ground ring conformations.

In the frozen-solution spectra of **c-1**, fairly large hfsc anisotropy was observed for the pseudoaxial phosphorus atom, whereas for the pseudoequatorial phosphorus the anisotropy was smaller. Hyperconjugation between the SOMO and the C–P bonds can explain not only the large isotropic hfsc but also the conformational dependence of the phosphorus anisotropy.

Experimental Section

ESR measurements were performed on a Bruker ESP 300 spectrometer equipped with a TM 110 cavity and an X-band

resonator (9.41 GHz). All ESR spectra were recorded at 100-kHz magnetic field modulations. The ESR samples (10^{-5} M in nitroxide) were deoxygenated by freeze and thaw cycles.

Cis- and *trans*-2,5-diethoxyphosphoryl-2,5-dimethylpyrrolidinoxyl radicals were isolated after the oxidation of the corresponding pyrrolidines.²⁰ *n*-Pentane (99%), methylene chloride (99.9%), and toluene (99.5%) were from SDS (France) and were used as received.

Acknowledgment. We thank the Hungarian Scientific Research Fund OTKA (grant T-032929), the CNRS, and the French Ministry of Research for financial support.

References and Notes

- (1) (a) McCarren, P. R.; Gordon, M. T.; Lowary, T. L.; Hadad, C. M. *J. Phys. Chem. A* **2001**, *105*, 5911. (b) Gordon, M. T.; Lowary, T. L.; Hadad, C. M. *J. Org. Chem.* **2000**, *65*, 4954. (c) Gordon, M. T.; Lowary, T. L.; Hadad, C. M. *J. Am. Chem. Soc.* **1999**, *121*, 9682. (d) Ma, B.; Schaefer, H. F., III; Allinger, N. L. *J. Am. Chem. Soc.* **1998**, *120*, 3411. (e) Bandyopadhyay, T.; Wu, J.; Stripe, W. A.; Carmichael, I.; Serianni, A. S. *J. Am. Chem. Soc.* **1997**, *119*, 1737. (f) Cros, S.; Hervé du Penhoat, C.; Pérez, S.; Imberty, A. *Carbohydr. Res.* **1993**, *248*, 81. (g) Cros, S.; Imberty, A.; Bouchemal, N.; Hervé du Penhoat, C.; Pérez, S. *Biopolymers* **1994**, *34*, 1433.
- (2) (a) Dzakula, Z.; DeRider, M. L.; Markley, J. L. *J. Am. Chem. Soc.* **1996**, *118*, 12796. (b) Haasnoot, C. A. G.; de Leeuw, F. A. A. M.; de Leeuw, H. P. M.; Altona, C. *Biopolymers* **1981**, *20*, 1211. (c) de Leeuw, F. A. A. M.; Altona, C.; Kessler, H.; Bermel, W.; Friedrich, A.; Krack, G.; Hull, W. E. *J. Am. Chem. Soc.* **1983**, *105*, 2237.
- (3) Rockenbauer, A.; Korecz, L.; Hideg, K. *J. Chem. Soc., Perkin Trans. 2* **1993**, 2149.
- (4) Siri, D.; Gaudel-Siri, A.; Tordo, P. *J. Mol. Struct.: THEOCHEM* **2002**, *582*, 171.
- (5) (a) Malloy, T. B., Jr.; Bauman, L. E.; Carreira, L. A. *Top. Stereochem.* **1979**, *11*, 97–185. (b) Kim, H.; Gwinn W. *J. Chem. Phys.* **1969**, *51*, 1815.
- (6) (a) Roberts, B. P.; Steel, A. J. *J. Chem. Soc., Perkin Trans. 2* **1992**, 2025. (b) Rolfe, R. E.; Sales, K. D.; Utley, J. H. P. *J. Chem. Soc., Perkin Trans. 2* **1973**, 1171. (c) Windle, J. J.; Kuhnle, J. A.; Beck, B. H. *J. Chem. Phys.* **1969**, *50*, 2630. (d) Ogawa, S.; Fessenden, R. W. *J. Chem. Phys.* **1964**, *41*, 994.
- (7) Shiotani, M.; Sjöqvist, L.; Lund, A.; Lunell, S.; Eriksson, L.; Huang, M. B. *J. Phys. Chem.* **1990**, *94*, 8081.
- (8) (a) Sjöqvist, L.; Lund, A.; Maruani, J. *J. Chem. Phys.* **1988**, *125*, 293. (b) Sjöqvist, L.; Lindgren, M.; Lund, A. *J. Chem. Phys. Lett.* **1989**, *156*, 323. (c) Kubuzono, Y.; Okada, M.; Aoyagi, M.; Yahiro, S.; Nakamura, H.; Matsuo, T. *Z. Naturforsch., A: Phys. Sci.* **1991**, *46*, 993.
- (9) (a) Fréjaville, C.; Karoui, H.; Tuccio, B.; Le Moigne, F.; Culcasi, M.; Pietri, S.; Lauricella, R.; Tordo, P. *J. Chem. Soc., Chem. Commun.* **1994**, 1793. (b) Fréjaville, C.; Karoui, H.; Tuccio, B.; Le Moigne, F.; Culcasi, M.; Pietri, S.; Lauricella, R.; Tordo, P. *J. Med. Chem.* **1995**, *38*, 258. (c) Rockenbauer, A.; Mercier, A.; Le Moigne, F.; Olive, G.; Tordo, P. *J. Phys. Chem.* **1997**, *101*, 7965.
- (10) (a) Rockenbauer, A.; Korecz, L. *Appl. Magn. Reson.* **1996**, *10*, 29. (b) Rockenbauer, A. *Mol. Phys. Rep.* **1999**, *26*, 117. (c) Rockenbauer, A.; Simon, P. *J. Magn. Reson.* **1975**, *18*, 320.
- (11) Chachaty, C.; Mathieu, C.; Mercier, A.; Tordo, P. *Magn. Reson. Chem.* **1998**, *36*, 46.
- (12) Heller, C.; McConnell, H. M. *J. Chem. Phys.* **1960**, *32*, 1535.
- (13) (a) Ament, S. S.; Wetherington, J. B.; Moncrief, J. W.; Flohr, K.; Mochizuki, M.; Kaizer, E. T.; *J. Am. Chem. Soc.* **1973**, *95*, 7896. (b) Wetherington, J. B.; Ament, S. S.; Moncrief, J. W. *Acta Crystallogr., Sect. B* **1974**, *30*, 568. (c) Chion, B.; Lajzerowicz, J. *Acta Crystallogr., Sect. B* **1975**, *31*, 1430. (d) Chion, B. *Cryst. Struct. Commun.* **1978**, *7*, 395. (e) Chion, B.; Lajzerowicz, J.; Collet, A.; Jacques, J. *Acta Crystallogr., Sect. B* **1976**, *32*, 339. (f) Keana, J. F.; Hideg, K.; Birrel, G. B.; Hankovszky, O. H.; Ferguson, G.; Parvez, M. *Can. J. Chem.* **1982**, *60*, 1439.
- (14) Altona, C.; Sundaralingam, M. *J. Am. Chem. Soc.* **1972**, *94*, 8205.
- (15) Dembrowski, L.; Finet, J.-P.; Fréjaville, C.; Le Moigne, F.; Maurin, R.; Mercier, A.; Pages, P.; Stipa, P.; Tordo, P. *Free Radical Res. Commun.* **1993**, *19*, S23.
- (16) Pèpe, G.; Siri, D. *Stud. Phys. Theor. Chem.* **1990**, *11*, 411.
- (17) Vila, F.; Tordo, P.; Siri, D.; Pèpe, G. *Free Radical Res. Commun.* **1993**, *19*, S17.
- (18) (a) Cremer, D.; Pople, J. A. *J. Am. Chem. Soc.* **1975**, *97*, 1354. (b) Essen, H.; Cremer, D. *Acta Crystallogr., Sect. B* **1984**, *40*, 418. (c) Cremer, D. *J. Phys. Chem.* **1990**, *94*, 5502.
- (19) French, A. D.; Tran, V. *Biopolymers* **1990**, *29*, 1599.
- (20) Le Moigne, F.; Tordo, P. *C. R. Acad. Sci.* **2001**, *4*, 585–590.

3 La dynamique moléculaire : principe et applications

3.1 Introduction

La mécanique moléculaire permet l'étude d'une molécule isolée, et de taille suffisamment raisonnable pour pouvoir effectuer son analyse conformationnelle (i.e. le parcours d'une partie de l'hypersurface d'énergie potentielle pour trouver les minima correspondant aux géométries les plus stables). Dès que l'on souhaite étudier des systèmes plus complexes, une molécule isolée comportant beaucoup d'atomes ou un système avec un grand nombre de particules, d'autres techniques sont utilisées. A ces systèmes ayant un grand nombre d'atomes correspondent un grand nombre de minima locaux proches en énergie à considérer et il n'est pas concevable d'espérer en visiter suffisamment manuellement par une succession de modifications géométriques et de minimisations de l'énergie stérique. La dynamique moléculaire (DM) est une des techniques possibles pour simuler des systèmes complexes. Ses applications sont très larges : étude conformationnelle de molécules biologiques (protéines, acides nucléiques) étude de liquides, de solutions, de la solvatation des ions, changements de phase (évaporation, liquéfaction, ...), étude des turbulences d'un fluide autour d'un solide, association de molécules en solution pour former des micelles ou des membranes ... La DM permet de simuler des systèmes macroscopiques à partir de modèles à l'échelle moléculaire. La DM consiste en la résolution numérique d'un problème à N corps de mécanique classique. On considère l'énergie totale du système $E_T = E_c + E_p$. On simule la dynamique réelle d'un système-modèle au cours du temps et le calcul de propriétés moyennées sur la durée de la simulation du modèle permet d'estimer des propriétés macroscopiques du système réel. Historiquement, la DM a d'abord été utilisée dans les années soixante pour étudier des systèmes de particules entrant en collision (atomes à l'état gazeux ou liquide). Les interactions entre particules étaient représentées par le modèle des sphères dures puis par un potentiel de Lennard-Jones. L'étude des molécules a débuté avec les liquides moléculaires (1971) puis les protéines (1977). L'ensemble des positions atomiques à l'instant t sont obtenues en résolvant les équations du mouvement de Newton. Les lois de Newton sont les suivantes :

1. Un corps évolue en ligne droite et à vitesse constante si aucune force n'agit sur lui.
2. La force est proportionnelle à l'accélération : $\vec{F} = m\vec{a}$.
3. A chaque action correspond une réaction de même intensité et de direction opposée.

La DM est une méthode déterministe i.e. l'état du système à un instant $t + \Delta t$ quelconque peut être prédit à partir de son état à l'instant t . La résolution des équations du mouvement pour un système de N atomes implique l'intégration numérique d'un système de N équations différentielles dépendant du temps. En effet, d'après la seconde loi de Newton, $\vec{F}_i = m\vec{a}_i$ pour chacune des $3N$ directions d'un système à N atomes, soit $\frac{\vec{F}_i}{m_i} = \frac{d^2\vec{r}_i}{dt^2}$. Pour intégrer numériquement ces équations, il faut choisir un pas d'intégration Δt . A chaque pas, les forces appliquées sur chaque atome sont recalculées et, en tenant compte des positions atomiques et des vitesses à l'instant t , les positions et les vitesses à l'instant $t + \Delta t$ sont calculées. On fait l'hypothèse que les forces agissant sur chaque atome sont constantes dans l'intervalle Δt donc Δt doit être très petit (de l'ordre de 10^{-14} à 10^{-15} s). Les positions atomiques générées au cours du temps par intégrations successives constituent une trajectoire. Pour une simulation de 1 ns (10^{-9} s) avec un pas de 10^{-15} s, 10^6 résolutions des N équations du mouvement pour l'ensemble des N atomes du système sont nécessaires. Une simulation de DM est divisée en trois parties : initialisation (positions et vitesses initiales), équilibration (on recherche entre autres E_T quasiment constante), acquisition de données et analyse des résultats.

3.2 Déroutement d'une simulation de dynamique moléculaire

3.2.1 Configuration initiale

Le choix de la configuration initiale est très important car un mauvais choix peut conduire à l'échec de la simulation. Tout d'abord, il est plus judicieux de choisir une configuration initiale du système proche de l'état qu'on souhaite simuler. Par exemple, pour un liquide, on construit une boîte contenant N molécules du liquide, réparties à peu près régulièrement avec des orientations aléatoires et une densité proche de la réalité. D'autre part, il faut éviter les « points chauds » (hot spots) ie les interactions à haute énergie qui entraînent des forces très importantes et irréalistes sur certains atomes, donc des accélérations erronées et une simulation instable. Afin d'éviter ce problème, il est préférable de minimiser l'énergie stérique de la configuration initiale avant de commencer toute simulation. Exemple : Les premières simulations de molécules biologiques ont donné des résultats irréalistes. Pourquoi ? Ces premiers calculs étaient effectués sur des protéines ou des acides nucléiques isolés alors que ces molécules sont en réalité dans un milieu aqueux. Les données expérimentales mesurées en milieu aqueux ne pouvaient être comparées aux calculs sur les molécules isolées. Les interactions entre le soluté et les molécules d'eau n'étant pas prises en compte, les interactions intramoléculaires entre acide aminés étaient surestimées et les géométries obtenues étaient beaucoup trop compactes. On peut prendre en compte le solvant en entourant la molécule d'une couche de molécules d'eau par exemple. Nous verrons par la suite que cette solution n'est pas la meilleure. Si l'épaisseur est suffisante, c'est comme si on avait placé la molécule dans une goutte d'eau. Cependant, cette technique augmente le nombre d'atomes du système, donc les temps de calcul et les espaces de stockage nécessaires. Par exemple, l'enzyme dihydrofolate reductase comporte 2500 atomes environ. Si on l'entoure d'une couche de molécules d'eau de 5Å d'épaisseur, le système comporte alors 8900 atomes ; et si la couche mesure 10Å d'épaisseur, le système comporte alors 14700 atomes !!

3.2.2 Equilibration

L'objectif de cette phase est de conduire le système à l'équilibre à partir de la configuration initiale choisie. Elle doit être poursuivie tant qu'un certain nombre de propriétés thermodynamiques ne sont pas stabilisées :

- distribution des vitesses atomiques : elle est représentée par une gaussienne à l'équilibre
- énergies totale, potentielle, cinétique : elles fluctuent autour d'une valeur moyenne à l'équilibre
- mesure du désordre dans un liquide. Dans un liquide, par opposition à un solide, les atomes ou les molécules se déplacent aléatoirement (translation) et sont orientés aléatoirement. On mesure le désordre par le calcul du déplacement quadratique moyen Δr^2 . A chaque instant t de la simulation, on peut calculer cette grandeur à l'aide la formule suivante : $\Delta \bar{x}^2(t) = \frac{1}{N} \sum [\vec{x}_i(t) - \vec{x}_i(0)]^2$ où N représente le nombre d'atomes du système, $\vec{x}_i(0)$ le vecteur-position initial de l'atome i et $\vec{x}_i(t)$ le vecteur-position à t de l'atome i . Dans le cas d'un liquide, le graphe représentant Δr^2 en fonction du temps est une courbe croissante du fait de l'éloignement constant de chaque atome de sa position initiale par translation et rotation. A l'équilibre, c'est même une droite croissante. Dans le cas d'un solide, on obtient quasiment une droite constante (oscillations autour des positions d'équilibre).

La phase d'équilibration dure quelques ps à quelques dizaines de ps suivant la complexité et la taille du système.

a) Techniques d'intégration numérique - méthode des différences finies

Dans cette famille de méthodes, on remplace dx , dt par des différences finies Δx , Δt et les équations différentielles par des équations à différences finies. De plus, pendant le laps de temps Δt (petit mais de valeur finie), on suppose que toutes les vitesses \vec{v}_i sont constantes. Tous les algorithmes partent du principe que les positions et les propriétés dynamiques (\vec{a}, \vec{v}) à $t+\Delta t$ peuvent s'exprimer sous la forme de série de Taylor en fonctions des positions, vitesses, accélérations connues à l'instant t .

$$\vec{x}(t + \Delta t) = \vec{x}(t) + \frac{d\vec{x}(t)}{dt} \Delta t + \frac{1}{2} \frac{d^2\vec{x}(t)}{dt^2} \Delta t^2 + \frac{1}{3!} \frac{d^3\vec{x}(t)}{dt^3} \Delta t^3 + \frac{1}{4!} \frac{d^4\vec{x}(t)}{dt^4} \Delta t^4 + \dots$$

soit

$$\vec{x}(t + \Delta t) = \vec{x}(t) + \vec{v}(t) \Delta t + \frac{1}{2} \vec{a}(t) \Delta t^2 + \frac{1}{3!} \vec{b}(t) \Delta t^3 + \frac{1}{4!} \vec{c}(t) \Delta t^4 + \dots$$

De même :

$$\vec{v}(t + \Delta t) = \vec{v}(t) + \vec{a}(t) \Delta t + \frac{1}{2} \vec{b}(t) \Delta t^2 + \frac{1}{3!} \vec{c}(t) \Delta t^3 + \dots$$

et

$$\vec{a}(t + \Delta t) = \vec{a}(t) + \vec{b}(t) \Delta t + \frac{1}{2} \vec{c}(t) \Delta t^2 + \dots$$

Ces méthodes introduisent deux types d'erreur : des erreurs dues à la troncature des séries de Taylor utilisées dans l'intégration numérique des erreurs d'arrondi dues à l'algorithme choisi et dépendant du calculateur utilisé. Ces erreurs peuvent s'amplifier au cours de la simulation, conduisant à des résultats erronés. On évalue une méthode des différences finies en dynamique moléculaire en testant sa capacité à conserver $E_{\text{tot}} = \text{constante}$. L'erreur de troncature est estimée par le premier terme non-nul de la série de Taylor qui a été négligé. Par exemple, voici une série de Taylor utilisée pour estimer la position $\vec{x}(t + \Delta t)$ à partir de $\vec{x}(t)$:

$$\vec{x}(t + \Delta t) = \vec{x}(t) + \frac{d\vec{x}(t)}{dt} \Delta t + \frac{1}{2} \frac{d^2\vec{x}(t)}{dt^2} \Delta t^2 + \frac{1}{3!} \frac{d^3\vec{x}(t)}{dt^3} \Delta t^3$$

Une méthode des différences finies où l'erreur de troncature est en $(\Delta t)^{n+1}$ est une méthode du $n^{\text{ème}}$ ordre. Ici, le premier terme non-nul de la série qui a été négligé est en Δt^4 donc la méthode est d'ordre 3. Le terme Δt est inférieur à 1 donc, plus l'ordre est élevé, plus l'erreur devient faible. De plus, cette erreur ne dépend que de la méthode choisie et est indépendante du calculateur utilisé, contrairement aux erreurs d'arrondi.

L'algorithme de Verlet¹ est l'algorithme le plus couramment utilisé en dynamique moléculaire. Il utilise les positions et les accélérations à l'instant t ainsi que les positions à $t - \Delta t$ pour calculer les positions à l'instant $t + \Delta t$. En effet, on peut écrire en s'arrêtant à l'ordre 3 :

$$\vec{x}(t + \Delta t) = \vec{x}(t) + \vec{v}(t) \Delta t + \frac{1}{2} \vec{a}(t) \Delta t^2 + \frac{1}{3!} \vec{b}(t) \Delta t^3$$

$$\vec{x}(t - \Delta t) = \vec{x}(t) - \vec{v}(t) \Delta t + \frac{1}{2} \vec{a}(t) \Delta t^2 - \frac{1}{3!} \vec{b}(t) \Delta t^3$$

En additionnant les deux équations, on obtient :

$$\vec{x}(t + \Delta t) + \vec{x}(t - \Delta t) = 2\vec{x}(t) + \vec{a}(t) \Delta t^2$$

Cet algorithme présente l'avantage d'être rapide, facile à programmer et de demander peu d'espace mémoire pour le stockage de données : à $t + \Delta t$, on a seulement besoin des informations $\vec{x}(t - \Delta t)$, $\vec{x}(t)$, $\vec{a}(t)$. Cependant, l'ensemble des positions atomiques $\vec{x}(t + \Delta t)$ est obtenue en ajoutant un terme très petit $\vec{a}(t) \Delta t^2$ à une différence entre deux termes d'un autre ordre de grandeur ($\vec{x}(t - \Delta t)$, $\vec{x}(t)$), d'où une perte de précision (erreur d'arrondi). De plus, les vitesses n'apparaissent pas explicitement dans l'algorithme. Un calcul supplémentaire est nécessaire pour les obtenir ; le plus simple est d'estimer la vitesse instantanée $\vec{v}(t)$ à l'aide de la vitesse moyenne $\frac{\vec{x}(t + \Delta t) - \vec{x}(t - \Delta t)}{2\Delta t}$ et il faut deux étapes successives pour avoir la vitesse $\vec{v}(t)$ donc on perd en précision. D'autre part, au début de la simulation ($t=0$), on ne peut pas calculer directement $\vec{x}(\Delta t)$. Il faut donc postuler $\vec{x}(-\Delta t)$. Pour cela, on utilise une série de Taylor tronquée au premier terme : $\vec{x}(-\Delta t) = \vec{x}(0) - \Delta t \vec{v}(0)$. On introduit donc une imprécision dès le début de la simulation.

L'algorithme leapfrog² a été développé pour pallier les inconvénients de l'algorithme de Verlet. Il est basé sur les équations suivantes :

1. L. Verlet, Phys. Rev. 1967, 159, 98-103.

2. R.W. Hockney, Meth. Comput. Phys. 1970, 9, 135-211.

$$\vec{x}(t + \Delta t) = \vec{x}(t) + \vec{v}\left(t + \frac{\Delta t}{2}\right) \Delta t$$

$$\vec{v}\left(t + \frac{\Delta t}{2}\right) = \vec{v}\left(t - \frac{\Delta t}{2}\right) + \Delta t \cdot \vec{a}(t)$$

Les vitesses sont d'abord calculées puis les positions en sont déduites. Le nom de l'algorithme provient du fait que les vitesses « jouent à saute-mouton » (leap frog en anglais) avec les positions. En effet, les positions sont connues à t , $t + \Delta t$, $t + 2\Delta t$, $t + 3\Delta t$, $t + 4\Delta t$, ... tandis que les vitesses sont calculées à $t + \Delta t/2$, $t + 3\Delta t/2$, $t + 5\Delta t/2$, $t + 7\Delta t/2$, ...

Dans cet algorithme, les vitesses sont explicitement incluses et ne requièrent pas un calcul supplémentaire par une différence entre deux nombres d'un ordre de grandeur différent. Cependant, les grandeurs \vec{x} et \vec{v} sont asynchrones. Le calcul de l'énergie potentielle dépend des positions tandis que le calcul de l'énergie cinétique dépend des vitesses. Cela pose un problème pour le calcul de l'énergie totale. On calcule donc les vitesses synchronisées avec les positions à l'aide d'une moyenne : $\vec{v}(t) = \frac{1}{2} [\vec{v}(t + \frac{\Delta t}{2}) + \vec{v}(t - \frac{\Delta t}{2})]$.

Beaucoup d'autres algorithmes sont également disponibles dans les logiciels de dynamique moléculaire, utilisant une méthode des différences finies de degrés plus ou moins élevés. L'idéal serait a priori de choisir l'algorithme le plus rapide, demandant le moins de mémoire et le plus facile à programmer (Verlet) mais le choix de l'algorithme n'est pas le plus important dans un logiciel de simulation de DM. En effet, dans tous les cas, le temps nécessaire à l'intégration des équations est minime par rapport aux autres calculs à effectuer. Quels sont ces autres calculs ? Ce qui requiert le plus de ressources informatiques est le calcul des forces agissant sur chaque atome du système ($1/2N(N - 1)$ calculs à chaque pas dans un potentiel de Lennard-Jones et beaucoup plus dans un potentiel de mécanique moléculaire). D'autre part, l'algorithme d'intégration doit avoir deux propriétés importantes :

- être conservatif : l'énergie totale doit être constante ie l'énergie potentielle et l'énergie cinétique doivent fluctuer d'une même quantité dans des directions opposées à tout instant de la simulation
- être réversible : si on remplace Δt par $-\Delta t$ à la fin de la trajectoire, on doit obtenir la trajectoire inverse aboutissant à l'état initial, d'où l'importance des erreurs de troncature et d'arrondi

b) Choix du pas d'intégration A chaque pas, le vecteur accélération doit être recalculé à partir des forces agissant sur chaque atome, ce qui permet de calculer les positions atomiques au pas suivant et de générer une trajectoire. Plus le pas Δt est réduit, plus la trajectoire devient une meilleure approximation de la trajectoire « réelle » des atomes, dans la limite des erreurs de troncature et d'arrondi du calcul numérique fini. Mais plus Δt est petit, plus un grand nombre de pas est nécessaire pour faire évoluer le système sur une période donnée. Si on utilise un pas trop grand, inadapté à la nature du système étudié, la simulation risque de devenir instable car la conservation de l'énergie totale n'est plus assurée. En effet, pendant le laps de temps Δt , les vitesses sont considérées constantes. Si Δt est grand, les grands déplacements atomiques pendant Δt peuvent entraîner des collisions (superpositions), conduisant à une augmentation très rapide de l'énergie potentielle et à une situation irréaliste. Avec un pas d'intégration approprié, la simulation de DM peut se dérouler correctement et les collisions peuvent être évitées car les atomes ont le temps de s'éloigner les uns des autres. Au sein d'un système, on peut distinguer plusieurs catégories de mouvements moléculaires : les mouvements d'ensemble (rotation, translation), les rotations internes (torsion), les vibrations des liaisons et des angles de valence. Les mouvements d'ensemble ne modifient pas les positions relatives des atomes d'une molécule et les torsions sont des mouvements relativement lents. Les mouvements les plus rapides correspondent aux vibrations des liaisons (stretching). Aux atomes les plus légers correspondent les fréquences de vibration les plus élevées. Par exemple, les liaisons C-H vibrent à la fréquence de 10^{14} Hz ce qui correspond à une période T_{\min} de 10 fs (10^{-14} s). Or Δt doit être petit par rapport à la période du mouvement le plus rapide afin que la simulation soit stable (conservation de l'énergie totale) donc on considère en général que $\Delta t = T_{\min}/10$ est un pas correct. Si les vibrations impliquant des atomes H sont empêchées en gelant les

longueurs de liaison A-H, le pas Δt peut être augmenté pour permettre des simulations plus longues sans perdre en stabilité.

c) Ensembles de simulation

Quand on intègre les équations du mouvement de Newton au cours d'une simulation de DM, l'énergie totale est conservée (le système est isolé). D'autre part, le nombre de particules est constant (le système est fermé). Une simulation de DM peut être effectuée en imposant à d'autres paramètres de rester constants. On travaille ainsi dans différents ensembles (Tableau 3.1). Le volume est contrôlé en fixant les dimensions de la cellule primaire. La température est contrôlée par un thermostat, à l'aide du couplage avec une bain thermostatique externe. La pression est contrôlée en ajustant les dimensions de la cellule primaire, par exemple avec un couplage à un "bain" de pression constante.

TABLE 3.1 – Ensembles à nombre constant de particules utilisés en dynamique moléculaire.

Ensemble	Paramètres constants	
micro-canonique	NVE	Simulation par défaut (la température peut varier)
canonique	NVT	Exemple : calorimètre (la pression peut varier)
isotherme-isobare	NPT	Exemple : à l'air libre (le volume du système peut varier)

N : nombre de particules, V : volume du système, E : énergie totale, T : température, P : pression

3.2.3 Phase de production et calcul de propriétés

Une fois l'équilibre atteint, la simulation est poursuivie pendant la durée jugée nécessaire. La trajectoire ainsi obtenue permet de calculer un certain nombre de propriétés qui sont sauvegardées à intervalle régulier. D'autres propriétés peuvent également être calculées et moyennées a posteriori, grâce à l'extraction de données du fichier trajectoire. On souhaite estimer des propriétés macroscopiques à partir de la trajectoire calculée sur un système de nature microscopique (moléculaire). Les propriétés macroscopiques résultent du comportement collectif de l'ensemble des N atomes du système. Pendant la simulation de durée finie, la plupart des propriétés ne sont pas constantes : leurs valeurs fluctuent car les molécules sont en perpétuel mouvement et entrent en collision. Par exemple, l'énergie cinétique et l'énergie potentielle oscillent autour d'une valeur moyenne à l'équilibre et ces fluctuations sont de l'ordre de 1 ps. Pour toute propriété macroscopique A recherchée, on suit la procédure suivante :

1. calcul de la trajectoire à l'équilibre
2. calcul de la propriété A à intervalle régulier
3. calcul de la moyenne en supposant que la simulation est assez longue pour assimiler la moyenne temporelle calculée sur le système microscopique sur une durée finie de simulation et la valeur moyenne macroscopique.

a) Propriétés statiques Voici quelques exemples de propriétés statiques : énergie potentielle, cinétique, totale, capacité calorifique, température, pression, volume, distribution des vitesses, fonction de distribution radiale, ...

b) Propriétés dynamiques Voici quelques exemples de propriétés dynamiques : fonctions de corrélation et d'autocorrélation, coefficient de diffusion (calculé à partir du déplacement quadratique moyen à l'aide de la relation d'Einstein).

c) Systèmes périodiques

En général, la DM est appliquée à des systèmes contenant plusieurs centaines ou plusieurs milliers d'atomes, ce qui est très inférieur au nombre d'Avogadro correspondant à un système macroscopique. De tels systèmes sont relativement petits pour le calcul de propriétés macroscopiques et dominés par les effets de surface ie les interactions des atomes avec l'extérieur du système (vide ou récipient).

Par exemple, pour simuler correctement 500 atomes à l'état liquide, le cube contenant les atomes doit avoir un côté de longueur au moins égale à 8,5 fois le diamètre atomique (interactions à longue distance entre atomes non-liés). Cependant, les interactions paroi/fluide s'étendent jusqu'à 4 voire 10 diamètres atomiques à partir de chaque paroi... donc une simulation de DM appliquée à un tel système fournirait des informations sur le comportement du liquide au voisinage des surfaces solides et non sur celui des molécules au coeur du liquide. D'un autre côté, on ne peut augmenter indéfiniment la taille du système à simuler car les moyens de calcul seraient astronomiques!! Il faut donc trouver une astuce pour pouvoir simuler des liquides avec un nombre limité de molécules, de telle sorte que les atomes subissent des forces comme s'ils étaient au coeur du liquide. On utilise alors des conditions périodiques. Il faut imaginer que les N atomes du système confinés dans le volume V ne représentent qu'une partie du système à l'étude. Le volume V correspond à la cellule primaire; elle représente le coeur du système car la cellule primaire est entourée de répliques exactes d'elle-même. Ces répliques sont appelées images. Chaque cellule-image contient N atomes, images des atomes de la cellule primaire, qui est ainsi répliquée périodiquement dans les trois directions de l'espace pour former un échantillon artificiellement macroscopique. Toute forme de volume qui pave parfaitement l'espace peut être utilisée. Le mieux est de choisir une forme qui reflète la géométrie du système (plutôt sphérique ou allongée). Les cellules sont séparées par des parois poreuses de telle sorte que les atomes peuvent librement entrer et sortir de n'importe quelle cellule mais le nombre N d'atomes dans chaque cellule doit rester constant. Si un atome i sort de la cellule primaire par une face, une image de cet atome entre instantanément par la face opposée. Les conditions périodiques présentent plusieurs avantages : on n'a besoin de conserver en mémoire que les positions atomiques de la cellule primaire, celles des images pouvant être recalculées si nécessaire par translation chaque atome-image subit exactement les mêmes forces que l'atome de la cellule primaire et suit la même trajectoire. Combien de cellules-images sont nécessaires? Tout dépend des forces intermoléculaires en jeu et de leur étendue. Chaque atome interagit avec les $N-1$ atomes de la cellule primaire et toutes leurs images. Avec les forces à courte distance telles que le potentiel de Lennard-Jones ($1/r^6$ et $1/r^{12}$), on peut utiliser la convention du minimum d'images (chaque atome n'entre en interaction qu'avec le plus proche des autres atomes, qu'il soit dans la même cellule ou dans une cellule-image adjacente). On peut également introduire un cut-off dans le calcul des interactions entre atomes non-liés, choisi de telle sorte qu'un atome n'entre en interaction avec aucune de ses images; le cut-off maximal correspond donc à la moitié du côté de la cellule. Les interactions électrostatiques entre charges ponctuelles sont ressenties à beaucoup plus longue distance (potentiel en $1/r$) que les interactions de Van der Waals. Elles nécessitent donc un traitement particulier : la méthode de la somme d'Ewald³ est la plus couramment utilisée. Toutes les interactions charge-charge sont calculées entre chaque atome, ses images et tous les autres atomes en considérant une infinité de cellules-images. Deux sommes convergent rapidement sont calculées, l'une dans l'espace réel, la seconde dans l'espace réciproque, et un cut-off est généralement introduit pour accélérer le calcul. La contribution électrostatique est le résultat de ces deux sommes.

3.3 Application à l'étude de nanocomposites à base de Montmorillonite

Le logiciel Cerius² et le champ de force UFF ont été utilisés afin de mener l'étude de l'intercalation du monomère ϵ -caprolactone et du polymère poly(ϵ -caprolactone) au sein de feuillet d'argile de type Montmorillonite. Ces travaux ont fait l'objet de deux publications et d'une communication orale.

3. a) P. Ewald, Ann. Phys. 1921, 64, 253-287. b) N. Karasawa, W.A. Goddard III, J. Phys. Chem. 1989, 93, 7320-7327.

Molecular Dynamics Study of ϵ -Caprolactone Intercalated in Wyoming Sodium Montmorillonite

Anouk Gaudel-Siri,^{†,‡} Patrick Brocorens,[†] Didier Siri,[§] Fabrice Gardebien,[†] Jean-Luc Brédas,^{†,||} and Roberto Lazzaroni^{*,†}

Service de Chimie des Matériaux Nouveaux, Université de Mons-Hainaut, 20 Place du Parc, B-7000 Mons, Belgium, Laboratoire RéSo – UMR 6516, Université d'Aix-Marseille 3, Faculté St. Jérôme, Av. Esc. Normandie-Niemen, 13397 Marseille Cedex 20, France, Laboratoire de Chimie Théorique et Modélisation Moléculaire, CNRS-UMR 6517, Universités d'Aix-Marseille 1 et 3, Faculté St. Jérôme, Av. Esc. Normandie-Niemen, 13397 Marseille Cedex 20, France, and School of Chemistry and Biochemistry, Georgia Institute of Technology, Atlanta, Georgia 30332-0400

Received March 21, 2003. In Final Form: July 14, 2003

The intercalation process of the ϵ -caprolactone monomer into sodium montmorillonite clay is modeled with a combined molecular mechanics/molecular dynamics approach. This study is aimed at understanding the initial stages of caprolactone polymerization within the channels of the clay, to form highly dispersed nanocomposites. The theoretical method is first validated by modeling dry and hydrated Wyoming sodium montmorillonite; the caprolactone-intercalated clay is then investigated, with particular emphasis on the energetics of the intercalation process and the nature of the interactions building up between the organic molecules and the channel walls and sodium counterions.

1. Introduction

Poly(ϵ -caprolactone) (PCL) is a biodegradable aliphatic polyester that is being intensively investigated for use in medical devices and degradable packaging. However, the mechanical properties of the PCL homopolymer are too poor to allow its direct use. To improve the mechanical properties and thermal stability, nanocomposites based on PCL and layered aluminosilicates (montmorillonite-type clay) represent a valuable alternative. Because of the dispersion of nanometer-size clay sheets, nanocomposites exhibit new and improved properties compared to microcomposites or filled polymers.^{1,2}

Polymer nanocomposites are usually prepared by melt intercalation; in that procedure, alkali-metal cations of the clay must first be replaced by organic surfactants in order to render the clay channels more organophilic and to allow the intercalation of the polymer. The physicochemical parameters governing the intercalation process and the influence of the organic counterions on the stability of the nanocomposites have been extensively investigated by model calculations (see refs 3–5 and references therein). Those studies allow for the a priori design of composite materials with a well-defined microstructure.

Remarkably, the need for those organophilic counterions can be circumvented if the polymer is directly generated

within the channels. It has been shown recently that the ϵ -caprolactone monomers (CL) spontaneously intercalate at ambient temperature between Na-montmorillonite sheets.⁶ Subsequent polymerization involving intercalated monomers then leads to composites with excellent dispersion of the clay sheets in the matrix. To exploit best this new route to polymer nanocomposites, it is essential to obtain a molecular scale description of the intercalation process for the monomer. Through a molecular modeling approach, this study aims at shedding light on (i) the structure of the intercalated system, that is, the spatial distribution of the CL molecules with respect to the clay walls and the counterions, and (ii) the nature of intermolecular interactions favoring intercalation. In turn, this will allow an understanding of whether the spontaneous intercalation of the monomer (and the subsequent polymerization leading to the nanocomposite) is specific to caprolactone, or this new route could be extended to the preparation of other polymer/Na-montmorillonite nanocomposites.

Here we focus on the modeling of the CL-intercalated Na-montmorillonite system. Montmorillonite belongs to the family of 2:1 phyllosilicates. Their crystal structure consists of layers of two silica tetrahedral sheets fused to an edge-shared octahedral sheet of aluminum hydroxide. Stacking of the layers leads to a regular van der Waals gap or interlayer. Isomorphic substitutions within the layers (silicon replaced by aluminum in the tetrahedral sheets and aluminum replaced by magnesium in the octahedral sheet) generate negative charges that are counterbalanced by cations residing in the interlayer region. The natural form of Wyoming montmorillonite contains hydrated Na⁺ or K⁺ cations. The layer charge of montmorillonite clays is usually between $-0.5 e$ and $-1.2 e$ per O₂₀(OH)₄ formula unit cell, and octahedral substitutions are responsible for about $2/3$ of the total charge. We

* To whom correspondence should be addressed. E-mail: Roberto@averell.umh.ac.be.

[†] Service de Chimie des Matériaux Nouveaux, Université de Mons-Hainaut.

[‡] Laboratoire RéSo – UMR 6516, Université d'Aix-Marseille 3.

[§] Laboratoire de Chimie Théorique et Modélisation Moléculaire, CNRS-UMR 6517, Universités d'Aix-Marseille 1 et 3.

^{||} School of Chemistry and Biochemistry, Georgia Institute of Technology.

(1) (a) Krishnamoorti, R.; Vaia, R. A.; Giannelis, E. P. *Chem. Mater.* 1996, 8, 1728. (b) Giannelis, E. P. *Adv. Mater.* 1996, 8, 29.

(2) Alexandre, M.; Dubois, P. *Mater. Sci. Eng.* 2000, R28, 1.

(3) Vaia, R. A.; Giannelis, E. P. *Macromolecules* 1997, 30, 8000.

(4) Giannelis, E. P.; Krishnamoorti, R.; Manias, E. *Adv. Polym. Sci.* 1999, 138, 107.

(5) Balazs, A. C.; Singh, C.; Zhulina, E.; Lyatskaya, Y. *Acc. Chem. Res.* 1999, 8, 651.

(6) (a) Lepoittevin, B.; Devalckenaere, M.; Pantoustier, N.; Alexandre, M.; Kubies, D.; Calberg, C.; Jérôme, R.; Dubois, P. *Polymer* 2002, 43, 4017. (b) Lepoittevin, B.; Devalckenaere, M.; Alexandre, M.; Pantoustier, N.; Calberg, C.; Jérôme, R.; Dubois, Ph. *Macromolecules* 2002, 35, 8385.

Table 1. Atomic Charges^a

		atom									
		C ₁	C ₂	C ₃	C ₄	C ₅	O ₆	C ₇	O ₈	H ₉	
charge/e		-0.20	-0.28	-0.28	-0.24	0.00	-0.52	0.64	-0.47	0.13	
		atom									
		H ₁₀	H ₁₁	H ₁₂	H ₁₃	H ₁₄	H ₁₅	H ₁₆	H ₁₇	H ₁₈	
charge/e		0.10	0.16	0.13	0.14	0.14	0.18	0.10	0.14	0.12	
		atom									
		Si	Al ^b	Mg	O (OH)	H	O (bridge)	O			
charge/e		1.2	3.0 or 0.2	2.0	-1.424	0.424	-1.0	-0.8			

^a For the CL molecule, atomic charges are optimized with the QEq algorithm; for montmorillonite, they are assigned according to the method due to Skipper et al. (ref 7a). ^b The partial charge of the Al atoms is 3.0 in the octahedral sites and 0.2 when they replace a Si atom in the tetrahedral sheet.

here consider the unit cell formula Na_{0.75}(Si_{7.75}Al_{0.25})-(Al_{3.5}Mg_{0.5})O₂₀(OH)₄ which represents a mineral with a charge of -0.75 *e*. This particular clay is chosen because of its wide use in the preparation of polymer nanocomposites.

Molecular dynamics (MD) simulations are performed to obtain information on the geometrical aspects of the intercalation process and to collect average data about the interlayer species. As a preliminary step aimed at evaluating the reliability of our approach, dry montmorillonite is simulated and our results for this system are compared to previous theoretical and experimental studies.⁷ We then proceed to the simulation of the CL-intercalated system; the results are analyzed in terms of the orientation of the CL molecules in the interlayer channel, their interaction with the Na⁺ cations, and the energetics of the intercalated system.

2. Computational Methodology

For this study, we used the molecular dynamics module and the energy minimizer of the Cerius² 4.0 package.⁸ Due to the presence of organic and inorganic species, the universal force field (UFF)⁹ was selected.

2.1. Caprolactone Molecule. The geometry of the isolated CL molecule was optimized with the UFF. During the energy minimization, the partial charges of the atoms were optimized with the QEq algorithm;¹⁰ they are reported in Table 1. As found in previous experimental and theoretical studies,¹¹ the seven-membered ring of CL preferentially adopts a chair conformation (Figure 1).

2.2. Dry Na-Montmorillonite. The simulation system consists of a periodically replicated, rectangular box that contains eight Na-montmorillonite unit cells (4 × 2 × 1). The dimensions of the starting box are *a* = 20.8 Å, *b* = 18.4 Å, and *c* = 12.0 Å. The starting system is monoclinic

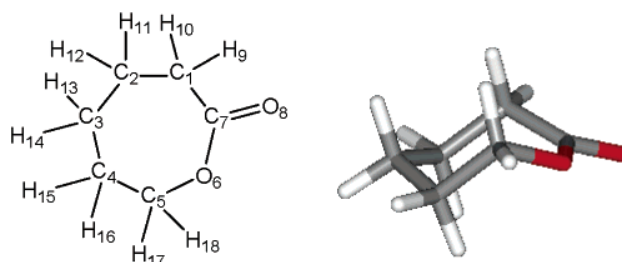


Figure 1. Atom numbering and chair conformation of the CL molecule.

with $\beta = 99^\circ$, as in the unit cell of dry montmorillonite.¹² The positions and charges of the sites in the unit cell of the clay are directly derived from the empirical model introduced by Skipper et al.^{7a} (Table 1): four isomorphous substitutions of trivalent Al atoms by divalent Mg atoms in the octahedral sheet and two isomorphous substitutions of tetravalent Si atoms by trivalent Al atoms in the tetrahedral sheets. Six Na⁺ counterions are placed in the interlayer region.

2.3. Na-Montmorillonite with Intercalated CL Molecules. In a preliminary MD study of hydrated Na-montmorillonite with the UFF, we have found that the density of water in the interlayer region (0.95) is very close to the density of liquid water. On that basis, we assume that the density of CL between the clay sheets is close to the density of liquid CL (1.03). Moreover, X-ray diffraction data^{6a} provide the *d*₀₀₁ parameter of Na-montmorillonite with intercalated CL molecules (19.6 Å). If we subtract the volume of the simulation cell of dry Na-montmorillonite at equilibrium (3735 Å³) from the calculated volume of a monoclinic Na-montmorillonite with *d*₀₀₁ = 19.6 Å (7410 Å³), we obtain a volume of 3675 Å³ occupied by CL molecules. With a density of 1.03, this corresponds to about 18 CL molecules in the simulation cell. Therefore, for the simulation of the CL-intercalated system, the starting point is the monoclinic system of dry Na-montmorillonite, with the *c* parameter enlarged to 20.0 Å and 18 CL monomer molecules inserted in the interlayer spacing. Let us recall that since the polymerization of caprolactone is most efficient when the medium is anhydrous, the clay is usually dried before the monomer incorporation.⁶ Therefore, water-free montmorillonite appears to be the most suitable system to model CL intercalation.

2.4. Molecular Dynamics Simulations. For the two periodic systems (dry and CL-intercalated Na-montmorillonite), the configuration of the starting simulation cell is replicated in all three spatial directions through periodic boundary conditions. Ewald summation methods¹³ are used to treat Coulombic and attractive van der Waals interactions with a standard cutoff. Repulsive van der Waals interactions are directly calculated with standard parameters. All simulations are performed at a constant temperature using a "weak coupling" algorithm¹⁴ and a coupling time constant of 500 fs. The Verlet algorithm and a time step of 1 fs are used for all dynamics simulations.

To reduce the computational effort, we impose that the atoms in the clay sheets remain at constant positions during the MD calculation, as the sheets are expected to

(7) (a) Skipper, N. T.; Refson, K.; McConnell, J. D. C. *J. Chem. Phys.* 1991, 94, 7434. (b) Karaborni, S.; Smit, B.; Heidug, W.; Urai, J.; Oort, E. v. *Science* 1996, 271, 1102. (c) Young, D. A.; Smith, D. E. *J. Phys. Chem. B* 2000, 104, 9163. (d) Park, S.-H.; Sposito, G. *J. Phys. Chem. B* 2000, 104, 4642. (e) Chavez-Paez, M.; Van Workum, K.; de Pablo, L.; de Pablo, J. J. *J. Chem. Phys.* 2001, 114, 1405.

(8) Molecular Simulations Inc., 9685 Scranton Road, San Diego, CA; 1997.

(9) (a) Rappé, A. K.; Casewit, C. J.; Colwell, K. S.; Goddard, W. A., III; Skiff, W. M. *J. Am. Chem. Soc.* 1992, 114, 10024. (b) Casewit, C. J.; Colwell, K. S.; Rappé, A. K. *J. Am. Chem. Soc.* 1992, 114, 10035. (c) Casewit, C. J.; Colwell, K. S.; Rappé, A. K. *J. Am. Chem. Soc.* 1992, 114, 10046.

(10) Rappé, A. K.; Goddard, W. A., III *J. Phys. Chem.* 1991, 95, 3358.

(11) (a) Abraham, R. J.; Gherzi, A.; Petrillo, G.; Sancassan, F. *J. Chem. Soc., Perkin Trans. 2* 1997, 1279. (b) Allen, F. H.; Howard, J. A. K.; Pitchford, N. A.; Vinter, J. G. *Acta Crystallogr., Sect. B* 1994, 382.

(12) Brindley, G. W.; Brown, G. *Crystal Structures of Clay Minerals and Their X-ray Identification*; Mineralogical Society: London, 1980.

(13) Karasawa, N.; Goddard, W. A., III *J. Phys. Chem.* 1989, 93, 7320.

(14) Berendsen, H. J. C.; Postma, J. P. M.; van Gunsteren, W. F.; DiNola, A.; Haak, J. R. *J. Chem. Phys.* 1984, 81, 3684.

be fully rigid. However, as a consequence, *NPT* dynamics simulations (i.e., performed at constant number of particles, pressure, and temperature) are not possible (since the volume would be allowed to change) and we have to carry out successive, alternating *NVT* dynamics simulations and energy minimization steps, also using the UFF. During *NVT* dynamics simulations, the clay sheets are immovable, but when energy minimizations are performed, registry and swelling motions are allowed. The "smart minimizer" of the Cerius² package is used with 2500–5000 iterations. The RMS-force criterion is 0.005 kcal mol⁻¹ Å⁻¹, the criterion on the energy difference is 10⁻⁵ kcal mol⁻¹, and the criterion on the RMS-shift is 3 × 10⁻⁵ Å.

For the clay with intercalated CL molecules, a procedure in three steps is followed:

(1) The initial optimization of the cell parameter *c* leads to a value of 19.4 Å. Then, the cell parameters are frozen and short *NVT* dynamics simulations (20 ps) are performed at increasing temperatures from 300 to 600 K in increments of 50 K. This first step allows the system to overcome potential barriers and rearrange itself into a state with improved interactions among CL molecules, between Na⁺ cations and CL molecules, and between the clay sheets and CL molecules at a starting cell parameter *c* of 19.4 Å.

(2) *NVT* dynamics simulations (20 ps) at 300 K alternate with energy minimizations in order to optimize the interlayer spacing. At first, the cell parameter *c* is the only degree of freedom. As soon as *c* is optimized in the monoclinic space group (*c* = 18.3 Å), registry motions are allowed: two degrees of freedom (α and β) are added. Therefore, the three parameters α , β , and *c* are simultaneously optimized and the equilibrium configuration is obtained. This step-by-step strategy prevents the system from evolving toward irrelevant and less stable configurations with a large sliding of the two clay sheets.

(3) We start from the equilibrium configuration found in step 2, and a *NVT* dynamics simulation of 460 ps is performed at 300 K. We observe that the system reaches equilibration after 50 ps; then average data are collected over 410 ps.

For dry Na-montmorillonite, steps 1 and 2 lead to the equilibrium configuration.

3. Results and Discussion

3.1. Dry Na-Montmorillonite. From this dynamics study with the UFF, we obtain $d_{001} = 9.88$ Å, $\alpha = 97^\circ$, and $\beta = 95^\circ$ for the equilibrium configuration (Figure 2). These results are very close to experimental data ($9.55 < d_{001} < 9.8 \pm 0.1$ Å, $\alpha = 90^\circ$, and $\beta = 99^\circ$) and previous MD and Monte Carlo calculations ($9.7 < d_{001} < 9.8$ Å).⁷ This clearly demonstrates the validity of our theoretical approach. We only note a slight registry motion of the clay sheets since α and β differ from the starting values. In agreement with previous studies, the equilibrium position of Na⁺ cations is in the hexagonal sites, where the cation is nestled within two hexagonal cavities of opposite tetrahedral sheets (Figure 2b). Most of the Na⁺ cations are 6 Å apart, but two of them, which are close to the isomorphous substitution of a Si atom, are only 5.0 Å apart (Figure 2b). From the analysis of the different energy terms, it appears that the stability of the clay is mainly due to electrostatic interactions.

3.2. Na-Montmorillonite with Intercalated CL Molecules. As a preliminary step to investigate the orientational behavior of the molecules, we placed 6 CL molecules in the interlayer spacing with different starting

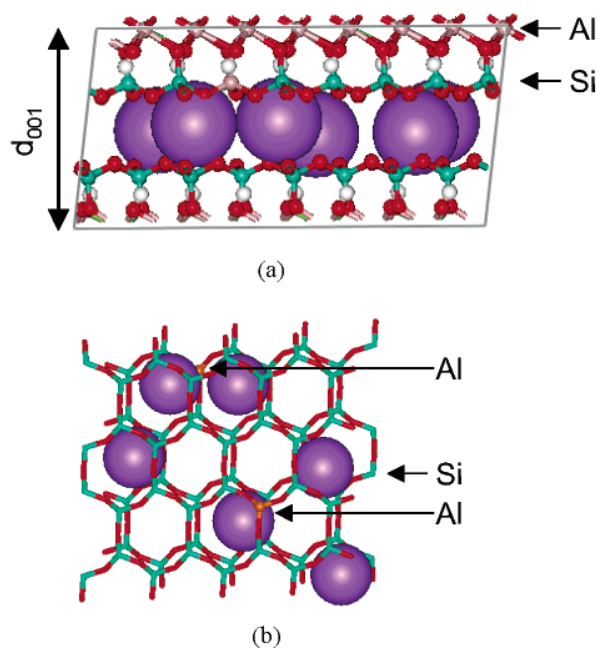


Figure 2. Equilibrium configuration of dry Na-montmorillonite. Only the Na⁺ cations are shown with their van der Waals radius. (a) Side view with the atoms of the clay sheets in a "ball and stick" representation. (b) Top view. Only the SiO₃ moieties (sticks) of the tetrahedral sheets surrounding the Na⁺ cations are shown.

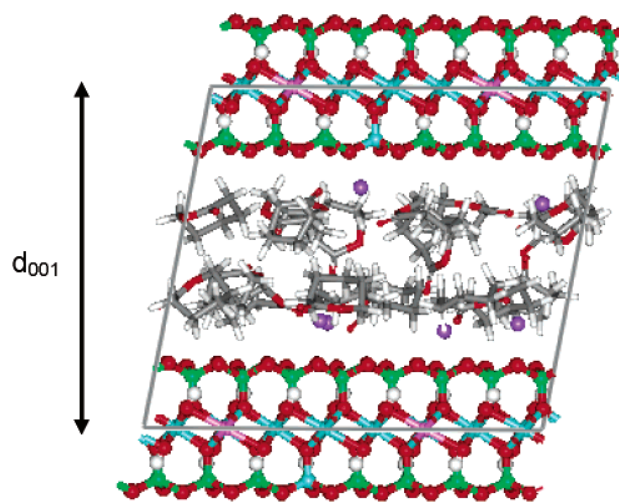


Figure 3. Equilibrium configuration of Na-montmorillonite intercalated with CL molecules.

orientations relative to the clay sheets. Short MD simulations led to a similar orientation, with the CL rings preferentially oriented to maximize their interaction with the surface of the sheet. Therefore, when considering the "fully loaded" system, the 18 CL molecules form two layers, roughly parallel to the channel walls. The Na⁺ counterions are distributed between the CL layers and the clay sheets. During MD simulations, the geometry of the CL rings is allowed to change but the partial charges are fixed.

From these calculations, we obtain $d_{001} = 18.17$ Å, $\alpha = 87.6^\circ$, and $\beta = 100.8^\circ$ for the equilibrium configuration (Figure 3). We find a slight registry motion of the clay sheets for this system as well. The volume of the box is 6824 Å³, implying that the remaining volume for CL molecules is 3090 Å³. This corresponds to a density of 1.10 for the interlayer phase (close to the density of liquid CL).

The average intercalation energy of a CL molecule in the interlayer spacing of dry Na-montmorillonite is defined as

$$\Delta U = [U(18) - U(0) - 18U(\text{CL})]/18$$

$U(18)$ and $U(0)$ are the equilibrium configuration potential energies of intercalated and dry Na-montmorillonite, respectively; and $U(\text{CL})$ is the potential energy of one CL molecule. We find a large negative value for ΔU (-35.9 kcal mol $^{-1}$). We have to subtract from that value the solvation energy of CL, which is included in $U(18)$ but not in $U(\text{CL})$; from a calculation on a cluster of 18 CL molecules, it is estimated to be around 20 kcal mol $^{-1}$. Therefore, the global stabilization upon intercalation is around 16 kcal mol $^{-1}$ per molecule, which indicates that from the energetic point of view, the spontaneous intercalation of CL molecules in Na-montmorillonite is highly favorable. The entropy balance of the intercalation process cannot be estimated from our calculations. However, for a similar system (polystyrene intercalated in montmorillonite channels), Vaia and Giannelis^{3,4} have performed detailed mean-field studies to evaluate the energetic and entropic aspects of the intercalation process. They have shown that the loss of conformational freedom of the molecules upon intercalation can be compensated by the entropic gain of the ions present in the cavity, due to the increase in the clay sheet separation. In particular, this compensation is complete (i.e., the entropic balance is neutral) when the gallery height increases by less than 1 nm, as is the case in our systems. Those results have been obtained for alkylammonium counterions; the same compensating effect must be at work in the Na-containing compounds studied here, even though to a significantly smaller extent (because the Na $^{+}$ cations tend to remain close to the channel walls, see below). Nevertheless, the entropic balance is expected not to be strongly unfavorable in our systems. This, combined with a clear energetic stabilization, is consistent with the observation of spontaneous intercalation.

To gain information on (i) the spatial distribution of the various species within the channels and (ii) the nature of the interactions among those species, average positional data are collected during the late stages of the MD simulations, after the system has reached equilibration. Radial distribution functions are calculated between Na $^{+}$ cations and the oxygen atoms of CL molecules in order to estimate the solvation of Na $^{+}$ cations by CL molecules; the interaction between Na $^{+}$ cations and the oxygen atoms of the clay is evaluated as well. Radial distribution functions are defined as follows:

$$g_{AB}(r) = \frac{dn_r}{4\pi\rho_B r^2 dr}$$

where dn_r is the number of B particles in a shell between r and $r + dr$ around each A particle and ρ_B is the density of B particles. The number of nearest neighbors is deduced from the radial distribution function:

$$N_{AB} = 4\pi\rho_B \int_0^{\text{cutoff}} g_{AB}(r)r^2 dr$$

where the cutoff is defined in order to consider only the first peak of the radial distribution function. The results are reported in Figure 4.

On average, the first solvation shell of Na $^{+}$ cations is composed of 3 carbonyl oxygen atoms ($d(\text{Na}-\text{O}) = 2.29$ Å) and 1.6 intracyclic oxygen ($d(\text{Na}-\text{O}) = 2.25$ Å) from CL

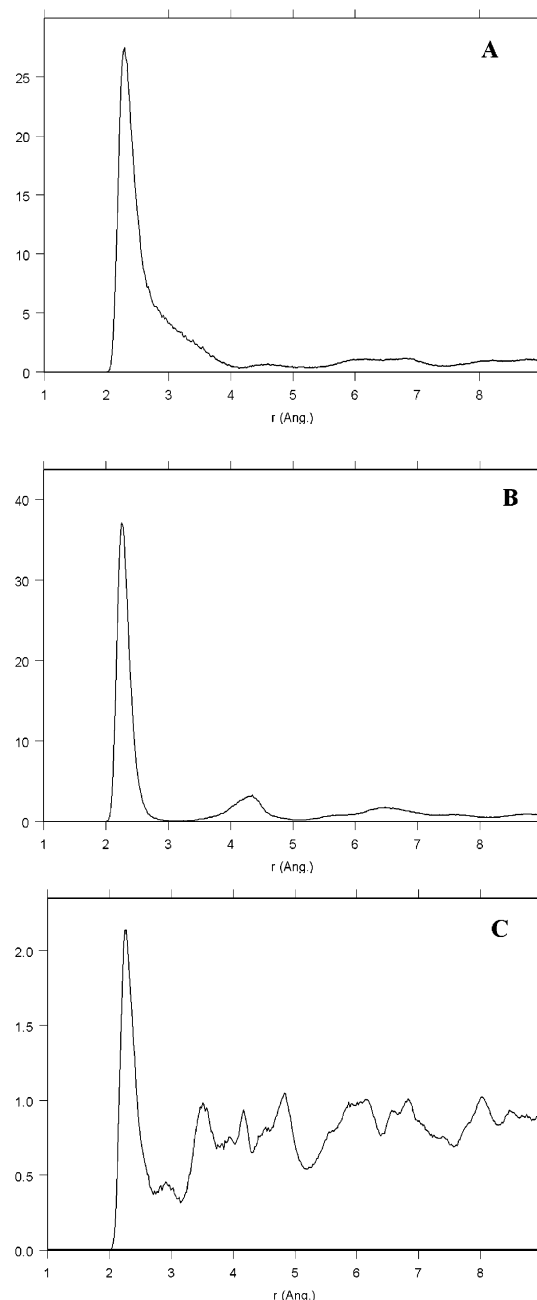


Figure 4. Radial distribution functions around Na $^{+}$ cations for (A) the carbonyl oxygen atoms of CL, (B) the intracyclic oxygen atoms of CL, and (C) the clay oxygen atoms.

molecules and 2 oxygen atoms from the silicate sheets ($d(\text{Na}-\text{O}) = 2.27$ Å). In terms of coordination number, these results are quite similar to those of recent calculations¹⁵ dealing with the hydration of Na $^{+}$ cations (5 or 6 water molecules in the first solvation shell). The ability of CL molecules to solvate the Na $^{+}$ cations in the interlayer spacing is therefore likely an important factor contributing to the spontaneous intercalation process.

Density profiles of the interlayer species are determined through calculations of their probability distribution

(15) (a) Degrève, L.; Quintale, C., Jr. *J. Chem. Phys.* 1994, 101, 2319. (b) Obst, S.; Bradaczek, H. *J. Phys. Chem.* 1996, 100, 15677. (c) Lee, S. H.; Rasaiah, J. C. *J. Phys. Chem.* 1996, 100, 1420. (d) Koneshan, S.; Rasaiah, J. C.; Lynden-Bell, R. M.; Lee, S. H. *J. Phys. Chem. B* 1998, 102, 4193. (e) White, J. A.; Schwegler, E.; Galli, G.; Gygi, F. *J. Chem. Phys.* 2000, 113, 4668.

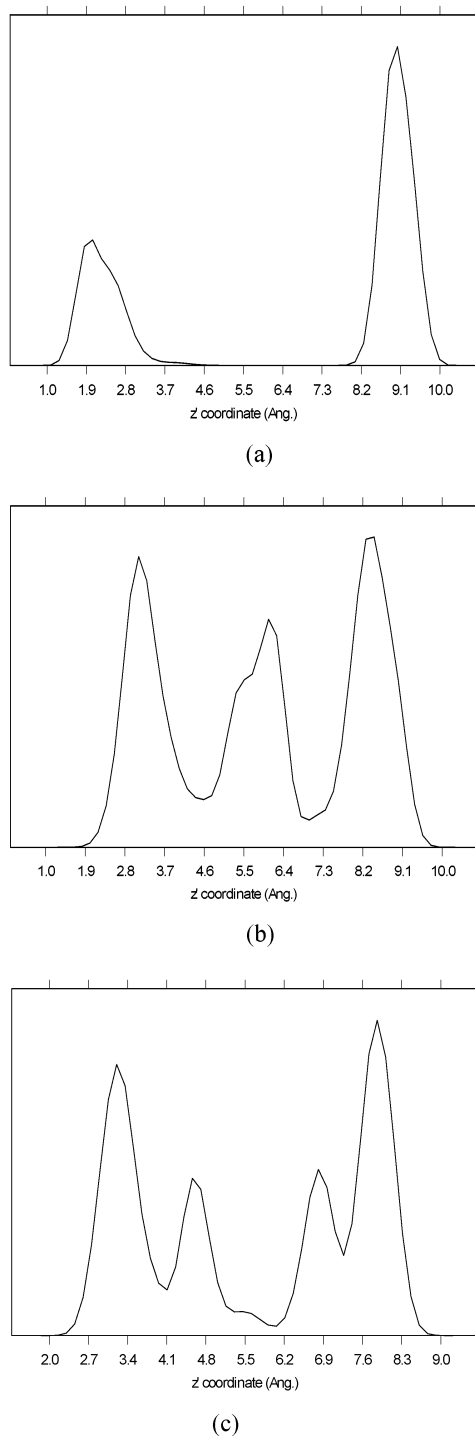


Figure 5. Density profiles for (a) the Na⁺ cations, (b) the carbonyl oxygen atoms of CL, and (c) the intracyclic oxygen atoms of CL. The z-coordinate corresponds to the direction perpendicular to the clay sheets.

functions in the z direction, that is, the direction perpendicular to the plane of the clay sheet (Figure 5). Na⁺ cations are distributed close to the clay sheets, while the

CL molecules form two layers with various orientations of the carbonyl and intracyclic oxygen atoms. The distribution of the Na⁺ cations is not symmetric: four cations are close to the first clay sheet while only two are close to the second sheet (Figure 5a). Most of the oxygen atoms are oriented toward Na⁺ cations and contribute to their solvation. This partial solvation of the Na⁺ cations (which are still in interaction with the clay sheets) is a driving force that is consistent with the spontaneous intercalation of CL molecules in Na-montmorillonite. Some carbonyl oxygen atoms are located in the middle of the interlayer spacing and are surrounded by two sheets of intracyclic oxygen atoms (Figure 5b,c). This corresponds to groups that do not participate in the solvation of Na⁺ cations. As a result, the spatial distribution of the oxygen atoms (and consequently that of the CL molecules) is symmetric with respect to the cavity wall (Figure 5b,c), despite the asymmetry in the distribution of the cations.

4. Concluding Remarks

The results of our MD study provide insight into the structure and energetics of Wyoming Na-montmorillonite intercalated with caprolactone monomers. The interaction between the clay sheets of Na-montmorillonite and CL molecules and the partial solvation of the Na⁺ cations by CL molecules are two energetic factors that favor the spontaneous intercalation of the monomers. These two factors are also at work to some extent for intercalated PCL. However, with respect to the monomer, the incorporation of the solvating groups in polymer chains is expected to decrease the efficiency of solvation and the strength of the interaction with the walls, especially in confined spaces such as clay channels. In addition, the loss of configurational freedom that the polymer chains undergo when intercalating raises the entropic price to be paid for their intercalation to a much higher level than for the CL molecules.³⁻⁵ Therefore, it appears that the enthalpic factor overcomes the entropic factor only for the monomer, since spontaneous intercalation is observed for the monomer and not for the polymer.^{6,16} More generally, we believe that the modeling approach followed in this work could be applied to investigate the structural and energetic aspects of the intercalation of other monomers in Na-montmorillonite, to determine a priori the feasibility of the in situ polymerization route. Clearly, this work indicates that favorable interactions with the channel walls and solvation of the Na⁺ cations are prerequisites for efficient monomer intercalation.

Acknowledgment. The authors are grateful to Ph. Dubois, M. Alexandre, and E. Pollet (Université de Mons-Hainaut) for many fruitful discussions. This project is supported by the Government of the Région Wallonne, in the framework of the WDU program (TECMAVER). Research in Mons is also partly supported by the Belgian Federal Government (IAP Project V/3) and the Belgian National Fund for Scientific Research FNRS/FRFC. R.L. is "Directeur de Recherches du Fonds National de la Recherche Scientifique" (FNRS - Belgium).

LA034491N

(16) LeBaron, P. C.; Wang, Z.; Pinnavaia, T. J. *Appl. Clay Sci.* 1999, 15, 11.

Molecular Dynamics Simulations of Intercalated Poly(ϵ -Caprolactone)-Montmorillonite Clay Nanocomposites

Fabrice Gardebien,^{*,†} Anouk Gaudel-Siri,[‡] Jean-Luc Brédas,^{†,§} and Roberto Lazzaroni[†]

Service de Chimie des Matériaux Nouveaux, Université de Mons-Hainaut, 20 Place du Parc, B-7000 Mons, Belgium, Laboratoire Réso - UMR 6178, Université Paul Cézanne, Faculté St Jérôme, Av. Esc. Normandie-Niemen, 13397 Marseille Cedex 20, France, and School of Chemistry and Biochemistry, Georgia Institute of Technology, Atlanta, Georgia 30332-0400

Received: February 16, 2004; In Final Form: May 11, 2004

The structure and energetics of poly(ϵ -caprolactone), PCL, chains confined between two platelets of organo-modified montmorillonite clay, are investigated using molecular dynamics techniques. The amount of PCL in the clay gallery has been systematically varied to assess the influence of the interlayer density on the molecular organization. The structural characteristics are examined in terms of interlayer density profiles, radial distribution functions, and dihedral angle distributions. The results show that the interlayer phase organizes into four layers, along with an enhancement of the proportion of extended zigzag chain conformations, with respect to the amorphous polymer bulk. Calculations of the interaction energies between the various subsystems (the PCL chains, the surfactant molecules, and the clay surfaces) clearly show the formation of polar as well as apolar interactions between PCL and the clay surfaces, which can significantly contribute to the polymer intercalation (in addition to the polymer–surfactant interactions).

1. Introduction

A promising area in polymer technology is the development of polymer–clay nanocomposites (PNCs). In this new class of materials, layered clay particles are distributed within a polymer matrix. Depending on the PNC constituents or the preparation route, three structural arrangements have been observed, termed: (a) intercalated, where the polymer chains are organized within the interlayer spaces formed by parallel arrangements of the clay layers, (b) exfoliated or delaminated, in which the individual clay layers are evenly dispersed in the polymer matrix, and (c) composites, where the polymer and the clay particles are immiscible and consist of stacks of clay layers spread inside the polymer matrix. For clay contents as low as 2 wt %, improvements in mechanical, thermal, or barrier properties have been evidenced for the PNCs with respect to conventional polymer microcomposites, with larger enhancement in properties achieved for exfoliated systems (for a review, see ref 1). Among the clays that are commonly employed in PNCs, the most prominent are smectite-type clays such as montmorillonite (mmt), whose crystal lattice consists of negatively charged aluminosilicate layers. It should be stressed that, in order to increase the miscibility between the polymer matrix (often hydrophobic) and the pristine clay (highly hydrophilic), many experiments are conducted using clays in which the natural metal cations that balance the charge deficiency have been substituted by organophilic cations such as alkylammoniums.^{2–7}

Prior to recent theoretical efforts devoted to PNCs, the structural arrangement and dynamical behavior of polymer chains confined between neutral solid planes had been studied using molecular simulations techniques.^{8–12} For the confined

polymer, the main structural observations are: (i) near the planes, the polymer chains are flattened and the density of chain ends is enhanced, regardless of the strength of the interaction between the polymer and the surface, and (ii) segments in the center of the polymer chains end up near the planes in the case of strong polymer–surface interactions (with an interfacial density higher than that of the polymer bulk value) and mainly away from the planes in the case of moderate interactions. Strong polymer–surface interactions also lower the mobility of the interfacial polymer segments in all directions.¹¹ As for the PNCs, mean-field approaches have provided a general framework for their description.^{13–16} Vaia et al. have developed a mean-field model to describe polymer melt intercalation in organically modified layered silicates;^{13,14} these authors discussed the entropic and enthalpic factors that favor intercalation and exfoliation. Balazs et al. derived useful criteria for facile intercalation: the polymer must contain a fragment that is highly attracted to the surface but also a longer fragment that is not attracted to the sheets.¹⁶ Lee et al.^{17,18} have investigated the intercalation process by simulating the flow of polymer chains represented by connected beads into a narrow slit. An important conclusion of these works is that increasing the polymer–surface interaction favors the intercalation; however, their results also indicate a decreased propensity for intercalation when polymer–silicate affinity is too high (for results compared within the same period of simulation time). The effects of both the polymer molecular weight and the polymer–surface interactions on the kinetics of the intercalation process have also been investigated by the same authors.¹⁹ For PNCs based on polystyrene^{20,21} and poly(ethylene oxide) (PEO),^{22–24} combined molecular dynamics (MD) and NMR studies showed important inhomogeneities in their dynamical behavior across the clay gallery and over a wide range of temperature;²³ confined PEO appears to be more disordered than its bulk amorphous counterpart.^{22–24} For PNCs based on nylon-6, systematic studies of the influence of the size

* To whom correspondence may be addressed. E-mail: Fabrice@averell.umh.ac.be. Fax: ++32-65-37-38-61.

[†] Université de Mons-Hainaut.

[‡] Université Paul Cézanne.

[§] Georgia Institute of Technology.

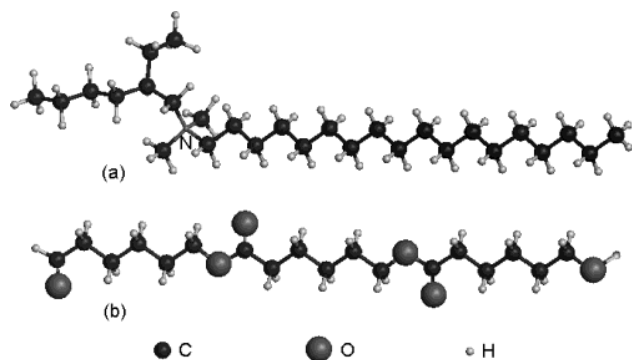


Figure 1. Molecular structures of (a) the dimethyl 2-ethylhexyl *n*-octadecylammonium ion that corresponds to the surfactant used throughout this study and (b) a PCL chain of 3 monomer units (3-mer).

of the organic modifier have established that the pristine mmt clay (with its natural metal cations) is preferred for a maximum interfacial strength with the polymer matrix.^{25,26} Besides these works on polymer–silicate systems, hydrated pristine silicates have been the topics of extensive studies in the literature (see, for example, ref 27 and the references therein).

The biodegradable and biocompatible polymer poly(ϵ -caprolactone) (PCL), a linear aliphatic polyester, has shown a great ability to form intercalated PNCs with mmt clays rendered organophilic by cation exchange. The intrinsic interesting properties of this polymer, combined with those potentially gained by PNC formation, have prompted joint experimental and theoretical studies of PCL-based nanocomposites.^{28–32} In this work, we present the results of MD simulations carried out on model systems for intercalated PCL nanocomposites. In these models, short PCL chains are confined between two parallel platelets of montmorillonite whose metal ions have all been replaced by dimethyl 2-ethylhexyl *n*-octadecylammoniums. Our goal is to probe the structural arrangements of the intercalated PCL chains using atomistic simulations that allow a close look at the material at the nanoscopic level and help in understanding the intimate organization between the three components of the systems (PCL, mmt, and surfactants). The interactions between the components were also examined. The results provide some insights into the factors that favor intercalation of the PCL. MD simulations were also conducted for amorphous samples of PCL, and their results are used throughout the analyses as a basis for comparison. This study of the intercalated system is our first contribution to the modeling of PNCs based on PCL; a forthcoming paper will present the results of simulations for exfoliated PCL–mmt models.

The paper is organized as follows: the Methodology section describes successively the selection procedure of the force field, the models used to treat our PNC system, the details of the MD simulations, and the procedures followed to derive initial configurations. The results of the simulations are presented and discussed in section 3. A final discussion is provided in the Conclusion.

2. Methodology

2.1. Force-Field Selection Procedure. To select an appropriate force field for the description of nanocomposite systems based on PCL chains (Figure 1) and organo-modified montmorillonite, a preliminary study was conducted to obtain an appropriate force field for the description of the polymer. This

is important since a correct description of the interactions between the polymer chains is essential for obtaining details of their structural properties at interfaces.³³ Three force fields were considered: the universal force field (UFF),³⁴ the Dreiding force field,³⁵ and a hybrid force field hereafter noted DT. The DT force field uses the Dreiding force-field parameters for the bond, angle, torsion, and inversion parameters and the Tripos parameters³⁶ for the nonbonded van der Waals parameters. In that force field, the H-bond term present in the Dreiding original force field has been turned off since no significant H bonds are expected in the polymer system and in our nanocomposite systems. For the electrostatic interactions, the charges are taken in all cases from an electrostatic potential calculation carried out on a smaller oligomer species (vide infra). The rationale behind the choice of using the Tripos nonbonded parameters comes from a previous comparative study of the van der Waals parameters of the three force fields (UFF, Dreiding, and Tripos) with *ab initio* MP2 calculations for an organic cluster adsorbed on a small aluminosilicate structure that mimics the clay surface.³⁷ A slightly better agreement with the results at the MP2 level were obtained for the Tripos van der Waals parameters.

MD simulations of amorphous PCL were considered for the three force fields in the NPT ensemble at 300 K. The simulation cells comprised 3 chains of 48 monomer units each. The amorphous polymer builder module and the OFF module available in the Cerius² modeling environment³⁸ were used for the generation of the amorphous configurations and for the molecular mechanics and dynamics calculations, respectively. Three configurations were generated; for each one, a NVT simulation using UFF at 300 K during 50 ps was first performed. For each of the resulting cells, two successive annealing cycles in the NVT ensemble were considered with the following temperatures and durations for both cycles: heating at 1000 K for 30 ps and then cooling at 700 K for 25 ps and at 300 K during 15 ps. Using the configurations obtained, NPT dynamics at 300 K followed during 100 ps to derive the final density value for the simulated amorphous PCL. The cell whose density comes closest to the experimental density was selected for runs according to the above-described procedure using the Dreiding and DT force fields: 50 ps of NVT dynamics at 300 K, followed by the two successive annealing cycles and ultimately by 100 ps of NPT dynamics. The densities obtained for the amorphous PCL are 1.04 and 1.01 g·cm⁻³ for UFF and the DT force field, respectively. The much lower value reached for simulations using the Dreiding force field, 0.93 g·cm⁻³, suggests an inadequacy between the van der Waals parameters of this force field and the calculated set of atomic charges for the chains. Since the results obtained with UFF better match the experimental density value of 1.09 g·cm⁻³ for amorphous PCL, this force field was selected for the simulations of our PNC.

2.2. Models for the Polymer Nanocomposite. For systems that correspond to chains confined between adsorbing surfaces, it has been argued that efficient packing of the chains in the interlayer space may favor a higher interlayer density.³⁹ Since no information about the efficiency with which the chains are packed inside the gallery is available, the *a priori* choice of an interlayer density value for the organic phase (which amounts to determining the quantity of PCL, since the number of organophilic cations is known and equals the total charge borne by a clay platelet, that is, 9 in our simulation cell) is delicate. Our approach was to extend our study over a narrow range of plausible interlayer organic densities which were derived using the procedure described below. To calculate the interlayer

density, only the volume available to the organic molecules was considered. This volume is estimated as $L_x L_y (L_z - 2d_z)$, where L_x and L_y are the lengths of the simulation box in the x and y directions and L_z is the distance between two facing planes of basal oxygen atoms in the z direction. The distance d_z is the minimum distance at which an organic molecule can approach the aluminosilicate surface, and it is taken as half the van der Waals radius of the basal oxygen atoms. On the basis of experimental observations for the PCL polymer, three initial interlayer densities, i.e., three amounts of PCL to be inserted inside the gallery, were considered. Experimental measurements for PCL have provided density values for the amorphous and crystalline parts at 300 K of 1.09 and 1.21 g·cm⁻³, respectively.⁴⁰ Accordingly, based on the assumption that the density of the organic phase in the gallery is the same as the density of the bulk polymer, the following two systems were considered: the first with 3 chains of 8 monomer units each (hereafter denoted system II) and the second with 2 chains of 14 monomers (system III), which correspond to a density of 1.11 and 1.19 g·cm⁻³ for the organic phase in the interlayer space, respectively. Additionally, since our force field slightly underestimates the experimental density for the amorphous polymer (see section 2.1), we chose the following lowest limit value, 1.03 g·cm⁻³, for the interlayer organic phase; this corresponds to a system made up of 2 chains of 10 monomer units (system I). As mentioned earlier, in addition to the polymer chains, the gallery of the three systems contains nine surfactant molecules.

2.3. Simulation Cell. Montmorillonite is an aluminosilicate made up of one aluminate octahedral sheet sandwiched by two silicate tetrahedral sheets. Isomorphous substitution of metal ions in the crystal lattice by cations of lower charge causes a net permanent negative charge which is balanced by cations in the interlayer space. The model chosen for the montmorillonite clay has been taken from the work of Skipper et al.⁴¹ The unit layer considered in this study with x and y dimensions of 31.7 Å by 18.3 Å bears a negative charge of 9 e, which results from the substitutions of Si atoms by Al atoms and Al atoms in octahedral positions by Mg atoms.

The third dimension of the simulation box, which corresponds to the interlayer distance, was chosen to match the experimental value determined by X-ray diffraction experiments for our PNC, 26.8 Å.^{30,31} The positive charges in the interlayer space were borne by 9 dimethyl 2-ethylhexyl *n*-octadecylammonium ions (Figure 1); this surfactant corresponds to the main organic modifier in the organically modified commercial montmorillonite Cloisite 25A.

2.4. Simulation Details. The calculations were performed within the Cerius² modeling environment.³⁸ The UFF³⁴ was considered for all simulations except where otherwise stated. Throughout all simulations, the positions of the atoms of the clay were fixed. These restraints on the clay atomic positions are commonly used and have proven to be pertinent since reliable results can be obtained with reasonable computational efforts.^{42–44} For the treatment of the electrostatic interactions, the Ewald summation method was used.⁴⁵ The charges on the atoms (see appendix) of the individual surfactant molecules and polymer chains (of lengths up to 8 units) were obtained by fits to the electrostatic potentials derived from ab initio HF/6-31G(d) calculations (CHELPG method⁴⁶ as implemented in the program system Gaussian 98⁴⁷). This approach is known to provide a more realistic description of the charge distribution, compared to the more commonly used charge-equilibration method⁴⁸ or Mulliken population analysis. For the longer polymer chains (10-, 14-, and 48-mer), the charges were

obtained with the same technique but performed on subunits. For example, the charges for the 48-mer were derived from a calculation made on an octamer. The 48-mer was then constructed as six octamers with the atomic charges at their junctions modified so as to match those of an ester function in the inner part of an octamer. The charges on all atoms were kept fixed during the simulations. For the van der Waals interactions, the Lennard-Jones potential was driven smoothly to zero for distances between 8 and 9 Å. Three-dimensional periodic boundary conditions were imposed in order to avoid boundary artifacts. All simulations were performed in the NVT ensemble and used a coupling to a Nosé–Hoover thermostat^{49–51} to maintain the temperature.

2.5. Procedure for Generating the Initial Configurations.

Two different procedures were followed for generating configurations for the MD simulations of nanocomposite systems I, II, and III. A first step common to both procedures was to find initial guess configurations for a surfactant or for a polymer chain as starting configurations in the interlayer space. These initial configurations were obtained by using the RIS Metropolis Monte Carlo (RMMC) method.⁵² The selected configurations had to satisfy two criteria: to have the lowest possible potential energy and a shape that fit in the simulation box.

Once individual configurations were generated for the molecules in the gallery, the first procedure consisted in increasing the interlayer distance by small steps of 1 Å from the initial value 26.8 Å up to 35 Å for the two systems of lowest densities I and II and up to 40 Å for system III, which corresponds to the highest interlayer density and to the longest PCL chains. While increasing the interlayer space, short MD runs of 8 ps were performed for each intermediate interlayer distance, at a temperature of 2500 K to speed up the conformational sampling. At the maximum interlayer space, the dynamics run was extended to 15 ps before decreasing back the interlayer distance toward its initial value by steps of 0.5 Å, again with short runs of 10 ps at 2500 K. When the interlayer distance of 26.8 Å is recovered, an annealing procedure is performed by cooling to 300 K over a 85-ps period.

The second procedure to derive initial configurations for systems I, II, and III was the following: after insertion in the gallery of the configurations generated for the individual organic molecules by using RMMC, we ran MD calculations using a force field properly modified to sample efficiently the conformational space of the organic phase. Since the UFF force field uses a set of functional forms to generate its parameters, we selected instead the Dreiding force field to impose relevant modifications of its bonded and nonbonded parameters. The Dreiding force field was modified as follows: the torsional barrier height k_{CC} around all CC bonds was set to zero. Additionally, the van der Waals and electrostatic 1–4 interactions were excluded from the total potential energy. Finally, in the 12-6 Lennard-Jones expression, the ϵ_H parameter was scaled down to favor configurational changes by decreasing the intermolecular interactions. For each system, an explorative MD calculation was run over 200 ps at 300 K. The following step was to extract only a few pertinent configurations from the generated set. This was done according to two criteria related to the potential energy: typically, three configurations were extracted for each of the three systems on the basis of both the lowest nonbonded energy and the lowest possible total torsional energy. The bond and angle energetic contributions were discarded from the selection criteria for two reasons. First, their large contributions to the potential energy may bias the selection toward, for example, configurations corresponding to high

nonbonded energy terms and accidentally low bond and angle potential terms. Second, the successive values of the bond and angle energy contributions cannot be directly related to the configuration changes of the whole interlayer system. Once some guess configurations have been generated, the true interatomic potential was restored. Using UFF, a simulated annealing cycle was then carried out for each selected configuration in order to find the lowest-energy configuration when all interatomic interactions are considered.

By use of the configurations resulting from these two procedures, MD simulations at 300 K were then run for 250 ps. Afterward, for each series associated to systems I, II, and III, the structure corresponding to the lowest potential energy was selected for the analyses. Note that the structure of lowest potential energy was derived from 250-ps simulations following the second procedure for the system of lowest density (system I) and following the first procedure for systems with the highest densities (systems II and III). For the analyses, we ensured that the structures were equilibrated by monitoring the potential energy, temperature, and the nonbond energy variations. The period of time required to achieve equilibration was typically in the range of 50–150 ps. The energy calculations of the intermolecular interactions are made for geometries minimized until a root-mean-square convergence ≤ 0.001 kcal/mol/Å in the energy gradient was achieved.

3. Results and Discussion

3.1. Description of the Molecular Organization. Figure 2 shows the final configurations obtained for the three PNC model systems I, II, and III. Apart from its ester function, the caprolactone monomer unit contains five successive methylene groups. One would therefore expect the corresponding polymer to prefer the most hydrophobic region of the interlayer gallery, that is, the central region of the slit. However, our simulations indicate that the polar ester functions show a tendency to interact with the clay surface. An explanation for this polymer–clay interaction resides in long-range electrostatic interactions between, on one hand, the ester function (polar group) and the polarized adjacent methylene group and, on the other hand, the clay layers; this seems to be the main force driving the polymer chains to the surface for subsequent electrostatic and van der Waals interactions with the clay atoms. The polarization of the methylene group adjacent to the ester function is due to hyperconjugation between one of its σ_{CH} molecular orbitals with the delocalized π system of the ester function, thus partly decreasing the electronic density on the corresponding methylene group. The calculated charge on the corresponding carbon (as obtained by the CHELPG method) is about $+0.45$ e, and the global charge for the corresponding CH_2 group is around $+0.40$ e (for comparison, the global charge on the following CH_2 neighbor decreases sharply to 0). When the PCL chains are still far from the clay surfaces, its positively charged methylenes appear to be the most effective polymer sites for bringing the polymer chains toward the negatively charged layers. Indeed, both oxygen atoms of the ester functions bear large negative charges (~ -0.6 e), and at long distance, they do not feel any attraction to the surface due to the negative charges in the clay layers. This result points out the importance of reliable charge determinations (such as those derived from electrostatic potentials using *ab initio* methods) and their incidence on the geometry adopted by the interlayer system. As is also suggested by mean-field models for the free energy of the polymer melt and closely spaced sheets,¹⁶ this PCL–mmt interaction could explain (at least partly) the intercalation of the polymer into

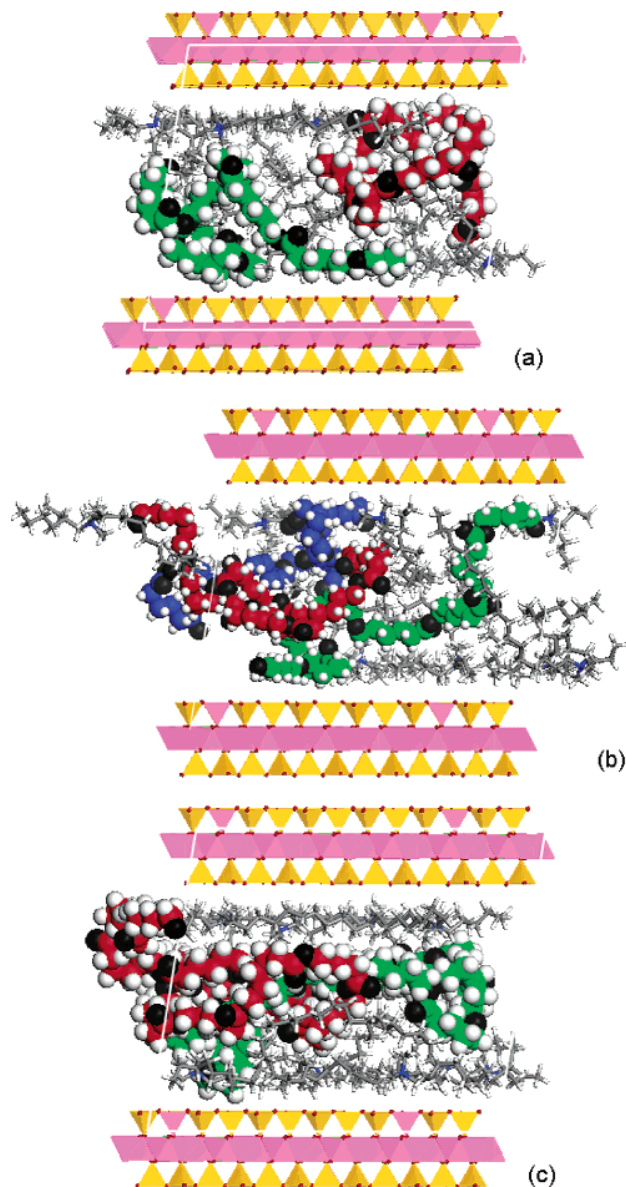


Figure 2. Snapshots of the simulations of (a) PNC system I, (b) PNC system II, and (c) PNC system III obtained after 250 ps of MD calculations. The clay layers are represented by one octahedral sheet sandwiched between two tetrahedral sheets. In the gallery, the surfactants are represented with sticks and the PCL chains with spheres; the carbon atoms are in green, red, and blue, the oxygen atoms in black, and the hydrogen atoms in white.

the mmt gallery, as observed experimentally, and also contributes to the miscibility between PCL and the clay.

When the polymer segments migrate toward the surface, some of the surfactant tails leave portions of the surface and move to the center of the slit (which is mostly hydrophobic) to interact with the rest of the PCL chains. In contrast to the hydrophobic tails, the charged heads of the surfactants remain, as expected, stuck to the surface. Hence, it appears that both types of chains (polymer and surfactant) show a dual behavior distributed over the center (mainly hydrophobic region) and onto the surfaces (hydrophilic region) inside the gallery. Structural and energetic analyses are provided hereafter in order to get some insight into the organization adopted by the organic phase in the interlayer space.

Figure 3 shows the contributions of the backbone atoms (carbon and oxygen) of the surfactants and the PCL chains to

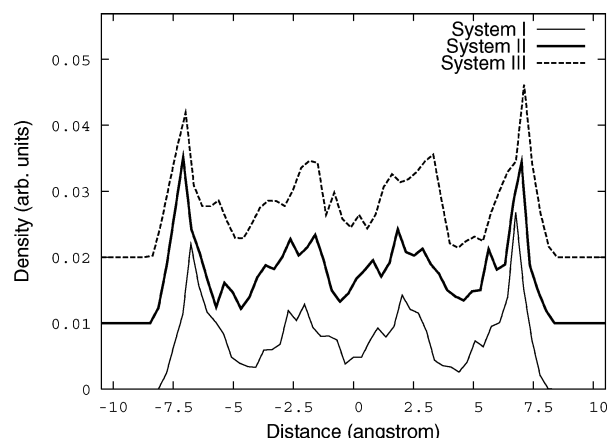


Figure 3. Density profiles for the backbone atoms of the surfactants and PCL chains in the direction normal to the clay layers, reported for the PNC systems I, II, and III. The positions of the two planes of basal oxygen atoms are at ± 10.5 Å. For clarity, the profiles for systems II and III have been shifted by 0.01 and 0.02 along the y axis, respectively.

the interlayer atomic density profile, in the direction normal to the clay platelets, for the three systems. In all three cases, one can see that the system organizes into four layers inside the gallery. This layering effect is well-known for confined liquids⁵³ and arises from solvation forces. However, the profile obtained for confined polymers cannot adopt the smooth aspect observed for confined liquids (at least when considering a simulation box of reasonable size) since the atoms have the additional constraint of being connected along chains that run across many adjacent organic layers. For a given system (I, II, or III), it is clear from Figure 3 that the four peaks have rather different heights and widths depending on their location inside the gallery. The two peaks closer to the clay layers turn out to be the highest; their height is actually related to the force of the interactions existing between the clay surface and the adsorbed chains; the stronger these interactions, the higher the associated peaks.¹¹ For both systems I and II, higher and sharper peaks are observed for the two layers closer to the clay surface, whereas broader and smaller peaks are obtained for the two innermost layers. For system III, the peaks associated to the two directly adsorbed organic layers are still sharp and high; however, the outlines of the two innermost layers are less clear-cut: the two central peaks are broad, and the valley at the center is not very deep (for this system, one might even discern the presence of a small fifth peak in the center of the gallery). The two central layers for this system are actually more spread than their counterparts in the lower density systems. The spreading of these two peaks can be interpreted as an indication that the interlayer phase has reached its highest density limit for this particular interlayer distance, as suggested by Hackett et al. in their work on organically modified layered silicates.⁵⁴ This is how the system tries to accommodate to the excess interlayer density. Since system III seems to correspond to the highest interlayer density limit, it is therefore reasonable to think that the three model systems we have chosen bracket a realistic amount of PCL present in the slit for the PNC model studied here.

It should also be noticed that, initially, all the models were constructed using a distribution of 4 and 5 surfactant molecules on the two inside clay surfaces of the simulation box. It is remarkable then that almost symmetrical density profiles are obtained despite this initial dissymmetry.

3.2. Energetics of the Intermolecular Interactions. For the configuration of lowest potential energy determined for each system, we have also split its total potential energy into

TABLE 1: van der Waals, Electrostatic, and Total Contributions to the Binding Energies (in kcal/mol) between the Three Subsystems PCL, Surfactants, and Montmorillonite Reported for the Three Nanocomposite Systems I, II, and III

		system		
		I	II	III
$E_{\text{mnt-surf}}$	total	799	793	876
	van der Waals	271	256	341
	electrostatic	528	537	535
$E_{\text{mnt-PCL}}$	total	139	136	62
	van der Waals	86	90	42
	electrostatic	53	46	20
$E_{\text{surf-PCL}}$	total	365	372	387
	van der Waals	321	321	342
	electrostatic	44	51	45

contributions that represent only the intermolecular interactions, or more precisely, the binding energy between the three subsystems: $E_{\text{mnt-surf}}$, $E_{\text{mnt-PCL}}$, and $E_{\text{surf-PCL}}$. These represent the negative of the interaction energy between montmorillonite and the surfactant molecules, between montmorillonite and the PCL chains, and between the surfactant molecules and the PCL chains, respectively. Starting from a minimized geometry of the complete system comprising the clay platelets, the surfactants, and the chains, the calculation of the $E_{\text{mnt-PCL}}$ energy, for example, requires first the deletion of all surfactant molecules from the system. It is then obtained as the energy difference between, on one hand, the sum of the potential energy of montmorillonite and the potential energy of the chains and, on the other hand, the potential energy of the interacting montmorillonite-PCL subsystem

$$E_{\text{mnt-PCL}} = E_{\text{pot,mnt}} + E_{\text{pot,PCL}} - E_{\text{pot,mnt-PCL}}$$

Similarly, the $E_{\text{mnt-surf}}$ and $E_{\text{surf-PCL}}$ binding energies have been calculated for systems I, II, and III and are collected in Table 1 along with their respective van der Waals and electrostatic components. We first discuss the total contributions to these binding energies. Despite the difference for the interlayer densities between systems I and II, similar binding energies for the three components $E_{\text{mnt-PCL}}$, $E_{\text{mnt-surf}}$, and $E_{\text{surf-PCL}}$ are obtained. In going from system II to system III, the variations of the $E_{\text{mnt-PCL}}$ and $E_{\text{mnt-surf}}$ energies are opposite, the energy loss for $E_{\text{mnt-PCL}}$ being compensated by an energy gain for $E_{\text{mnt-surf}}$ (74 vs 83 kcal/mol). In contrast, the $E_{\text{surf-PCL}}$ energy remains nearly the same for the three systems. The relatively low $E_{\text{mnt-PCL}}$ energies calculated for the three PNC models (from 62 to 139 kcal/mol, compared to values close to 400 and 800 kcal/mol for the other two binding energies) are consistent with the prediction of Vaia et al. that systems with weak polymer-surface interactions should correspond to the intercalated structural arrangement.¹³ The evolution of the $E_{\text{mnt-PCL}}$ energetic value with respect to the density of the three systems is directly connected with the amount of polymer segments adsorbed on the clay layers. For example, the variation in the number of adsorbed segments is particularly well exemplified by comparing the geometries of systems II and III: most of the polymer segments end up in the center of the gallery for the latter system (in Figure 2c, the clay surface is mostly covered by surfactant tails) while many adsorbed segments are observed in the former (Figure 2b). Presumably, the number of adsorbed PCL segments, which decreases between system II (consisting of 3 PCL 8-mers) and system III (2 PCL 14-mers), is not resulting from the difference in the PCL chain length but is most likely related to the increase in

interlayer density. Indeed, the number of adsorbed PCL segments appears to remain approximately the same from system I to system II (as revealed by the similar $E_{\text{mnt-PCL}}$ energy values), whereas the chain length decreases from decamers to octamers. This is another result that exemplifies the discontinuities observed in the behavior of system III.

The sum of the two energy contributions where the polymer is involved, $E_{\text{surf-PCL}}$ and $E_{\text{mnt-PCL}}$, is about the same for systems I and II (~ 500 kcal/mol) and is lower by ~ 50 kcal/mol for system III. The sum of the three binding energies $E_{\text{mnt-PCL}}$, $E_{\text{mnt-surf}}$, and $E_{\text{surf-PCL}}$, which is not equivalent to the negative of the total nonbonded interaction energy since these three energies do not take into account the nonbonded interactions in a given subsystem (PCL, montmorillonite, or surfactants), amounts to 1303, 1301, and 1325 kcal/mol for systems I, II, and III, respectively. These values should not be used to evaluate the relative stability among the three systems since they represent only a fraction of the total potential energy but rather to highlight the energetic consistency between systems I and II.

The binding energies $E_{\text{surf-PCL}}$, $E_{\text{mnt-PCL}}$, and $E_{\text{mnt-surf}}$ between the various subsystems can be further separated into their van der Waals and electrostatic contributions (Table 1). In all cases, hydrophobic interactions correspond to almost 90% of the binding energy between the surfactants and the polymer chains (van der Waals term of $E_{\text{surf-PCL}}$). Large hydrophobic interactions also exist between the clay atoms and the surfactants (through mainly their hydrophobic tails) as revealed by the large van der Waals contribution (about 35% of $E_{\text{mnt-surf}}$ in all cases). Note also that both van der Waals and electrostatic energies have significant contributions to $E_{\text{mnt-PCL}}$. Therefore, if we can argue that long-range electrostatic forces could play a major role for bringing the polymer chains closer to the surface, the separation of the $E_{\text{mnt-PCL}}$ energy for the three systems is instrumental in demonstrating the importance of the van der Waals interactions between the clay and the polymer, since these constitute the dominant portion of the binding energy. This is an important conclusion from this study on polymer-charged clay interactions. A similar result has been derived by Murgich et al., but it was in the case of interactions of organic molecules with a noncharged clay platelet.⁵⁵

3.3. Conformations of the PCL Chains. For the three systems under consideration, we have also calculated the carbon-carbon radial distribution functions (RDF) for the carbon atoms of the PCL chains. This allows the study of preferential arrangements of the polymer chains inside the gallery. The profile calculated for all the polymer chains of the three systems are shown in Figure 4, along with the profile obtained for an amorphous sample of PCL consisting of 3 48-mers (this system converged toward a density of $1.04 \text{ g}\cdot\text{cm}^{-3}$, close to the value $1.09 \text{ g}\cdot\text{cm}^{-3}$ corresponding to pure amorphous PCL).⁴⁰ The peaks at ~ 1.5 and ~ 2.5 Å correspond to carbon atoms separated by one and two bonds from a reference carbon atom, respectively. The peaks at ~ 3.2 and ~ 3.9 Å correspond to pairs of carbon atoms separated by three bonds in gauche and trans conformations, respectively. For larger interatomic distances, a sharp peak exists at ~ 5.0 Å for systems I and II, while no prominent peak is visible for system III for this distance. The peak at ~ 5.0 Å arises from the occurrence of two successive trans conformations along a 5-atom-long sequence (stretched conformation comprising dihedrals of the kinds CCCC, CCCO, or CCOC). For system III, almost the same peak heights are observed at ~ 5.0 Å (for trans-trans 1-5 pairs) and at ~ 4.5 Å (for trans-gauche 1-5 pairs). The peaks beyond

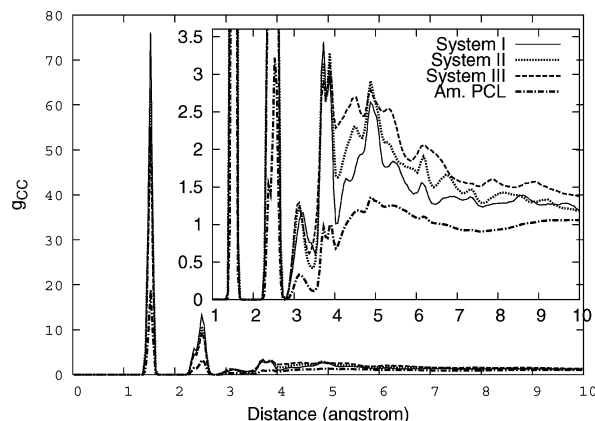


Figure 4. Radial distribution function $g_{\text{cc}}(r)$ for the carbon-carbon correlation for all PCL chains in systems I, II, and III as well as in an amorphous sample of PCL.

TABLE 2: Proportion (%) of trans Dihedral Angles for the PCL Chains and for the Surfactants Calculated for the Systems I, II, and III and for the Pure Amorphous PCL

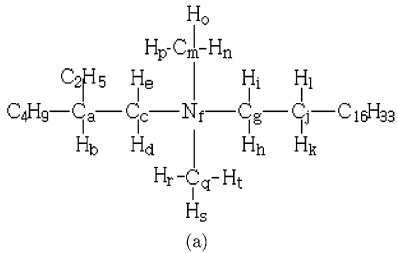
system	PCL	I	II	III
PCL chains	53	61	63	50
surfactants		54	56	51

5 Å correspond to correlations between carbon atoms separated by at least 5 bonds; they are quite small and do not provide further insight into the particular arrangements of the corresponding dihedral sequences of the polymer chains.

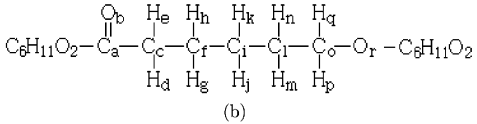
The existence of a prominent peak at 5.0 Å for systems I and II therefore indicates that many dihedral sequences along the PCL chains adopt a fully stretched conformation. The determination of the proportion of trans and gauche dihedral angles for the backbone of the chains (comprising also CCCO or CCOC dihedral types) indicates that a majority of backbone dihedrals are indeed in a trans conformation. For the three systems, the percentages of trans and gauche conformations for the backbone atoms of the PCL chains and the two aliphatic tails of all surfactants are reported in Table 2. We have also reported the corresponding percentage for the amorphous sample of PCL. It is noteworthy that the same percentages of trans conformations are obtained in systems I and II for the PCL chains on one hand (61 and 63%) and for the surfactants on the other hand (54 and 56%). In these two systems, one can also notice the higher percentage of trans angles for the polymer chains, relative to those of system III or the pure amorphous polymer sample. The proportion of trans dihedrals for system III is about the same as for the amorphous sample of PCL.

Therefore it appears that, in the two systems with lower density (I and II), the polymer chains adopt more trans conformations than in the amorphous bulk counterpart, despite the constraints they meet in the gallery. These constraints are (i) the confinement between two platelets a few tens of Å apart and (ii) the chain organization into well-defined organic layers, which both correspond to entropic penalties for the polymer chains.¹³ On the other hand, as we have seen, there are also enthalpic benefits that come from the global conformations adopted by the polymer chains, which allow interactions with both the clay surfaces (van der Waals and electrostatic interactions) and the surfactants (through mainly hydrophobic interactions) as well as a decrease in the torsional energies $\langle U_{\text{tors}} \rangle$ of the polymer chains with respect to those in amorphous bulk. In addition, the entropic penalties for the polymer chains are (at least partially) compensated by the increase in configurational freedom for the surfactant tails, as the interlayer space is

TABLE 3: Atomic Charges for (a) Selected Atoms of the Surfactant Molecule and for (b) a Caprolactone Sequence as an Example of the Typical Charges Obtained along the PCL Polymer Chains



(a)



(b)

atom index	a	b	c	d	e	f	g	h	i	j	k	l	m	n	o	p	q	r	s	t
surfactant	0.27	-0.05	-0.19	0.10	0.07	0.32	-0.25	0.11	0.12	0.07	0.01	0.00	-0.24	0.14	0.14	0.10	-0.21	0.12	0.14	0.10
PCL chain	1.04	-0.69	-0.42	0.10	0.10	0.23	-0.02	-0.02	-0.06	0.01	0.01	-0.09	0.04	0.04	0.43	-0.02	-0.02	-0.65		

enlarged in the intercalation process.^{13–15,56} The relatively low fraction of trans dihedral angles obtained for the surfactants in our results (between 51 and 56%) with respect to the much higher fractions obtained for organo-modified clay (higher than 70%) testifies to the decrease of conformational order for the surfactants after the intercalation process.^{54,57}

4. Concluding Remarks

Molecular dynamics simulations were conducted for an intercalated nanocomposite consisting of PCL chains and montmorillonite whose natural cations have been substituted with alkylammonium surfactants. To explore the influence of the amount of polymer on the molecular organization in the clay galleries, three model systems with increasing interlayer density, namely, I, II, and III, have been considered. The difference in density is brought in by modifying the length and number of polymer chains in the gallery. From a theoretical viewpoint, the consistency of models I and II indicates that the results obtained from the simulations are independent, to a certain extent, of: (i) the value of the density chosen for the organic phase; (ii) the number of polymer chains; (iii) the length of those chains. The latter two points should be taken with due caution since they are based on results obtained for models that remain of relatively modest size due to computational limitations. In contrast, the abrupt changes observed for both structural and energetic results for model III are attributable to the upper limit reached for the density of the interlayer organic phase, causing the observed discontinuities. The corresponding system should thus be regarded as modeling a limiting case.

In terms of the interactions among the components (clay, surfactant molecules, polymer chains), electrostatic interactions are of utmost importance due to the presence of the charged clay layers. Therefore, the determination of reliable charges for the polymer chains (as obtained from the *ab initio* derived electrostatic potentials and validated by simulations made for the polymer and compared with experiments) is important not only to describe the electrostatic interactions but also to enable a realistic balance between the two nonbonded potential energy terms (electrostatic and van der Waals), thus resulting in a more accurate description of the nanocomposite structure. On the basis of the predictive mean-field model of Balazs et al. for polymer nanocomposites,¹⁶ the relatively small polymer–clay binding energies obtained (with respect to the other binding energies calculated between the polymer, clay, and surfactant subsystems) are consistent with the intercalated structural arrangement observed experimentally for this material. It is important to stress that while van der Waals type interactions account for the major part of the polymer–surfactant interactions (90% of the total polymer–surfactant binding energy), the van der Waals and

electrostatic terms contribute almost equally to the polymer–clay interactions (with a slightly larger contribution from the former interaction type in the three models). From our binding energy calculations, it was found that PCL–mmt interactions account for slightly less than half (about $2/5$) of the PCL–surfactant interactions. In particular, the calculated charges have revealed the importance of hyperconjugation of the methylene group in the α position of the ester π system. This process creates an electronic deficiency on that methylene group, resulting in a large net positive charge that strongly interacts with the negatively charged clay surfaces. Thus, this hyperconjugation effect contributes to the miscibility between the PCL and the clay phases and is a driving force for the intercalation observed for this polymer; it should also be important for the intercalation of polylactide, another aliphatic polyester for which the same hyperconjugation effect exists.

The comparison between the results obtained from RDF analyses and from the dihedral angle distributions for the PCL chains in the bulk and in the intercalated nanocomposite provides evidence for a higher conformational order for the chains in the latter system. To our knowledge, the tendency toward an *increase* in conformational order has not been observed yet for a polymer/cation-exchanged clay nanocomposite by means of atomistic molecular simulations (the tendency toward an increase of stretched configurations has been observed only for models consisting of chains represented by beads interacting through a Lennard-Jones potential with confining walls).^{19,39,54,58} We conjecture that this tendency should also correspond to an increase in packing efficiency of the PCL chains inside the galleries, which may therefore explain the formation of PCL crystallites on montmorillonite surfaces, as observed experimentally for the corresponding nanocomposite.⁵⁹

Acknowledgment. The authors are grateful to Ph. Dubois, E. Pollet, M. Alexandre, and P. Brocorens (Université de Mons-Hainaut) for many fruitful discussions. Many thanks also to James Wescott (Accelrys) for providing tools for the analysis of the interlayer profiles. This project is supported by the government of the Région Wallonne, in the framework of the WDU program (TECMAVER). Research in Mons is also partly supported by the Belgian Science Policy Program (IAP Project V/3) and the Belgian National Fund for Scientific Research FNRS/FRFC.

Appendix A

For the surfactant and the oligomers, the charges were obtained with the CHELPG procedure (as implemented in the program system Gaussian 98)⁴⁷ that fits the atomic charges to the electrostatic potential calculated at the HF/6-31G* level of

TABLE 4: Valence Parameters (r_0 in Angstroms and θ_0 in Degrees) for the Element O in a PCL Chain for the Force Fields UFF and Dreiding

	UFF		Dreiding	
	r_0	θ_0	r_0	θ_0
O_R	0.680	110	0.660	120
O_2	0.634	120	0.560	120

TABLE 5: Lennard-Jones Parameters (r_0 in Angstroms and ϵ_0 in kcal/mol) for the Elements H, C, N, and O for the Force Fields UFF,³⁴ Dreiding,³⁵ and Tripos³⁶

	UFF		Dreiding		Tripos	
	r_0	ϵ_0	r_0	ϵ_0	r_0	ϵ_0
H	2.886	0.044	3.195	0.0152	3.000	0.042
C	3.851	0.105	3.8983	0.0951	3.400	0.107
N	3.660	0.069	3.6621	0.0774	3.100	0.095
O	3.500	0.060	3.4046	0.0957	3.040	0.116

TABLE 6: Distance (in Angstroms) and Energy (in kcal/mol) Parameters of the Lennard-Jones (6-12) Potential for UFF and Two Force Fields, Used in Recently Published Works, Reported for the Elements Si, Al, and O in a Clay Layer Environment

	UFF		ref 60		ref 61	
	r_0	ϵ_0	r_0	ϵ_0	r_0	ϵ_0
Si	4.295	0.402	4.700	0.400	4.550	0.040
Al	4.499	0.505	4.700	0.500	2.941	0.043
O	3.500	0.060	3.980	0.060	3.210	0.228

theory. The charges were derived for minimized geometry of the surfactant and the oligomers. The minimized conformation of the surfactant is shown in Figure 1 and was obtained from a previous RMMC exploration of its potential energy surface. For the PCL chains, an all trans minimized conformation was used for the charge calculations. The atomic charges reported for the surfactant are those around the nitrogen where the positive charge is mainly localized.

Appendix B

For the simulation of the amorphous PCL, three force fields were tested: UFF, Dreiding, and a hybrid force field that uses the Dreiding bonded parameters and the Tripos nonbonded parameters (see section 2.1). Table 4 reports the bond-stretching and angle-bending parameters for the two types of oxygen atoms in a PCL chain for UFF and Dreiding. For these two force fields, the valence parameters for C, N, and H are not shown: the respective r_0 values differ by 0.03 Å at most while the θ_0 values are all identical. The Lennard-Jones (6-12) distance (in Å) and energy (in kcal/mol) parameters of force fields UFF, Dreiding, and Tripos are reported in Table 5 for the elements H, C, N, and O.

Appendix C

In our simulations, the atoms of the clay layer are maintained in fixed positions. Thus, only nonbonded parameters for these atoms deserve attention. Table 6 reports the Lennard-Jones 6-12 parameters for UFF and for two other force fields recently used in the literature for a study of alkyl chains adsorbed on a clay surface (ref 60) and for the study of elastic properties of a montmorillonite nanoplate (ref 61).

The ϵ_0 parameters of the three force fields are the same for the three elements except for oxygen in the force field of ref 61 as its ϵ_0 parameter differs strongly with the other two parameters. The parameters r_0 in the force field of ref 60 are higher by 0.4, 0.2, and 0.5 Å than those of UFF for Si, Al, and

O, respectively. When comparing the van der Waals diameters of UFF and of the force field in ref 61, differences of ~ 0.3 Å are observed for Si and O while this parameter differs by ~ 1.6 Å for Al.

References and Notes

- (1) Alexandre, M.; Dubois, P. *Mater. Sci. Eng.* **2000**, *28*, 1.
- (2) Gloaguen, J. M.; Lefebvre, J. M. *Polymer* **2001**, *42*, 5841.
- (3) Weimer, M. W.; Chen, H.; Giannelis, E. P.; Sogah, D. Y. *J. Am. Chem. Soc.* **1999**, *121*, 1615.
- (4) Suh, D. J.; Lim, Y. T.; Park, O. O. *Polymer* **2000**, *41*, 8557.
- (5) Morgan, A. B.; Gilman, J. W.; Jackson, C. L. *Macromolecules* **2001**, *34*, 2735.
- (6) Huang, X.; Brittain, W. J. *Macromolecules* **2001**, *34*, 3255.
- (7) Zanetti, M.; Camino, G.; Thomann, R.; Mulhaupt, R. *Polymer* **2001**, *42*, 4501.
- (8) Theodorou, D. N. *Macromolecules* **1988**, *21*, 1391.
- (9) Theodorou, D. N. *Macromolecules* **1988**, *21*, 1400.
- (10) Madden, W. G. *J. Chem. Phys.* **1987**, *87*, 1405.
- (11) Bitsanis, I.; Hadziioannou, G. *J. Chem. Phys.* **1990**, *92*, 3827.
- (12) Vega, L. F.; Panagiotopoulos, A. Z.; Gubbins, K. E. *Chem. Eng. Sci.* **1994**, *49*, 2921.
- (13) Vaia, R. A.; Giannelis, E. P. *Macromolecules* **1997**, *30*, 7990.
- (14) Vaia, R. A.; Giannelis, E. P. *Macromolecules* **1997**, *30*, 8000.
- (15) Balazs, A. C.; Singh, C.; Zhulina, E. *Macromolecules* **1998**, *31*, 8370.
- (16) Balazs, A. C.; Singh, C.; Zhulina, E.; Lyatskaya, Y. *Acc. Chem. Res.* **1999**, *8*, 651.
- (17) Lee, J. Y.; Baljon, A. R. C.; Loring, R. F.; Panagiotopoulos, A. Z. *J. Chem. Phys.* **1998**, *109*, 10321.
- (18) Lee, J. Y.; Baljon, A. R. C.; Loring, R. F. *J. Chem. Phys.* **1999**, *111*, 9754.
- (19) Baljon, A. R. C.; Lee, J. Y.; Loring, R. F. *J. Chem. Phys.* **1999**, *111*, 9068.
- (20) Zax, D. B.; Yang, D. K.; Santos, R. A.; Hegemann, H.; Giannelis, E. P.; Manias, E. *J. Chem. Phys.* **2000**, *112*, 2945.
- (21) Manias, E.; Kупpa, V. *ACS Symp. Ser.* **2001**, *804*, 193.
- (22) Hackett, E.; Manias, E.; Giannelis, E. P. *Chem. Mater.* **2000**, *12*, 2161.
- (23) Kупpa, V.; Manias, E. *J. Chem. Phys.* **2003**, *118*, 3421.
- (24) Kупpa, V.; Menakanit, S.; Krishnamoorti, R.; Manias, E. *J. Polym. Sci. B: Polym. Phys.* **2003**, *41*, 3285.
- (25) Tanaka, G.; Goettler, L. A. *Polymer* **2002**, *43*, 541.
- (26) Fermiglia, M.; Ferrone, M.; Pricl, S. *Fluid Phase Equilib.* **2003**, *212*, 315.
- (27) Chávez-Páez, M.; Van Workum, K.; de Pablo, L.; de Pablo, J. J. *J. Chem. Phys.* **2001**, *114*, 1405.
- (28) Pantoustier, N.; Alexandre, M.; Degée, P.; Calberg, C.; Jérôme, R.; Henrist, C.; Cloots, R.; Rulmont, A.; Dubois, P. *e-Polymer* **2001**, *9*, 1.
- (29) Viville, P.; Lazzaroni, R.; Pollet, E.; Alexandre, M.; Dubois, P.; Borcia, G.; Pireaux, J. J. *Langmuir* **2003**, *19*, 9425.
- (30) Lepoittevin, B.; Devalckenaere, M.; Pantoustier, N.; Alexandre, M.; Kubies, D.; Calberg, C.; Jérôme, R.; Dubois, P. *Polymer* **2002**, *43*, 4017.
- (31) Lepoittevin, B.; Pantoustier, N.; Devalckenaere, M.; Alexandre, M.; Kubies, D.; Calberg, C.; Jérôme, R.; Dubois, P. *Macromolecules* **2002**, *35*, 8385.
- (32) Gaudel-Siri, A.; Brocorens, P.; Siri, D.; Gardebien, F.; Brédas, J. L.; Lazzaroni, R. *Langmuir* **2003**, *19*, 8287.
- (33) Yoon, D. Y.; Vacatello, M.; Smith, G. D. In *Monte Carlo and Molecular Dynamics Simulations in Polymer Science*; Binder, K., Ed.; Oxford University Press: New York, 1995.
- (34) Rappe, A. K.; Casewit, C. J.; Colwell, K. S.; Goddard, W. A.; Skiff, W. M. *J. Am. Chem. Soc.* **1992**, *114*, 10024.
- (35) Mayo, S. L.; Olafson, B. D.; Goddard, W. A. *J. Phys. Chem.* **1990**, *94*, 8897.
- (36) Clark, M.; Cramer, R. D., III; Opdenbosch, N. V. *J. Comput. Chem.* **1989**, *10*, 982.
- (37) Capkova, P.; Burda, J. V.; Weiss, Z.; Schenk, H. *J. Mol. Model.* **1999**, *5*, 8.
- (38) Accelrys, formerly Molecular Simulation Inc., 9685 Scranton Road, San Diego, CA, 1997.
- (39) Cui, S. T.; Cummings, P. T.; Cochran, H. D. *J. Chem. Phys.* **2001**, *114*, 6464.
- (40) Perret, R.; Skoulios, A. *Die Makromol. Chem.* **1972**, *156*, 157.
- (41) Skipper, N. T.; Chang, F. C.; Sposito, G. *Clays Clay Miner.* **1995**, *43*, 285.
- (42) Smith, D. E. *Langmuir* **1998**, *14*, 5959.
- (43) Chang, F.; Skipper, N. T.; Sposito, G. *Langmuir* **1998**, *14*, 1201.
- (44) Greathouse, J. A.; Refson, K.; Sposito, G. *J. Am. Chem. Soc.* **2000**, *122*, 11459.
- (45) Karasawa, N.; Goddard, W. A., III. *J. Phys. Chem.* **1989**, *93*, 7320.

- (46) Breneman, C. M.; Wiberg, K. B. *J. Comput. Chem.* **1990**, *11*, 361.
- (47) Frisch, M. J.; Trucks, G. W.; Schlegel, H. B.; Scuseria, G. E.; Robb, M. A.; Cheeseman, J. R.; Zakrzewski, V. G.; Montgomery, J. A., Jr.; Stratmann, R. E.; Burant, J. C.; Dapprich, S.; Millam, J. M.; Daniels, A. D.; Kudin, K. N.; Strain, M. C.; Farkas, O.; Tomasi, J.; Barone, V.; Cossi, M.; Cammi, R.; Mennucci, B.; Pomelli, C.; Adamo, C.; Clifford, S.; Ochterski, J.; Petersson, G. A.; Ayala, P. Y.; Cui, Q.; Morokuma, K.; Malick, D. K.; Rabuck, A. D.; Raghavachari, K.; Foresman, J. B.; Cioslowski, J.; Ortiz, J. V.; Stefanov, B. B.; Liu, G.; Liashenko, A.; Piskorz, P.; Komaromi, I.; Gomperts, R.; Martin, R. L.; Fox, D. J.; Keith, T.; Al-Laham, M. A.; Peng, C. Y.; Nanayakkara, A.; Gonzalez, C.; Challacombe, M.; Gill, P. M. W.; Johnson, B. G.; Chen, W.; Wong, M. W.; Andres, J. L.; Head-Gordon, M.; Replogle, E. S.; Pople, J. A. *Gaussian 98*, revision A.7; Gaussian, Inc.: Pittsburgh, PA, 1998.
- (48) Rappe, A. K.; Goddard, W. A. *J. Phys. Chem.* **1991**, *95*, 3358.
- (49) Nosé, S.; Klein, M. *Mol. Phys.* **1983**, *50*, 1055.
- (50) Nosé, S. *J. Chem. Phys.* **1984**, *81*, 511.
- (51) Hoover, W. *Phys. Rev. A* **1985**, *31*, 1695.
- (52) Dodd, L. R.; Theodorou, D. N. *Adv. Pol. Sci.* **1994**, *116*, 249.
- (53) Israelachvili, J. N. *Intermolecular and Surface Forces*; Academic Press: San Diego, CA, 1992.
- (54) Hackett, E.; Manias, E.; Giannelis, E. P. *J. Chem. Phys.* **1998**, *108*, 7410.
- (55) Murgich, J.; Rodriguez, J.; Izquierdo, A.; Carbognani, L.; Rogel, E. *Energy Fuels* **1998**, *12*, 339.
- (56) Manias, E. In *Advanced Composites*; Hyer, M. W., Loos, A. C., Ed.; Technomic Publishing Co, Inc., VA, 2001.
- (57) Venkataraman, N. V.; Vasudevan, S. *J. Phys. Chem. B* **2001**, *105*, 1805.
- (58) Cui, S. T.; Cummings, P. T.; Cochran, H. D. *J. Chem. Phys.* **2001**, *114*, 7189.
- (59) Jimenez, G.; Ogata, N.; Kawai, H.; Ogihara, T. *J. Appl. Polym. Sci.* **1997**, *64*, 2211.
- (60) Heinz, H.; Castelijns, H. J.; Suter, U. W. *J. Am. Chem. Soc.* **2003**, *125*, 9500.
- (61) Manevitch, O. L.; Rutledge, G. C. *J. Phys. Chem. B* **2004**, *108*, 1428.

4 La chimie quantique : méthodes et applications

4.1 Méthodes quantiques : survol des différentes approches théoriques

En chimie quantique, la résolution exacte de l'équation de Schrödinger est seulement possible pour un système comportant un unique électron (atome d'hydrogène, ion H_2^+). Pour résoudre l'équation de Schrödinger du tout système polyélectronique (atome ou molécule), nous devons faire une succession d'approximations.¹

4.1.1 Approximation de Born-Oppenheimer

Les noyaux étant presque 2000 fois plus lourds que les électrons, leurs mouvements sont beaucoup plus lents. On peut donc considérer que les N électrons s'adaptent instantanément à tout mouvement des noyaux. C'est-à-dire que les électrons sont soumis au champ des noyaux considérés fixes. Dans l'Hamiltonien total, on sépare donc les termes concernant exclusivement les noyaux : l'énergie cinétique des noyaux est négligée et le terme de répulsion entre noyaux est considéré constant. Seul l'Hamiltonien électronique est pris en compte : $H_{elec} = -\sum \frac{1}{2} \nabla^2 - \sum \sum \frac{Z_A}{r_{iA}} + \sum \sum \frac{1}{r_{ij}}$.

4.1.2 Approximation orbitale

La fonction d'onde polyélectronique, fonction propre de l'Hamiltonien électronique, s'exprime à partir de N fonctions d'ondes monoélectroniques normées (orbitales).

4.1.3 Déterminant de Slater

Les N électrons étant indiscernables, une orbitale particulière ne doit pas être attribuée à chaque électron. D'autre part, la fonction d'onde polyélectronique doit être antisymétrique par rapport à l'échange de deux électrons afin de respecter le principe d'exclusion de Pauli. Le déterminant de Slater respecte ces deux conditions ; c'est la représentation usuelle d'une fonction d'onde polyélectronique.

4.1.4 Application aux molécules : méthode LCAO

Dans cette approximation, les N fonctions d'onde monoélectroniques sont considérées comme des combinaisons linéaires d'orbitales atomiques, seules fonctions connues analytiquement à partir de la résolution de l'équation de Schrödinger pour l'atome d'hydrogène. Les orbitales atomiques de l'atome H sont les orbitales de Slater qui possèdent une fonction radiale en $\exp(-\alpha r)$. Dans les méthodes *ab initio* et basées sur la fonctionnelle de la densité, ces fonctions de Slater sont remplacées par des combinaisons linéaires de fonctions gaussiennes (partie radiale de type $\exp(-\zeta r^2)$) afin d'accélérer les calculs des intégrales biélectroniques multicentriques (termes d'échange et de corrélation).

4.1.5 Méthode Hartree-Fock - Principe variationnel

La méthode Hartree-Fock permet une résolution approchée de l'équation de Schrödinger incluant les approximations précédentes. Etant donné les approximations considérées, cette méthode converge vers une énergie E_{HF} qui sera toujours supérieure à l'énergie exacte. On applique alors le principe variationnel : en minimisant l'énergie Hartree-Fock, on se rapproche d'autant plus de l'énergie exacte.

1. a) Szabo, A., Ostlund, N. S. Modern quantum chemistry McGraw-Hill, 1982. b) Leach, A. Molecular modelling, principles and applications, Longman, 1998. c) Jensen, F. Introduction to computational chemistry, Wiley, 1999.

La minimisation de E_{HF} est effectuée en optimisant les coefficients de chaque orbitale atomique (OA) dans chaque orbitale moléculaire (OM). C'est une méthode itérative où l'équation de Schrödinger polyélectronique est remplacée par un système de N équations monoélectroniques couplées : $F_i \varphi_i = \varepsilon_i \varphi_i$ où F_i représente l'opérateur de Fock monoélectronique. L'écart d'énergie $\Delta E = E_{\text{HF}} - E_{\text{exacte}}$ qui subsiste provient de la perte d'une grande partie de l'énergie de corrélation électronique.

4.1.6 UHF/RHF et contamination de spin

En fonction de la nature du système moléculaire étudié, on est amené à considérer, non pas les orbitales mais les spin-orbitales. Dans ce cas, la fonction d'espace n'est pas contrainte à être identique pour les électrons α et β d'une même orbitale : on parle alors de méthode UHF (Unrestricted Hartree-Fock) par opposition à la méthode RHF (Restricted Hartree-Fock). Ce traitement est indispensable dans les systèmes radicalaires où l'électron célibataire α de la SOMO polarise les électrons α des niveaux inférieurs. Les spin-orbitales α sont alors stabilisées et leur distribution dans l'espace peut être affectée également.

4.1.7 Méthodes semi-empiriques

Dans les méthodes semi-empiriques, différentes approximations sont prises en compte afin d'accélérer les calculs et de traiter des systèmes de plus grande taille. Dans la majorité de ces méthodes, seuls les électrons de valence sont pris en compte et ils sont décrits à l'aide d'orbitales de Slater au lieu de combinaisons de gaussiennes. Une base minimale est utilisée et seules les orbitales s et p sont en général considérées (sauf MNDO/D, SAM1d et PM6 qui introduisent des orbitales d). Le nombre de coefficients à déterminer pour chaque orbitale moléculaire est ainsi nettement réduit. Les méthodes semi-empiriques sont basées sur le principe du recouvrement différentiel nul (ZDO) : considérant un électron i , le produit de 2 fonctions de base localisées sur 2 centre différents est nul ($\mu_A(i) \cdot \nu_B(i) = 0$). Cela conduit à une matrice de recouvrement S réduite à la matrice unité. D'autre part, des intégrales sont négligées et d'autres sont paramétrées. Par exemple, les intégrales monoélectroniques sur 3 centres sont négligées et toutes les intégrales biélectroniques sur 3 et 4 centres sont négligées. Les intégrales biélectroniques sur 2 centres sont soit négligées (méthode CNDO) soit paramétrées (méthodes AM1, PM3) sur la base du calcul de données expérimentales : potentiel d'ionisation, énergies d'excitation. Etant donné le grand nombre d'approximations effectuées, ces méthodes souffrent de défauts importants. En général, les barrières de rotation sont très sous-estimées et les interactions à longue distance sont mal décrites. La méthode PM3 décrit mal les atomes d'azote et conduit à des liaisons hydrogène trop courtes tandis que la méthode AM1 reproduit mal les géométries des alcools, des composés phosphorés ou peroxylés.

4.1.8 Problème de la corrélation électronique

Le principal inconvénient de la méthode HF est qu'elle ne tient pas compte de la corrélation électronique. En effet, dans la réalité, les mouvements des électrons sont corrélés. Cependant, dans la théorie HF, chaque électron ne "voit" pas les électrons voisins individuellement mais est seulement soumis au champ moyen des autres électrons. La position instantanée d'un électron n'est pas conditionnée par celle d'un électron voisin : les déplacements électroniques ne sont pas corrélés sauf pour les électrons de même spin puisque la règle de Hund est respectée. On définit l'énergie de corrélation comme la différence entre l'énergie HF et l'énergie exacte. Toutes les méthodes post-HF ont pour objectif de s'approcher de l'énergie exacte en prenant en compte une partie de la corrélation électronique.

D'autre part, certains systèmes ne sont pas correctement décrits par une méthode monodéterminante : une combinaison linéaire de déterminants est nécessaire. C'est par exemple le cas d'un système biradicalaire singulet.

4.1.9 Corrélation statique : méthodes des perturbations post-HF, méthodes multi-références (CI, CAS)

Møller et Plesset ont proposé une méthode basée sur la théorie des perturbations pour prendre en compte une partie de la corrélation électronique. On considère que l'Hamiltonien exact H est la somme

d'un Hamiltonien d'ordre zéro H_0 et d'une perturbation V . L'Hamiltonien d'ordre zéro est constitué de la somme des opérateurs de Fock et Ψ_0 est la fonction propre de H_0 . La fonction propre Ψ de H est alors une combinaison linéaire de Ψ_i qui prend en compte les excitations (simples, doubles, ...) du système. L'énergie totale E est alors corrigée par les valeurs des énergies de perturbation calculées à l'ordre 2 voire 3 ou 4 selon les méthodes MP2, MP3 ou MP4 utilisées. L'avantage de cette méthode est qu'elle est indépendante de la taille du système contrairement à l'interaction de configurations (CI).

Dans la méthode basée sur l'interaction de configurations, la fonction propre Ψ de l'Hamiltonien exact H est une combinaison linéaire de fonctions constituées de :

- Ψ_0 fonction propre de l'Hamiltonien H_0 , obtenue par la méthode HF
- Ψ_1 fonctions d'ondes monoexcitées
- Ψ_2 fonctions d'ondes diexcitées
- ...

La méthode consiste à déterminer les coefficients de la combinaison linéaire en considérant un plus ou moins grand nombre d'états excités (interaction de configurations). Pour une infinité d'états excités, on obtient la solution exacte Ψ . On peut se limiter aux excitations simples (CIS), doubles (CID), simples et doubles (CISD) ou considérer toutes les excitations possibles (full CI). Grâce au principe variationnel, l'énergie du système est minimisée et les coefficients de la combinaison linéaire sont déterminés. Plus le système est complexe, plus le nombre d'états à considérer est élevé et plus l'interaction de configurations demande du temps de calcul. D'autre part, les orbitales moléculaires sont gelées, autrement dit, les coefficients des orbitales atomiques au sein de chaque orbitale moléculaire ne sont pas optimisés au cours de cette procédure. On lui préfère donc les méthodes MCSCF (multiconfiguration self-consistent field methods) qui permettent d'obtenir des énergies plus proches de l'énergie exacte en optimisant à la fois les orbitales moléculaires et leurs coefficients dans la combinaison linéaire de la fonction d'onde totale. Dans la méthode CASSCF par exemple, les orbitales moléculaires (OM) sont divisées en trois ensembles : OM virtuelles, OM doublement occupées et OM actives constituées d'OM occupées et virtuelles. Toutes les excitations sont considérées au sein de cet espace actif. La fonction d'onde totale est alors une combinaison linéaire de tous les états optimisés.

4.1.10 Corrélation dynamique

La méthode multiconfigurationnelle CASSCF permet de prendre en compte la corrélation statique dans le calcul de l'énergie du système. Cependant, l'obtention de valeurs d'énergie d'activation et d'énergie de réaction correctes nécessite de prendre en compte la corrélation dynamique qui provient de la réorganisation électronique pendant la formation et la rupture de liaisons. En effet, ces énergies sont systématiquement sous-estimées par la méthode CASSCF. La corrélation dynamique peut être en partie estimée grâce à un calcul de perturbations au second ordre (CASPT2, MRMP2) sur la fonction d'onde issue du calcul CASSCF.

4.1.11 Approche par DFT

Dans la théorie de la fonction d'onde (Hartree-Fock, post-Hartree-Fock), l'objectif est de déterminer les orbitales moléculaires de l'état fondamental du système ainsi que leurs énergies en appliquant le principe variationnel. Les propriétés électroniques de la molécule, dont la densité électronique, en sont déduites a posteriori. Dans la théorie de la fonctionnelle de la densité (DFT), on adopte la démarche inverse : les orbitales moléculaires, leurs énergies et toutes les propriétés électroniques sont déterminées à partir de la densité électronique ρ .

L'avantage principal de la DFT réside dans sa rapidité de calcul ; elle est donc largement utilisée pour les systèmes comportant plusieurs dizaines d'atomes. D'autre part, les résultats obtenus par DFT tiennent compte de la corrélation dynamique pour le même coût qu'un calcul Hartree-Fock. Cependant, un grand nombre de fonctionnelles sont à notre disposition et résultent d'une paramétrisation pour traiter l'échange et la corrélation. Cette paramétrisation est effectuée sur des séries de molécules et de réactions modèles et il est parfois difficile de déterminer la fonctionnelle la mieux adaptée au problème. D'autre part, les fonctionnelles ne sont pas toujours performantes pour décrire correctement une SEP

et localiser des points stationnaires. Les barrières d'énergie sont également souvent sous-estimées².

Parmi les nombreuses familles de fonctionnelles, on peut distinguer les fonctionnelles LDA (local density approximation basée simplement sur la densité de spin locale), GGA (generalized gradient approximation, utilisant la densité de spin et le gradient de la densité de spin) meta-GGA (un paramètre supplémentaire est pris en compte : les densités d'énergie cinétique électronique), hybrides (avec proportion variable d'échange non-local Hartree-Fock), double-hybrides (proportion variable d'échange non-local et de corrélation non-locale Hartree-Fock). Des études comparatives basées sur des critères précis (bases de données de réactions chimiques variées et de propriétés électroniques) sont disponibles dans la littérature afin de choisir la fonctionnelle la mieux adaptée au système modélisé. Par exemple, la publication récente³ offre une large vision des fonctionnelles plus ou moins récentes.

4.2 Application à la réactivité des N-alcoxyamines

Plusieurs méthodes quantiques ont été utilisées afin d'étudier l'effet de substituant sur la dissociation des N-alcoxyamines : la méthode semi-empirique PM3 et la fonctionnelle B3P86. Ces travaux ont fait l'objet de trois publications dont deux sont reportées ci-après. Deux communications orales et deux communications par affiche ont également porté sur ce sujet. D'autres méthodes de calcul telles que la méthode composée G3MP2-RAD⁴ sont plus appropriées pour évaluer des enthalpies de dissociation (BDE) cependant, elles ne sont envisageables que pour des systèmes comportant jusqu'à 20 atomes environ.

2. X. Xu, I.M. Alecu, D.G. Truhlar, *J. Chem. Theor. Comput.* **2011**, 7, 1667-1676.

3. R. Peverati, D.G. Truhlar, *Phil. Trans. R. Soc. A* **2014**, 372. doi :10.1098/rsta.2012.0476

4. D.J. Henry, M.B. Sullivan, L. Radom *J. Chem. Phys.* **2003**, 118, 4849-4860.

Homolysis of *N*-alkoxyamines: A Computational Study

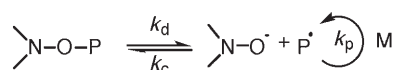
Anouk Gaudel-Siri, Didier Siri,* and Paul Tordo^[a]

During nitroxide-mediated polymerization (NMP) in the presence of a nitroxide $R^2(R^1)NO\cdot$, the reversible formation of *N*-alkoxyamines $[P-ON(R^1)R^2]$ reduces significantly the concentration of polymer radicals ($P\cdot$) and their involvement in termination reactions. The control of the livingness and polydispersity of the resulting polymer depends strongly on the magnitude of the bond dissociation energy (BDE) of the $C-ON(R^1)R^2$ bond. In this study, theoretical BDEs of a large series of model *N*-alkoxyamines are calculated with the PM3 method. In order to provide a predictive tool,

correlations between the calculated BDEs and the cleavage temperature (T_c), and the dissociation rate constant (k_d), of the *N*-alkoxyamines are established. The homolytic cleavage of the $N-OC$ bond is also investigated at the B3P86/6-311++G(d,p)//B3LYP/6-31G(d), level. Furthermore, a natural bond orbital analysis is carried out for some *N*-alkoxyamines with a $O-C-ON(R^1)R^2$ fragment, and the strengthening of their $C-ON(R^1)R^2$ bond is interpreted in terms of stabilizing anomeric interactions.

Introduction

Controlled/"living" radical polymerizations enable the design of polymers with complex architectures and polydispersities well below the theoretical limit for conventional free-radical polymerization processes. Among controlled/"living" radical polymerization procedures, nitroxide-mediated polymerization^[1] (NMP) is based on the reversible trapping of growing polymer radicals by a stable nitroxide to form dormant *N*-alkoxyamines (Scheme 1). The thermally labile *N*-alkoxyamines decompose on heating to release nitroxide molecules and reactive polymeric chains that may add monomers before recombining with the nitroxide to give *N*-alkoxyamines with higher molecular weights.



Scheme 1. Controlled/"living" polymerization in the presence of nitroxide.

The process is based on the persistent radical effect^[2] and the efficiency of the control depends on the ratio of the dissociation and recombination rate constants, k_d/k_c [Eq. (1)]:

$$k_d/k_c = (A_d/A_c)\exp(-\Delta H_r^\circ/RT) \quad (1)$$

where A_d and A_c are the Arrhenius prefactors for the *N*-alkoxyamine dissociation and recombination, respectively. It is commonly assumed that A_d/A_c is roughly constant for a set of similar compounds. Thus, the polymerization process is partly controlled by the magnitude of $-\Delta H_r^\circ$, which is the bond dissociation enthalpy (BDE) of the $NO-C$ bond. If the $NO-C$ bond is too labile, the polymerization process is not controlled; whereas it is inhibited if the $NO-C$ bond is too strong. The experi-

mental determination of BDE ($NO-C$) for a given *N*-alkoxyamine is a tedious task that requires the determination of E_{ad} and E_{acr} , the activation energies for the *N*-alkoxyamine dissociation and recombination respectively. So, the strength of the $NO-C$ bond is often indirectly studied with the help of k_d or the cleavage temperature T_c . The determination of k_d requires many kinetic runs at a given temperature and, to determine T_c values, a precise protocol^[3m] using electron spin resonance (ESR) was followed: the temperature of the sample was increased stepwise by 5 °C, and the rough T_c corresponds to the temperature where the ESR signal of the nitroxide appears. Cleavage temperatures of *N*-alkoxyamines are also directly correlated to the strength of the $NO-C$ bond, since the stronger the $NO-C$ bond is, the higher the temperature of dissociation should be. E_{ac} for the combination of carbon-centered radicals with nitroxides are small and, if we assume that they are not significantly influenced by the structure of the trapped radical,^[4] then Equation (2) is obtained:

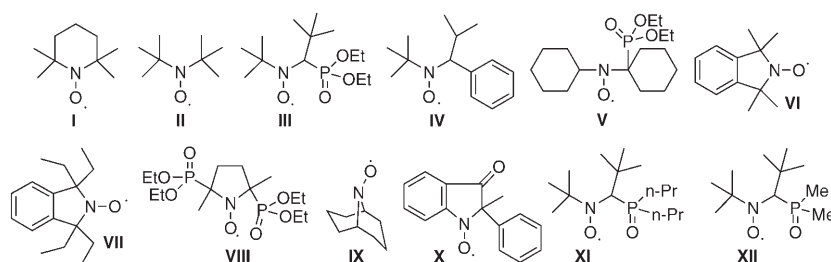
$$\log k_d \propto -E_{ad}/RT \propto -BDE(NO-C)/RT \quad (2)$$

A correlation similar to Equation (2) between the experimental values of $\log k_d$ and T_c has already been reported.^[3m]

[a] Dr. A. Gaudel-Siri,⁺ Prof. D. Siri, Prof. P. Tordo
UMR-CNRS 6517, Universit s d'Aix-Marseille 1 et 3
Facult  des Sciences de St-J r me, Case 521
13397 Marseille Cedex 20 (France)
Fax: (+33)491-288-841
E-mail: didier.siri@up.univ-mrs.fr

[*] Current address:
UMR-CNRS 6178, Universit  Paul C zanne-Aix-Marseille
Facult  des Sciences et Techniques, Case D12
13397 Marseille Cedex 20 (France)

Many experimental^[3] but few theoretical^[3a,f,g,j-k,m-o,5] studies have been performed to estimate factors influencing the BDE (NO–C) of *N*-alkoxyamines. Experimental results show that narrow polydispersities and high polymerization rates depend on the ease of the NO–C bond homolysis.^[3f] Both experimental and theoretical results have established that the more stabilized the released radical is, or the more destabilized the starting *N*-alkoxyamine is, the easier is the dissociation of the NO–C bond.^[3b,f,m,5] Nitroxides such as 2,2,6,6-tetramethylpiperidine-1-oxyl (TEMPO, I), di-*tert*-butylnitroxide (DTBN, II), and *N,N*-(2-methylpropyl-1)-(1-diethylphosphono-2,2-dimethyl-propyl-1)-*N*-oxyl (SG1, III) (Scheme 2) have been extensively used for NMP of styrene. Nitroxide III was shown to be efficient also during



Scheme 2. Chemical structures of the nitroxides I–XII.

the NMP of various acrylic monomers. Nevertheless, to extend NMP to other types of monomers, or to improve the previous reported results, the development of appropriate nitroxides is still a challenge. Molecular modeling could be of great help to estimate, before their synthesis, the efficiency of new nitroxides for NMP. Moreover, a rapid procedure to estimate a priori the BDE (NO–C) or the dissociation rate constant k_d of new *N*-alkoxyamines may help organic and polymer chemists in the design of suitable controllers.

The present work is a theoretical study of the dissociation reactions of various *N*-alkoxyamines. In the first section, we give the results of our BDE (NO–C) calculations for various *N*-alkoxyamines. We show that good correlations exist between their calculated BDE (NO–C) and their T_c and k_d values. These correlations provide a valuable tool for evaluating the ability of new nitroxides to control the NMP of styrene and acrylate monomers. Furthermore, for *N*-alkoxyamines, the competition between two different dissociation pathways is studied and shows the limitations of NMP procedures. The results are completed by a natural bond orbital (NBO) analysis^[6] for three *N*-alkoxyamines. The NBO analysis allows the separation of the energy contributions due to hyperconjugation from those caused by electrostatic and steric interactions, so that the influence of hyperconjugative interactions can be studied separately.

Computational Section

Semiempirical calculations were performed with the PM3^[7] method of the AMPAC software.^[8] In addition to its low computational cost,

three other main reasons supported the choice of the PM3 method:

- the better description^[9] of nitroxides and *N*-alkoxyamines obtained with PM3, compared to MNDO,^[10a] AM1,^[10b] or SAM1^[10c]
- the satisfactory parametrization of the phosphorus atom in PM3
- among semiempirical methods, PM3 gives the most satisfying calculated bond lengths and BDEs. In a recent study^[11a] with a series of 28 compounds, the mean absolute error value for the calculated BDEs of X–X and X–Y bonds was 7 kJ mol^{-1} at the B3P86/6-311G(2d,2p)//PM3 level and 10 kJ mol^{-1} at the B3P86/6-311G(2d,2p)//AM1 level. This result can be accounted for by the better accuracy of the PM3 calculated bond lengths.

In the first step, for each *N*-alkoxyamine, the lowest-energy geometry was determined by simulated annealing^[12] and highest occupied molecular orbital/lowest unoccupied molecular orbital (HOMO/LUMO) configuration interaction. The energy of the radical species was calculated with a minimal configuration interaction over the HOMO (highest doubly occupied MO), singly occupied MO SOMO, and LUMO frontier orbitals. All minima were confirmed by the calculation of vibrational frequencies. Bond dissociation enthalpies were calculated from Equations (3) and (4):

$$\text{BDE}_{\text{CO}}(298 \text{ K}) = \Delta H_f^\circ(\text{nitroxide}) + \Delta H_f^\circ(\text{R}) - \Delta H_f^\circ(\text{N-alkoxyamine}) \quad (3)$$

$$\text{BDE}_{\text{NO}}(298 \text{ K}) = \Delta H_f^\circ(\text{aminyl}) + \Delta H_f^\circ(\text{RO}) - \Delta H_f^\circ(\text{N-alkoxyamine}) \quad (4)$$

where the energy of the open-shell species is recalculated with a minimal configuration interaction over the two SOMOs (keywords OPEN(2,2) C.I.=2) in order to minimize size-consistency problems. Density functional theory (DFT) calculations were performed with the Gaussian 03 package.^[13] In some recent studies,^[4a,11] various standard functionals have been tested to calculate the BDEs of C–X and X–Y bonds belonging to a large panel of compounds. The best results were obtained with the B3P86 functional and the best correlation constants between the experimental and calculated values were obtained^[11c] at the B3P86/6-311++G(d,p)//B3LYP/6-31G(d) level: 0.991 for all the compounds, 0.969 for C–X bonds, and 0.945 for X–Y bonds with a systematic underestimation of the BDEs. Herein, the geometry optimization and the calculation of vibrational frequencies were performed at the B3LYP/6-31G(d) level and a single point at the B3P86/6-311++G(d,p) level was used to calculate the energy. All minima were confirmed by a calculation of vibrational frequencies. For thermodynamic calculations, as recommended by Wong,^[14] a scale factor of 0.9804 was applied to vibrational frequencies. Bond dissociation enthalpies were calculated by Equation (5):

$$\text{BDE} = \Delta H_f^\circ(298 \text{ K}) = D_e + \Delta ZPE + \Delta H_{\text{trans}} + \Delta H_{\text{rot}} + \Delta H_{\text{vib}} + RT \quad (5)$$

where D_e is the classical electronic bond dissociation energy; ΔZPE is the difference in zero-point energy between products and the *N*-alkoxyamine; ΔH_{trans} , ΔH_{rot} , ΔH_{vib} are the contributions from translational, rotational, and vibrational degrees of freedom.

An NBO analysis was performed at the B3P86/6-31+G(d) level, using the NBO 3.1 program^[15] included in the Gaussian 03 package.

Results and Discussion

Experimental and Calculated BDE (NO–C)

Only few experimental BDEs of *N*-alkoxyamines or hydroxylamines have been reported in the literature.^[3a–d,5a,16] When these scarce experimental data were compared to calculated BDEs (Table 1), we first noted that, in most cases, PM3 calculations slightly overestimated the BDE values (mean error value of 5 kJ mol^{−1}), while B3P86/6-31G(d)//HF/6-31G(d) calculations underestimated them (mean error value of 16 kJ mol^{−1}). BDEs calculated at the DFT level offered a better correlation (Figure 1 a) with experimental data ($r^2 = 0.999$), but PM3 results were also satisfactory ($r^2 = 0.962$). Steric effects were well-described with a decrease in BDE (NO–C) from a primary (–CH₂Ph, Table 1, entry 4) to a secondary (–styryl, Table 1, entry 5), and a tertiary (–cumyl, Table 1, entry 6) leaving group (Scheme 3 shows the structures of the leaving groups used in this study). Moreover, with a given leaving group, the BDE (NO–C) of *N*-alkoxyamines derived from III were always lower than those of *N*-alkoxyamines derived from I. These results for alkyl leaving groups are in very good agreement with experimental data. However, at the PM3 level of calculation, some BDEs were overestimated, while others were underestimated (Table 1): then, individual absolute values must be considered carefully. Consequently, the PM3 method appears to be a valuable tool for estimating relative BDEs of a series of *N*-alkoxyamines with alkyl leaving groups within reasonable calculation times, while a higher-level method is recommended for calculating accurate BDEs. In order to also validate the PM3 method for *N*-alkoxyamines with electron-withdrawing groups, we compared PM3 results with those obtained at the B3P86/6-311++G(d,p)//B3LYP/6-31G(d) level (Table 2, Figure 1b). PM3 predicts BDEs in good agreement with B3P86 results ($r^2 = 0.995$). In most cases, PM3 BDEs were slightly underestimated; the particular case of *N*-alkoxyamine 40 will be discussed below.

Correlations Between Experimental Data and Calculated BDE (NO–C)

The *N*-alkoxyamine T_c values were determined by experimental chemists in our laboratory.^[3m] As expected, they were strongly

<i>N</i> -alkoxyamine or hydroxylamine	BDE _{PM3} [kJ mol ^{−1}]	Signed error ^[b] [kJ mol ^{−1}]	BDE _{DFT} ^[c] [kJ mol ^{−1}]	Signed error ^[b] [kJ mol ^{−1}]	BDE _{exp} [kJ mol ^{−1}]
1 II–H	295	10	275	−10	285 ^[16b]
2 I–H	296	5	279	−12	291 ^[16a]
3 I–Me	178	−19	185	−12	197 ^[3a]
4 I–CH ₂ Ph	161	16	121	−24	145 ^[5a]
5 I–styryl	130	1	110	−19	129 ^[5a]
6 I–cumyl	105	−5	89 ^[d]	−21	110 ^[3d]
7 III–CH ₂ Ph	157	31	–	–	126 ^[5a]
8 III–styryl ^[a]	118	1	–	–	117 ^[5a]
mean signed error		5		−16	

[a] Mean value for the SR/RS and RR/SS diastereomers. [b] Signed errors in calculated BDE (O–R). [c] Ref. [5a] with B3P86/6-31G(d)//HF/6-31G(d) method. [d] *T* was set to 358 K.

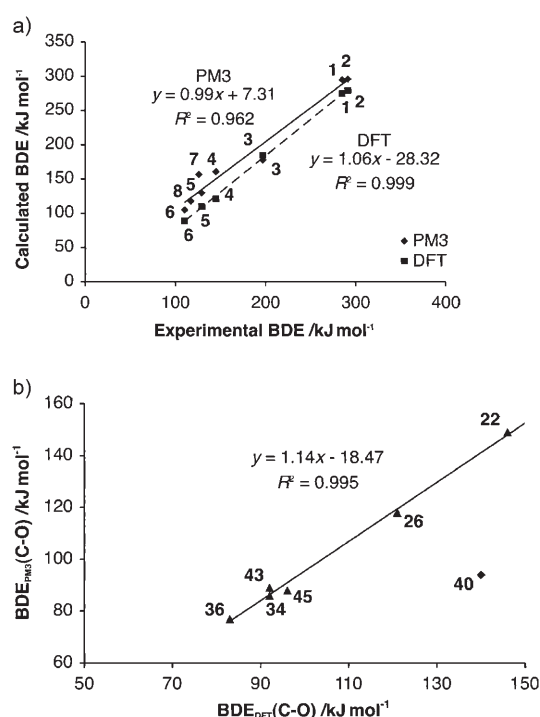
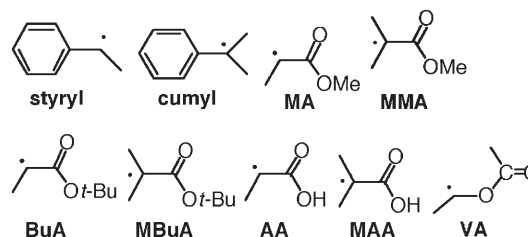


Figure 1. a) Correlation between experimental and theoretical BDEs for the NO–C homolytic cleavage of various *N*-alkoxyamines with an alkyl or a π -delocalized alkyl leaving group. (■) PM3 calculations. (♦) B3P86/6-31G(d)//HF/6-31G(d) calculations. b) Comparison between BDEs calculated with PM3 and BDEs calculated at the B3P86/6-311++G(d,p)//B3LYP/6-31G(d) level for the NO–C homolytic cleavage of various *N*-alkoxyamines with an electron-withdrawing leaving group.



Scheme 3. Chemical structures of leaving groups.

Table 2. Comparison between the PM3 method and the B3P86/6-311++G(d,p)//B3LYP/6-31G(d) level at 298 K for various *N*-alkoxyamines with an electron-withdrawing leaving group.

<i>N</i> -alkoxyamine	BDE _{PM3} (OR) [kJ mol ⁻¹]	BDE _{DFT} (OR) [kJ mol ⁻¹]	Signed error ^[a] [kJ mol ⁻¹]
22 I-CH ₂ C(O)OMe	149	146	3
26 I-MA	118	121	-3
34 I-MMA	86	92	-6
36 II-MMA	77	83	-6
40 IX-MMA	94	140	-46
43 I-CMe ₂ CN	89	92	-3
26 VI-CMe ₂ CN	88	96	-8

[a] BDE_{PM3} (OR) - BDE_{DFT} (OR).

dependent on the structure of the leaving radical (Table 3). From a qualitative point of view:

- T_c decreased when the substitution at the radical center of the leaving radical increased (see for example, *N*-alkoxyamines entries **9**, **11** and **10**, **12**)
- for a given released radical, *N*-alkoxyamines derived from III exhibited a lower T_c than those derived from I (see for example, *N*-alkoxyamines entries **10**, **11** or **12**, **13**).

These results are in agreement with the BDE values of the NO-C bond calculated with the PM3 method. However, no direct correlation between T_c and BDE (NO-C) was found for the whole series of *N*-alkoxyamines, because the polar effects of the nitroxide moiety and the leaving radical must be also considered. Hence, we first defined three sets of *N*-alkoxyamines according to the nature of the radical released during the dissociation: an alkyl radical, a π -delocalized alkyl radical, and a radical bearing an electron-withdrawing group.

Interesting correlations were obtained within the three sets of *N*-alkoxyamines (Figure 2 and Figure 3). Slightly better correlations were obtained between $\log k_d$ and BDE (NO-C) than between T_c and BDE (NO-C). The same slope was obtained for the correlations corresponding to leaving groups expected to exert similar polar effects, such as alkyl groups and π -delocalized alkyl groups. We noted a slightly larger slope for leaving groups bearing an electron-withdrawing substituent, such as -CN or -C(O)OR. The combination of both steric and electron-withdrawing effects for the released radical (e.g., methylmethacrylate MMA) led to a significant increase in the dissociation rate. In addition to experimental T_c and k_d values, calculated T_c and k_d values are reported in Table 3 (italic). These values were calculated with the correlations of Figures 4 and 6, and Figures 5 and 7, respectively. The predicted k_d value for entry **20** (1.99 s^{-1} at 120°C) is in agreement with the value estimated by Marque and co-workers^[3m] (1.7 s^{-1} at 120°C).

The whole series of *N*-alkoxyamines studied in this work can be represented by the three general formula shown in Scheme 4. If the transition state of the NO-C bond homolysis is stabilized by polar contributions, the homolysis of *N*-alkoxyamines B (Scheme 4) is expected to be favored, while no signifi-

Table 3. Comparison between T_c determined by ESR, k_d measured by ESR (393 K), and BDE (NO-C) calculated by PM3 at 298 K.

<i>N</i> -alkoxyamine	T_c ^[b] [°C]	BDE _{PM3} [kJ mol ⁻¹]	k_d ^[e] [s ⁻¹]	$\log k_d$
9 III-(CH ₂) ₅ CH ₃	160 ^[3m]	148	8.00E-09 ^[3m]	-8.10
10 I-cy-Hex	170 ^[3m]	129	< 2.80E-08 ^[3m]	> -7.55
11 III-cy-Hex	140 ^[3m]	122	6.40E-08 ^[3m]	-7.19
12 I-t-Bu	110 ^[3m]	94	1.00E-05 ^[3m]	-5.00
13 III-t-Bu	95 ^[3m]	77	6.50E-05 ^[3m]	-4.19
4 I-CH ₂ Ph	115 ^[3m]	161	1.10E-05 ^[3m]	-4.96
14 II-CH ₂ Ph	121 ^[c]	162	1.90E-04 ^[3]	-3.72
7 III-CH ₂ Ph	80 ^[3m]	157	3.30E-04 ^[3m]	-3.48
5 I-styryl	95 ^[3m]	131	5.20E-04 ^[3m]	-3.28
15 II-styryl	84 ^[c]	131	1.40E-02 ^[3]	-1.89
8 III-styryl ^[a]	60 ^[3m]	118	5.50E-03 ^[3m]	-2.26
16 VI-styryl ^[a]	65 ^[3m]	116	3.30E-03 ^[3m]	-2.48
17 VIII-styryl	100 ^[17]	123	-	-
18 XI-styryl	35 ^[17]	97	1.80E-01 ^[f]	-0.74
19a XII-styryl (SR/RS)	49 ^[c]	113	4.60E-02 ^[3]	-1.34
19b XII-styryl (SS/RR)	46 ^[c]	109	7.50E-02 ^[3]	-1.12
8 I-cumyl	45 ^[3m]	105	8.50E-02 ^[3m]	-1.07
20 III-cumyl	≈ 15 ^[3m]	74	1.99 ^[f]	0.30
21 I-CH ₂ C(O)Or-Bu	145 ^[3m]	156	8.10E-08 ^[3m]	-7.09
22 I-CH ₂ C(O)OMe	145 ^[18]	149	8.10E-08 ^[18]	-7.09
23 III-CH ₂ C(O)OMe	100 ^[3m]	145	3.60E-06 ^[3m]	-5.44
24 III-CH ₂ C(O)OH	100 ^[d]	146	2.30E-06 ^[h]	-5.64
25 III-CH ₂ CN	90 ^[i]	148	2.00E-04 ^[h]	-3.70
26 I-MA	115 ^[18]	118	3.40E-05 ^[18]	-4.47
27 I-BuA	115 ^[3m]	122	3.40E-05 ^[3m]	-4.47
28 II-BuA	96 ^[d]	119	1.10E-03 ^[3]	-2.96
29 III-MA ^[a]	75 ^[3m]	112	-	-
29a III-MA (RS/SR)	-	113	3.00E-03 ^[3m]	-2.52
29b III-MA (RR/SS)	-	110	1.00E-03 ^[3m]	-3.00
30 III-AA	64 ^[d]	111	5.30E-04 ^[h]	-3.28
31 IV-MA ^[a]	90 ^[3m]	120	4.50E-04 ^[3m]	-3.35
32 V-MA	85 ^[i]	121	5.10E-04 ^[g]	-3.29
33 III-CH(Me)CN ^[a]	70 ^[17]	116	2.80E-03 ^[i]	-2.55
34 I-MMA	50 ^[18]	86	2.20E-02 ^[18]	-1.66
35 I-MBuA	50 ^[3m]	94	2.20E-02 ^[3m]	-1.66
36 II-MMA	15 ^[19]	77	4.80E-01 ^[g]	-0.32
37 II-MBuA	39 ^[d]	84	3.10E-01 ^[3]	-0.51
38 III-MMA	≈ 15 ^[3m]	66	8.00 ^[i]	0.90
39 VIII-MMA	60 ^[19]	67	-	-
40 IX-MMA	165 ^[19]	94	-	-
41 X-MMA	90 ^[19]	121	6.50E-05 ^[g]	-4.19
42 III-MMA	18 ^[d]	66	2.80E-01 ^[h]	-0.55
43 I-CMe ₂ CN	46 ^[d]	89	1.30E-01 ^[3]	-0.89
44 III-CMe ₂ CN	20 ^[i]	72	1.31 ^[h]	0.12
45 VI-CMe ₂ CN	46 ^[d]	88	1.90E-02 ^[3]	-1.72
46 VII-CMe ₂ CN	35 ^[d]	81	1.60E-01 ^[3]	-0.80

[a] T_c or k_d measured for the racemic and mean value of BDE calculated for the two diastereomers. [b] The error in T_c measurements is $\pm 5^\circ\text{C}$. [c] Estimated T_c values obtained from the correlation of Fig. 4. [d] Estimated T_c values obtained from the correlation of Figure 6. [e] The error in k_d measurements is $\pm 10\%$. [f] Estimated k_d values obtained from the correlation of Figure 5. [g] Estimated k_d values obtained from the correlation of Figure 7. [h] S. Marque, D. Gigmes, personal communication. [i] To be published.

cant influence of polar contributions is expected for *N*-alkoxyamines A and C.

In Figure 4, only π -delocalized alkyl leaving groups of similar electronegativities were considered, and two satisfactory corre-

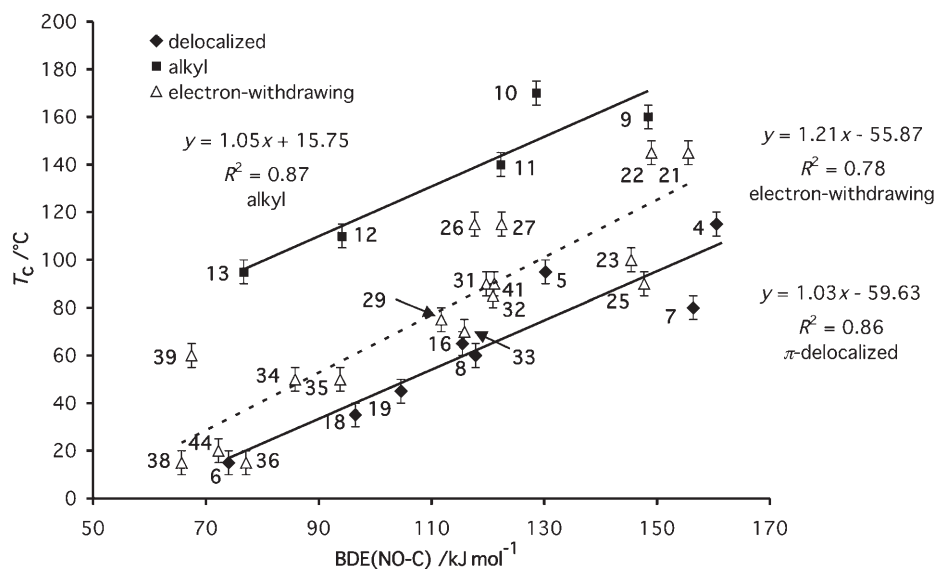


Figure 2. Correlations between BDE (NO–C) calculated with the PM3 method and available experimental T_c considering three series of leaving groups: alkyl, π -delocalized alkyl, and electron-withdrawing moieties.

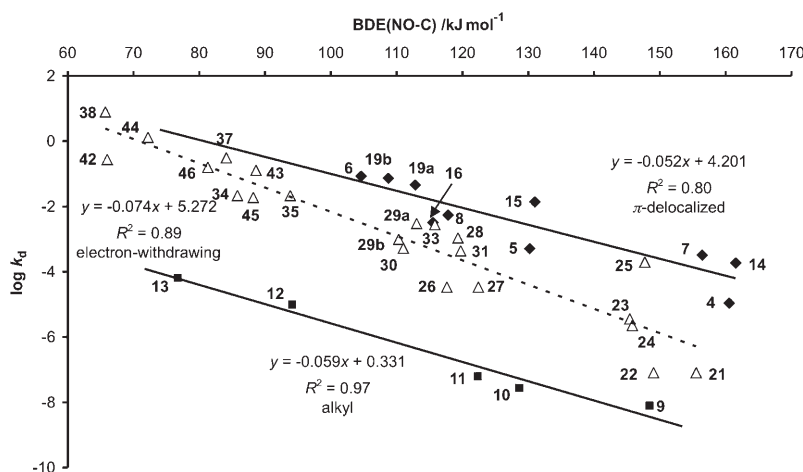


Figure 3. Correlations between BDE (NO–C) calculated with the PM3 method and available experimental k_d values considering three series of leaving groups: alkyl (■), π -delocalized alkyl (◆), and electron-withdrawing (△) moieties.

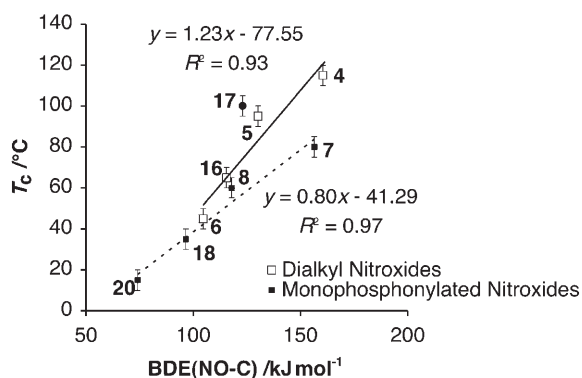


Figure 4. Correlations between BDE (NO–C) calculated with the PM3 method and experimental T_c considering alkyl π -delocalized leaving groups and dialkyl or monophosphonylated nitroxides.

lations were obtained according to the presence or the absence of an electron-withdrawing substituent on the nitroxide moiety. A better correlation, and a significantly smaller slope, was obtained for monophosphonylated nitroxides (III, XI, XII) than for dialkyl ones (I, IV). The polar contribution represented by B is expected to be more stabilizing than that represented by A and, as observed, a smaller slope was expected for the correlation involving the *N*-alkoxyamines based on monophosphonylated nitroxides (III, XI, XII). The diphenylated cyclic *N*-alkoxyamine 17 (VIII-styryl) did not correlate to any linear fit. As already pointed out by Moad and Rizzardo,^[3f] a decrease in the $\theta(\text{CNC})$ valence angle leads to a higher BDE (NO–C) and then, an increase in T_c . However, more experimental data from a series of cyclic and acyclic diphenylated nitroxides should be analyzed in order to draw any conclusions on the effect of the two phosphonyl substituents. In Figure 5, a slightly larger slope was also obtained for dialkyl nitroxides (I, II, IV) than for the monophosphonylated ones (III, XI, XII).

The *N*-alkoxyamines considered in Figures 6 and 7 are A and C types. Good correlations were obtained. Note again the synergy of the polar and steric effects of the leaving group with a larger slope in the case of dialkyl nitroxides (I, II, IV, VI, VII). The lower slope for *N*-alkoxyamines based on III and V is due to the larger steric hindrance of the nitroxide moiety (Figure 6). *N*-alkoxyamines 39 and 40 were considered (BDE (NO–C) = 67 kJ mol⁻¹, T_c = 60 °C and BDE (NO–C) = 94 kJ mol⁻¹, T_c = 165 °C,^[19] respectively), but neither correlated with a linear fit. For *N*-alkoxyamine 17, we note significant differences in the valence angle $\theta(\text{CNC})$ for 39 and 40, compared to 34 and 36 (Table 4), and an increase in the BDE (NO–C) and in the cleavage temperature was again observed.

In conclusion, satisfactory correlations were obtained between calculated BDE (NO–C) with the PM3 method and experimental T_c or $\log k_d$. In order to test new nitroxides in NMP, correlations found in this section might help organic chemists, if they first estimate T_c or k_d values for new model *N*-alkoxy-

Table 4. Comparison of structural parameters of acyclic (**36**), cyclic (**34**, **39**), and bicyclic (**40**) *N*-alkoxyamines according to PM3 calculations. The $\omega(\text{CCON})$ dihedral angle measures the pyramidalization angle of the N atom.

<i>N</i> -alkoxyamine	$\theta(\text{CNC})$ [deg]	$d(\text{NO}-\text{C})$ [Å]	$\omega(\text{CCON})$ [deg]
34	119(118) ^[a]	1.436(1.433) ^[a]	29(32) ^[a]
36	121	1.434	28
39	110	1.438	35
40	110(110) ^[a]	1.420(1.442) ^[a]	35(38) ^[a]

[a] Experimental X-ray data values are given in italics.

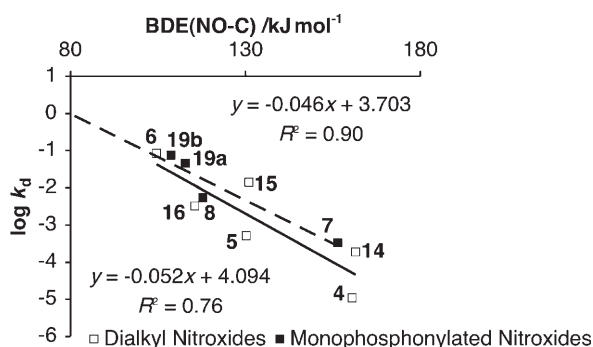


Figure 5. Correlations between BDE (NO–C) calculated with the PM3 method and experimental k_d values considering alkyl leaving radicals and dialkyl or monophosphonylated nitroxides.

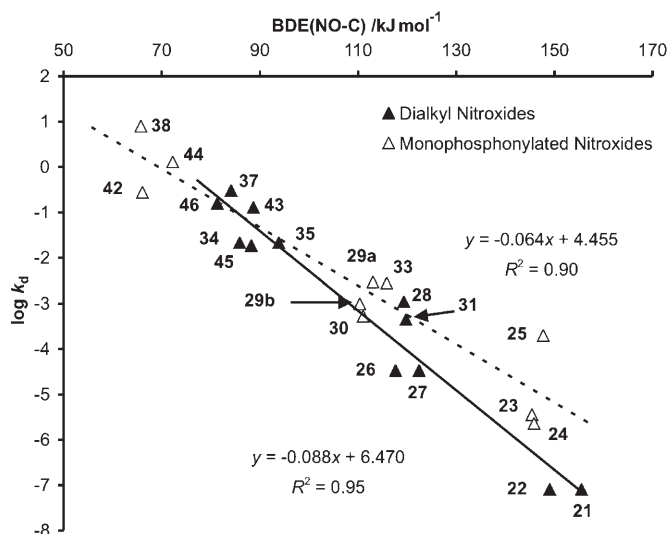
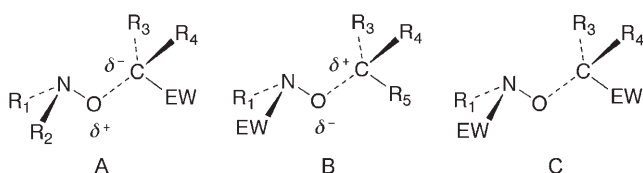


Figure 7. Correlations between BDE (NO–C) calculated with the PM3 method and experimental k_d values considering electron-withdrawing leaving radicals and dialkyl or monophosphonylated nitroxides.



Scheme 4. General formula of the *N*-alkoxyamines studied.

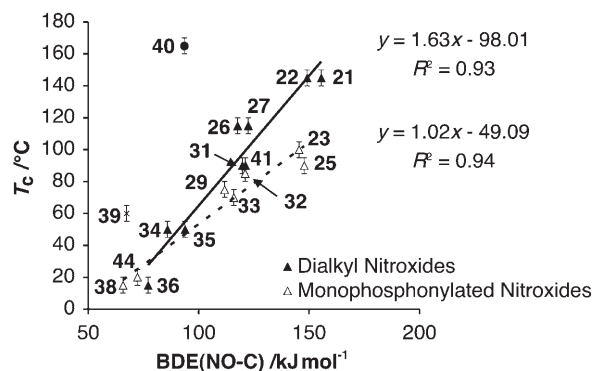
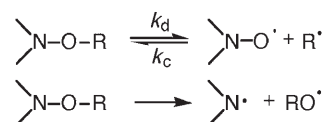


Figure 6. Correlations between BDE (NO–C) calculated with the PM3 method and experimental T_c considering electron-withdrawing leaving groups and dialkyl or monophosphonylated nitroxides.

amines before their experimental determination, which requires many kinetic runs.

NO–C versus N–OC Bond Cleavage

The cleavage temperature of *N*-alkoxyamines releasing a primary alkyl radical is very high (e.g., **9**). Then, NMP of ethylenic monomers should be conducted at very high temperature and pressure. The NO–C bond in *N*-alkoxyamines is usually considered as the most labile but, at high temperatures, the competitive N–OC homolytic bond cleavage must be also considered. This pathway is not reversible and leads to two reactive radicals: an aminyl radical and an alkoxy radical (Scheme 5), which are both able to initiate radical reactions. Hereafter, we present our computations on the BDE of the NO–C and N–OC bonds for a series of *N*-alkoxyamines.



Scheme 5. Competition between homolytic N–OC and NO–C bond cleavage in *N*-alkoxyamines.

At first, some representative *N*-alkoxyamines were chosen to test the ability of the PM3 method to give BDE (N–OC) values in agreement with experimental observations (Table 5).

In agreement with experimental results for *N*-alkoxyamines releasing primary or secondary alkyl radicals, semiempirical BDE (NO–C) were very high (130–155 kJ mol^{-1}). However, BDE (N–OC) of I-*n*-hexyl and III-*n*-hexyl were significantly lower than BDE (NO–C). This result was not in agreement with the experimental determination of BDE (NO–C) of I-Me,^[3a] which indicates that $\text{BDE (NO–C)} < \text{BDE (N–OC)}$ for I-*n*-alkyl. *N*-alkoxyamines releasing tertiary radicals (cumyl and MMA) showed highly labile NO–C bonds, in agreement with experimental data. However, spurious results were obtained for primary and secondary π -delocalized radicals. In order to determine if these

Table 5. Comparison of BDE (NO–C) and BDE (N–OC) at 298 K calculated with the PM3 method and at the B3P86/6-311++G(d,p)//B3LYP/6-31G(d) level for a series of *N*-alkoxyamines.

<i>N</i> -alkoxyamine	BDE _{PM3} (NO–C) [kJ mol ⁻¹]	BDE _{PM3} (N–OC) [kJ mol ⁻¹]	BDE _{DFT} (NO–C) [kJ mol ⁻¹]	BDE _{DFT} (N–OC) [kJ mol ⁻¹]
6 I-cumyl	105	130	87	–
5 I-styryl	130	112	108	174
4 I-CH ₂ Ph	161	107	119	–
26 I-MA	118	–	121	180
34 I-MMA	86	117	–	–
47 I-(CH ₂) ₅ CH ₃	151	104	176 ^[a]	189 ^[a]
9 III-(CH ₂) ₅ CH ₃	148	77	–	–
48 I-VA	142	107	179	176
49a III-VA (SR) ^[b]	135	75	–	–
49b III-VA (SS) ^[b]	129	69	–	–

[a] The *n*-hexyl moiety was replaced by a methyl group. [b] The configuration of the nitroxyl chiral center is given first.

discrepancies were due to the use of a semiempirical method, BDE (N–OC) and BDE (NO–C) were calculated with the B3P86/6-311++G(d,p)//B3LYP/6-31G(d) method. Results are reported in Table 5. In order to model the polyethylene chain, the methyl group was taken to reduce calculation times. Table 5 shows that BDEs calculated with the DFT method were in better agreement with experimental data. Only I-MA and I-styryl have a labile NO–C bond (110–120 kJ mol⁻¹). In contrast to the PM3 results, all the *N*-alkoxyamines had strong N–OC bonds (175–190 kJ mol⁻¹) and BDE (NO–C) of I-Me was then lower than BDE (N–OC). For I-VA, BDE (N–OC) and BDE (NO–C) were similar and very high. These values were in agreement with the absence of experimental cleavage temperature for III-VA to 140 °C.^[20]

This study showed that a comparison of BDE (NO–C) and BDE (N–OC) calculated with the PM3 method did not give reliable relative values. This result can be explained considering the characteristics of the two bonds: a NO–C bond with only one heteroatom and experimental data used in the parametrization of PM3 versus a N–OC bond between two heteroatoms. Moreover, it is known that lone-pair–lone-pair repulsions are not always well represented by semiempirical methods.^[21]

Hyperconjugation in *N*-alkoxyamines: Structural and NBO Analysis

The special cases of the *N*-alkoxyamines I-VA and III-VA is particularly interesting. The steric hindrance in I-VA and I-MA is similar, but their T_c are very different, showing a dramatic strengthening of the NO–C bond in I-VA. Ciriano et al.^[3a] have published a study of TEMPO *N*-alkoxyamines derived from tetrahydrofuran and triethylamine. Stronger BDE (NO–C) were attributed to the presence of the heteroatom in the α -position of the NO group. The *N*-alkoxyamine is stabilized by an anomeric interaction^[22] between the lone pairs of the heteroatom and the $\sigma^*(\text{NO})$ bond. The NO–C bond is then strengthened while the N–OC bond is weakened. In order to understand the unusual strength of the NO–C bond in I-VA better, a NBO anal-

ysis was carried out where the hyperconjugation in I-VA and I-MA was compared. The hyperconjugation in III-VA was also studied. Starting from the crystal structure of III-VA, the geometry optimization of III'-VA was performed at the B3P86/6-31G(d) level of calculation, and a diffuse function on the nitrogen and oxygen atoms was added to deal with the lone pairs properly. Nitroxide III' differs from III because the ethoxyl moieties attached to the phosphorus atom are substituted by methoxyl groups, in order to reduce the calculation time.

Optimized geometries of I-VA and I-MA are reported in Figures 8 and 9. Some structural variations can be noted in favor

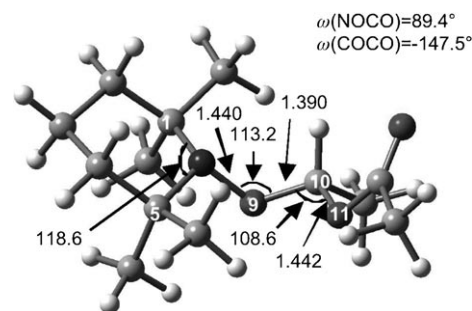


Figure 8. Structural parameters of I-VA optimized at the B3P86/6-31+G(d) level. Bond lengths in angstroms, angles in degrees.

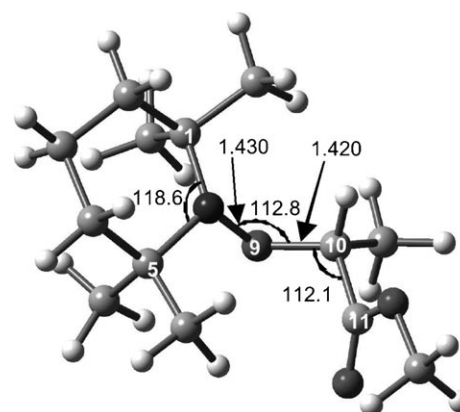


Figure 9. Structural parameters of I-MA optimized at the B3P86/6-31+G(d) level. Bond lengths in angstroms, angles in degrees.

of an anomeric interaction in the (N)O9C10O11C moiety of I-VA. At first, the (N)O9–C10 bond of I-VA was significantly shortened (3×10^{-2} Å) while the N–OC bond length did not change. On the other hand, the C10–O11 bond was significantly lengthened (3×10^{-2} Å). Moreover, the $\omega(\text{NOCO})$ dihedral angle was close to 90° (89.4°) and the $\theta(\text{O9C10O11})$ angle was significantly more acute, compared to the equivalent $\theta(\text{O9C10C11})$ angle in I-MA. All these facts support a hyperconjugation between a lone pair of the nitroxyl oxygen O9 and the adjacent antibonding σ^* (C10O11) orbital.^[3a,23] In order to confirm this hypothesis, we carried out a NBO analysis^[6] of I-VA and I-MA.

Table 6 shows a strong stabilizing interaction (17.9 kcal mol⁻¹) between a p lone pair of O9 and the polar antibonding

Table 6. Main hyperconjugative interactions in I-VA.			
Interaction	Stabilization [kcal mol ⁻¹]	Lone-pair delocalization	
$n(\text{N}) \rightarrow \sigma^*(\text{C1C}_{\text{axial}})$	7.7	96.1 %	$\text{sp}^3(\text{N})$
		0.7 %	$\text{p}(\text{C1})$
		0.6 %	$\text{sp}^3(\text{C}_{\text{axial}})$
$n(\text{N}) \rightarrow \sigma^*(\text{C5C}_{\text{axial}})$	7.8	96.1 %	$\text{sp}^3(\text{N})$
		0.7 %	$\text{p}(\text{C5})$
		0.6 %	$\text{sp}^3(\text{C}_{\text{axial}})$
$n(\text{O9}) \rightarrow \sigma^*(\text{C10O11})$	17.9	95.2 %	$\text{p}(\text{O9})$
		2.3 %	$\text{p}(\text{C10})$
		0.9 %	$\text{sp}(\text{O11})$

$\sigma^*(\text{C10O11})$ orbital. A similar interaction is also noted in I-MA, but the stabilizing energy is much weaker and close to that resulting from the delocalization of the N lone-pair in the nonpolar axial $\sigma^*(\text{C-Me})$ orbitals (Table 7, Figure 10). Some structural

Table 7. Main hyperconjugative interactions in I-MA.			
Interaction	Stabilization [kcal mol ⁻¹]	Lone-pair delocalization	
$n(\text{N}) \rightarrow \sigma^*(\text{C1C}_{\text{axial}})$	7.8	96.0 %	$\text{sp}^3(\text{N})$
		0.7 %	$\text{p}(\text{C1})$
		0.6 %	$\text{sp}^3(\text{C}_{\text{axial}})$
$n(\text{N}) \rightarrow \sigma^*(\text{C5C}_{\text{axial}})$	7.8	96.1 %	$\text{sp}^3(\text{N})$
		0.7 %	$\text{p}(\text{C5})$
		0.6 %	$\text{sp}^3(\text{C}_{\text{axial}})$
$n(\text{O9}) \rightarrow \sigma^*(\text{C10C11})$	8.8	96.6 %	$\text{p}(\text{O9})$
		0.9 %	$\text{p}(\text{C10})$
		0.8 %	$\text{sp}(\text{O11})$

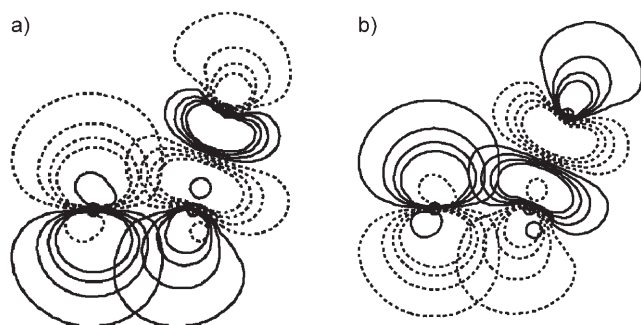


Figure 10. a) Hyperconjugation in I-VA between the O9 lone pair and the antibonding $\sigma^*(\text{C10O11})$ orbital. b) Hyperconjugation in I-MA between the O9 lone pair and the antibonding $\sigma^*(\text{C10C11})$ orbital.

variations could also be noted in favor of an anomeric interaction in the (N)O9C10O11C moiety of III'-VA (Figure 11). The (N)O9–C10 bond of III'-VA is shortened (1.403 Å), while the N–OC and C10–O11 bonds are lengthened, showing a hyperconjugation between a lone pair of the nitroxyl oxygen O9 and the adjacent antibonding $\sigma^*(\text{C10O11})$ orbital. Table 8 shows a strong stabilizing interaction (15.6 kcal mol⁻¹) between a p lone pair of O9 and the polar antibonding $\sigma^*(\text{C10O11})$ orbital. This interaction is similar to the anomeric interaction noted in I-VA, but it is less stabilizing. This is in agreement with the

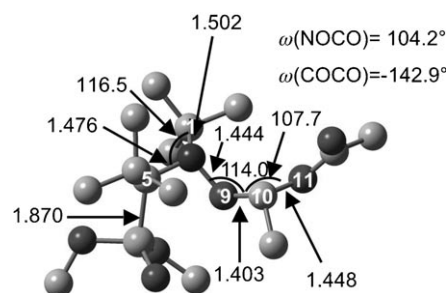


Figure 11. Structural parameters of III'-VA optimized at the B3P86/6-31+G(d) level with an additional diffuse function for the N and O atoms. Bond lengths in angstroms, angles in degrees. For clarity, hydrogen atoms have not been drawn.

Table 8. Main hyperconjugative interactions in III'-VA.			
Interaction	Stabilization [kcal mol ⁻¹]	Lone-pair delocalization	
$n(\text{N}) \rightarrow \sigma^*(\text{C1C}_{\text{p}})$	6.9	96.2 %	$\text{sp}^3(\text{N})$
		0.6 %	$\text{p}(\text{C1})$
		0.5 %	$\text{sp}^3(\text{C}_{\text{p}})$
$n(\text{N}) \rightarrow \sigma^*(\text{C5P})$	4.7	96.2 %	$\text{sp}^3(\text{N})$
		0.7 %	$\text{p}(\text{C5})$
		0.5 %	$\text{s}(\text{P})$
$n(\text{O9}) \rightarrow \sigma^*(\text{C10O11})$	15.6	95.3 %	$\text{p}(\text{O9})$
		2.1 %	$\text{p}(\text{C10})$
		0.8 %	$\text{sp}(\text{O11})$

usual lower BDE (NO–C) of III'-based *N*-alkoxyamines compared to I-based *N*-alkoxyamines.

In Table 9 are reported the natural charges of the NOCO and NOCC moieties of I-VA, I-MA, and III'-VA. Natural charges are preferred to Mulliken population analysis, because of instabili-

Table 9. Comparison of natural charges in I-MA, I-VA, and III'-VA.				
Natural charge	N	O9	C10	C11 or O11
I-MA	–0.230	–0.458	–0.009	0.797
I-VA	–0.227	–0.463	0.370	–0.581
III'-VA (SS) ^[a]	–0.208	–0.461	0.393	–0.582

[a] The configuration of the nitroxyl chiral center is given first.

ties with respect to basis expansion and underestimation of ionic character in bonds between atoms with large electronegativity differences.^[6d] The charge of either the nitrogen atom or the oxygen atom of the nitroxide moiety is not affected by the nature of the leaving group. On the other hand, the charge of the C10 carbon atom is dramatically modified by the presence of O11 in I-VA and III'-VA, leading to a highly polarized O9–C10 bond. This charge separation again does not favor the homolytic cleavage of the *N*-alkoxyamine NO–C bond.

The NBO analysis showed that the NO–C bond cleavage in *N*-alkoxyamines releasing a VA radical is not favored, because of an anomeric stabilization and a more polar NO–C bond.

Conclusions

Herein, we reported a semiempirical study of the homolysis of *N*-alkoxyamines. The PM3 method is a valuable tool for estimating relative BDE (NO–C) within a series of *N*-alkoxyamines, and correlations between calculated BDE (NO–C) and the experimental T_c or k_d may be useful for finding new nitroxide controllers for NMP of acrylic or styrenic monomers. These correlations showed the strong influence of steric effects in the NO–C bond cleavage, but polar substituents in the nitroxide are important too, as they modify the polar contributions in the transition state of the homolysis.

PM3 failed to give reliable relative values of BDE (N–OC) and BDE (NO–C). A higher level of theory was necessary to compare the homolytic cleavage of these two bonds. DFT calculations herein were in good agreement with experimental data.

Furthermore, the NBO analysis of two *N*-alkoxyamines releasing a VA radical clearly showed that the control of the polymerization of VA derivatives with nitroxides is unlikely.

Acknowledgments

The authors thank AtoFina for financial support, and are grateful for computational facilities on a Silicon Graphics Origin2000 server from the "Centre Régional de Compétences en Modélisation Moléculaire" (CRMM, Marseille). Thanks to Dr. S. Marque for fruitful discussions and kinetic data.

Keywords: bond energy · density functional calculations · *N*-alkoxyamines · radicals · semiempirical calculations

- [1] a) C. J. Hawker, *Acc. Chem. Res.* **1997**, *30*, 373–382; b) C. J. Hawker, J. L. Hedrick, *Macromolecules* **1995**, *28*, 2393–29955; c) K. Matyjaszewski, S. Gaynor, D. Greszta, D. Mardare, T. Shigemoto, *J. Phys. Org. Chem.* **1995**, *8*, 306–315; d) C. J. Hawker, *J. Am. Chem. Soc.* **1994**, *116*, 11185–11186; e) C. Le Mercier, J.-F. Lutz, S. Marque, F. Le Moigne, P. Tordo, P. Lacroix-Desmazes, B. Boutevin, J.-L. Couturier, O. Guerret, R. Martschke, J. Sobek, H. Fischer, *ACS Symp. Ser.* **2000**, 768.
- [2] a) H. Fischer, *Macromolecules* **1997**, *30*, 5666–5672; b) H. Fischer, *J. Polym. Sci. A* **1999**, *37*, 1885–1901.
- [3] a) M. V. Ciriano, H.-G. Korth, W. B. von Scheppingen, P. Mulder, *J. Am. Chem. Soc.* **1999**, *121*, 6375–6381; b) W. G. Skene, S. T. Belt, T. J. Connolly, P. Hahn, J. C. Scaiano, *Macromolecules* **1998**, *31*, 9103–9105; c) S. A. F. Bon, G. Chambard, A. L. German, *Macromolecules* **1999**, *32*, 8269–8276; d) T. Kothe, S. Marque, R. Martschke, M. Popov, H. Fischer, *J. Chem. Soc., Perkin Trans. 2* **1998**, 1553–1560; e) P. S. Engel, S. Duan, G. B. Arhancet, *J. Org. Chem.* **1997**, *62*, 3537–3541; f) G. Moad, E. Rizzardo, *Macromolecules* **1995**, *28*, 8722–8728; g) R. D. Puts, D. Y. Sogah, *Macromolecules* **1996**, *29*, 3323–3325; h) I. Li, B. A. Howell, K. Matyjaszewski, T. Shigemoto, P. B. Smith, D. B. Priddy, *Macromolecules* **1995**, *28*, 6692–6693; i) D. W. Grattan, D. J. Carlsson, J. A. Howard, D. M. Wiles, *Can. J. Chem.* **1979**, *57*, 2834–2842; j) C. Le Mercier, A. Gaudel, D. Siri, P. Tordo, S. Marque, R. Martschke, H. Fischer, *Polym. Prepr. Am. Chem. Soc., Div. Polym. Chem.* **1999**, 313–314; k) P. M. Kazmaier, K. A. Moffat, M. K. Georges, R. P. N. Veregin, G. K. Hamer, *Macromolecules* **1995**, *28*, 1841–1846; l) S. Marque, C. Le Mercier, P. Tordo, H. Fischer, *Macromolecules* **2000**, *33*, 4403–4410; m) C. Le Mercier, S. Acerbis, D. Bertin, F. Chauvin, D. Gigmes, O. Guerret, M. Lansalot, S. Marque, F. Le Moigne, H. Fischer, P. Tordo, *Macromol. Symp.* **2002**, *182*, 225–247; n) R. Braslau, N. Naik, H. Zipse, *J. Am. Chem. Soc.* **2000**, *122*, 8421–8434; o) R. Cuatrecasas-Diaz, M. Albores-Valesco, E. Saldivar-Guerra, F. B. Jimenez, *Polymer* **2004**, *45*, 815–824.
- [4] a) J. Chateaufneuf, J. Luszyk, K. U. Ingold, *J. Org. Chem.* **1988**, *53*, 1629–1631; b) A. L. J. Beckwith, V. W. Bowry, G. Moad, *J. Org. Chem.* **1988**, *53*, 1632–1641; c) J. Sobek, R. Martschke, H. Fischer, *J. Am. Chem. Soc.* **2001**, *123*, 2849–2857.
- [5] a) P. Marsal, M. Roche, P. Tordo, P. de Sainte Claire, *J. Phys. Chem. A* **1999**, *103*, 2899–2905; b) J. M. Cogen, *Polym. Degrad. Stab.* **1994**, *44*, 49–53.
- [6] a) J. P. Foster, F. Weinhold, *J. Am. Chem. Soc.* **1980**, *102*, 7211; b) A. E. Reed, F. Weinhold, *J. Chem. Phys.* **1985**, *83*, 1736; c) A. E. Reed, L. A. Curtiss, F. Weinhold, *Chem. Rev.* **1988**, *88*, 899; d) F. Weinhold in *Encyclopedia of Computational Chemistry*, Vol. 3 (Ed: P. v. R. Schleyer), Wiley, New York, **1998**, pp. 1792–1810.
- [7] J. P. P. Stewart, *J. Comput. Chem.* **1989**, *10*, 209–220.
- [8] Ampac 7.0, Semichem, P.O. Box 1649, Shawnee Mission, KS 66222, **2001**.
- [9] A. Gaudel, *Ph.D. Thesis*, Université d'Aix-Marseille 3, France, **1999**.
- [10] a) M. J. S. Dewar, W. Thiel, *J. Am. Chem. Soc.* **1977**, *99*, 4899–4906; b) M. J. S. Dewar, E. G. Zoebisch, E. F. Healy, J. P. P. Stewart, *J. Am. Chem. Soc.* **1985**, *107*, 3902–3909; c) M. J. S. Dewar, C. Jie, J. Yu, *Tetrahedron* **1993**, *49*, 5003–5038.
- [11] a) E. R. Johnson, O. J. Clarkin, G. A. DiLabio, *J. Phys. Chem. A* **2003**, *107*, 9953–9963; b) X.-Q. Yao, X.-J. Hou, H. Jiao, H.-W. Xiang, Y.-W. Li, *J. Phys. Chem. A* **2003**, *107*, 9991–9996; c) Y. Feng, L. Liu, J.-T. Wang, H. Huang, Q.-X. Guo, *J. Chem. Inf. Comput. Sci.* **2003**, *43*, 2005–2013.
- [12] F. Bockisch, D. Liotard, J.-C. Rayez, B. Duguay, *Int. J. Quantum Chem.* **1992**, *44*, 619–642.
- [13] Gaussian 03, Revision B.03, M. J. Frisch, G. W. Trucks, H. B. Schlegel, G. E. Scuseria, M. A. Robb, J. R. Cheeseman, J. A. Montgomery, Jr., T. Vreven, K. N. Kudin, J. C. Burant, J. M. Millam, S. S. Iyengar, J. Tomasi, V. Barone, B. Mennucci, M. Cossi, G. Scalmani, N. Rega, G. A. Petersson, H. Nakatsuji, M. Hada, M. Ehara, K. Toyota, R. Fukuda, J. Hasegawa, M. Ishida, T. Nakajima, Y. Honda, O. Kitao, H. Nakai, M. Klene, X. Li, J. E. Knox, H. P. Hratchian, J. B. Cross, V. Bakken, C. Adamo, J. Jaramillo, R. Gomperts, R. E. Stratmann, O. Yazyev, A. J. Austin, R. Cammi, C. Pomelli, J. W. Ochterski, P. Y. Ayala, K. Morokuma, G. A. Voth, P. Salvador, J. J. Dannenberg, V. G. Zakrzewski, S. Dapprich, A. D. Daniels, M. C. Strain, O. Farkas, D. K. Malick, A. D. Rabuck, K. Raghavachari, J. B. Foresman, J. V. Ortiz, Q. Cui, A. G. Baboul, S. Clifford, J. Cioslowski, B. B. Stefanov, G. Liu, A. Liashenko, P. Piskorz, I. Komaromi, R. L. Martin, D. J. Fox, T. Keith, M. A. Al-Laham, C. Y. Peng, A. Nanayakkara, M. Challacombe, P. M. W. Gill, B. Johnson, W. Chen, M. W. Wong, C. Gonzalez, J. A. Pople, Gaussian, Inc., Pittsburgh PA, **2003**.
- [14] M. W. Wong, *Chem. Phys. Lett.* **1996**, *256*, 391–399.
- [15] E. D. Glendenning, A. E. Reed, J. E. Carpenter, F. Weinhold, NBO Version 3.1, Gaussian, Inc., Pittsburgh PA, **1992**.
- [16] a) L. R. Mahoney, G. D. Mendenhall, K. U. Ingold, *J. Am. Chem. Soc.* **1973**, *95*, 8610–8614; b) F. G. Bordwell, W.-Z. Liu, *J. Am. Chem. Soc.* **1996**, *118*, 10819–10823.
- [17] C. Le Mercier, *Ph.D. Thesis*, Université de Provence, France, **2000**.
- [18] G. Ananchenko, S. Marque, D. Gigmes, D. Bertin, P. Tordo, *Org. Biomol. Chem.* **2004**, *2*, 709–715.
- [19] S. Acerbis, *Ph.D. Thesis*, Université de Provence France, **2003**.
- [20] J.-F. Lutz, P. Lacroix-Demazes, B. Boutevin, C. Le Mercier, D. Gigmes, D. Bertin, P. Tordo, *Polym. Prepr. Am. Chem. Soc., Div. Polym. Chem.* **2002**, *43*, 287–288.
- [21] M. C. Zerner, *Rev. Comput. Chem.* **1991**, *2*, 313–365.
- [22] a) D. G. Gorenstein, *Chem. Rev.* **1987**, *87*, 1047–1077; b) E. Juaristi, G. Cuevas, *Tetrahedron* **1992**, *48*, 5019–5087.
- [23] S. Marque, H. Fischer, E. Baier, A. Studer, *J. Org. Chem.* **2001**, *66*, 1146–1156.

Received: June 10, 2005

Alkoxyamines of Stable Aromatic Nitroxides: N–O vs. C–O Bond Homolysis

by **Didier Gigmes**^{*a)}, **Anouk Gaudel-Siri**^{b)}, **Sylvain R. A. Marque**^{a)}, **Denis Bertin**^{a)}, **Paul Tordo**^{a)}, **Paola Astolfi**^{c)}, **Lucedio Greci**^{*c)}, and **Corrado Rizzoli**^{d)}

^{a)} UMR 6517 case 542, Université de Provence, Avenue Escadrille Normandie-Niemen, F-13397 Marseille Cedex 20 (fax: +33-4-91-28-87-58; e-mail: didier.gigmes@up.univ-mrs.fr)

^{b)} UMR-CNRS 6178, Université Paul Cézanne/Aix-Marseille, Faculté des Sciences et Techniques, Case D12, F-13397 Marseille Cedex 20

^{c)} Dipartimento di Scienze dei Materiali e della Terra, Università Politecnica delle Marche, via Brecce Bianche, I-60131 Ancona (fax: +39-071-2204714; e-mail: l.greci@univpm.it)

^{d)} Dipartimento di Chimica Generale ed Inorganica, Chimica Analitica, Chimica Fisica, Università, viale G. P. Usberti, I-43100 Parma

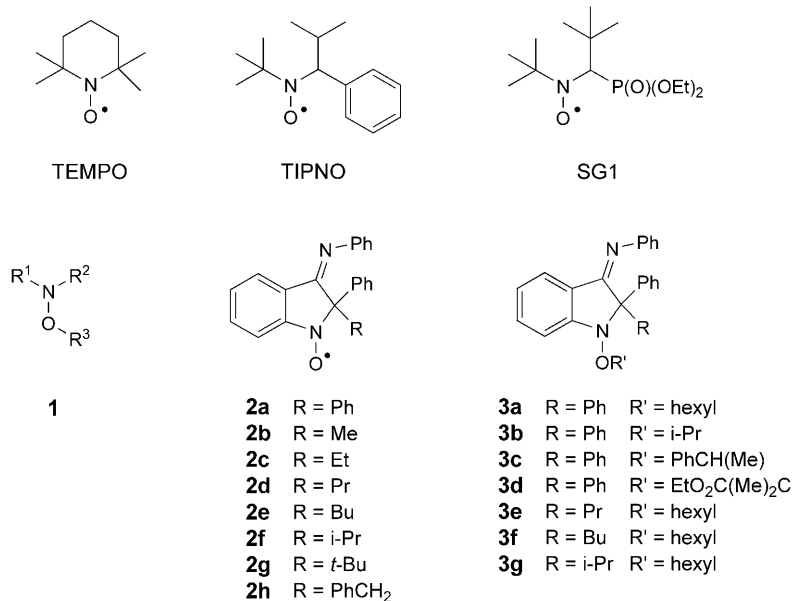
Dedicated to the memory of Professor *Hanns Fischer*

A series of stable 2,2-disubstituted 3-(phenylimino)indol-1-oxyls, the alkoxyamines **3**, were prepared, characterized, and tested as possible candidates in controlled radical polymerization (CRP). The structures of **3d** and **10** were additionally solved by X-ray diffraction. The lability of the N–O(C) and (N)O–C bonds of compounds **3** were compared, and the possibility of N–O vs. O–C bond cleavage was evaluated by thermal degradation, ESR spin trapping, MS experiments, and DFT calculations. Alkoxyamines with a primary- or secondary-alkyl group bound to the O-atom of the nitroxide function (hexyl and *i*-Pr) mainly underwent (undesired) N–O bond homolysis. When the *O*-alkyl radical was a tertiary or a benzyl group (crotonyl or styryl), O–C bond cleavage occurred as the main process, thus suggesting a possible use of these compounds in CRP processes.

1. Introduction. – Two decades ago, *Rizzardo* and co-workers [1], as well as *Georges et al.* [2] showed that it is possible to prepare well-defined polymers by using nitroxyl radicals or alkoxyamines as catalysts. Nitroxide-mediated polymerization (NMP) was, thus, born [3][4], and it inspired several studies with the aim to understand the mechanism [5] and kinetics of polymerization [6–11], to prepare new polymers [3][12–14], and to develop more-efficient initiators/controllers [15–22].

Among the few commercially available nitroxides, TEMPO (=2,2,6,6-tetramethylpiperidinoxy radical) has been widely used, although it proved to be efficient only in the polymerization of styrene derivatives [23]. To overcome this limitation, the synthesis of new nitroxides has been developed. The use of TEMPO-based nitroxides and, above all, of acyclic nitroxides having a H-atom on one of the α -C-atoms, such as TIPNO [17] and SG1 [24], and their corresponding alkoxyamines **1**, represents a breakthrough in the field of NMP. After the development of these new nitroxide radicals, it is now possible to polymerize acrylates, acrylamides, 1,3-dienes, and acrylonitrile monomers [23] with accurate control.

Up to now, the major drawback of NMP has been the difficulty in controlling the polymerization of methacrylate derivatives [25]: livingness and control could be

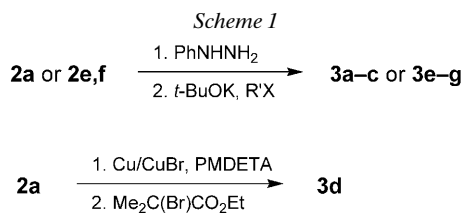


reached only in the presence of a small amount of co-monomer [26]. Recently, we overcame this limitation by using alkoxyamines based on DPAIO (**2a**) nitroxides, which allowed us to control the polymerization of methyl methacrylate at 100°, with 60% conversion [27]. Compound **2a** belongs to the family of ‘indolinonic nitroxides’ [28], aromatic nitroxides with the nitroxide function being in conjugation with the benzene ring. Usually, these radical species are more stable than tetramethylpiperidino- and tetramethylpyrrolidino derivatives. In particular, nitroxides **2a–c** do not significantly decompose when heated at 200° in *Dowtherm* solution [29]. Compounds **2f–h** are less stable due to the easy elimination of alkyl radicals (*i*-Pr, *t*-Bu, Bn) from the C-atom in position 2 [28]. The nitroxides **2g** and **2h** have a low thermal stability, and they decompose even at 100°.

To evaluate the efficiency of these nitroxides in NMP, the alkoxyamines **3a–d** were synthesized by alkylation of **2a**, which is one of the most stable compounds among the above selection. In particular, compound **3a** was synthesized to study its activity in the polymerization of ethylene (= ethene) [30], which is normally carried out at 250° under a pressure of 2000 atmospheres. The alkoxyamine **3d** was designed for the controlled polymerization of methyl methacrylate. Finally, the alkoxyamines **3e–g** were synthesized from **2d–f**, respectively, to ascertain the role, if any, of the alkyl group at C(2).

2. Results. – 2.1. *Synthesis.* The alkoxyamines **3a–g** (with the exception of **3d**) were prepared from the nitroxides **2a**, **2e**, and **2f**, which were reduced *in situ* with phenylhydrazine in the presence of a stoichiometric amount of potassium *tert*-butoxide (*t*BuOK) to give the corresponding hydroxylamine anions (*Scheme 1*). Addition of the appropriate alkyl halide to these anions led to the formation of the desired alkoxyamines **3**. Compound **3d** was easily prepared from **2a** according to the atom-transfer radical-addi-

tion (ATRA) method [31] using the corresponding activated bromide in the presence of Cu^{I} and a small amount of Cu^{0} (Scheme 1). In all cases, the yields were very high, ranging from 80 to 91% (see *Exper. Part*).



The alkoxyamines **3a–g** were identified on the basis of their spectroscopic data. Both the IR and $^1\text{H-NMR}$ spectra were very similar for all the compounds synthesized. In particular, the IR spectra showed two characteristic bands typical of the indoline structures [32], one at *ca.* 1650 cm^{-1} for the $\text{C}=\text{N}$ group, the other, the so-called *Witkop* band, at *ca.* 1595 cm^{-1} for the $\text{Ph-N}-(\text{OR})-\text{C}$ group. Compound **3d** showed an additional IR band at 1732 cm^{-1} for the $\text{C}=\text{O}$ group. In the $^1\text{H-NMR}$ spectra, as expected, the same pattern was evident for the aromatic H-atoms of each alkoxyamine. However, compounds **3b** and **3c** did not show well-resolved peaks for the Me groups, most likely due to hindered rotation of the alkyl group about the N-O-R bonds.

2.2. X-Ray Crystallographic Analyses. **2.2.1. Structure of 3d.** The bond distances and angles in **3d** were as expected (see *Table 1* and *Fig. 1*). The distance $\text{N}(2)-\text{C}(2)$ (1.270 \AA) and the $\text{C}(2)-\text{N}(2)-\text{C}(13)$ angle (120.0°) are in agreement with the interaction of a double bond. The indoline ring is not planar, with maximum deviations from planarity of $-0.240(3)$ and $0.222(2)\text{ \AA}$ for $\text{C}(1)$ and $\text{N}(1)$, respectively. The three Ph rings ($\text{C}(13)$ to $\text{C}(18)$, $\text{C}(19)$ to $\text{C}(25)$, and $\text{C}(25)$ to $\text{C}(30)$) form with the mean plane of the indoline ring dihedral angles of 81.4 , 89.2 , and 76.7° , respectively. *Van der Waals* interactions are the main contacts among the molecules in the crystal. The two intermolecular interactions between $\text{O}(2)$, $\text{N}(2)$, and C-H of two Ph rings may be interpreted as weak H-bonds: *a*) $\text{C}(16)\cdots\text{O}(2)^{\text{i}}$, $3.581(3)\text{ \AA}$; $\text{H}(16)\cdots\text{O}(2)^{\text{i}}$, 2.72 \AA ; $\text{C}(16)-\text{H}(16)\cdots\text{O}(2)^{\text{i}}$, 154.2° ; *b*) $\text{C}(29)\cdots\text{N}(2)^{\text{ii}}$, $3.676(4)\text{ \AA}$; $\text{H}(29)\cdots\text{N}(2)^{\text{ii}}$, 2.81 \AA ; $\text{C}(29)-\text{H}(29)\cdots\text{N}(2)^{\text{ii}}$, 155.2° ($\text{i}=1+x, y, 1+z$; $\text{ii}=1.5-x, -y, -0.5+z$).

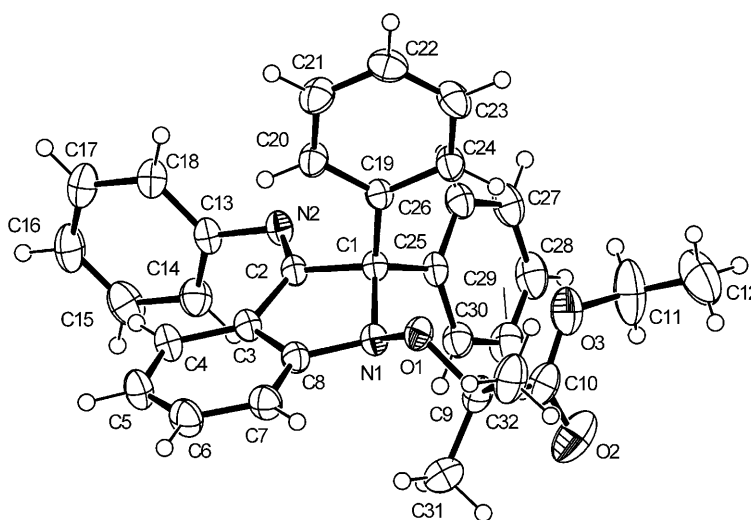
2.2.2. Structure of 10. The structure of **10** (see below) could also be solved by X-ray crystallography (*Fig. 2*). Bond distances and angles again fell in the expected range (*Table 1*). The indoline ring is approximately planar, with maximum deviations from planarity of -0.092 and 0.071 \AA for $\text{C}(2)$ and $\text{N}(1)$, respectively. The dihedral angles formed by the Ph rings ($\text{C}(9)$ to $\text{C}(14)$, $\text{C}(15)$ to $\text{C}(20)$, and $\text{C}(21)$ to $\text{C}(26)$) with the mean plane of the indoline ring are 86.9 , 88.4 , and 68.5° , respectively. Two weak $\text{C-H}\cdots\text{N}$ intramolecular H-bond interactions are observed: *a*) $\text{C}(22)\cdots\text{N}(1)$, 2.795 \AA ; $\text{H}(22)\cdots\text{N}(1)$, 2.43 \AA ; $\text{C}(22)-\text{H}(22)\cdots\text{N}(1)$, 103.5° ; *b*) $\text{C}(26)\cdots\text{N}(2)$, 3.028 \AA ; $\text{H}(26)\cdots\text{N}(2)$, 2.60 \AA ; $\text{C}(26)-\text{H}(26)\cdots\text{N}(2)$, 108.9° .

Here, the crystal packing is mainly determined by *Van der Waals* contacts.

2.3. Mass Spectrometry. The mass spectra of compounds **3a–d** were very significant, the fragmentation pattern depending on the nature of the *O*-alkyl group. In fact, **3a** and **3b** (both having a primary *O*-alkyl group) showed very low intensities of the molecular-

Table 1. Selected Bond Distances (in Å) and Angles (in °) for **3d** and **10**

3d			
O(1)–N(1)	1.432(2)	N(1)–O(1)–C(9)	113.0(1)
O(1)–C(9)	1.459(2)	C(10)–O(3)–C(11)	118.8(2)
O(2)–C(10)	1.195(4)	O(1)–N(1)–C(1)	113.3(1)
O(3)–C(10)	1.320(3)	O(1)–N(1)–C(8)	112.1(1)
O(3)–C(11)	1.468(4)	C(1)–N(1)–C(8)	107.0(1)
N(1)–C(1)	1.512(3)	C(2)–N(2)–C(13)	120.0(2)
N(1)–C(8)	1.414(3)		
N(2)–C(2)	1.270(3)		
N(2)–C(13)	1.419(2)		
10			
O(1)–C(7)	1.374(5)	C(7)–O(1)–C(27)	116.6(3)
O(1)–C(27)	1.425(5)	C(1)–N(1)–C(8)	109.1(3)
N(1)–C(1)	1.486(5)	C(2)–N(2)–C(9)	120.8(3)
N(1)–C(8)	1.386(5)		
N(2)–C(2)	1.259(5)		
N(2)–C(9)	1.411(5)		

Fig. 1. X-Ray crystal structure of **3d**. ORTEP View (40%-probability ellipsoids).

ion peak in their mass spectra, the most important peak in both cases appearing at m/z 359, which corresponds to the fragment originating from the parent alkoxyamine after loss of an hexyloxy or an isopropoxyloxy group, respectively. Compounds **3c** and **3d** gave mass spectra in which the molecular-ion peaks were clearly visible. Other well-defined peaks were found at m/z 375 and 359, corresponding to the fragments derived from the cleavage of the O–C and N–O bonds of the alkoxyamine moiety, respectively (see below).

2.4. ESR Spin-Trapping Experiments and Thermal Stability of **3a–g**. The stability of the nitroxides **2a–h** has already been described [29]. The data reported in the literature

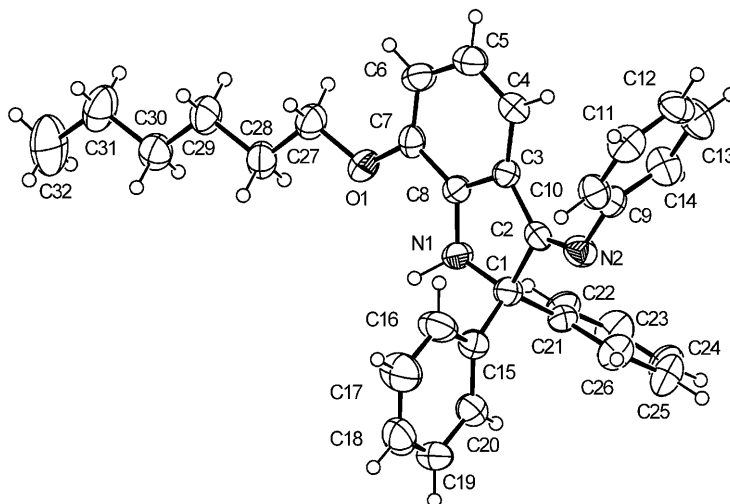


Fig. 2. X-Ray crystal structure of **10**. ORTEP View (40%-probability ellipsoids).

indicate that the thermal stability of these nitroxides depends on the nature of the substituent R at C(2) of the indole moiety. The higher the stabilization of the radical R, the lower the stability of the nitroxide. For this reason, **2g** and **2h** having a *t*-Bu and a Bn group at C(2), respectively, are less stable and decompose at temperatures $< 100^\circ$. Nitroxide **2a**, in which two Ph groups are present at C(2), is very stable, similar as nitroxides with a primary alkyl group at C(2). For this reason, we focused our attention on alkoxyamines derived from **2a**.

To gain information on the stabilities of the alkoxyamines **3a–d**, their benzene solutions were heated at 80° directly inside the ESR cavity, and the identification of alkyl or alkoxy radicals eventually formed was achieved by means of the spin-trapping technique, with ‘*tert*-butyl- α -phenylnitronne’ (PBN, **4**)¹⁾ being used as the spin trap. Thermal decomposition may occur according to two different pathways (*Scheme 2*).

The radical adduct formed from the trapping of the aminyl radical **6** by PBN (**4**) was not detected because it is thermally unstable and, if formed, would have rapidly decomposed. In addition, its formation could be inhibited by crowding around the radical center. The different radical species generated during the thermal decomposition of **3a–d** in the presence of PBN (**4**) were identified from the experimental ESR spectra with the aid of computer simulations [33]. The results are summarized in *Table 2*.

From *Table 2*, it is clear that different radical adducts were formed (in different ratios) from the various alkoxyamines depending on the nature of the alkyl group R'. In particular, the ESR spectrum of **3a** (not shown) was found to be the superposition of two different signals in a 95 : 5 ratio, one corresponding to that of the nitroxide **7a**, the other belonging to the acyl nitroxide **8**, respectively.

¹⁾ Systematic name: *N*-(1,1-dimethylethyl)-*N*-(phenylmethylidene)amine oxide.

Scheme 2

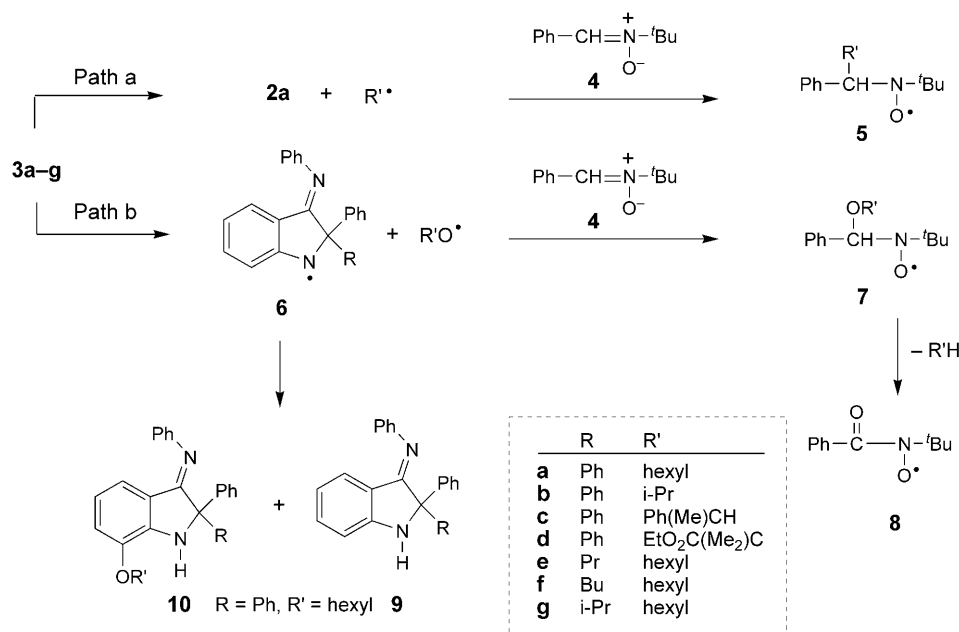


Table 2. Product Distribution (in %) of the Different Radical Species Observed by ESR During Thermal Decomposition of Alkoxyamines **3**. Conditions: in benzene solution for 40 min at 80° in the presence of PBN (**4**).

Starting material	2a	5	7	8
3a	–	–	95	5
3b	–	–	92	8
3c	43	15	–	42
3d	79	7	14	–
3d^a	60	40	–	–

^a) After 10 min of heating.

The same radical adducts were obtained from the thermal decomposition of compound **3b** in the presence of PBN (**4**), and in fact, nitroxides **7b** and **8** were obtained in a 92 : 8 ratio, respectively (Fig. 3). Simulation of the experimental spectrum recorded from alkoxyamine **3c** was in agreement with the superposition of three different signals due to nitroxides **2a**, **5c**, and **8** (Fig. 4). A similar behavior was observed for compound **3d**: after 40 min of heating, a composite spectrum exhibiting the signals of nitroxides **2a**, **5d**, and **7d** in a ratio of 79 : 7 : 14, respectively, was recorded (not shown). In this last case, after 10 min of heating, a spectrum was formed only by the signal of **2a** and **5d** (Fig. 5). The hyperfine-coupling constants of the formed nitroxides are collected in Table 3. Note that compounds **3e–g**, when heated at 80°, behave like compound **3a**.

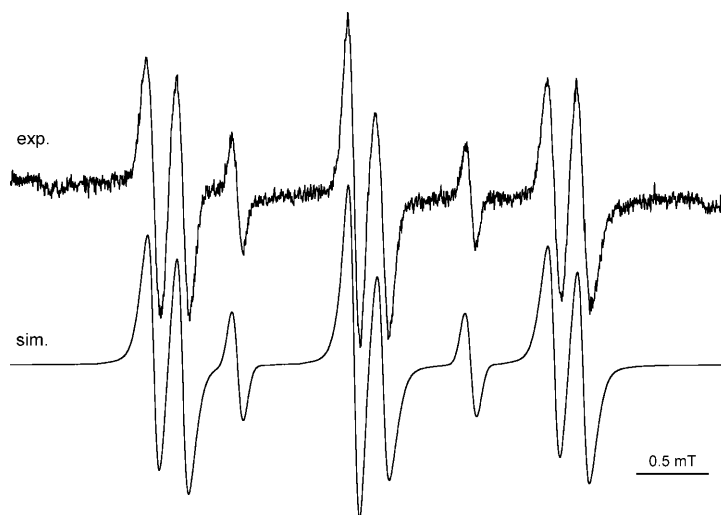


Fig. 3. Experimental (exp.) vs. simulated (sim.) ESR spectra for the radical adducts formed in the thermal decomposition of **3b** in the presence of PBN (**4**) after 40 min at 80°

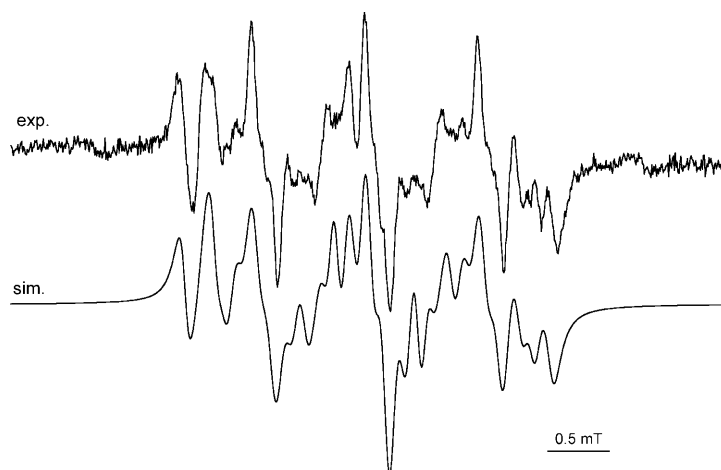


Fig. 4. Experimental (exp.) vs. simulated (sim.) ESR spectra for the radical adducts formed in the thermal decomposition of **3c** in the presence of PBN (**4**) after 40 min at 80°

2.5. *Preparative-Scale Thermal Decomposition.* Compound **3a** was thermally decomposed on a preparative scale by heating a *tert*-butylbenzene solution of the alkoxyamine under reflux for 1.5 h. In agreement with the ESR spin-trapping experiment, DPAIO was not formed, and compound **9** (70%) was the main product, together with **10** (30%).

2.6. *Bond-Dissociation-Enthalpy (BDE) Calculations.* The BDE values for the alkoxyamines **3a–d** were calculated to compare the lability of the corresponding N–

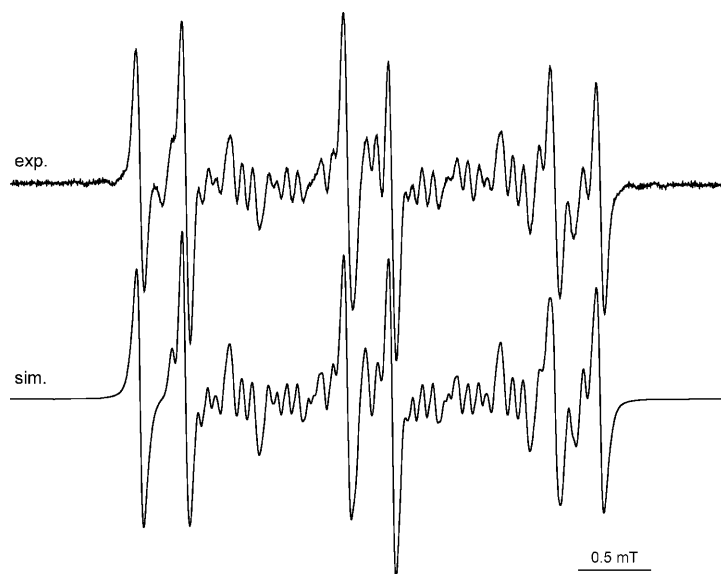


Fig. 5. Experimental (exp.) vs. simulated (sim.) ESR spectra for the radical adducts formed in the thermal decomposition of **3d** in the presence of PBN (**4**) after 10 min at 80°

Table 3. ESR Hyperfine Coupling Constants (in mT) for Selected Compounds. Conditions: in benzene at 80° (see Exper. Part).

Radical	$a(\text{N})$	$a(\text{H})$
2a ^{a)}	0.943	–
5d	1.443	0.313
7a	1.405	0.229
7d	1.393	0.203
7c	1.400	0.232
8	0.811	–

^{a)} Values for other atoms: $a_{\text{H}(5)} = 0.314$, $a_{\text{H}(7)} = 0.303$, $a_{\text{H}(4)} = a_{\text{H}(6)} = 0.104$, $a_{\text{N}(\text{exo})} = 0.072$.

O(C) and (N)O–C bonds. The BDEs for the two competitive pathways at 298 K are defined by Eqns. 1 and 2:

$$\text{BDE}_{\text{C-O}} = \Delta H_{\text{f}}^{\circ}(\text{nitroxide}) + \Delta H_{\text{f}}^{\circ}(\text{R}^{\bullet}) - \Delta H_{\text{f}}^{\circ}(\text{N-alkoxyamine}) \quad (1)$$

$$\text{BDE}_{\text{N-O}} = \Delta H_{\text{f}}^{\circ}(\text{aminyl}) + \Delta H_{\text{f}}^{\circ}(\text{RO}^{\bullet}) - \Delta H_{\text{f}}^{\circ}(\text{N-alkoxyamine}) \quad (2)$$

Density-functional-theory (DFT) calculations were performed with the Gaussian03 software package [34]. Recently [35][36], various standard functionals have been tested to calculate BDE values of C–X and X–Y bonds belonging to a large panel of compounds. The best results were obtained with the B3P86 functional, and the best correlation constants between the experimental and calculated values were

obtained at the B3P86/6-311++G(d,p)//B3LYP/6-31G(d) level. Herein, the geometry optimization and the calculation of vibrational frequencies were performed at the B3LYP/6-31G(d) level, and a single point at the B3P86/6-311++G(d,p) level was used to calculate the energy. All minima were confirmed by a calculation of vibrational frequencies. For thermodynamic calculations, as recommended by Wong [37], a scale factor of 0.9804 was applied to the vibrational frequencies. The BDEs were then calculated according to Eqn. 3 (for $T = 298$ K):

$$\text{BDE} = \Delta H_r^\circ = D_e + \Delta(\text{ZPE}) + \Delta H_{\text{trl}} + \Delta H_{\text{rot}} + \Delta H_{\text{vib}} + RT \quad (3)$$

Here, D_e is the classical electronic bond-dissociation energy, $\Delta(\text{ZPE})$ is the difference in zero-point energy between the products and the *N*-alkoxyamine, and ΔH_{trl} , ΔH_{rot} , and ΔH_{vib} are the contributions from translational, rotational, and vibrational degrees of freedom, respectively. The results of these studies are reported in Table 4.

Table 4. Comparison of the Bond-Dissociation Enthalpies (BDE) for the (N)O–C vs. N–O(C) Cleavage of **3** at 298 K. All values calculated at the B3P86/6-311++G(d,p)//B3LYP/6-31G(d) level.

Compound	BDE [kJ mol ⁻¹]	
	(N)O–C	N–O(C)
3a	175	136
3b	173	141
3c	118	137
3d	102	126

3. Discussion. – According to the experiments carried out on the thermal decomposition of **3a–d**, as described above, it is clear that the pathway followed in the thermal homolysis is related to the nature of the R' group. When R' is a nonstabilized alkyl group, as in **3a,b**, the bond-dissociation enthalpy (BDE) for the N–O(C) bond is lower than that for the (N)O–C bond. When R' is a stabilized substituent, the BDEs for the two bonds are closer to each other, as in the case of **3c**. For compound **3d**, the BDE for the (N)O–C bond is smaller than for N–O(C). These data are in agreement with those obtained from the MS analyses of the different alkoxyamines (see above). In fact, the most-important mass peaks in the spectra of all studied compounds (with the exception of **3c** and **3d**) are due to the aminyl radical **6** formed from the starting alkoxyamine after N–O(C) bond cleavage, with loss of the *O*-alkyl moiety. This result is also supported by the thermal-decomposition experiment. When **3a** was refluxed in *tert*-butylbenzene, no DPAIO was recovered, and the main product isolated corresponded to **9** (70%) derived from the aminyl fragment **6**. The second product, compound **10**, was also formed *via* the intermediate aminyl radical. Compounds **3c** and **3d**, *i.e.*, *O*-styryl and *O*-methylcrotonate, showed in their mass spectra both the peaks of the nitroxide **2a** and of the aminyl fragment **6** (R = Ph), the latter being less intense than that of the nitroxide in the case of **3d**.

The thermal decomposition of **3a–d** at 80° in the presence of PBN (**4**) inside the ESR cavity were also convincing. With the exception of **3c** and **3d**, the spectra recorded during the decomposition of all the other alkoxyamines correspond to the *O*-alkyl–

PBN spin adduct **7** and to the acyl nitroxide **8**, its thermal decomposition product (see *Fig. 3*). In the case of **3c** and **3d**, the ESR spectrum of **2a** was also detected, thus indicating that O–C bond cleavage occurs. In particular, in the case of **3d**, the spin adduct **5d** was observed (see *Fig. 5*). The spin adducts **5** and **7** were identified on the basis of the hyperfine coupling for the α -H-atom, which should be *ca.* 0.3 mT when an alkyl group is attached to the same C-atom, and *ca.* 0.2 mT when an alkoxy group is present [38].

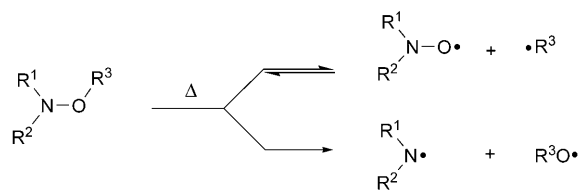
The above data may be rationalized by the observation that N–O(C) bond cleavage easily occurs because of the formation of the resonance-stabilized aminyl radical **6**; however, when the radical bonded to the O-atom in these aromatic nitroxides is sufficiently stabilized, as in the case of styryl and methyl crotonate-1-yl, the cleavage of the O–C bond also occurs (**3c** and **3d**). With **3d**, (N)O–C cleavage is favored compare to **3c** due to an increase of the steric hindrance of the released alkyl fragment. Compared to **3a** and **3b**, the (N)O–C cleavage of **3c** is the main process due to both increased steric hindrance and stabilization of the released alkyl part; DFT calculations support these experimental results (*Table 4*). In fact, the calculated BDE_{N-O} values are quite constant ($\Delta BDE_{N-O} = 19 \text{ kJ mol}^{-1}$), while the calculated BDE_{O-C} values are strongly influenced by the nature of the substituents attached to the C-atom ($\Delta BDE_{O-C} = 73 \text{ kJ mol}^{-1}$).

For **3a** and **3b**, the BDE_{N-O} values are significantly lower than the BDE_{O-C} ones (ΔBDE *ca.* 35 kJ mol^{-1}), and in fact, amine and alkoxy radicals are formed, being the sole products observed. In the case of **3c** and **3d**, the (N)O–C bond is the most labile, and its homolysis is favored with respect to N–O(C) homolysis. This can be rationalized by the released radical being stabilized by π -electron delocalization, whereas the parent alkoxyamine is destabilized by steric hindrance. As already pointed out [35], the combination of both steric and electron-withdrawing effects for the released radical (**3d**) leads to a significant decrease in the BDE_{O-C} value. For **3c,d**, a small gap (*ca.* 20 kJ mol^{-1}) between BDE_{O-C} and BDE_{N-O} was observed, which justifies the detection of both aminyl and nitroxyl radicals in the ESR spin-trapping experiments. The gap between the BDE values for the two different bonds is larger for **3d**, with BDE_{O-C} being considerably lower than BDE_{N-O} , and, indeed, a higher ratio of nitroxyl/aminyl radicals was detected.

Introduction of an alkyl group, *i.e.*, Pr, i-Pr, or Bu on C(2) of the indole ring, as in alkoxyamines **3e–g**, does not affect the behavior of these compounds. As in the case of **3a**, during their thermal decomposition, the aminyl radical was mainly formed, which suggests that, for the studied compound, it is the nature of the group attached to the O-atom of the nitroxide function that determines the particular kind of homolysis, *i.e.*, N–O(C) *vs.* (N)O–C cleavage, with no influence by the other groups present on the indole ring.

4. Conclusions. – During our investigation on the use of DPAIO alkoxyamines in NMP, we discovered that the thermal decomposition may occur in two different ways (*Scheme 3*). Thereby, there may be a competition between (N)O–C and N–O(C) bond cleavage. The possibility and the extent of bond cleavage depend on the nature of the alkyl moiety R^3 bound to the O-atom of the nitroxide function, as deduced by detailed studies of the thermal decomposition of the alkoxyamines **3a–d** by means of ESR spin-trapping experiments, MS analyses, laboratory-scale experiments, and DFT calculations.

Scheme 3



It is obvious that, except for **3d**, the studied alkoxyamines **3** are not suitable to mediate controlled radical polymerization since their thermal decomposition occurs predominantly between the N–O(C) bond. However this alkoxyamines can afford an interesting way to produce alkoxy radicals at medium-to-high temperatures. In a forthcoming paper, we will present a successful living controlled radical polymerization of a different substrate (MMA) using **3d**-type initiators/controllers [27].

University of Provence and CNRS are kindly acknowledged for financial support.

Experimental Part

1. *General*. The nitroxides **2a–h** were prepared starting from 2-phenyl-3-phenylimino-3*H*-indole *N*-oxide [39] according to a procedure reported previously [28]. Solvents and chemicals were purchased from *Carlo Erba* and *Sigma-Aldrich* and used as received. Melting points (m.p.) were measured with an electrothermal apparatus; uncorrected. IR Spectra: *Perkin-Elmer Spectrum MGXI* spectrophotometer equipped with a Spectra Tech ‘Collector’ for DRIFT measurements; in cm^{-1} . $^1\text{H-NMR}$ Spectra: *Varian Gemini-200* spectrometer; at r.t. in CDCl_3 soln.; δ in ppm rel. to Me_4Si , Δ in Hz. ESR Spectra: upgraded *Bruker ER-200D* spectrometer. GC/MS: *Carlo Erba QMD-1000* mass spectrometer equipped with a *Fisons GC-8060* chromatograph; in *m/z*.

2. *Synthesis of 3a–c and 3e–g* (General Procedure). To a soln. of **2a** (1 mmol) and the appropriate alkyl halide (6 mmol) in THF (10 ml) was added phenylhydrazine (1 mmol) under Ar gas. Upon reduction, the color changed from red to yellowish. Then, $^t\text{BuOK}$ (2 mmol) was added, and the mixture was stirred at r.t. for 1 h. The mixture was diluted with Et_2O (25 ml) and washed with dist. H_2O (3×20 ml). The org. phase was dried (Na_2SO_4) and evaporated, and the residue was crystallized from the appropriate solvent (see below).

N-[1-(Hexyloxy)-1,2-dihydro-2,2-diphenyl-3*H*-indol-3-ylidene]aniline (**3a**). Yield: 89%. M.p. $85\text{--}86^\circ$ (ligroin, b.p. $40\text{--}60^\circ$). IR: 1652 (C=N), 1596 (Ph–N(O–hexyl)–C). $^1\text{H-NMR}$ (200 MHz, CDCl_3): 0.86 (unresolved *t*, 3 H); 1.20–1.25 (*m*, 6 H); 1.48–1.62 (*m*, 2 H); 3.85 (*t*, $J=6.8$, 2 H); 6.40 (*d*, $J=6.8$, 1 H); 6.62 (*t*, $J=7.2$, 1 H); 6.79 (*d*, $J=7.2$, 2 H); 7.05–7.15 (*m*, 2 H); 7.27–7.36 (*m*, 10 H); 7.51–7.56 (*m*, 3 H). EI-MS (pos.): 461 (2.5, $[M+1]^+$), 375 (5), 361 (30), 359 (100), 283 (18), 254 (14), 205 (26) 165 (39), 152 (44). Anal. calc. for $\text{C}_{32}\text{H}_{32}\text{N}_2\text{O}$: C 83.44, H 7.0, N 6.08; found: C 84.47, H 7.04, N 6.12.

N-[1,2-Dihydro-1-[(1-methylethyl)oxy]-2,2-diphenyl-3*H*-indol-3-ylidene]aniline (**3b**). Yield: 90%. M.p. $152\text{--}153^\circ$ (ligroin, b.p. $60\text{--}100^\circ$). IR: 1657 (C=N), 1596 (Ph–N(O i Pr)–C). $^1\text{H-NMR}$ (200 MHz, CDCl_3): 1.17 (br. *s*, 6 H); 3.93 (*sept.*, 1 H); 6.40 (*d*, $J=7.8$, 1 H); 6.61 (*t*, $J=7.2$, 1 H); 6.79 (*d*, $J=7.2$, 2 H); 7.08–7.13 (2 arom. H); 7.28–7.34 (9 arom. H); 7.50–7.59 (br. *s*, 4 H). EI-MS (pos.): 418 (1.3, M^+), 375 (1.2), 361 (30), 360 (100), 2.81 (7), 254 (8), 205 (18). Anal. calc. for $\text{C}_{29}\text{H}_{26}\text{N}_2\text{O}$: C 83.22, H 6.26, N 6.69; found: C 83.14, H 6.22, N 6.71.

N-[1,2-Dihydro-2,2-diphenyl-1-[(1-phenylethyl)oxy]-3*H*-indol-3-ylidene]aniline (**3c**). Yield: 91%. M.p. $162\text{--}163^\circ$ (benzene/petroleum ether). IR: 1657 (C=N), 1596 (Ph–N(O–styryl)–C). $^1\text{H-NMR}$ (200 MHz, CDCl_3): 1.36 (br. *s.*, 3 H); 4.61 (*q*, $J=7.8$, 1 H); 6.34 (*d*, $J=8.9$, 1 H); 6.55 (*t*, $J=7.8$, 1 H);

7.03–7.38 (*m*, 15 H); 7.53–7.65 (*m*, 4 H); 7.73 (*d*, $J=7.8$, 2 H). EI-MS (pos.): 480 (7, M^+), 376 (27), 375 (30), 362 (17), 360 (52), 299 (38), 285 (23), 284 (100), 205 (33), 165 (19). Anal. calc. for $C_{34}H_{28}N_2O$: C 84.97, H 5.87, N 5.83, found: C, 84.95, H 5.91, N 5.87.

N-[1-(Hexyloxy)-1,2-dihydro-2-phenyl-2-propyl-3H-indol-3-ylidene]aniline (**3e**). M.p. 64–66° (ligroin, b.p. 60–100°). IR: 1661(C=N), 1598(Ph–N(OPr)–C). 1H -NMR (200 MHz, $CDCl_3$): 0.87 (*t*, $J=6$, 3 H); 0.98 (*t*, $J=6$, 3 H); 1.15–1.56 (*m*, 12 H); 2.43 (*m*, 1 H); 2.51–2.61 (*m*, 1 H); 3.71–3.79 (*m*, 1 H); 3.83–3.90 (*m*, 1 H); 6.34 (*d*, $J=9$, 1 H); 6.57 (*t*, $J=9$, 1 H); 6.77 (*d*, $J=9$, 2 H) 7.05–7.10 (*m*, 2 H); 7.23–7.35 (*m*, 6 H); 7.52 (*d*, $J=9$, 2 H). EI-MS (pos.): 426 (3, M^+), 325 (100), 283 (17). Anal. calc. for $C_{29}H_{34}N_2O$: C 81.43, H 8.86, N 6.40; found: C 81.65, H 8.83, N 6.57.

N-[2-Butyl-1-(hexyloxy)-1,2-dihydro-2-phenyl-3H-indol-3-ylidene]aniline (**3f**). M.p. 44–45° (ligroin, b.p. 60–100°). IR: 1661(C=N), 1597(Ph–N(OBu)–C). 1H -NMR (200 MHz, $CDCl_3$): 0.87 (*t*, $J=6$, 3 H); 0.92 (*t*, $J=6$, 3 H); 1.16–1.42 (*m*, 10 H); 1.52–1.64 (*m*, 2 H); 2.35–2.45 (*m*, 1 H); 2.54–2.63 (*m*, 1 H); 3.73–3.80 (*m*, 1 H); 3.84–3.91 (*m*, 1 H); 6.35 (*t*, $J=9$, 1 H); 6.58 (*t*, $J=6$, 1 H); 6.77 (*d*, $J=6$, 2 H); 7.05–7.11 (*m*, 2 H); 7.23–7.35 (*m*, 6 H); 7.51 (*d*, $J=6$, 2 H). EI-MS (pos.): 440 (10, M^+), 384 (13), 340 (100), 295 (45), 283 (39). Anal. calc. for $C_{30}H_{36}N_2O$: C 81.78, H 8.24, N 6.36; found: C 81.97, H 8.36, N 6.15.

N-[1-(Hexyloxy)-1,2-dihydro-2-(1-methylethyl)-2-phenyl-3H-indol-3-ylidene]aniline (**3g**). M.p. 109–110° (ligroin, b.p. 60–100°). IR: 1667(C=N), 1597 (Ph–N(OⁱPr)–C). 1H -NMR (200 MHz, $CDCl_3$): 0.90 (*t*, $J=6$, 3 H); 1.07 (*t*, $J=6$, 3 H); 1.15 (*d*, $J=6$, 3 H); 1.25–1.45 (*m*, 6 H); 1.61–1.70 (*m*, 2 H); 3.15–3.29 (*t*, $J=6$, 1 H); 3.91–4.08 (*m*, 2 H); 6.31 (*d*, $J=9$, 1 H); 6.52 (*t*, $J=9$, 1 H); 6.78 (*d*, $J=9$, 2 H); 7.02–7.11 (*m*, 2 H); 7.25–7.31 (*m*, 6 H); 7.60 (*d*, $J=9$, 2 H). EI-MS (pos.): 426 (9, M^+), 383 (86), 325 (100), 299 (62), 282 (75). Anal. calc. for $C_{29}H_{34}N_2O$: C 81.43, H 8.86, N 6.40; found: C 81.49, H 8.78, N 6.53.

The Nitroxides **2d–f** were transformed into the corresponding hexyl-substituted compounds **8e–g** as reported for compounds **3a–c**.

3. *Synthesis of Ethyl 2-[[2,3-Dihydro-2,2-diphenyl-3-(phenylimino)-1H-indol-1-yl]oxy]-2-methylpropanoate (3d)*. Compound **2a** (1 mmol) and ethyl 2-bromoisobutyrate (2 mmol) were dissolved in anhyd. toluene (5 ml) in a 50-ml round-bottom flask, and degassed with Ar. In another 50-ml flask, Cu (2 mmol) and CuBr (2 mmol) were suspended in anhyd. toluene (5 ml), degassed for 10 min with Ar, and then treated with pentamethyl-diethylenetriamine (PMDTA; 1 mmol), and finally degassed again for another 10 min. Next, the content of the first flask was poured into that of the second under Ar atmosphere. The resulting reaction mixture was stirred for 30 min and then diluted with Et_2O (60 ml). The org. layer was washed with H_2O (3×20 ml), dried (Na_2SO_4), and evaporated. The residue was purified by column chromatography (CC) (SiO_2 ; petroleum ether/ Et_2O 9 : 1) and recrystallized from ligroin. Yield of **3d**: 80%. M.p. 106–107° (ligroin, b.p. 60–100°). IR: 1732 (C=O), 1660 (C=N), 1594 (Ph–N(OCMe₂CO₂Et)–C). 1H -NMR (200 MHz, $CDCl_3$): 1.19 (*t*, $J=7.5$, 3 H); 1.32 (*s*, 6 H); 3.88 (br. *s*, 2 H); 6.4 (*d*, $J=7.5$, 1 H); 6.67 (*t*, $J=7.5$, 1 H); 6.78 (*d*, $J=8.2$, 2 H); 7.03–7.14 (*q*-like, 1 H); 7.28–7.33 (*m*, 10 H); 7.41 (br. *s*, 4 H). EI-MS (pos.): 490 (8, M^+), 375 (45), 360 (13), 299 (11), 283 (40), 205 (18), 165 (18), 78 (100). Anal. calc. for $C_{32}H_{30}N_2O_3$: C 78.34, H 6.16, N 5.71; found: C 78.39, H 7.62, N 5.76. X-Ray crystal structure: see Fig. 1, Exper. 6.1, and Table 5.

4. *ESR Measurements*. A soln. of the appropriate compound **3** (2 mg) and PBN (**4**; 2 mg) in anhyd. benzene (1 ml) was transferred to an ESR tube, accurately degassed by bubbling with Ar gas, and heated at 80°. The final spectra resulted from ten accumulations in 40 min. Computer-simulated ESR spectra were calculated with the WinSim program in the NIEHS public ESR software-tools package (see <http://www.epr.niehs.nih.gov/>) [33].

5. *Thermal Decomposition of 3a*. Compound **3a** (100 mg) was heated at 160° in 5 ml of *tert*-butylbenzene for 1.5 h. After this time, the reaction soln. was reduced to a small volume (*ca.* 1 ml) and then subjected to prep. TLC (SiO_2 ; cyclohexane/AcOEt 95 : 5). Compound **9** was obtained in 70% yield, together with **10** (30%). Compound **9** was identified by comparison with an authentic sample [40]; compound **10** was characterized spectroscopically (see below).

Data of N-[7-(Hexyloxy)-1,2-dihydro-2,2-diphenyl-3H-indol-3-ylidene]aniline (10). M.p. 100–101° (ligroin, b.p. 40–60°). IR: 1657(C=N), 1591(Ph–N(O–hexyl)–C). 1H -NMR (200 MHz, $CDCl_3$):

Table 5. X-Ray Diffraction Data for **3d** and **10**

Compound	3d	10
Formula	C ₃₂ H ₃₀ N ₂ O ₃	C ₃₂ H ₃₂ N ₂ O
<i>M_r</i>	490.6	460.6
Space group	<i>P2₁2₁2₁</i>	<i>Pbcn</i>
<i>a</i> [Å]	10.272(2)	38.136(6)
<i>b</i> [Å]	28.347(4)	7.2893(11)
<i>c</i> [Å]	9.056(2)	18.683(3)
α, β, γ [°]	90	90
<i>V</i> [Å ³]	2636.9(9)	5193.4(14)
<i>Z</i>	4	8
<i>T</i> [°C]	23(2)	25(2)
λ [Å]	1.54178	0.71073
ρ_{calc} [g cm ⁻³]	1.236	1.178
μ [cm ⁻¹]	6.30	0.71
Transmission coefficient	0.978–1.000	0.994–1.000
<i>R</i> ^a)	0.037	0.037
<i>wR</i> ₂	0.094	0.044
GOF	1.019	0.646
Observed refl.	3936	991
Independent refl. (<i>I</i> > 2σ(<i>I</i>))	4747	3734
Refined refl.	4747	3734
Variables	335	320

7.05–7.15 (*m*, 2 H); 7.27–7.41 (*m*, 10 H); 7.48–7.63 (*m*, 3 H). EI-MS (pos.): 461(2, *M*⁺), 260 (92.15), 384 (26), 383 (100), 299 (64), 221 (32), 167 (45), 165 (29), 77 (48). Anal. calc. for C₃₂H₃₂N₂O: C 83.44, H 7.0, N 6.08; found: C 84.41, H 7.15, N 6.18.

6. X-Ray Crystallography²⁾. 6.1. Compound **3d**. C₃₂H₃₀N₂O₃, *M_r* 490.6, orthorhombic, space group *P2₁2₁2₁*; *a* = 10.272(2), *b* = 28.347(4), *c* = 9.056(2) Å, *V* = 2636.9(9) Å³, *Z* = 4; ρ = 1.236 g cm⁻³; $\lambda(\text{CuK}\alpha)$ = 1.54178 Å, $\mu(\text{CuK}\alpha)$ = 6.30 cm⁻¹; colorless prism (0.14 × 0.15 × 0.20 mm). The structure was solved by direct methods (SIR97 [41]) and anisotropically refined for all non-H atoms. The H-atoms were located from a difference *Fourier* map and thereafter treated as riding atoms, the isotropic displacement parameter *U*_{iso}(H) set at 1.2 *U*_{eq}(C). The structure was refined on *F*² values (SHELX97 [42]) by using the weighting scheme $w = 1/[\sigma^2(F_o^2) + (0.0515 P)^2]$, where $P = (F_o^2 + 2 F_c^2)/3$. For 4747 unique reflections having *I* > 0 collected at *T* = 296(2) K on an *Enraf-Nonius CAD4* diffractometer ($3 < 2\theta < 140^\circ$), the final *R* value was 0.037 (*wR*₂ = 0.094; *S* = 1.019). See also Table 5.

6.2. Compound **10**. C₃₂H₃₂N₂O, *M_r* 460.6, orthorhombic, space group *Pbcn*; *a* = 38.136(6), *b* = 7.2893(11), *c* = 18.683(3) Å, *V* = 5193.4(14) Å³, *Z* = 8; ρ = 1.178 g cm⁻³; $\lambda(\text{MoK}\alpha)$ = 0.71072 Å, $\mu(\text{MoK}\alpha)$ = 0.71 cm⁻¹; yellow plate (0.03 × 0.09 × 0.15 mm). The structure was solved by direct methods (SIR 97 [41]) and anisotropically refined for all the non-H-atoms. The H-atom bound to N(1) was located from a difference *Fourier* map and refined isotropically. All other H-atoms were located from a difference *Fourier* map and thereafter treated as riding atoms, the isotropic displacement parameter *U*_{iso}(H) set at 1.2 *U*_{eq}(C) for Me H-atoms. The structure was refined on *F*² values (SHELX97 [42]) with the

²⁾ The crystallographic data of **3d** and **10** have been deposited with the *Cambridge Crystallographic Data Centre* as supplementary publication numbers CCDC-605374 and CCDC-605375, resp. Copies of the data can be obtained, free of charge, via the internet at http://www.ccdc.cam.ac.uk/data_request/cif.

weighting scheme $w = 1/[\sigma^2(F_o^2)]$. For 3734 unique reflections with $I > 0$ collected at 298(2) K on a *Bruker SMART CCD* diffractometer ($2.8 < 2\theta < 45.6^\circ$), the final R value was 0.037 ($wR_2 = 0.044$; $S = 0.646$). See also *Table 5*.

REFERENCES

- [1] D. H. Solomon, E. Rizzardo, P. Cacioli, US Pat. 4,581,429; Eur. Pat. Appl. 135280 (*Chem. Abstr.* **1985**, 102, 221335q).
- [2] M. K. Georges, R. P. N. Veregin, P. M. Kazmaier, G. K. Hamer, *Macromolecules* **1993**, 26, 2987.
- [3] C. J. Hawker, *Acc. Chem. Res.* **1997**, 30, 373.
- [4] C. J. Hawker, A. W. Bosman, E. Harth, *Chem. Rev.* **2001**, 101, 3661, and refs. cit. therein.
- [5] D. Greszta, K. Matyjaszewski, *Macromolecules* **1996**, 29, 7661, and refs. cit. therein.
- [6] H. Fischer, M. Souaille, *Chimia* **2001**, 55, 109.
- [7] T. Fukuda, A. Goto, K. Ohno, *Macromol. Rapid Commun.* **2000**, 21, 151.
- [8] H. Fischer, *Chem. Rev.* **2001**, 101, 3581, and refs. cit. therein.
- [9] A. Goto, T. Fukuda, *Prog. Polym. Sci.* **2004**, 29, 329, and refs. cit. therein.
- [10] T. Fukuda, A. Goto, Y. Tsujii, in 'Handbook of Radical Polymerization', Eds. K. Matyjaszewski, T. P. Davis, John Wiley & Sons, New York, 2002, p. 407, and refs. cit. therein.
- [11] H. Fischer, *ACS Symp. Ser.* **2003**, 854, 10.
- [12] K. Matyjaszewski, 'Controlled Radical Polymerization', American Chemical Society, Washington, DC, 1998, Vol. 685.
- [13] 'Controlled-Living Radical Polymerization: Progress in ATRP, NMP, and RAFT', Ed. K. Matyjaszewski, American Chemical Society, Washington, DC, 2000, Vol. 768.
- [14] K. Matyjaszewski, *Macromol. Symp.* **2001**, 174, 51.
- [15] G. Moad, E. Rizzardo, *Macromolecules* **1995**, 28, 8722.
- [16] S. Grimaldi, F. Le Moigne, J.-P. Finet, P. Tordo, P. Nicol, M. Plechot, Int. Pat. WO 96/24620, 15 August, 1996.
- [17] D. Benoit, V. Chiplinski, R. Braslau, C. J. Hawker, *J. Am. Chem. Soc.* **1999**, 121, 3904.
- [18] M.-O. Zink, A. Kramer, P. Nesvadba, *Macromolecules* **2000**, 33, 8106.
- [19] P. Nesvadba, M.-O. Zink, A. Kramer, DE 19909767, 1999 (*Chem. Abstr.* 131:229170).
- [20] J.-L. Couturier, O. Guerret, D. Gigmes, S. Marque, F. Chauvin, P.-E. Dufils, D. Bertin, P. Tordo, Pat. FR2843394, 2004; WO 2004014926.
- [21] C. Wetter, J. Gierlich, C. A. Knoop, C. Müller, T. Schulte, A. Studer, *Chem. – Eur. J.* **2004**, 10, 1156.
- [22] E. Drockenmüller, J.-M. Catala, *Macromolecules* **2002**, 35, 2461.
- [23] C. J. Hawker, in 'Handbook of Radical Polymerization', Eds. K. Matyjaszewski, T. P. Davis, J. Wiley & Sons, New York, 2002, p. 463, and refs. cit. therein.
- [24] D. Benoit, S. Grimaldi, S. Robin, J.-P. Finet, P. Tordo, Y. Gnanou, *J. Am. Chem. Soc.* **2000**, 122, 5929.
- [25] K. Matyjaszewski, *ACS Symp. Ser.* **2003**, 854, 2.
- [26] J. Nicolas, L. Mueller, J. Belleney, B. Charleux, *Macromolecules* **2005**, 38, 5485.
- [27] Y. Guillauneuf, P. Astolfi, D. Gigmes, S. R. A. Marque, P. Tordo, L. Greci, D. Bertin, *J. Am. Chem. Soc.*, submitted.
- [28] C. Berti, M. Colonna, L. Greci, L. Marchetti, *Tetrahedron* **1975**, 31, 1745.
- [29] A. Alberti, P. Carloni, L. Greci, P. Stipa, C. Neri, *Polym. Degrad. Stab.* **1993**, 39, 215.
- [30] E. Minaux, L. Greci, M. Buback, P. Tordo, T. Senninger, P. Stipa, P. Carloni, E. Damiani, G. Tommasi, EP Pat. 1120430, 2001.
- [31] K. Matyjaszewski, B. E. Woodworth, X. Zhang, S. Gaynor, Z. Metzner, *Macromolecules* **1998**, 31, 5955.
- [32] B. Witkop, J. B. Patrik, *J. Am. Chem. Soc.* **1951**, 73, 713.
- [33] D. R. Duling, *J. Magn. Reson., B* **1994**, 104, 105.
- [34] M. J. Frisch, G. W. Trucks, H. B. Schlegel, G. E. Scuseria, M. A. Robb, J. R. Cheeseman, J. A. Montgomery Jr., T. Vreven, K. N. Kudin, J. C. Burant, J. M. Millam, S. S. Iyengar, J. Tomasi, V. Barone, B. Mennucci, M. Cossi, G. Scalmani, N. Rega, G. A. Petersson, H. Nakatsuji, M. Hada, M. Ehara, K. Toyota, R. Fukuda, J. Hasegawa, M. Ishida, T. Nakajima, Y. Honda, O. Kitao, H. Nakai, M. Klene,

- X. Li, J. E. Knox, H. P. Hratchian, J. B. Cross, C. Adamo, J. Jaramillo, R. Gomperts, R. E. Stratmann, O. Yazyev, A. J. Austin, R. Cammi, C. Pomelli, J. W. Ochterski, P. Y. Ayala, K. Morokuma, G. A. Voth, P. Salvador, J. J. Dannenberg, V. G. Zakrzewski, S. Dapprich, A. D. Daniels, M. C. Strain, O. Farkas, D. K. Malick, A. D. Rabuck, K. Raghavachari, J. B. Foresman, J. V. Ortiz, Q. Cui, A. G. Baboul, S. Clifford, J. Cioslowski, B. B. Stefanov, G. Liu, A. Liashenko, P. Piskorz, I. Komaromi, R. L. Martin, D. J. Fox, T. Keith, M. A. Al-Laham, C. Y. Peng, A. Nanayakkara, M. Challacombe, P. M. W. Gill, B. Johnson, W. Chen, M. W. Wong, C. Gonzalez, J. A. Pople, Gaussian03, Revision C.02, *Gaussian, Inc.*, Wallingford CT, U.S.A., 2004.
- [35] A. Gaudel-Sri, D. Siri, P. Tordo, *ChemPhysChem* **2006**, *7*, 430.
- [36] E. R. Johnson, O. J. Clarkin, G. A. DiLabio, *J. Phys. Chem., A* **2003**, *107*, 9953; X.-Q. Yao, X.-J. Hou, H. Jiao, H.-W. Xiang, Y.-W. Li, *J. Phys. Chem., A* **2003**, *107*, 9991; Y. Feng, L. Liu, J.-T. Wang, H. Huang, Q.-X. Guo, *J. Chem. Inf. Comput. Sci.* **2003**, *43*, 2005.
- [37] M. W. Wong, *Chem. Phys. Lett.* **1996**, *256*, 391.
- [38] E. Janzen, B. J. Blackburn, *J. Am. Chem. Soc.* **1969**, *91*, 44; A. Ledwith, P. Russel, L. H. Sutcliffe, *Proc. R. Soc. A* **1973**, *151*, 332.
- [39] C. Rizzoli, P. Sgarabotto, F. Ugozzoli, P. Carloni, E. Damiani, L. Greci, P. Stipa, *J. Heterocycl. Chem.* **1993**, *30*, 637, and refs. cit. therein.
- [40] C. Berti, L. Greci, L. Marchetti, *J. Chem. Soc., Perkin Trans. 2* **1977**, 1032.
- [41] A. Altomare, M. C. Burla, M. Camalli, G. Cascarano, C. Giacovazzo, A. Guagliardi, A. G. G. Moliterni, G. Polidori, R. Spagna, *J. Appl. Crystallogr.* **1999**, *32*, 115.
- [42] G. M. Sheldrick, SHELXL97, University of Göttingen, Göttingen, 1997.

Received April 28, 2006

4.3 Application à la réactivité des ènediynes

Ces travaux ont fait l'objet de deux publications (2012 et 2014). La première étude porte sur la compétition entre deux transferts possibles d'atome d'hydrogène à l'issue d'une réaction de Myers-Saito. Suivant les substituants, le transfert 1,6 est favorisé ou non par rapport au transfert 1,5. Depuis cette publication, une autre étude a été menée sur la mémoire de configuration à partir de composés de type ènediynes. Ces travaux font partie de la thèse de doctorat de Mr Damien Campolo soutenue le 13 décembre 2013. Par l'étude des chemins réactionnels complets en compétition, nous avons mis en évidence l'origine de la mémoire configurationnelle conduisant à 95% d'excès énantiomérique et la régénération de stéréocentres via des intermédiaires stéréolabiles. Ce phénomène essentiellement dû à de fortes barrières de rotations permet la synthèse des composés polycycliques énantio-purs par voie purement radicalaire. En effet, à partir d'un intermédiaire réactionnel commun A, quatre profils réactionnels compétitifs sont envisageables par rotations autour de deux liaisons (C-C et C-N). Nous avons pu montrer que seule la rotation autour de la liaison C-C est possible à partir de l'intermédiaire réactionnel I. D'autre part, la rotation dans le sens des aiguilles d'une montre est nettement favorisée, conduisant à un énantiomère unique. L'autre énantiomère serait obtenu par rotations successives autour de la liaison C-C puis de la liaison C-N et ce chemin est nettement moins favorable. L'ensemble des résultats sont reportés dans les deux publications ci-après.

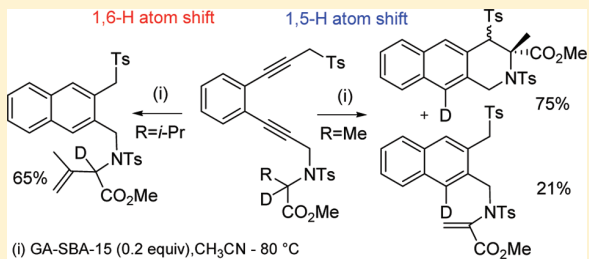
Mechanistic Investigation of Eneidyne-Connected Amino Ester Rearrangement. Theoretical Rationale for the Exclusive Preference for 1,6- or 1,5-Hydrogen Atom Transfer Depending on the Substrate. A Potential Route to Chiral Naphthoazepines

Damien Campolo,[†] Anouk Gaudel-Siri,^{*,†} Shovan Mondal,[†] Didier Siri,[†] Eric Besson,[†] Nicolas Vanthuynne,[‡] Malek Nechab,^{*,†} and Michèle P. Bertrand^{*,†}

[†]Institut de Chimie Radicale, CNRS UMR 7273, Equipes CMO and CTM, and [‡]ISM2, CNRS UMR 7313, Equipe Chirosciences, Aix-Marseille Université, 13397 Cedex 20, Marseille, France

Supporting Information

ABSTRACT: Memory of chirality (MOC) and deuterium-labeling studies were used to demonstrate that the cascade rearrangement of enediynes connected amino esters **1a** and **1b** evolved through exclusive 1,5- or 1,6-hydrogen atom transfer, subsequent to 1,3-proton shift and Saito–Myers cyclization, depending on the structure of the starting material. These results were independently confirmed by DFT theoretical calculations performed on model monoradicals. These calculations clearly demonstrate that in the alanine series, 1,5-hydrogen shift is kinetically favored over 1,6-hydrogen shift because of its greater exergonicity. In the valine series, the bulk of the substituent at the nitrogen atom has a major influence on the fate of the reaction. *N*-Tosylation increases the barrier to 1,5-hydrogen shift to the benefit of 1,6-hydrogen shift. The ready availability of 1,6-hydrogen atom transfer was explored as a potential route for the enantioselective synthesis of naphthoazepines.



INTRODUCTION

We have recently reported the enantioselective cascade rearrangement of enediyne **1a** which evolved through the mechanism depicted in Scheme 1.^{1,2} The reaction proceeded with memory of chirality³ and retention of the configuration of the starting material owing to the generation of intermediate **C** in a chiral conformation. The racemization half-life time of the captodative center in diradical **C** is long compared to the time scale of the recombination step (d). By opposition to enantiopure enediynes in which the stereogenic center was included in a 5-membered ring,^{1,2} substrate **1a** led to an undesired olefinic product (**3a**) that resulted from a disproportionation step (e),⁴ which competed with the biradical recombination leading to tetrahydrobenzoisoquinolines **2a**. These reactions that were initially performed using alumina as the base were shown to proceed very readily with a recoverable nanocatalyst, i.e., mesoporous silica grafted with a tertiary amino group (GA-SBA-15).⁵ Overall yields were significantly improved, and the reaction could be carried out indifferently in benzene or in acetonitrile. The main drawback in this methodology was the lack of diastereoselectivity which resulted in the formation of two enantioenriched diastereomers with two contiguous stereocenters. This drawback was very recently overcome by designing a one-pot strategy.⁶ Tandem Crabbé homologation (leading to monosubstituted allenes)/Myers–Saito cyclization-induced rearrangement was shown to lead to heterocyclic compounds bearing only one stereocenter

that was nearly totally controlled by the MOC phenomenon. We discuss herein the comparative behavior of structurally related enediynes derived from valine and alanine, respectively.

RESULTS AND DISCUSSION

Synthetic Results. When enediyne (*S*)-**1b** was submitted to similar experimental conditions (in the presence of 0.2 equiv of GA-SBA-15), (*S*)-**4b** was isolated as the only product at the expense of any tricyclic product issued from a recombination process (eq 1). Intrigued by the formation of olefin **4b**, while **3b** was expected on the ground of the common prevalence of 1,5-hydrogen shifts, we have checked the influence of other experimental conditions on the fate of (*rac*)-**1b**. In the presence of an excess of base, **3b** could also be formed, but indirectly. It resulted from **4b** through the slow migration of the double bond (eq 2).

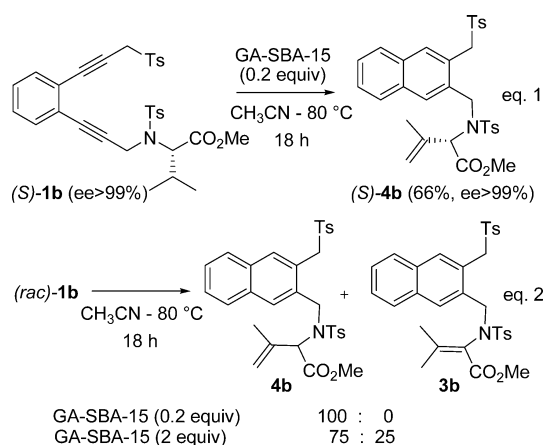
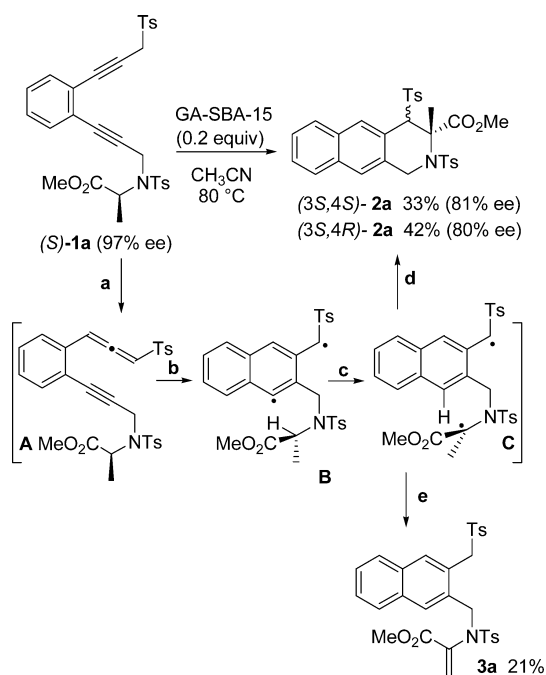
It became obvious that **4b** was the kinetic product and, therefore, that it resulted from 1,6-hydrogen atom transfer rather than from 1,5-transfer of the hydrogen atom in captodative position.

The kinetic preference for 1,6-hydrogen shift was unambiguously demonstrated by measuring the optical purity of **4b** generated as the unique reaction product from optically pure **1b** (ee >99%) (eq 1); the reaction proceeded without loss of

Received: December 21, 2011

Published: February 16, 2012

Scheme 1. General Mechanism

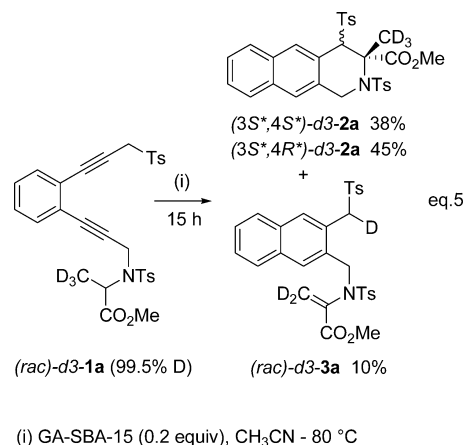
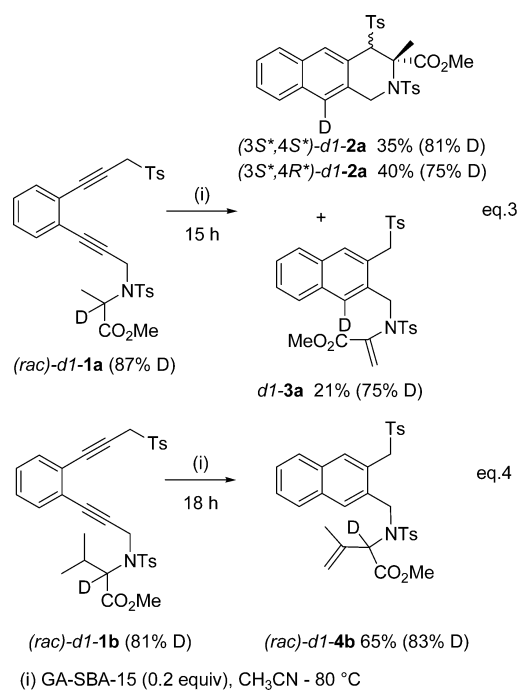


chirality. The enantiopurity of the starting material was entirely recovered in the product.

The formation of **3a** through 1,5-hydrogen shift to 1-naphthyl radical **B** (Scheme 1) was therefore questioned. The pathways leading to **3a** and **3b** were confirmed by deuterium labeling of substrates **1a** and **1b** as reported in eqs 3–5, respectively.

Racemic **1a** and **1b**, monodeuterated at the captodative position, were prepared from monodeuterated racemic *N*-tosylalanine and *N*-tosylvaline methyl esters, respectively. Deuteration of the precursors was accomplished upon treatment with K₂CO₃ in MeOD (99% D) at 70 °C (see the Supporting Information).

As shown in eq 3, both monodeuterated products **2a** and **3a** resulting from the rearrangement of **(rac)-d1-1a** were labeled exclusively at the aromatic ring, as expected from exclusive 1,5-hydrogen shift. The rate of deuteration with respect to the starting material was determined from the relative area of the residual singlet signal of the unlabeled aromatic proton. Errors

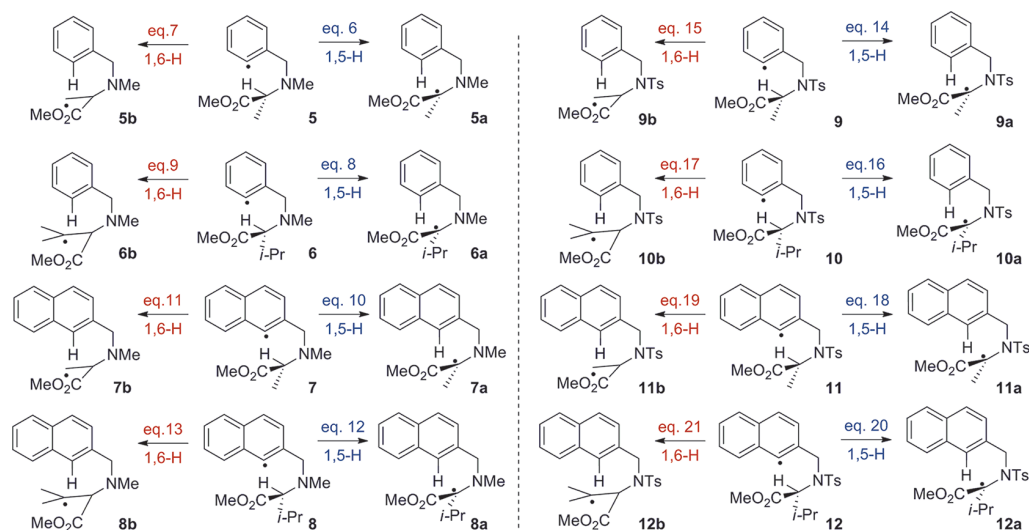


originating from the integration of aromatic signals are probably responsible for the gap between the effective and the theoretical rate of deuteration.⁷ Conversely, as shown in eq 4, the unique product resulting from **(rac)-d1-1b**, i.e., **(rac)-d1-4b**, was exclusively deuterated at the captodative position, which confirmed that in this case only 1,6-hydrogen shift had occurred.

The rearrangement of **(rac)-d3-1a**, prepared from the corresponding commercially available **(rac)-d3-alanine** (99.5% D), is reported in eq 5. It corroborated the results reported in eq 3. Deuterium was recovered exclusively in the CD₃ group in the tricyclic diastereomeric products (**(rac)-d3-2a**). In addition, in **d3-3a** deuterium was scrambled between the terminal olefinic carbon and the methylene group of the benzylic sulfone. In all likelihood, disproportionation is an intramolecular pathway.

An interesting feature was noted. The relative ratio of isolated products **(3S,4S)-2a**:**(3S,4R)-2a**:**3a** that was initially 42:33:21 (Scheme 1) or 40:35:21 (eq 3)⁵ became 45:38:10 in the experiment performed on **(rac)-d3-1a** (eq 5). A primary kinetic isotope effect slowed down disproportionation and

Chart 1



increased the global yield of tricyclic products from 75 to 83% at the expense of *d*3-3a.⁸ It is to be noted that apparently disproportionation affected similarly the pathways leading to both diastereomers (the ratio of which remained constant within the limits of experimental errors).

Examples of 1,5-hydrogen abstraction are widespread in the literature. Applications of Barton and Hoffmann–Loeffler reactions, based on *O*- and *N*-centered radicals, respectively, are well documented.⁹ Similarly, many synthetic strategies are based on radical translocation from vinyl or aryl radicals which have become very popular and powerful synthetic tools.^{9c,d,10} Comparatively, examples of 1,6-hydrogen shift are less numerous.¹¹

Peculiar attention was given to literature data where 1,5- and 1,6-hydrogen shifts could be competitive pathways.^{12–14} As a rule of thumb, 1,5-hydrogen shift is generally favored over 1,6-hydrogen shift. According to theoretical calculations based on butoxy and pentoxy radical, the preference for 1,5-hydrogen shift (six-membered ring transition state) over 1–6 hydrogen shift (seven-membered ring transition state), results from the more favorable activation entropy of the former. Activation enthalpy of the rearrangement of pentoxy radical was found only 0.7 kcal per mole lower than that of butoxy radical.¹⁵ Exceptions to the rule occur when 1,6-hydrogen shift is more exothermic than 1,5-migration, however, in most cases, mixtures of products resulting from the competition between these two processes were formed.

The unique example of recent theoretical calculations using B3LYP DFT functional, and concerning independent 1,5- and 1,6-hydrogen abstractions by aryl radical, deals with the methodology developed by Curran¹³ from *o*-iodoanilide derivatives.^{16,17}

According to Schiesser data, the rate constant for 1,5-hydrogen transfer from a captodative position in such structures ranges between 1.0 and $4.9 \times 10^7 \text{ s}^{-1}$.¹⁸ In the very same paper, the authors have observed that 1,6- or 1,7-radical translocations competed with 1,5-hydrogen shift depending on the structure. However, these structures are completely different from ours, particularly in regard of the planarity of the anilide moiety and extrapolations to the fate of radicals of type **B** (Scheme 1) might be hazardous.

The only data found in the literature concerning 1-naphthyl radicals have been reported by De Mesmaeker.^{14,19} The latter also mentioned competitive 1,5-, 1,6-, and 1,7-H transfers, but even these results cannot be correlated to ours, since in these reactions, 1-naphthyl radicals abstracted hydrogen atoms from an aliphatic chain located in position 8 and not in position 2.

The above disclosed rearrangement of **1b** was rather surprising since 1,6-hydrogen shift is kinetically favored to the exclusion of any 1,5-hydrogen shift, even though the latter should be more, or at least, as exothermic as the previous one. DFT calculations were undertaken on model monoradicals to confirm or infirm these observations.

Computational Section. First the translocation reaction was investigated starting from simple models, i.e., radicals **5–8** bearing a methyl group as substituent at nitrogen, for the sake of reducing calculation time (Chart 1, eqs 6–13). Then, based on these data, new explorations of the potential energy surface were achieved to calculate the transition state geometries for the rearrangements of *N*-tosylated monoradicals **9–12** (Chart 1, eqs 14–21). The latter are closely related to the intermediate biradicals involved in the enediyne cascade transformation.

Computational Details. DFT calculations were performed to determine the profiles of the competitive reactions using the Gaussian 09 program.²⁰ The geometries were fully optimized at the UB3LYP/6-31G(d) level of theory. Vibrational frequencies were calculated at the UB3LYP/6-31G(d) level to determine the nature of the located stationary points. Zero-point energies and thermodynamic data were calculated using the specified scaling factor (0.9603).²¹ All transition-state geometries were confirmed by intrinsic reaction coordinates (IRC) calculations. In order to enhance the accuracy of the calculations, single-point energies were calculated at the UB3LYP/6-311++G-(3df,3pd) level of theory. The spin contamination was low for all radical species ($\langle S^2 \rangle$ values ranged between 0.754 and 0.760).

Some model reactions (Chart 1, eqs 6–9) were also calculated at the G3(MP2)-RAD level of theory to validate the selection of UB3LYP/6-311++G(3df,3pd)//UB3LYP/6-31G(d) method. B3LYP methods are known to underestimate energies values, however the energy gaps are consistent with those obtained from G3(MP2)-RAD calculations which are

known to be highly reliable for radical species (Figure 1, Table 1).²²

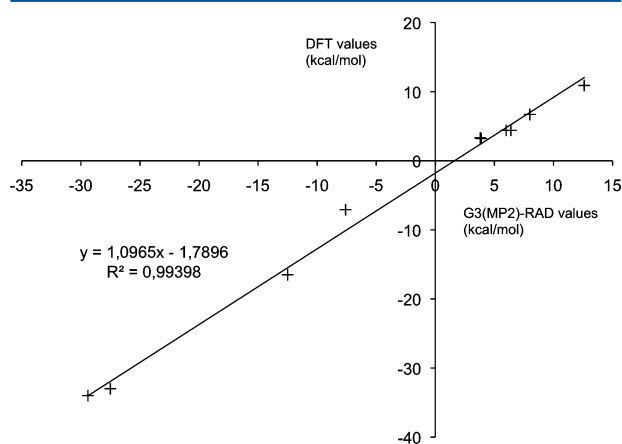


Figure 1. Linear correlation between free energy values calculated at the UB3LYP/6-311++G(3df,3pd)//UB3LYP/6-31G(d) and the G3(MP2)-RAD levels.

Computational Data. The activation free energy (ΔG^\ddagger), the activation enthalpy (ΔH^\ddagger), and entropy (ΔS^\ddagger), together with the reaction exergonicity (ΔG_0) are reported in Table 1 for each reaction (Chart 1, eqs 6–21). It must be noticed that the intrinsic reaction coordinate (IRC) calculations led, in most cases, to slightly different conformations of the reactive starting radical depending on the nature of the transition state (six- or seven-membered ring). The free energy differences ΔG_{conf} between these conformers of the starting radical are given in Table 1. The conformations obtained from the seven-membered transition states are the least stable ones for *N*-methylated model radicals and the situation is reversed for *N*-tosylated radicals. IRC calculations show that the conformer predisposed to 1,5-H shift is less stable than the conformer

predisposed to 1,6-H shift, in the case of radicals **9**, **10** and **12**. No energy difference is observed in the case of radical **11** (see ΔG_{conf} in Table 1).

The predicted ratio of products **Xa** and **Xb** ($X = 5-12$), issued from the competitive 1,5- and 1,6-H shift reactions, respectively, are given in Table 1 (they were determined from the calculated $\Delta\Delta G^\ddagger$ values). From the calculations performed on the series of *N*-methyl model radicals derived from alanine (radicals **5** and **7**), 1,5-H transfer is obviously much faster than 1,6-H transfer (see ΔG^\ddagger in Table 1). It must be noted that the least stable conformer (ready to undergo 1,6-H shift from the methyl group) of any of these starting radicals should account for less than 1% at 298 K according to Boltzmann partition.

According to theoretical calculations, 1,5-H transfer remains favored over 1,6-H transfer, even in the valine series (radicals **6**, **8**), but the barrier for 1,6-hydrogen shift is decreased as compared to the alanine series (the incidence of the reaction exergonicity is discussed in the following). Both aryl and 1-naphthyl radicals behave similarly.

In this first series of model radicals, i.e., *N*-methyl derivatives, in all cases, 1,6-H shift is enthalpically disfavored and the activation enthalpic governs the fate of the radical, although the activation entropy is more favorable for the seven-membered ring transition state (ΔS^\ddagger values show that the six-membered ring transition state geometry for 1,5-H transfer is more constrained in most cases but radical **8**).

It must be noted that, not surprisingly, the homolysis of the captodative C–H bond corresponds to the most exergonic reactions (see $\Delta\Delta G_0$ in Table 1). Due to the difference between the bond dissociation energy (BDE) of the C–H bond in the methyl group and that of the tertiary C–H bond in the isopropyl group the enthalpic factors should contribute to a lesser extend to the activation barrier in the case of valine derivatives.

The captodative character of radicals **9–12** may be questioned,²³ and the simple comparison of the calculated free energy of reactions (ΔG_0) involving 1,5-H migration, i.e.,

Table 1. ΔG_{conf} , ΔG^\ddagger , $\Delta\Delta G^\ddagger$, ΔH^\ddagger , ΔG_0 , $\Delta\Delta G_0$, and ΔG^\ddagger_i in kcal/mol and ΔS^\ddagger in cal/mol/K, for 1,5- and 1,6- Translocations of Radicals **5–12**, Calculated at 298 K at the UB3LYP/6-311++G(3df,3pd)//UB3LYP/6-31G(d) Level of Theory

reaction	ΔG_{conf}^b	$\Delta G^{\ddagger a-c}$	$\Delta\Delta G^{\ddagger d}$ (X_a/X_b)	ΔH^\ddagger	ΔS^\ddagger	ΔG_0^{a-c}	$\Delta\Delta G_0^e$	ΔG^\ddagger_i
5→5a	0.0	4.4 (6.4)	−6.5 (5.8×10^4)	2.8	−5.5	−34.0 (−29.4)	−26.9	17.2
5→5b	3.2 (3.9)	10.9 (12.6)		10.0	−2.9	−7.1 (−7.6)		12.3
6→6a	0.0	4.4 (6.0)	−2.3 (49)	2.3	−6.9	−33.0 (−27.5)	−16.5	16.8
6→6b	3.3 (3.8)	6.7 (8.0)		5.0	−5.6	−16.5 (−12.5)		11.1
7→7a	0.0	3.6	−7.3 (2.2×10^5)	1.9	−5.8	−34.4	−26.8	16.2
7→7b	2.7	10.9		9.6	−4.5	−7.6		12.8
8→8a	0.0	4.2	−3.3 (2.6×10^2)	1.4	−9.4	−31.6	−14.7	16.2
8→8b	2.0	7.5		4.6	−9.7	−16.9		12.6
9→9a	0.9	5.3	−2.6 (81)	3.7	−5.3	−28.1	−17.8	15.5
9→9b	0.0	7.9		6.2	−5.7	−10.3		12.5
10→10a	3.5	9.0	4.2 (8.3×10^{-4})	8.2	−2.6	−22.2	−0.5	15.7
10→10b	0.0	4.8		5.5	+2.4	−21.7		13.5
11→11a	0.0	3.8	−4.3 (1.4×10^3)	2.7	−3.6	−26.9	−15.8	14.1
11→11b	0.0	8.1		6.2	−6.4	−11.1		13.1
12→12a	5.2	10.8	3.3 (3.8×10^{-3})	8.4	−7.9	−20.9	−0.2	16.0
12→12b	0.0	7.5		6.1	−4.6	−20.7		16.2

^aG3(MP2)-RAD values are given in parentheses. ^bFree energy difference between the two most stable conformers of radicals **5–12** resulting from IRC calculations. ^cFree energies of the competitive 1,5- and 1,6-hydrogen atom transfers are given relative to the most stable conformer. ^d $\Delta\Delta G^\ddagger = \Delta G^\ddagger_{(1,5\text{-H})} - \Delta G^\ddagger_{(1,6\text{-H})}$. $X_a/X_b = e^{-\Delta\Delta G^\ddagger/RT}$ is the product ratio resulting from the competitive 1,5- and 1,6-hydrogen atom transfers. ^e $\Delta\Delta G_0 = \Delta G_{0(1,5\text{-H})} - \Delta G_{0(1,6\text{-H})}$.

5→5a/9→9a, 6→6a/10→10a, 7→7a/11→11a, 8→8a/12→12a, shows that the stabilization energy of radicals bearing a *N*-Ts group at nitrogen is lower than that of radicals bearing a *N*-Me group by 5.9 to 10.9 kcal/mol. However, it is difficult to estimate the relative contribution of electronic and steric effects.²⁴

In agreement with Hammond's postulate,²⁵ the activation free energy is influenced by the reaction exergonicity. In Marcus formalism,²⁶ the activation free energy (ΔG^\ddagger) is the sum of an intrinsic activation free energy (ΔG_i^\ddagger) and a thermodynamic contribution including the reaction free enthalpy (ΔG_0) (Figure 2). The intrinsic barrier represents

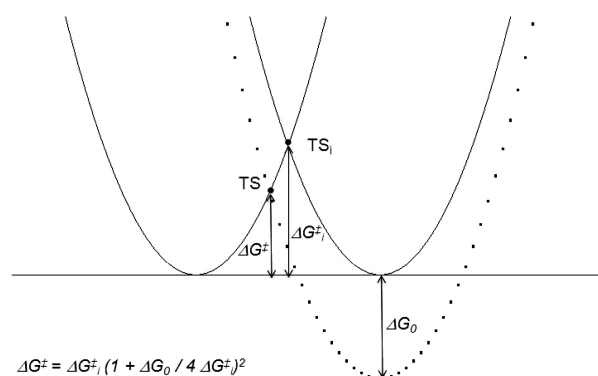


Figure 2. Relationships between ΔG_0 , ΔG^\ddagger , and ΔG_i^\ddagger in Marcus formalism.

pure transition states effects for thermoneutral process. The thermodynamic contribution lowers the activation free energy for exergonic processes, or conversely increases the activation free energy for endergonic reactions.

The values of the intrinsic barriers (ΔG_i^\ddagger) clearly indicate that 1,6-hydrogen shift should be largely favored over 1,5-hydrogen shift in nearly all cases but radicals **11** and **12**, for which a competition should be expected between the two reactions. The exergonicity driving force is responsible for the lowering of the activation free energy and for the exclusive preference for 1,5-H shift predicted in the case of radicals **5–9**.

Due to the higher exergonicity of the process, the transition state of 1,5-H migration is earlier than that of 1,6-H shift, which should alleviate steric crowding. The C–H distances in the corresponding transition structures are given in Table 2, where *L* (eq 22) is a measure of the precocity of the transition state.²⁷ As expected in the alanine series, the transition state for 1,5-H shift is much earlier than the transition state for 1,6-H shift; the difference in *L* parameters is less pronounced in the valine series.

$$L = \frac{d(\text{C}\cdots\text{H})^\ddagger - d(\text{C}\cdots\text{H})_{\text{rad}}}{d(\text{C}_{\text{Ar}}\cdots\text{H})^\ddagger - d(\text{C}_{\text{Ar}}\cdots\text{H})_{\text{product}}} \quad (22)$$

Calculations suggest that the nature of the substituent at nitrogen has a determining influence on the kinetics of the two competitive reactions. In the case of *N*-tosyl derivatives the situation becomes strongly dependent on the nature of the amino ester moiety. In the alanine series (radicals **9** and **11**), whatever the structure of the radical (aryl or 1-naphthyl), and even though 1,6-H shift remains intrinsically favored (ΔG_i^\ddagger in Table 1), 1,5-H shift is much faster owing to the high exergonicity of this process (ΔG^\ddagger and ΔG_0 in Table 1).

Table 2. Calculated C–H Distances (in Å) in the Transition States for 1,5- And 1,6-translocations of radicals **5–12** at the UB3LYP/6-311++G(3df,3pd)//(UB3LYP/6-31G(d) Level at 298 K

reaction	$d(\text{C}\cdots\text{H})$	$d(\text{C}-\text{H})$ (substrate)	$d(\text{C}_{\text{Ar}}\cdots\text{H})$	$d(\text{C}_{\text{Ar}}-\text{H})$ product	<i>L</i>
5→5a	1.234	1.097	1.505	1.086	0.327
5→5b	1.286	1.104	1.399	1.087	0.583
6→6a	1.228	1.097	1.515	1.087	0.306
6→6b	1.249	1.097	1.468	1.085	0.397
7→7a	1.232	1.096	1.509	1.087	0.322
7→7b	1.286	1.094	1.401	1.087	0.611
8→8a	1.224	1.097	1.520	1.089	0.295
8→8b	1.254	1.097	1.467	1.086	0.412
9→9a	1.231	1.098	1.503	1.088	0.320
9→9b	1.291	1.094	1.395	1.087	0.640
10→ 10a	1.238	1.099	1.482	1.087	0.352
10→ 10b	1.255	1.097	1.451	1.088	0.435
11→ 11a	1.227	1.098	1.501	1.089	0.313
11→ 11b	1.289	1.094	1.399	1.088	0.627
12→ 12a	1.24	1.098	1.482	1.088	0.360
12→ 12b	1.247	1.098	1.460	1.088	0.404

In these cases, 1,6-H shift is disfavored not only enthalpically but also entropically. The difference in activation entropy between six- and seven-membered ring transition states varies between 0.4–2.8 cal/mol/K, which corresponds to 0.12–0.83 kcal/mol at 298 K.

The situation is completely reversed in the valine series (radicals **10** and **12**), since the exergonicities of the two processes become similar. According to calculations, for these radicals 1,6-H shift should be favored and moreover be the only pathway, which is attested by the experimental results obtained from **1b**. By opposition to radicals **9** and **11**, in the cases of radicals **10** and **12**, 1,6-H shift is favored both enthalpically and entropically.

The reaction profiles and geometries of transition states for the competitive evolutions of radical **11** and **12** are given in Figures 3 and 4, respectively. Figure 4 gives clear evidence that the bulky substituent attached to nitrogen controls the preferred conformation of radical **12** and contributes to increase the activation free energy of 1,5-hydrogen shift.

The main differences in torsional interactions around C–N and C–S single bonds are illustrated in Figure 5. The simple examination of the main torsional angles accounts for the higher energy of the conformer predisposed to 1,5-H transfer.

Experimental Evidence for the Influence of *N*-Tosyl Group. In order to test the validity of the theoretical prediction, enediyne (\pm)-**13** was prepared from *N*-methylvaline methyl ester. The difficulties in preparing strictly the *N*-methyl analogue of **1b** led us to use the strategy recently devised using one-pot Crabbé homologation/tandem enynyne–allene (\pm)-**14** rearrangement.⁶ The experimental results are reported in Scheme 2.

The one-pot multistep reaction led to a mixture of products (\pm)-**15** (28%) and (\pm)-**16** (25%), resulting from exclusive 1,5-H shift but from both the captodative position and the methyl group. Despite the reaction enthalpy is in favor of hydrogen

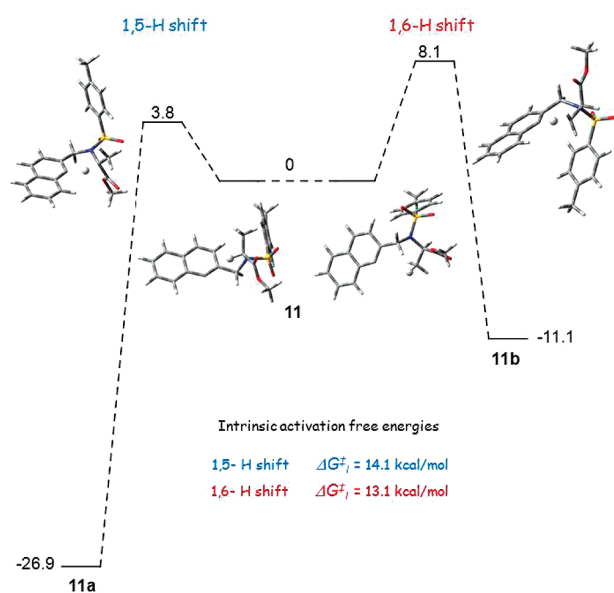


Figure 3. Competitive reaction pathways for the translocation of radical 11 (activation free energies and exergonicities in kcal/mol).

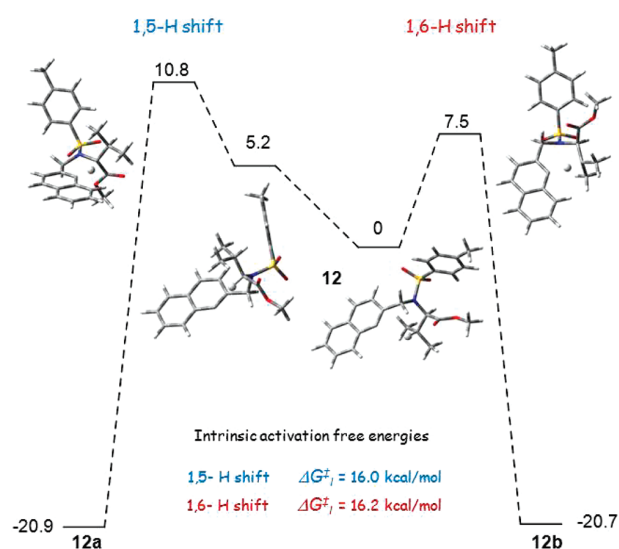


Figure 4. Competitive reaction pathways for the translocation of radical 12 (activation free energies and exergonicities in kcal/mol).

abstraction from the captodative position, hydrogen abstraction from the methyl group competes. It is enhanced by the statistic factor (3H/1H) and probably by steric effects. Side products resulting from oxidative degradation were detected in the crude mixture that could not be quantified nor identified. These data confirmed the dramatic incidence of the methyl group on the fate of diradical D the isolated products resulted from 1,5-H shift in agreement with theoretical predictions made for radical 8 (Chart 1, eqs 12 and 13, and Table 1). The additional incidence of the absence of substituent at the benzylic radical center, contributes to an important slowing down of the disproportionation pathway. No product resulting from disproportionation was isolated or detected in the crude mixture.⁶

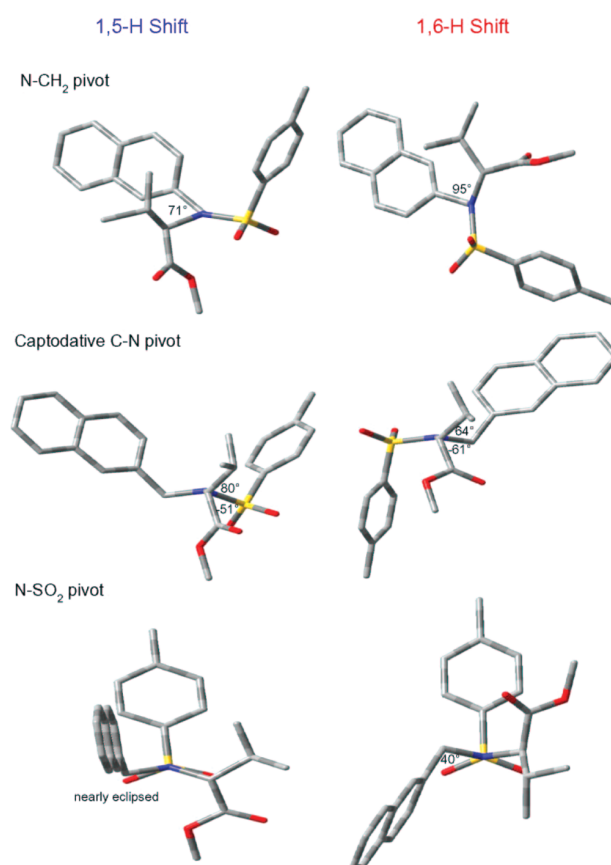
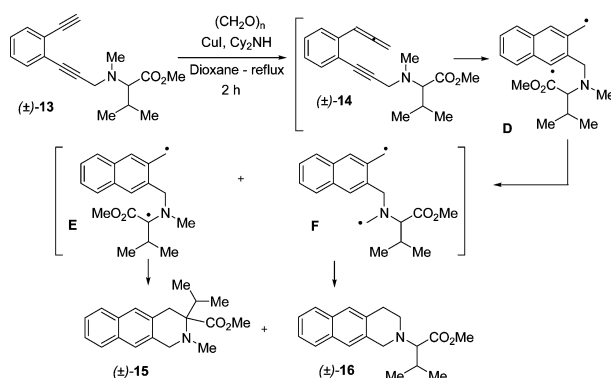


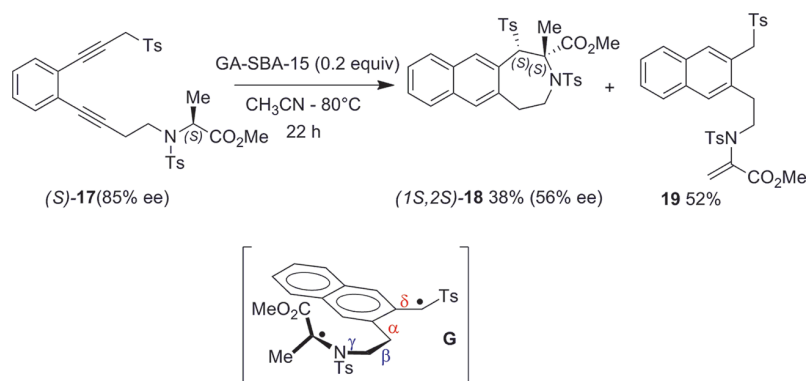
Figure 5. Compared torsional interactions around the two C–N and the C–S bonds in the two reactive conformers of radical 12 (on the left, views of the conformer predisposed for 1,5-H shift; on the right, views of the conformer predisposed to 1,6-H shift. Hydrogen atoms were removed for the sake of clarity).

Scheme 2. Tandem Crabbe Homologation/Rearrangement of (\pm)-13

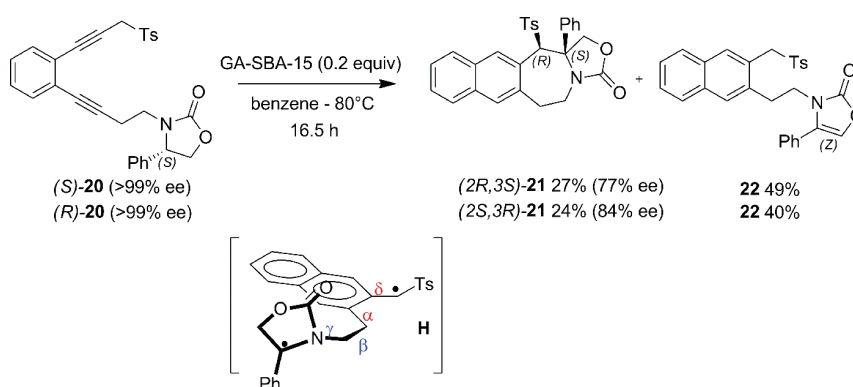


Cascade Rearrangements Leading to Naphthoazepines. The availability of tricyclic products resulting from 1,6-hydrogen shift should be reinforced by favorable enthalpic factors. Thus, in the absence of any competitive 1,5-H shift, the enantioselective synthesis of seven-membered ring cyclic amino esters bearing a quaternary stereogenic center was an obvious application of the methodology.

Homopropargylic aminoester (*S*)-17 (85% ee) was prepared from (*S*)-*N*-tosylalanine methyl ester. Submitted to the action

Scheme 3. Cyclization of (*S*)-17

Scheme 4. Rearrangement of 4



of GA-SBA-15, (*S*)-17 led to (*1S,2S*)-18 in 38% yield and 56% ee (Scheme 3).²⁸ The major product 19 resulted again from disproportionation.

In spite of the increased number of rotational degrees of freedom in the side chain bearing the reactive captodative center in biradical **G** and as this radical center (issued this time from 1,6-hydrogen transfer) was formed in a chiral conformation, memory of chirality was still observed. This means that recombination via rotation around the two single bonds adjacent to the aromatic system, i.e., bonds α and δ , remained the fastest pathway. Naphtho-azepine **18** was isolated as a single isomer in 56% ee.²⁹

In order to suppress any competitive disproportionation, attempts to synthesize optically pure enediyne derived from phenyl glycine failed, and only the racemic starting material could be obtained (this is due to the acidity of the proton in the benzylic captodative position).

In order to overcome the increased acidity of the proton in the synthesis of the enediyne substrate, and at the same time to improve the level of memory of chirality by reducing the conformational flexibility, enediyne (*S*)- and (*R*)-**20** were prepared from the oxazolidinones derived from (*S*)- and (*R*)-phenyl glycinols, respectively. The results are shown in Scheme 4. Previous studies had shown that the tetracyclic sulfones derived from these oxazolidinones were easily epimerized in acetonitrile. Therefore, the rearrangement of **20** was achieved under different experimental conditions, and benzene was first selected as the most suitable solvent to minimize the possible epimerization of the *cis* and *trans* isomers of product **21**.³⁰

Much to our disappointment, the increased flexibility of the side chain promoted a disproportionation, that is, hydrogen

migration from the position α to oxygen in the oxazolidinone ring to the benzylic radical center leading to **22** in 40 or 49% yield. The reaction is enantioselective, oxazepin **21** was obtained as a single diastereomer in 24% yield and 84% ee from (*R*)-**20** and its enantiomer was isolated in 27% yield and 77% ee from (*S*)-**20**.²⁹

The high ee provides an indirect proof that the rotations around the non benzylic C–C and C–N single bonds β and γ are still hindered as compared to rotation around bond α in diradical **H**. However, this investigation showed that the increased flexibility in the side chain enables disproportionation pathways that were not observed in experiments performed on the previous set of homologous propargylic substrates, undergoing the closure of six-membered rings in the last elementary step of the cascade rearrangement.¹ This is a severe limitation to the yield in enantio-enriched naphthoazepines that could be prepared according to this pathway.

CONCLUSION

In summary, the cascade rearrangement of enediynes of type **1**, starting with 1,3-proton shift immediately followed by Saito–Myers cyclization, was shown to evolve via exclusive 1,5- or 1,6-hydrogen shift depending on the structure of the starting material. Computational data confirmed these kinetic preferences. The dramatic influence of the substituent attached to the nitrogen atom of the amino ester moiety was emphasized. In the alanine derivative **1a**, exclusive 1,5-hydrogen abstraction of the hydrogen atom in captodative position is well accounted for by the incidence of the greater exergonicity of this process as compared to 1,6-hydrogen shift from the methyl group.

Conversely, the “exclusive” kinetic preference for 1,6-hydrogen abstraction over 1,5-migration of the hydrogen atom in captodative position, observed in the rearrangement of the valine derivative **1b**, is quite unexpected. It is the bulky tosyl group attached to nitrogen which contributes to increase the activation free energy of 1,5-hydrogen shift. This is rationalized, according to theoretical calculations, by the higher energy of the conformation that must be reached for model radical **12** to be ready to transfer the hydrogen atom from the captodative position. The validity of calculations was confirmed by the rearrangement of *rac*-enediynes **13**.

The ready occurrence of 1,6-hydrogen transfer was tentatively exploited, with compounds where no competitive 1,5-hydrogen shift is available, to achieve the enantioselective synthesis of naphthoazepines based on the phenomenon of memory of chirality. The main drawback is that, whenever possible without introducing torsional constraints, disproportionation becomes the major pathway with respect to recombination in the last elementary step.

EXPERIMENTAL SECTION

Rearrangement of (S)-1b. A solution of (S)-**1b** (95 mg, 0.16 mmol) and GA-SBA-15 (23 mg, 0.03 mmol) in CH₃CN (10 mL) was stirred for 18 h at 80 °C. Then the solvent was removed in vacuo, and the residue was purified by flash chromatography on silica gel (pentane/Et₂O, 90/10 to 50/50). This led to **4b** (63 mg, 66%) as a yellow oil.

Methyl (2S)-3-Methyl-2-[N-[[3-[[4-methylbenzene)sulfonyl]methyl]naphthalen-2-yl)methyl](4-methylbenzene)sulfonamido]but-2-enoate (4b). ee > 99% (Chiralpak IA, hexane/EtOH 70/30, 1 mL/min, *t_R*(R) = 11.44 min, *t_R*(S) = 12.69 min, *k*(R) = 2.81, *k*(S) = 3.23, α = 1.15, R_S = 1.74). [α]_D²⁵ +29 (c 1.7, CHCl₃). HRMS (ESI): *m/z* calcd for [M + NH₄]⁺ C₃₂H₃₇N₂O₆S₂ 609.2088, found 609.2091. ¹H NMR (400 MHz, CDCl₃) δ: 7.92 (1H, s), 7.71–7.69 (1H, br d, *J* = 8.2), 7.64–7.62 (1H, br d, *J* = 7.5), 7.54 (2H, d, *J* = 8.0), 7.51 (2H, d, *J* = 8.0), 7.47–7.40 (2H, m), 7.39 (1H, s), 7.23 (2H, d, *J* = 8.0), 7.16 (2H, d, *J* = 8.0), 5.07 (1H, s), 4.81 (1H, s), 4.74 (1H, s), 4.66 (2H, s), 4.62 (1H, d (A part of AB pattern), *J* = 14.3), 4.55 (2H, d (B part of AB pattern), *J* = 14.3), 3.43 (3H, s), 2.43 (3H, s, CH₃), 2.36 (3H, s), 1.58 (3H, s). ¹³C NMR (100 MHz, CDCl₃) δ: 170.0, 144.9, 143.7, 138.8, 136.7, 135.4, 134.2, 133.1, 132.2, 132.1, 129.9, 129.7 (2 × C), 129.4 (2 × C), 128.9 (2 × C), 127.8, 127.5, 127.4 (2 × C), 126.8, 126.4, 124.6, 117.4, 64.4, 60.0, 52.0, 46.3, 21.8, 21.6, 21.5.

Methyl 3-Methyl-2-[N-[[3-[[4-methylbenzene)sulfonyl]methyl]naphthalen-2-yl)methyl](4-methylbenzene)sulfonamido]but-2-enoate (3b). A solution of (S)-**4b** (67 mg, 0.11 mmol) and GA-SBA-15 (160 mg, 0.23 mmol) in CH₃CN (7 mL) was stirred for 7 days at 80 °C. Then the mixture was filtered and washed with dichloromethane. The solvent was removed in vacuo, and the residue was purified by flash chromatography on silica gel (pentane/Et₂O, 80/20 to 40/60). This led to **3b** (47 mg, 70%) as a yellow oil. HRMS (ESI): *m/z* calcd for [M + NH₄]⁺ C₃₂H₃₇N₂O₆S₂ 609.2088, found 609.2087. ¹H NMR (400 MHz, CDCl₃) δ: 7.89 (2H, d, *J* = 8.3), 7.79–7.69 (5H, m), 7.53–7.44 (2H, m), 7.39 (1H, s), 7.35 (4H, d, *J* = 8.0), 5.54 (1H, d, *J* = 13.8), 5.38 (1H, d, *J* = 13.8), 4.38 (1H, d, *J* = 13.5), 4.31 (1H, d, *J* = 13.8), 4.31 (3H, s), 2.47 (3H, s), 2.46 (3H, s), 1.87 (3H, s), 1.31 (3H, s). ¹³C NMR (100 MHz, CDCl₃) δ: 164.9, 160.04, 144.9, 143.53, 136.6, 136.5, 133.3, 133.06, 133.00, 132.1, 132.0, 129.9 (2 × C), 129.5 (2 × C), 128.8 (2 × C), 128.0 (2 × C), 127.9, 127.6, 127.1, 126.9, 125.4, 121.4, 59.1, 51.1, 50.9, 23.8, 22.0, 21.8, 21.7.

Rearrangement of (rac)-d1-1a. A solution of (rac)-**d1-1a** (183 mg, 0.32 mmol) and GA-SBA-15 (46 mg, 0.06 mmol) in CH₃CN (18 mL) was stirred for 15 h at 80 °C. Then the solvent was removed in vacuo, and the residue was purified by flash chromatography on silica gel (dichloromethane/Et₂O, 100/00 to 99/1). This led to three products, (3S*, 4R*)-**d1-2a** (73 mg, 40%, 75% deuterium labeling),

(3S*, 4S*)-**d1-2a** (63 mg, 35%, 81% deuterium labeling), and **d1-3a** (38 mg, 21%, 75% deuterium labeling).

Methyl (3S*, 4R*)-3-Methyl-2,4-bis[[4-methylbenzene)sulfonyl](10-²H)-1H,2H,3H,4H-benzo[*g*]isoquinoline-3-carboxylate (d1-2a). HRMS (ESI): *m/z* calcd for [M + NH₄]⁺ C₃₀H₃₂DN₂O₆S₂ 582.1837, found 582.1833. ¹H NMR (400 MHz, CDCl₃) δ: 7.85 (2H, d, *J* = 8.3), 7.73 (1H, br d, *J* = 8.8), 7.59 (1H, br d, *J* = 7.8), 7.50–7.40 (2.25H, dt (2H) plus superimposed residual s (0.25H)), 7.33–7.26 (5H, m (s superimposed to two d)), 7.08 (2H, d, *J* = 7.9), 4.89 (1H, d, *J* = 15.3, A part of an AB pattern), 4.73 (1H, s), 4.63 (1H, d, *J* = 15.1, B part of an AB pattern), 3.15 (3H, s), 2.42 (3H, s), 2.39 (3H, s), 2.34 (3H, s). ²H NMR (61.4 MHz, acetone) δ: 7.73 (br s).

Methyl (3S*, 4S*)-3-Methyl-2,4-bis[[4-methylbenzene)sulfonyl](10-²H)-1H,2H,3H,4H-benzo[*g*]isoquinoline-3-carboxylate (d1-2a). HRMS (ESI): *m/z* calcd for [M + NH₄]⁺ C₃₀H₃₂DN₂O₆S₂ 582.1837, found 582.1835. ¹H NMR (400 MHz, CDCl₃) δ: 7.99 (2H, d, *J* = 8.3), 7.77 (1H, d, *J* = 7.9), 7.57 (0.19H, s, residual CH₂), 7.54–7.46 (1H, m), 7.43 (2H, m), 7.33 (1H, d, *J* = 8.1), 7.36–7.29 (1H, m), 7.25 (2H, d, *J* = 8.1), 7.00 (2H, d, *J* = 8.1), 6.86 (1H, s), 4.60 (2H, br s), 4.50 (1H, s), 4.01 (3H, s), 2.44 (3H, s), 2.33 (3H, s), 1.76 (3H, s). ²H NMR (61.4 MHz, acetone) δ: 7.85 (br s).

Methyl 2-[N-[[3-[[4-methylbenzene)sulfonyl](²H)₃]methyl]naphthalen-2-yl)methyl](4-methylbenzene)sulfonamido](²H)₂-prop-2-enoate (d1-3a). HRMS (ESI): *m/z* calcd for [M + NH₄]⁺ C₃₀H₃₂DN₂O₆S₂ 582.1837, found 582.1840. ¹H NMR (400 MHz, CDCl₃) δ: 7.88 (2H, d, *J* = 8.3), 7.77 (1H, s), 7.74 (2H, d, *J* = 8.3), 7.79–7.64 (2H, superimposed m), 7.50–7.44 (2H, m), 7.43 (0.25H, residual s), 7.37–7.32 (4H, 2 × d, *J* = 8.1), 6.14 (1H, s), 5.44 (1H, s), 4.84 (2H, s), 4.77 (2H, s), 3.53 (3H, s), 2.48 (3H, s), 2.47 (3H, s). ²H NMR (61.4 MHz, acetone) δ: 7.75 (br s).

Rearrangement of (rac)-d1-1b. Monodeuterated (rac)-**d1-4b** was prepared according to the procedure already described for the synthesis of **4b**, using (rac)-**d1-1b** (101 mg, 0.17 mmol) and GA-SBA-15 (24 mg, 0.03 mmol) in CH₃CN (10 mL). The reaction mixture was stirred for 18 h at 80 °C. After workup, purification by liquid chromatography on silica gel (pentane/Et₂O, 70/30 to 60/40) led to (rac)-**d1-4b** (66 mg, 65% yield, and 83% deuterium labeling) as a yellow oil.

(rac)-Methyl 3-methyl-2-[N-[[3-[[4-methylbenzene)sulfonyl]methyl]naphthalen-2-yl)methyl](4-methylbenzene)sulfonamido](²-H)but-3-enoate (d1-4b). HRMS (ESI): *m/z* calcd for [M + NH₄]⁺ C₃₂H₃₆DN₂O₆S₂ 610.2150, found 610.2136. ¹H NMR (400 MHz, CDCl₃) δ: 7.92 (1H, s), 7.71–7.69 (1H, m), 7.64–7.62 (1H, m), 7.53 (2H, d, *J* = 8.3), 7.51 (2H, d, *J* = 8.3), 7.47–7.40 (2H, m), 7.39 (1H, s), 7.23 (2H, d, *J* = 8.0), 7.16 (2H, d, *J* = 8.0), 5.07 (0.16H, residual s), 4.81 (1H, s), 4.74 (1H, s), 4.66 (2H, s), 4.62 (1H, d (A part of AB pattern), *J* = 14.3), 4.55 (2H, d (B part of AB pattern), *J* = 14.3), 3.43 (3H, s), 2.43 (3H, s), 2.36 (3H, s), 1.58 (3H, s). ²H NMR (61.4 MHz, acetone) δ: 5.08 (br s).

Rearrangement of (rac)-d3-1a. A solution of (rac)-**d3-1a** (200 mg, 0.35 mmol) and GA-SBA-15 (50 mg, 0.07 mmol) in CH₃CN (20 mL) was stirred for 15 h at 80 °C. Then the solvent was removed in vacuo, and the residue was purified by flash chromatography on silica gel (pentane/dichloromethane, 50/50 to 80/20). This led to three products, (3S*, 4R*)-**d3-2a** (90 mg, 45%, 100% deuterium labeling), (3S*, 4S*)-**d3-2a** (77 mg, 38%, 100% deuterium labeling), and **d3-3a** (20 mg, 10%, 100% deuterium labeling).

Methyl (3S, 4R)-3-(²H)₃Methyl-2,4-bis[[4-methylbenzene)sulfonyl]-1H,2H,3H,4H-benzol[*g*]isoquinoline-3-carboxylate (d3-2a). HRMS (ESI): *m/z* calcd for [M + NH₄]⁺ C₃₀H₃₀D₃N₂O₆S₂ 584.1963, found 584.1958. ¹H NMR (400 MHz, CDCl₃) δ: 7.87 (2H, d, *J* = 8.3), 7.75 (1H, br d, *J* = 7.9), 7.61 (1H, br d, *J* = 7.6), 7.50 (1H, s), 7.50–7.40 (2H, m), 7.33–7.26 (5H, m (s superimposed to two d)), 7.08 (2H, d, *J* = 7.9), 4.91 (1H, d, *J* = 15.3, A part of an AB pattern), 4.74 (1H, s), 4.63 (1H, d, *J* = 15.1, B part of an AB pattern), 3.17 (3H, s), 2.40 (3H, s), 2.37 (3H, s). ²H NMR (61.4 MHz, acetone) δ 2.34 (br s).

Methyl (3S, 4S)-3-(²H)₃Methyl-2,4-bis[[4-methylbenzene)sulfonyl]-1H,2H,3H,4H-benzol[*g*]isoquinoline-3-carboxylate

(d3-2a). HRMS (ESI): m/z calcd for $[M + NH_4]^+ C_{30}H_{30}D_3N_2O_6S_2$ 584.1963, found 584.1958. 1H NMR (400 MHz, $CDCl_3$) δ : 7.99 (2H, d, $J = 8.3$), 7.77 (1H, d, $J = 7.9$), 7.57 (1H, s), 7.54–7.46 (1H, m), 7.45–7.40 (2H, m), 7.33 (2H, d, $J = 8.1$), 7.25 (2H, d, $J = 8.3$), 7.00 (2H, d, $J = 8.1$), 6.87 (1H, s), 4.60 (2H, br s), 4.50 (1H, s), 4.01 (3H, s), 2.44 (3H, s), 2.33 (3H, s). 2H NMR (61.4 MHz, acetone) δ 1.67 (br s).

Methyl 2-*N*-[3-[[4-(4-methylbenzene)sulfonyl]-(2H_1)methyl]naphthalen-2-yl)methyl](4-methylbenzene)sulfonamido]-(2H_2)-prop-2-enoate (d3-3a). HRMS (ESI): m/z calcd for $[M + NH_4]^+ C_{30}H_{30}D_3N_2O_6S_2$ 584.1963, found 584.1961. 1H NMR (400 MHz, $CDCl_3$) δ : 7.88 (2H, d, $J = 8.3$), 7.77 (1H, s), 7.77–7.72 (3H, superimposed m), 7.69–7.64 (1H, m), 7.52–7.45 (2H, m), 7.43 (1H, s), 7.37–7.32 (4H, 2 superimposed d, $J = 8.1$), 4.84 (1H, s), 4.77 (2H, s), 3.53 (3H, s), 2.48 (3H, s), 2.47 (3H, s). 2H NMR (61.4 MHz, acetone) δ : 6.15 (br s), 5.63 (br s), 5.00 (br s).

Rearrangement of (\pm)-13. (CH_2O)_n (26 mg, 0.88 mmol), CuI (34 mg, 0.18 mmol), 1,4-dioxane (1 mL), enediyne (\pm)-13 (100 mg, 0.35 mmol), and dicyclohexylamine (115 mg, 0.63 mmol) were added sequentially into a flask equipped with a reflux condenser under an argon atmosphere. The resulting mixture was stirred at reflux for 2 h. Solvent was evaporated under vacuo, the residue was dissolved in DCM and filtered over a short pad of Celite, and the filtrate was concentrated and purified by column chromatography on silica gel using pentane/Et₂O (95:5 to 90:10) as eluent to afford (\pm)-15 (29 mg, 28%) and (\pm)-16 (26 mg, 25%).

Methyl 2-Methyl-3-(propan-2-yl)-1*H*,2*H*,3*H*,4*H*-benzo[*g*]isoquinoline-3-carboxylate (\pm)-15. HRMS (ESI): m/z calcd for $[M + H]^+ C_{19}H_{24}NO_2$ 298.1802, found 298.1801. 1H NMR (400 MHz, $CDCl_3$) δ : 7.75–7.69 (2H, m), 7.62 (1H, s), 7.46 (1H, s), 7.40–7.33 (2H, m), 4.10 (1H, d (A part of AB pattern), $J = 16.3$), 3.77 (1H, d (B part of AB pattern), $J = 16.3$), 3.60 (3H, s), 3.31 (1H, d (A part of AB pattern), $J = 16.3$), 3.02 (1H, d (B part of AB pattern), $J = 16.3$), 2.58 (3H, s), 2.45 (1H, sept, $J = 6.8$), 1.06 (3H, d, $J = 6.8$), 1.00 (3H, d, $J = 6.8$). ^{13}C NMR (100 MHz, $CDCl_3$) δ : 173.8, 133.0, 132.6, 132.2, 132.0, 127.3, 127.2, 126.5, 125.2, 125.1, 124.0, 68.6, 55.3, 51.1, 38.2, 31.3, 29.8, 18.0, 16.6.

Methyl 2-[1*H*,2*H*,3*H*,4*H*-Benzo[*g*]isoquinolin-2-yl]-3-methylbutanoate (\pm)-16. HRMS (ESI): m/z calcd for $[M + H]^+ C_{19}H_{24}NO_2$ 298.1802, found 298.1803. 1H NMR (400 MHz, $CDCl_3$) δ : 7.74–7.69 (2H, m), 7.57 (1H, s), 7.50 (1H, s), 7.40–7.35 (2H, m), 4.00–3.90 (2H, AB pattern, $J_{AB} = 16.3$), 3.73 (3H, s), 3.10–3.02 (3H, m), 3.01 (1H, d, $J = 10.8$), 2.79 (1H, m), 2.27–2.16 (1H, m), 1.03 (3H, d, $J = 6.8$), 0.95 (3H, d, $J = 6.8$). ^{13}C NMR (100 MHz, $CDCl_3$) δ : 172.3, 134.2, 133.6, 132.4, 132.0, 127.3, 127.2, 126.8, 125.3, 125.3, 124.6, 74.4, 53.3, 50.8, 47.2, 30.4, 27.3, 20.0, 19.5.

Rearrangement of (S)-17. Compound (S)-17 (100 mg, 0.17 mmol) and GA-SBA-15 (24 mg, 0.03 mmol) were dissolved in CH_3CN (10 mL). The mixture was heated at 80 °C for 22 h. Then the solvent was removed in vacuo, and the residue was purified by flash chromatography on silica gel (pentane/dichloromethane, 50/50 to 0/100). This led to (1*S*,2*S*)-18 (38 mg, 38%) as a yellow oil and 19 (52 mg, 52%) as a yellow oil.

Methyl (1*S*,2*S*)-2-Methyl-1,3-bis[4-(4-methylbenzene)sulfonyl]-1*H*,2*H*,3*H*,4*H*,5*H*-naphtho[2,3-*d*]azepine-2-carboxylate (18). ee = 56% (Chiralpak IC, hexane/EtOH 50/50, 1 mL/min, $t_R(1*S*,2*S*) = 15.80$ min, $t_R(1*S*,2*S*) = 28.43$ min, $k(1*R*,2*R*) = 4.27$, $k(1*R*,2*S*) = 8.45$, $\alpha = 1.98$, $R_S = 7.05$). $[\alpha]_D^{25} +23$ (c 0.6, $CHCl_3$). HRMS (ESI): m/z calcd for $[M + NH_4]^+ C_{31}H_{35}N_2O_6S_2$ 595.1931, found 595.1928. 1H NMR (400 MHz, $CDCl_3$) δ : 7.73 (1H, d, $J = 8.0$), 7.62 (1H, s), 7.47 (2H, d, $J = 8.3$), 7.41 (1H, dt, $J = 1.0$ and 6.8), 7.33–7.29 (3H, m), 7.22 (1H, d, $J = 8.0$), 7.11 (2H, d, $J = 8.0$), 7.05 (2H, d, $J = 8.0$), 6.68 (1H, s), 5.95 (1H, s), 4.11 (1H, ddd, $J = 6.8$, 11.8 and 14.8), 3.92–3.80 (2H, m), 3.62 (3H, s), 3.00 (1H, ddd, $J = 1.8$, 5.3 and 14.8), 2.55 (3H, s), 2.35 (3H, s), 2.32 (3H, s). ^{13}C NMR (100 MHz, $CDCl_3$) δ 172.5, 145.7, 142.8, 139.3, 136.2, 135.9, 135.7, 133.7, 131.7, 129.3, 129.3 (2 × C), 129.22 (2 × C), 129.21 (2 × C), 129.0, 127.7, 127.1, 126.8, 126.4 (2 × C), 125.7, 78.4, 66.6, 53.4, 45.4, 33.0, 23.3, 21.6, 21.5. The *cis* stereochemistry was assigned from 2D NMR experiments. The NOESY spectrum shows a clear cross-peak between

the signal of the proton at 5.95 ppm and the signal of the methyl protons at 2.55 ppm.

Methyl 2-*N*-[2-(3-[[4-(4-methylbenzene)sulfonyl]methyl]naphthalen-2-yl)ethyl](4-methylbenzene)sulfonamido]prop-2-enoate (19). HRMS (ESI): m/z calcd for $[M + NH_4]^+ C_{31}H_{35}N_2O_6S_2$ 595.1931, found 595.1928. 1H NMR (400 MHz, $CDCl_3$) δ : 7.73 (1H, d, $J = 8.0$), 7.69–7.66 (1H, m), 7.68 (1H, superimposed s), 7.66 (1H, superimposed s, CH_{ar}), 7.62 (2H, d, $J = 8.5$), 7.59 (2H, d, $J = 8.5$), 7.50–7.41 (2H, m), 7.26 (2H, d, $J = 8.0$), 7.23 (2H, d, $J = 8.0$), 6.44 (1H, s), 5.81 (1H, s), 4.49 (2H, br s), 3.65 (3H, s), 3.64–3.60 (2H, m), 2.97–2.93 (2H, m), 2.43 (3H, s), 2.43 (3H, s). ^{13}C NMR (100 MHz, $CDCl_3$) δ : 164.3, 145.0, 143.8, 136.0, 135.7, 135.2, 133.5, 132.6, 132.1, 129.8 (2 × C), 129.6 (2 × C), 129.2, 128.8, 128.7 (2 × C), 127.8 (2 × C), 127.7, 127.2, 127.0, 126.2, 124.8, 59.6, 52.6, 50.3, 32.5, 21.8, 21.7. One carbon is missing probably due to overlapping.

Rearrangement of (R)-20. (R)-20 (100 mg, 0.21 mmol) and GA-SBA-15 (29 mg, 0.04 mmol) were dissolved in benzene (10 mL). The mixture was heated at 80 °C for 16.5 h. The solvent was removed in vacuo, and the residue was purified by flash chromatography on silica gel (pentane/AcOEt, 80/20 to 50/50). This led to (2*S*,3*R*)-21 (24 mg, 24%) as a yellow amorphous solid and 22 (40 mg, 40%) as a yellow amorphous solid.

(2*S*,3*R*)-2-[[4-(4-methylbenzene)sulfonyl]-3-phenyl-5-oxa-7-azatetracyclo[8.8.0.0^{3,7}.0^{12,17}]octadeca-1(18),10,12(17),13,15-pentaen-6-one (21). ee = 84% (Chiralpak IB, hexane/EtOH/chloroform 60/30/10, 1 mL/min, $t_R(2*S*,3*R*) = 6.56$ min, $t_R(2*R*,3*S*) = 8.21$ min, $k(2*S*,3*R*) = 1.19$, $k(2*R*,3*S*) = 1.68$, $\alpha = 1.41$ and $R_S = 2.70$). $[\alpha]_D^{25} -103$ (c 0.48, $CHCl_3$). HRMS (ESI): m/z calcd for $[M + NH_4]^+ C_{29}H_{29}N_2O_4S$ 501.1843, found 501.1842. 1H NMR (400 MHz, $CDCl_3$) δ : 7.59 (1H, d, $J = 8.0$), 7.43–7.23 (10H, m), 7.15 (1H, tt, $J = 8.3$ and 1.5), 6.98 (1H, s), 6.91 (2H, d, $J = 8.0$), 5.72 (1H, d, $J = 9.0$), 5.19 (1H, s), 4.40 (1H, ddd, $J = 14.3$, 7.3 and 2.8), 4.25 (1H, br t, $J = 14.0$), 4.07 (1H, d, $J = 9.0$), 3.26 (1H, pseudo t, $J = 13.0$), 2.80 (1H, br dd, $J = 15.3$ and 4.0), 2.12 (3H, s). ^{13}C NMR (100 MHz, $CDCl_3$) δ : 158.2, 144.9, 140.0, 138.1, 136.4, 135.8, 132.8, 131.4, 130.0, 129.5 (2 × C), 129.2 (2 × C), 128.8, 128.5 (2 × C), 128.3, 127.3, 127.0, 126.9, 126.1, 125.9 (2 × C), 77.8, 74.0, 67.7, 40.9, 35.8, 21.4. In full agreement with the Chem-3D model showing a π -stacking interaction, the stereochemistry was assigned from 2D NMR experiments. The NOESY spectrum shows a clear cross-peaks between the signal of the proton in position *alpha* to the tosyl group at 5.19 ppm and the *s* signal of one aromatic proton of the naphthyl group at 6.98 ppm and the *d* of one proton of the CH_2O group of the carbamate ring at 5.72 ppm.

3-[2-(3-[[4-(4-methylbenzene)sulfonyl]methyl]naphthalen-2-yl)ethyl]-4-phenyl-2,3-dihydro-1,3-oxazol-2-one (22). HRMS (ESI): m/z calcd for $[M + NH_4]^+ C_{29}H_{29}N_2O_4S$ 501.1843, found 501.1840. 1H NMR (400 MHz, $CDCl_3$) δ : 7.69–7.65 (2H, m), 7.54 (2H, d, $J = 8.3$), 7.51 (1H, s), 7.49–7.37 (6H, m), 7.23 (2H, d, $J = 8.3$), 7.13–7.09 (2H, m), 6.74 (1H, s), 4.28 (2H, s), 3.82–3.77 (2H, m), 2.96–2.91 (2H, m), 2.42 (3H, s). ^{13}C NMR (100 MHz, $CDCl_3$) δ : 156.1, 145.0, 135.5, 134.5, 133.5, 132.8, 132.2, 129.9, 129.8 (2 × C), 129.7, 129.4, 129.3 (2 × C), 128.8 (2 × C), 128.6 (2 × C), 127.8, 127.2, 127.1, 126.3, 126.3, 124.7, 123.9, 59.3, 43.0, 31.8, 21.8.

Rearrangement of (S)-20. (S)-20 (200 mg, 0.41 mmol) and GA-SBA-15 (58 mg, 0.08 mmol) were dissolved in benzene (20 mL). The mixture was heated at 80 °C for 16.5 h. The solvent was removed in vacuo, and the residue was purified by flash chromatography on silica gel (pentane/AcOEt, 80/20 to 50/50). This led to (2*R*,3*S*)-21 (54 mg, 27%) as a yellow amorphous solid and 22 (98 mg, 49%) as a yellow amorphous solid.

(2*R*,3*S*)-2-[[4-(4-methylbenzene)sulfonyl]-3-phenyl-5-oxa-7-azatetracyclo[8.8.0.0^{3,7}.0^{12,17}]octadeca-1(18),10,12(17),13,15-pentaen-6-one (21). ee = 77% (Chiralpak IB, hexane/EtOH/chloroform 60/30/10, 1 mL/min, $t_R(2*S*,3*R*) = 6.56$ min, $t_R(2*R*,3*S*) = 8.21$ min, $k(2*S*,3*R*) = 1.19$, $k(2*R*,3*S*) = 1.68$, $\alpha = 1.41$ and $R_S = 2.70$). $[\alpha]_D^{25} +118$ (c 0.45, $CHCl_3$).

■ ASSOCIATED CONTENT

● Supporting Information

Synthesis of starting materials, HPLC analyses, NMR spectra for all new compounds, and computational details. This material is available free of charge via the Internet at <http://pubs.acs.org>

■ AUTHOR INFORMATION

Corresponding Authors

*(A.G.S.) E-mail: anouk.siri@univ-cezanne.fr.

*(M.N.) E-mail: malek.nechab@univ-provence.fr.

*(M.P.B.) E-mail: michele.bertrand@univ-cezanne.fr.

Notes

The authors declare no competing financial interest.

■ ACKNOWLEDGMENTS

We thank the ANR (JCJC MOCER2) for financial support and the Université de Provence for the postdoctoral grant of Dr S. Mondal. This work was also supported by the computing facilities of the CRCMM.

■ REFERENCES

- (1) Nechab, M.; Campolo, D.; Maury, J.; Perfetti, P.; Vanthuyne, N.; Siri, D.; Bertrand, M. P. *J. Am. Chem. Soc.* **2010**, *132*, 14742–14744.
- (2) For selected examples of other cascade rearrangements of enediynes, following on from Bergman or Saito–Myers cyclizations, see: (a) Grissom, J. W.; Klingberg, D.; Huang, D.; Slattery, B. J. *J. Org. Chem.* **1997**, *62*, 603–626 and references therein. (b) Li, H.; Petersen, J. L.; Wang, K. K. *J. Org. Chem.* **2003**, *68*, 5512–5518. (c) Tarli, A.; Wang, K. K. *J. Org. Chem.* **1997**, *62*, 8841–8847. (d) Wang, K. K.; Wang, Z.; Tarli, A.; Gannett, P. J. *Am. Chem. Soc.* **1996**, *118*, 10783–10791. (e) Wang, K. K.; Zhang, H.-R.; Petersen, J. L. *J. Org. Chem.* **1999**, *64*, 1650–1656.
- (3) (a) Fujii, K.; Kawabata, T. *Chem.—Eur. J.* **1998**, *4*, 373–376. (b) Zhao, H.; Hsu, D. C.; Carlier, P. R. *Synthesis* **2005**, 1–16. (c) Kawabata, T.; Fujii, K. In *Topics in Stereochemistry*; Denmark, S. E., Ed.; Wiley and Sons, Inc.: New York, 2003; Vol. 23, pp 175–205.
- (4) For examples of disproportionation of biradicals, see: (a) Bucher, G.; Mahajan, A. A.; Schmittel, M. *J. Org. Chem.* **2009**, *74*, 5850–5860. (b) Choe, T.; Khan, S. I.; Garcia-Garibay, M. A. *Photochem. Photobiol. Sci.* **2006**, *5*, 449–451. (c) Wagner, P. J.; Laidig, G. *Tetrahedron Lett.* **1991**, *32*, 895–898. (d) Wagner, P. J.; Chiu, C. *J. Am. Chem. Soc.* **1979**, *101*, 7134–7135.
- (5) Nechab, M.; Besson, E.; Campolo, D.; Perfetti, P.; Vanthuyne, N.; Bloch, E.; Denoyel, R.; Bertrand, M. P. *Chem. Commun.* **2011**, *47*, 5286–5288.
- (6) Mondal, S.; Nechab, M.; Vanthuyne, N.; Bertrand, M. P. *Chem. Commun.* **2012**, *48*, 2549–2551.
- (7) For (3S*,4S*)-*d1-2a* the deuterated position gives rise to a residual s at 7.57 ppm (0.19H)/CHTs s at 4.50 ppm (1H). For (3S*,4R*)-*d1-2a* the deuterated position gives rise to a residual s superimposed to a m between 7.51 and 7.59 ppm (2.25H)/CHTs s at 4.72 ppm (1H). For *d1-3a* the deuterated position gives rise to a residual s at 7.43 ppm (0.25H)/=CH at 6.14 (1H) and 5.41 (1H), respectively.
- (8) For the competitive migration of H/D in Schmittel rearrangement, see: Bucher, G.; Mahajan, A. A.; Schmittel, M. *J. Org. Chem.* **2009**, *74*, 5950–5860.
- (9) For reviews, see: (a) Cekovic, Z. *J. Serb. Chem. Soc.* **2005**, *70*, 287–318. (b) Cekovic, Z. *Tetrahedron* **2003**, *59*, 8073. (c) Feray, L.; Kuznetsov, N.; Renaud, P. In *Radicals in Organic Synthesis*; Renaud, P., Sibi, M. P., Eds.; Wiley-VCH: Weinheim, 1998; Vol. 2, pp 246–278. (d) Togo, H. In *Advanced Free Radical Reactions for Organic Synthesis*; Elsevier: Oxford, 2004; pp 171–186.
- (10) (a) Dénès, F.; Beaufils, F.; Renaud, P. *Synlett* **2008**, 2389–2399. (b) Renaud, P.; Beaufils, F.; Dénès, F.; Imboden, C.; Kuznetsov, N. *Chimia* **2008**, *62*, 510–513. (c) Robertson, J.; Pillai, J.; Lush, R. K. *Chem. Soc. Rev.* **2001**, *30*, 94–103.
- (11) For examples of exclusive 1,6-hydrogen shift without possible competition of 1,5-hydrogen shift, see: (a) Gramain, J.-C.; Remuson, R.; Vallée, D. *J. Org. Chem.* **1985**, *50*, 710–712. (b) Furata, K.; Nagata, T.; Yamamoto, H. *Tetrahedron Lett.* **1988**, *29*, 2215–2218. (c) Kraus, G. A.; Chen, L. *J. Am. Chem. Soc.* **1990**, *112*, 3464–3466. (d) Bosch, E.; Bachi, M. D. *J. Org. Chem.* **1993**, *58*, 5581–5582. (e) Bogen, S.; Fensterbank, L.; Malacria, M. *J. Am. Chem. Soc.* **1997**, *119*, 5037–5038. (f) Manabe, T.; Yanagi, S.-I.; Ohe, K.; Uemura, S. *Organometallics* **1998**, *17*, 2942–2944. (g) Lin, H.; Schall, A.; Reiser, O. *Synlett* **2005**, 2603–2606. (h) Sakaguchi, N.; Hirano, S.; Matsuda, A.; Shuto, S. *Org. Lett.* **2006**, *8*, 3291–3294. (i) Yoshimura, Y.; Yamazaki, Y.; Wachi, K.; Satoh, S.; Takahata, H. *Synlett* **2007**, 111–114.
- (12) For competitive processes, see: (a) Ayer, W. A.; Law, D. A.; Piers, K. *Tetrahedron Lett.* **1964**, *5*, 2959–2963. (b) José, I. C.; Francisco, C. G.; Hernández, R.; Salazar, J. A.; Suárez, E. *Tetrahedron Lett.* **1984**, *25*, 1953–1956. (c) McDonald, C. E.; Beebe, T.; Beard, M.; McMillen, D.; Selski, D. *Tetrahedron Lett.* **1989**, *30*, 4791–4794. (d) Bogen, S.; Fensterbank, L.; Malacria, M. *J. Org. Chem.* **1999**, *64*, 819–825. (e) Wille, U. *Chem.—Eur. J.* **2002**, *8*, 340–347. (f) Wille, U. *J. Am. Chem. Soc.* **2002**, *124*, 14–15. (g) Wille, U.; Heuger, G.; Jargstorff, C. *J. Org. Chem.* **2008**, *73*, 1413–1421 and previous references cited therein. (h) Harrowen, D. C.; Stenning, K. J.; Whiting, S.; Thompson, T.; Walton, R. *Org. Biomol. Chem.* **2011**, *9*, 4882–4885. (i) Francisco, C. G.; Freire, R.; Herrere, A. J.; Pérez-Martín, I.; Suárez, E. *Tetrahedron* **2007**, *63*, 8910–8920.
- (13) (a) Curran, D. P.; Kim, D.; Liu, H. T.; Shen, W. *J. Am. Chem. Soc.* **1988**, *110*, 5900–5902. (b) Snieckus, V.; Cuevas, J.-C.; Sloan, C. P.; Liu, H.; Curran, D. P. *J. Am. Chem. Soc.* **1990**, *112*, 896–898. (c) Curran, D. P.; Somayajula, K. V.; Yu, H. *Tetrahedron Lett.* **1992**, *33*, 2295–2298. (d) Curran, D. P.; Shen, W. *J. Am. Chem. Soc.* **1993**, *115*, 6051–6059. (e) Yamasaki, N.; Eichenberger, E.; Curran, D. P. *Tetrahedron Lett.* **1994**, *35*, 6623–6626. (f) Curran, D. P.; Xu, J. Y. *J. Am. Chem. Soc.* **1996**, *118*, 3142–3147. (g) Curran, D. P.; Liu, W.; Chen, C. H.-T. *J. Am. Chem. Soc.* **1999**, *121*, 11012–11013.
- (14) (a) Denenmark, D.; Hoffmann, P.; Winkler, T.; Waldner, A.; De Mesmaeker, A. *Synlett* **1991**, 621–624. (b) Denenmark, D.; Winkler, T.; Waldner, A.; De Mesmaeker, A. *Tetrahedron Lett.* **1992**, *33*, 621–624.
- (15) (a) Dorigo, A. E.; Houk, K. N. *J. Am. Chem. Soc.* **1987**, *109*, 2195–2197. Conversely, in Norrish II photochemical reactions, 1,5-hydrogen transfer would be favored over 1–6 hydrogen migration by both enthalpic and entropic factors, see: (b) Dorigo, A. E.; McCarrick, M. A.; Loncharic, R. J.; Houk, K. N. *J. Am. Chem. Soc.* **1990**, *112*, 7508–7514.
- (16) Rey, V.; Pierini, A.; Peññory, A. B. *J. Org. Chem.* **2009**, *74*, 1223–1230.
- (17) For calculations of 1,5-H migration following on from a Bergman rearrangement, see: Baroudi, A.; Mauldin, J.; Alabugin, I. V. *J. Am. Chem. Soc.* **2010**, *132*, 967–979.
- (18) Zeng, L.; Kaoudi, T.; Schiesser, C. H. *Tetrahedron Lett.* **2006**, *47*, 7911–7914.
- (19) It can be noted that the presence of a nitrogen atom protected as an acetamide or a trifluoroacetamide in the chain makes the enthalpically favored 1,7-H migration of a benzylic hydrogen atom compete with 1,5-hydrogen shift.
- (20) Gaussian 09, Revision A.02: Frisch, M. J.; Trucks, G. W.; Schlegel, H. B.; Scuseria, G. E.; Robb, M. A.; Cheeseman, J. R.; Scalmani, G.; Barone, V.; Mennucci, B.; Petersson, G. A.; Nakatsuji, H.; Caricato, M.; Li, X.; Hratchian, H. P.; Izmaylov, A. F.; Bloino, J.; Zheng, G.; Sonnenberg, J. L.; Hada, M.; Ehara, M.; Toyota, K.; Fukuda, R.; Hasegawa, J.; Ishida, M.; Nakajima, T.; Honda, Y.; Kitao, O.; Nakai, H.; Vreven, T.; Montgomery, J. A., Jr.; Peralta, J. E.; Ogliaro, F.; Bearpark, M.; Heyd, J. J.; Brothers, E.; Kudin, K. N.; Staroverov, V. N.; Kobayashi, R.; Normand, J.; Raghavachari, K.; Rendell, A.; Burant, J. C.; Iyengar, S. S.; Tomasi, J.; Cossi, M.; Rega, N.; Millam, N. J.; Klene, M.; Knox, J. E.; Cross, J. B.; Bakken, V.; Adamo, C.; Jaramillo, J.; Gomperts, R.; Stratmann, R. E.; Yazyev, O.

Austin, A. J.; Cammi, R.; Pomelli, C.; Ochterski, J. W.; Martin, R. L.; Morokuma, K.; Zakrzewski, V. G.; Voth, G. A.; Salvador, P.; Dannenberg, J. J.; Dapprich, S.; Daniels, A. D.; Farkas, Ö.; Foresman, J. B.; Ortiz, J. V.; Cioslowski, J.; Fox, D. J. Gaussian, Inc., Wallingford, CT, 2009.

(21) Scott, A. P.; Radom, L. *J. Phys. Chem.* **1996**, *100*, 16502–16513.

(22) (a) Henry, D.; Sullivan, M.; Radom, L. *J. Chem. Phys.* **2003**, *118*, 4849–4860.

(23) Viehe, H. G.; Janousek, Z.; Merenyi, R.; Stella, L. *Acc. Chem. Res.* **1985**, *18*, 148–154.

(24) For recent discussions on radical stabilization energies, see:

(a) Coote, M. L.; Lin, C. Y.; Beckwith, A. L. J.; Zavitsas, A. A. *Phys. Chem. Chem. Phys.* **2010**, *12*, 9597–9610. (b) Menon, A. S.; Wood, G. P. F.; Moran, D.; Radom, L. *J. Phys. Chem. A* **2007**, *111*, 13638–13644.

(c) Poutsma, M. L. *J. Org. Chem.* **2011**, *76*, 270–276. (d) Wood, G. P. F.; Moran, D.; Jacob, R.; Radom, L. *J. Phys. Chem. A* **2005**, *109*, 6318–6325.

(25) Hammond, G. S. *J. Am. Chem. Soc.* **1955**, *77*, 334–338.

(26) (a) Marcus, R. A. *Annu. Rev. Phys. Chem.* **1964**, *15*, 155–196. (b) Marcus, R. A. *J. Phys. Chem.* **1968**, *72*, 891–899. (c) For applications to reactions involving intermolecular hydrogen atom transfers, see ref 15b and Newcomb, M.; Manek, M. B.; Glenn, A. G. *J. Am. Chem. Soc.* **1991**, *113*, 949–958. For an application to radical cyclizations, see: (d) Alabugin, I. V.; Manoharan, M. *J. Am. Chem. Soc.* **2005**, *127*, 12583–12594. (e) Alabugin, I. V.; Timokhin, V. I.; Abrams, J. N.; Manoharan, M.; Abrams, R.; Ghiviriga, I. *J. Am. Chem. Soc.* **2008**, *130*, 10984–10995.

(27) For calculations referring to hydrogen abstraction by imide-*N*-oxyl radicals, see: Arnaud, R.; Milet, A.; Adamo, C.; Einhorn, C.; Einhorn, J. *J. Chem. Soc., Perkin Trans. 2* **2002**, 1967–1972 and references cited therein.

(28) The absolute configurations, resulting from retention of the configuration of the starting stereocenter, were assigned by analogy with our previous results; see ref 1.

(29) Stereochemistry was assigned from a NOESY experiment which showed cross-peaks between the proton α to the tosyl group at 5.95 ppm and the protons of the methyl group at 2.55 ppm.

(30) Effectively, the enantiomeric excess of naphthoazepine (2*R*,3*S*)-**33** formed in acetonitrile was only 65% instead of 84% in benzene.

Theoretical Study To Explain How Chirality Is Stored and Evolves throughout the Radical Cascade Rearrangement of Enyne-allenes

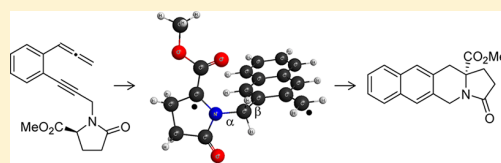
Anouk Gaudel-Siri,^{*,†} Damien Campolo,[†] Shovan Mondal,[‡] Malek Nechab,[†] Didier Siri,[†] and Michèle P. Bertrand[†]

[†]Aix-Marseille Université, CNRS, Institut de Chimie Radicalaire (UMR-7273), 13397 Marseille Cedex 20, France

[‡]Department of Chemistry, Visva Bharati University, Santiniketan, Birbhum, West Bengal 731235, India

S Supporting Information

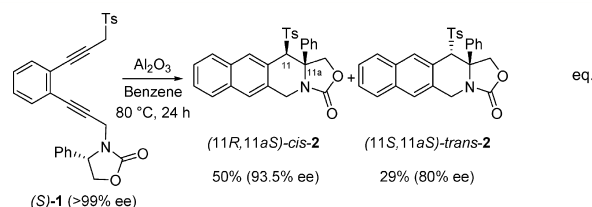
ABSTRACT: This article reports a theoretical study to explain how the intrinsic property of chirality is retained throughout the radical cascade rearrangement of an enantiopure chiral enyne-allene (bearing one stereogenic center) selected as a model for this family of reactions. Calculations at the MRPT2/6-31G(d)//CASSCF(10,10)/6-31G(d) level of theory were used to determine the entire reaction pathway which includes singlet state diradicals and closed-shell species. The cascade process involves three elementary steps, i.e., by chronological order: Myers–Saito cycloaromatization (M-S), intramolecular hydrogen atom transfer (HAT), and recombination of the resulting biradical. The enantiospecificity of the reaction results from a double transmission of the stereochemical information, from the original center to an axis and eventually from this axis to the final center. The first two steps lead to a transient diradical intermediate which retains the chirality via the conversion of the original static chirogenic element into a dynamic one, i.e., a center into an axis. The only available routes to the final closed-shell tetracyclic product imply rotations around two σ bonds ($\sigma(\text{C}-\text{C})$ and $\sigma(\text{C}-\text{N})$, bonds β and α respectively). The theoretical calculations confirmed that the formation of the enantiomerically pure product proceeds via the nonracemizing rotation around the $\sigma(\text{C}-\text{C})$ pivot. They ruled out any rotation around the second $\sigma(\text{C}-\text{N})$ pivot. The high level of configurational memory in this rearrangement relies on the steric impediment to the rotation around the C–N bond in the chiral native conformation of the diradical intermediate produced from tandem M-S/1,S-HAT.



INTRODUCTION

The discovery of the powerful antitumor properties of enediyne-containing natural products¹ has stimulated innovative research in multidisciplinary fields. The biological activity of these compounds is related to their aptitude to rearrange into highly reactive diradicals,^{2,3} capable of abstracting hydrogen atoms from DNA strands, which induces DNA cleavage and eventually cell death. Even though an impressive volume of literature data has been devoted to the cycloaromatization processes responsible for these properties, an ever sustained activity attests to the impact of these reactions in fields as diverse as biology, medicinal chemistry, and materials science.^{4,5} In a recent review, Kraka et al. pointed out how much the enediyne reactivity has also impacted computational methodologies.⁶

We have recently investigated chirality transfer⁷ in the cascade rearrangement of enediynes bearing a suitably located stereogenic center.⁸ A first series of results was obtained from enediynes such as **1**, where the enyne-allene intermediate was generated in situ via base-catalyzed 1,3-proton shift (eq 1).^{8a,b} These reactions were shown to proceed with a high level of retention of configuration at the original stereogenic center. However, due to the absence of control of the allene configuration in this procedure and to the creation of two stereocenters in the final product of which only one was controlled, the reaction led to a mixture of diastereomers as exemplified in eq.

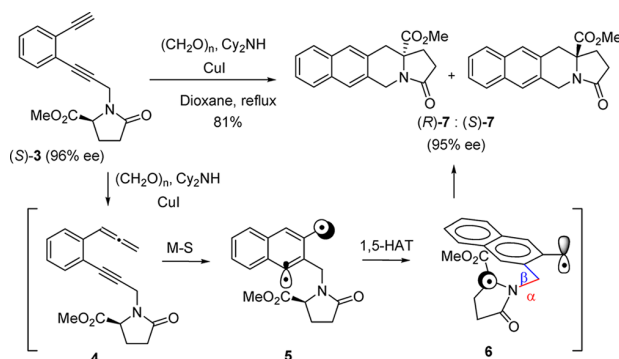


At this point, the choice of the proper terminology regarding the experimental results must be explained.⁹ The concise and figurative expression of *memory of chirality* (MOC) was originally used to describe our experimental results.⁸ This terminology introduced by Fuji and Kawabata is rather widespread in the literature.¹⁰ This concept inspired our strategy. It was considered appropriate to our reaction, as during the process, (i) the static chirality of the starting material related to its chirogenic carbon center is destroyed, (ii) but the chirality is retained (memorized) via the generation of a transient radical intermediate where the new chirogenic element is an axis (dynamic chirality); (iii) the stereocenter is regenerated in the final product. It must be noted that the use of this idiomatic expression (MOC) has been severely criticized by Cozzi and

Received: June 30, 2014

Published: September 8, 2014

Scheme 1. Rearrangement of Enediyne (S)-3: Proposed Mechanism



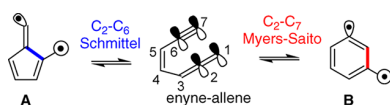
Siegel¹¹ and questioned by Wolf.¹² Since then, the term of MOC has been abandoned by Carlier^{10b,13} who recommends the use of “self-regeneration of stereocenters via transient stereolabile intermediates”, which refers to the seminal work of Seebach.¹⁴ The expression “memory of configuration” has also been adopted by Clayden.¹⁵

Back to our problem, to clearly demonstrate the mechanism of regeneration of the stereocenter, Crabbé's homologation of terminal alkynes was used for the in situ generation of achiral allene moieties from enantiopure enediyne such as compound 3.¹⁶ As summarized in Scheme 1, the cascade rearrangement of 3 involves the formation of the nonisolable intermediate enyne-allene 4, which is followed successively by Myers–Saito cycloaromatization leading to the (σ,π) diradical 5, 1,5-hydrogen atom transfer, and eventually recombination of the resulting diradical 6. The model substrate 3 (96% ee) led to 7 in 81% yield with 95% ee (level of chirality transfer close to 99% within the limits of experimental errors). Due to stereoelectronic factors, intramolecular HAT from the stereogenic center to the σ radical center in 5 necessarily generates 6 in a native chiral conformation, and this dynamic chirality is preserved all along the recombination step. The nearly total level of preservation of chirality observed in this reaction was rationalized according to reasonable conjectures about the relative rates of rotation around σ bonds α and β in the native conformation of diradical 6. This work reports a theoretical investigation of the three-step pathway leading from 4 to 7 in support to the origin of configurational memory in this rearrangement.¹⁷

COMPUTATIONAL DETAILS

It is well established that, depending on their substitution pattern, enyne-allenes can undergo cycloaromatization, leading either to a six-membered (σ,π) 1,4-diradical through C_2-C_7 Myers–Saito³ (M-S) reaction or to a five-membered (σ,π) 1,4-diradical through C_2-C_6 Schmittl¹⁸ reaction (Scheme 2).¹⁹

Scheme 2. Cyclization Pathways Transforming the Enyne-allene Framework into (σ,π) 1,4-Diradicals A and B



The activation barrier is higher for Schmittl cyclization than for M-S rearrangement, which is the preferred pathway.²⁰ The singlet–triplet

(S-T) gap in both systems A and B is small because σ and π radical centers are orthogonal and through-bond spin-polarization is weak. Experimentally, the S-T gap in α -3-didehydrotoluene B was estimated ≤ 5 kcal/mol.²¹ MCSCF calculations indicated that the ground state is a singlet and that the S-T gap is -3.0 kcal/mol.²² In the M-S reaction, the reactant is a singlet closed-shell species, whereas the product is an open-shell singlet diradical. Moreover, the electronic population in the transition state is intermediate between a diradical state and a closed-shell state. Therefore, a multiconfigurational method is required for a correct description of transition states and diradical intermediates. High-level ab initio methods (CCSD(T), MR-MP2, ...) have been applied to model Schmittl and Myers–Saito reactions from the bare enyne-allene framework shown in Scheme 2.^{20,23} Brueckner's approach²⁴ derived from the coupled-cluster²⁵ method has led to very good quantitative results on this model compound. It must be pointed out that geometry optimizations with these methods are too time-consuming to be applied to compounds 3–7. However, at the same time, the singlet diradicals have a typical two-configurational character that can only correctly be taken into account by a multideterminantal method. In other words, it was necessary to find a compromise. Whereas a monodeterminantal description of substituted enyne-allene derivatives with DFT methods is not a priori the best methodological choice, some recent works using the unrestricted broken spin-symmetry DFT (UBS-DFT) method on large substituted enediyne (Bergman cyclization) and enyne-allenes (Myers–Saito and Schmittl rearrangements) have led to valuable qualitative results.^{26–28} For this reason, to investigate the rearrangement of enyne-allene 4, stationary points were located on the potential energy surface (PES) by using the restricted M06-2X/6-31G(d) method²⁹ for closed-shell species and the UBS-M06-2X/6-31G(d) method for diradical species and transition states. Calculations were performed with the Gaussian09 program package.³⁰ As the reaction occurs in apolar solvents (benzene or dioxane), calculations were carried out in vacuum. All stationary points (transition states and minima) were confirmed by a frequency calculation. The intrinsic reaction coordinate (IRC) was followed to validate transition states. The stability of the wave function was tested with STABLE=OPT keyword. As expected, spin contamination in the singlet ground state occurs. Pure diradical singlet states are not provided by

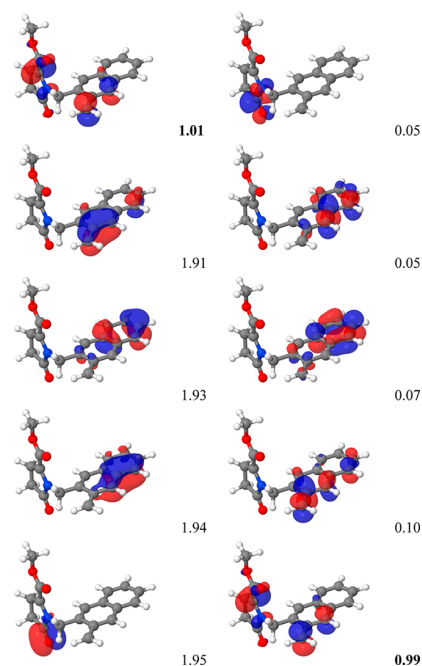


Figure 1. Selected natural orbitals of the active space and their occupancy in the case of diradical 6.

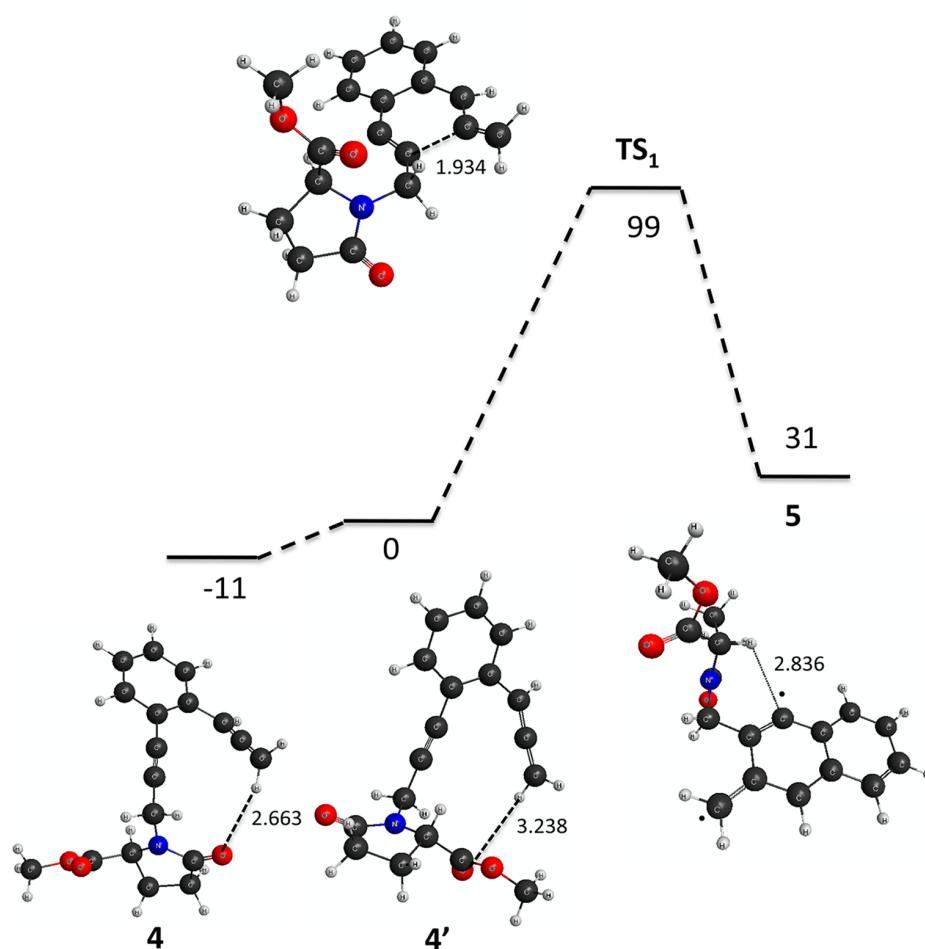


Figure 2. Reaction pathway leading to the (σ,π) diradical intermediate **5**. Relative ΔG values are given in kJ mol^{-1} at room temperature and 1 atm at the MRPT2/6-31G(d)//CASSCF(10,10)/6-31G(d) level. Distances are given in Å.

this monodeterminantal method where $\langle S^2 \rangle$ values are close to 1.0 for diradicals **5** and **6**.

To circumvent this problem, our choice was to carry out this study with a multireference method. Starting from these structures, all stationary points were reoptimized at the CASSCF(10,10)/6-31G(d) level.³¹ Calculations were performed with GAMESS package.³² Ten orbitals related to all valence π and π^* orbitals of enyne-allene **4** were included. As an illustration, these 10 orbitals correspond to the 10 orbitals shown in Figure 1 in the case of diradical **6**.

All configurations in the active space were generated. Only the singlet ground state was considered. All stationary points (transition states and minima) were confirmed by a frequency calculation. The intrinsic reaction coordinate (IRC) was again followed from the transition states to the reactants and the products. It is known that CASSCF activation energies are dramatically underestimated. Therefore, single point calculations at the multiconfigurational second-order perturbation theory MRPT2/6-31G(d)³³ level were performed to recover dynamic electron correlation. All given energies are ΔG values at the MRPT2/6-31G(d)//CASSCF(10,10)/6-31G(d) level at 298.15 K and 1 atm.

RESULTS AND DISCUSSION

As already stated, Myers–Saito (M-S) cycloaromatization is the very first step in the rearrangement of enantiopure enyne-allene intermediate (*S*)-**4** issued from Crabbé's homologation (Figures 2 and 3). The most stable conformation of enyne-allene (*S*)-**4** shows a stabilizing electrostatic interaction between the allenic proton and the carbonyl group of the cyclic amide ($d(\text{H}\cdots\text{O}) = 2.663$ Å). The IRC calculation shows that the M-S

cycloaromatization proceeds via the less stable conformer (*S*)-**4'** which results from a 180° rotation around the $\text{C}_{\text{sp}}-\text{CH}_2$ pivot. In both conformers (*S*)-**4** and (*S*)-**4'**, a dihedral angle of 32° is noted between the allenic moiety and the plane which contains the phenyl group conjugated to the triple bond. This value is larger than in hepta-1,2,4-trien-6-yne shown in Scheme 2 ($\phi(\text{C}2-\text{C}3-\text{C}4-\text{C}5) = 24.7^\circ$ at the CASSCF(10,10)/6-31G(d) level^{20c}) and can result from steric interactions between the allene framework and the substituted five-membered ring. Whereas the M-S reaction is exothermic by 63 kJ mol^{-1} for the above-mentioned parent system, the transformation of **4'** to **5** is slightly endothermic (19.5 kJ mol^{-1}). The cycloaromatization is the rate-determining step with a 99 kJ mol^{-1} activation free energy (Table 1, Figure 2) and a 89 kJ mol^{-1} ZPE-corrected activation energy. This value is consistent with the literature data reported for hepta-1,2,4-trien-6-yne. The activation free energy was determined experimentally ($\Delta G_{298\text{K}}^\ddagger = 106 \pm 2 \text{ kJ mol}^{-1}$),³⁴ and the activation energy was calculated by Sakai and Nishitani at the MRPT2(10,10)/6-311+G(d,p) level ($\Delta E_{0\text{K}}^\ddagger = 69 \text{ kJ mol}^{-1}$).^{20c,35}

The transition state has a diradicaloid character (see the NOON and the calculated biradical character³⁶ in Table 1). In transition state TS_1 , as in the reactant, the terminal allenic methylene is out of the plane formed by the conjugated moiety of the molecule with a dihedral angle of 30° . The methylene group has not fully rotated in the plane of the forming naphthyl

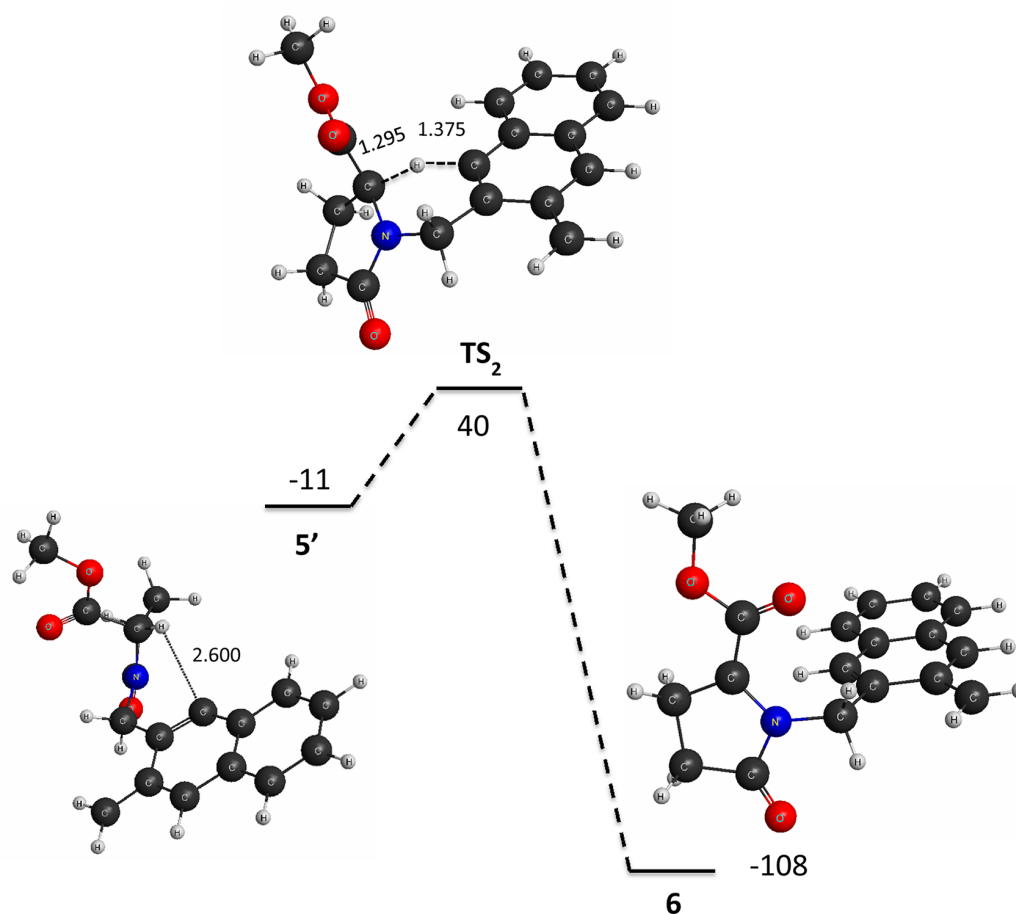


Figure 3. Intramolecular 1,5-HAT reaction pathway leading to the (π,π) diradical intermediate **6**. Relative ΔG values are given in kJ mol^{-1} at room temperature and 1 atm at the MRPT2/6-31G(d)//CASSCF(10,10)/6-31G(d) level. Distances are given in Å.

ring. In TS_1 , as in the resulting (σ,π) diradical **5**, the pyroglutamate ring adopts an envelope conformation where the CH_2 group in the β position relative to the amide carbonyl group is out-of-plane. The methyl carboxylate group lies in an equatorial position. The pyroglutamate ring undergoes pseudorotation to adopt the envelope conformation **5'** (with the CO_2Me moiety in the axial position) more prone to evolve via 1,5-hydrogen atom transfer (HAT). This conformer is more stable by 40 kJ mol^{-1} than **5**, and the H atom in the captodative position is closer to the σ radical center (Figure 2). Intermediate **5'** is readily converted by intramolecular HAT (51 kJ mol^{-1} activation free energy) into the highly stabilized (π,π) diradical **6** more stable by 108 kJ mol^{-1} than the reactive conformer **4'** of the enyne-allene (Figure 3).

The S-T gap in diradicals **5'** and **6** was calculated (-9 and $\sim 0 \text{ kJ mol}^{-1}$, respectively). During the 1,5-HAT step, the static central chirality of diradical **5** is converted into the dynamic axial chirality of diradical **6**. In the native conformation of diradical **6** the naphthyl group and the five-membered ring are orthogonal. Both singly occupied orbitals are degenerate. They have a π character and are delocalized for both radical centers which are planar (Figure 4). The largest coefficients correspond to the p orbitals located on the carbon and the nitrogen atoms in regard to the captodative moiety; the benzylic radical center is stabilized by conjugation with the naphthyl group (the main contribution comes from the ortho aromatic C(H)).

At this stage of the process, rotations around sigma bonds α and β (Scheme 1) can both formally occur on the route to the final product **7** by intramolecular coupling of the two radical centers (Scheme 3, Figure 4b,c). Whereas a rotation around the bond β can itself lead to (*R*)-**7**, the rotation around bond α cannot; the latter must necessarily be accompanied by a rotation around bond β .

Rotation around the C–N bond α either clockwise or counterclockwise is sterically impeded (huge steric interaction between the naphthyl moiety and the substituents of the rotating five-membered ring). A relaxed manual rotation with a step of 1° was performed in the triplet configuration at UM06-2X/6-31G(d) level because of convergence problems in the diradical singlet state. The results clearly showed that the two moieties bump into each other, and even the less energy demanding counterclockwise rotation around the C–N bond cannot proceed without concomitant rotation around the C–C bond β . As soon as the $\varphi(\text{C}-\text{CH}_2-\text{N}-\text{C}(=\text{O}))$ dihedral angle is reduced from 98° to 53° , the distance between the intracyclic carbonyl group and the naphthyl ring is close to 3 \AA and a rotation around the C–C bond is required to reduce steric hindrance.³⁷ Therefore, such a pathway, which would finally induce the formation of (*S*)-**7**, cannot contribute to the formation of **7**.

Conversely two competitive rotations around the C–C bond β can be considered: clockwise rotation (Scheme 3, Table 1, Figure 5, $\text{TS3b} \rightarrow \mathbf{6b}$) and counterclockwise rotation (Scheme 3,

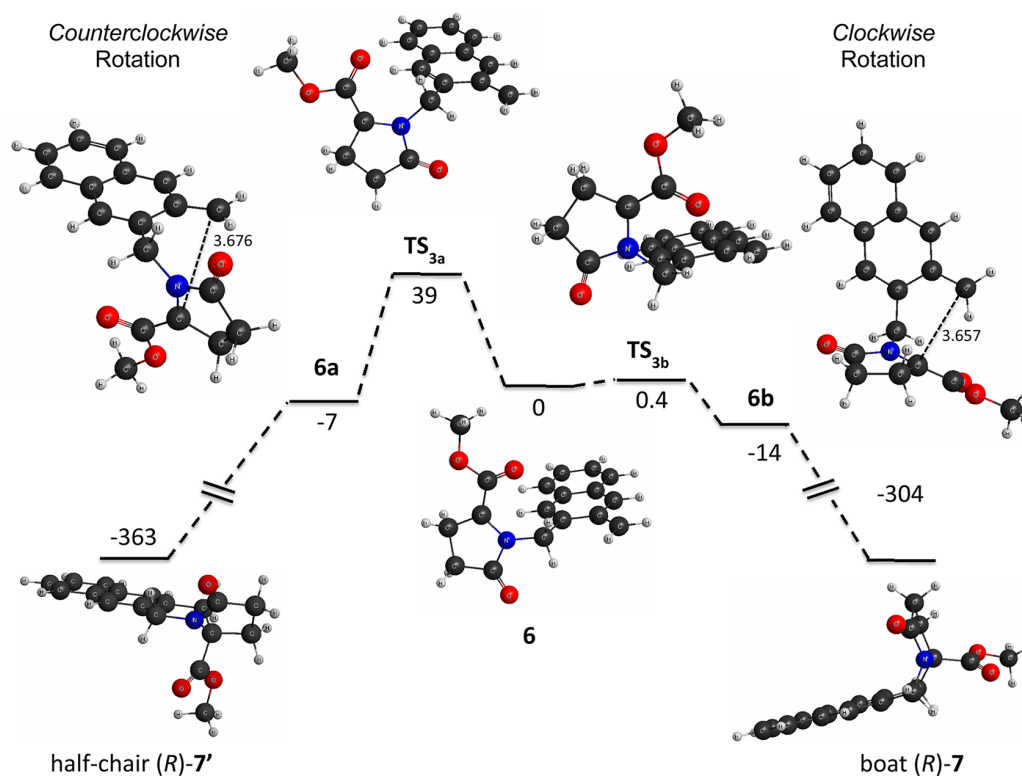
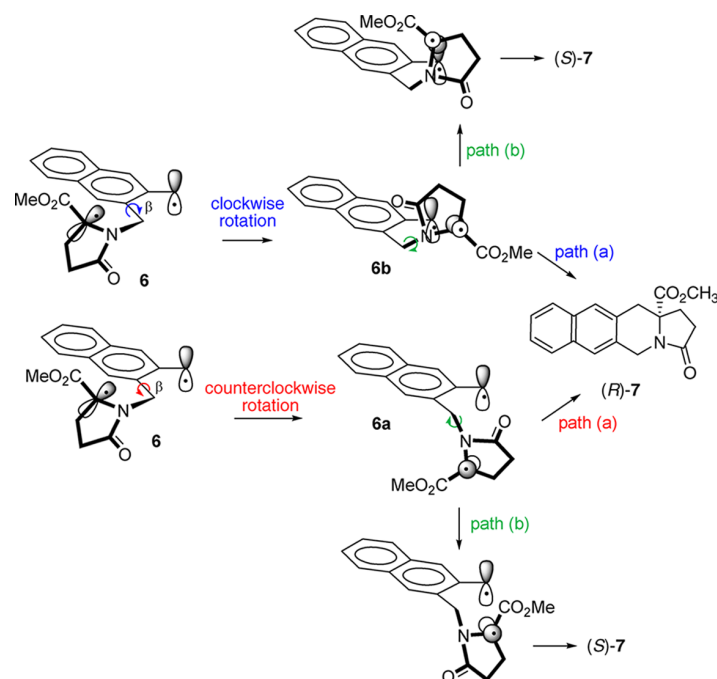
Scheme 3. Investigated Rotations around the Two σ Bond Pivots in the Intermediate (π,π) Diradical **6**²²

Figure 5. Clockwise and counterclockwise rotations around the C–C bond β in (π,π) diradical **6**, leading to the final product (R) -**7**. Relative ΔG values in kJ mol^{-1} at room temperature and 1 atm at the MRPT2/6-31G(d)//CASSCF(10,10)/6-31G(d) level. Distances are given in Å.

Any partially racemizing route leading to the (S) -enantiomer of the final product **7** (path b) would necessarily imply an additional rotation around the C–N pivot, i.e., an additional energetic cost compared to path a. Due to the very low activation

barrier calculated for the clockwise rotation in path a, the formation of (S) -**7** is highly unlikely.³⁸ The observed rearrangement obeys the “least motion principle”,³⁹ and the level of chirality transfer reaches 99%.

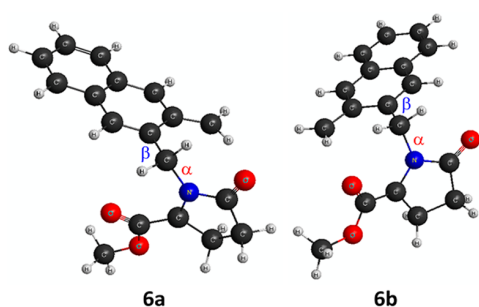


Figure 6. Structures of (π, π) diradical conformers **6a** and **6b** at the CASSCF(10,10)/6-31G(d) level of calculation.

CONCLUSION

The entire description of the three-step transformation leading from enyne-allene **4** to (*R*)-**7** was achieved by using MRPT2/6-31G(d)//CASSCF(10,10)/6-31G(d) calculations selected to correctly account for the optimized geometries and energetics of the pure ground-state singlet species (diradicals, diradicaloid transition state, diradical transition states, and closed-shell systems) involved in the reaction path. The extremely low rotational barrier around the benzylic C–C pivot (bond β), which excludes rotation around the second σ pivot (C–N bond α) in the conformationally chiral diradical intermediate **6**, explains how the chirality is stored and evolves throughout the multistep radical rearrangement, in other words it provides a rationale to the configurational memory observed in this process. Both clockwise and counterclockwise rotations around the C–C bond account for the formation of the enantiopure (*R*)-product in the critical recombination step. However, the experimentally observed retention of configuration is more likely to result from the clockwise rotation mode, as the free energy of the corresponding transition state (TS_{3a}) was found significantly lower than that of the counterclockwise rotation mode (TS_{3b}).

ASSOCIATED CONTENT

Supporting Information

Structures, MRPT2 energies, and Gibbs free energy correction values for all stationary points at the MRPT2/6-31G(d)//CASSCF(10,10)/6-31G(d) level of calculation; structures and energy values for transition states located in triplet configuration at the UM06-2X/6-31G(d) level of calculation. This material is available free of charge via the Internet at <http://pubs.acs.org>.

AUTHOR INFORMATION

Corresponding Author

*E-mail: anouk.siri@univ-amu.fr.

Notes

The authors declare no competing financial interests.

ACKNOWLEDGMENTS

The authors acknowledge Professor C. Roussel for stimulating comments. This work was supported by the computing facilities of the CRCMM, “Centre Régional de Compétences en Modélisation Moléculaire de Marseille”. The authors thank Aix-Marseille University, CNRS, for financial support. DST (Government of India) is also acknowledged for financial support to S.M. through Inspire Faculty Award.

REFERENCES

- (a) Smith, A. L.; Nicolaou, K. C. *J. Med. Chem.* **1996**, *39*, 2103–2117 and references therein. (b) Nicolaou, K. C.; Dai, W. M. *Angew. Chem., Int. Ed. Engl.* **1991**, *30*, 1387–1416 and references therein. (c) Nicolaou, K. C.; Dai, W. M.; Tsay, S. C.; Estevez, V. A.; Wrasidlo, W. *Science* **1992**, *256*, 1172–1178. (d) Ahlert, J.; Shepard, E.; Lomovskaya, N.; Zazopoulos, E.; Staffa, A.; Bachmann, B. O.; Huang, K.; Fonstein, L.; Czisny, A.; Whitwam, R. E.; Farnet, C. M.; Thorson, J. S. *Science* **2002**, *297*, 1173–1176.
- Jones, R.; Bergman, R. G. *J. Am. Chem. Soc.* **1972**, *94*, 660–661.
- (a) Myers, A. G.; Kuo, E. Y.; Finney, N. S. *J. Am. Chem. Soc.* **1989**, *111*, 8057–8059. (b) Myers, A. G.; Dragovich, P. S.; Kuo, E. Y. *J. Am. Chem. Soc.* **1992**, *114*, 9369–9386. (c) Nagata, R.; Yamanaka, H.; Murahashi, E.; Saito, I. *Tetrahedron Lett.* **1990**, *31*, 2907–2910.
- (a) Hamann, P. R.; Upeslakis, J.; Borders, D. B. In *Anticancer Agents from Natural Products*, 2nd ed.; Cragg, G. M.; Kingston, D. G. I.; Newman, D. J., Eds.; CRC Press: Boca Raton, FL, 2012; pp 575–621. (b) Breiner, B.; Kaya, K.; Roy, S.; Yang, W.-Y.; Alabugin, I. V. *Org. Biomol. Chem.* **2012**, *10*, 3974–3987. (c) Joshi, M. C.; Rawat, D. S. *Chem. Biodiversity* **2012**, *9*, 459–498. (d) Polukhtina, A.; Karpov, G.; Pandithavidana, D. R.; Kuzmin, A.; Popik, V. V. *Aust. J. Chem.* **2010**, *63*, 1099–1107. (e) Toshima, K. *Synlett* **2012**, *23*, 2025–2052. (f) Shao, R.-G. *Curr. Mol. Pharmacol.* **2008**, *1*, 50–60. (g) Kar, M.; Basak, A. *Chem. Rev.* **2007**, *107*, 2861–2890.
- (a) Xiao, Y.; Hu, A. *Macromol. Rapid Commun.* **2011**, *32*, 1688–1698. (b) Boerner, L. J. K.; Dye, D. F.; Kopke, T.; Zaleski, J. M. *Coord. Chem. Rev.* **2013**, *257*, 599–620. (c) Li, Z.; Song, D.; Zhi, J.; Hu, A. *J. Phys. Chem. C* **2011**, *115*, 15829–15833. (d) Sun, S.; Zhu, C.; Song, D.; Li, F.; Hu, A. *Polym. Chem.* **2014**, *5*, 1241–1247. (e) Yang, X.; Li, Z.; Zhi, J.; Ma, J.; Hu, A. *Langmuir* **2010**, *26*, 11244–11248. (f) Ito, S.; Iida, T.; Kawakami, J.; Okujima, T.; Morita, N. *Eur. J. Org. Chem.* **2009**, *31*, 5355–5364. (g) Mondal, S.; Dumur, F.; Barbarat, B.; Grauby, O.; Gignes, D.; Olive, D.; Bertrand, M. P.; Nechab, M. *Colloids Surf., B* **2013**, *112*, 513–520.
- (a) Kraka, E.; Cremer, D. *WIREs Comput. Mol. Sci.* **2013**, DOI: 10.1002/wcms.1174. (b) Schreiner, P. R.; Navarro-Vazquez, A.; Prall, M. *Acc. Chem. Res.* **2005**, *38*, 29–37. (c) Gräfenstein, J.; Kraka, E.; Filatov, M.; Cremer, D. *Int. J. Mol. Sci.* **2002**, *3*, 360–394.
- For a recent review on chirality transfer, see: Campolo, D.; Gastaldi, S.; Roussel, C.; Bertrand, M. P.; Nechab, M. *Chem. Soc. Rev.* **2013**, *42*, 8434–8466.
- (a) Nechab, M.; Campolo, D.; Maury, J.; Perfetti, P.; Vanthuyne, N.; Siri, D.; Bertrand, M. P. *J. Am. Chem. Soc.* **2010**, *132*, 14742–14744. (b) Nechab, M.; Besson, E.; Campolo, D.; Perfetti, P.; Vanthuyne, N.; Bloch, E.; Denoyel, R.; Bertrand, M. P. *Chem. Commun.* **2011**, *47*, 5286–5288. (c) Campolo, D.; Gaudel-Siri, A.; Mondal, S.; Siri, D.; Besson, D.; Vanthuyne, N.; Nechab, M.; Bertrand, M. P. *J. Org. Chem.* **2012**, *77*, 2773–2783. (d) Mondal, S.; Nechab, N.; Campolo, D.; Vanthuyne, N.; Bertrand, M. P. *Adv. Synth. Catal.* **2012**, *354*, 1987–2000.
- This digression was included to address a reviewer’s remark and draw the reader’s attention to the importance for the scientific writer to use appropriate terms and evaluate the risk of propagating metaphors that might be misinterpreted.
- (a) Fuji, K.; Kawabata, T. *Chem.—Eur. J.* **1998**, *4*, 373–376. (b) Zhao, H.; Hsu, D. C.; Carlier, P. R. *Synthesis* **2005**, *1*, 1–16. (c) Kawabata, T.; Fuji, K. In *Topics in Stereochemistry*; Denmark, S. E., Ed.; Wiley and Sons Inc.: New York, 2003, Vol. 23, pp 175–205.
- Cozzi, F.; Siegel, J. S. *Org. Biomol. Chem.* **2005**, *3*, 4296–4298.
- Wolf, C. In *Dynamic Stereochemistry of Chiral Compounds: Principles and Applications*; Royal Society of Chemistry: Cambridge, UK, 2008; pp 282–289.
- (a) Carlier, P. R.; Hsu, D. C.; Bryson, S. A. In *Stereochemical Aspects of Organolithium Compounds*; Gawley, R. E., Ed.; Topics in Stereochemistry; Siegel, J. S., Series, Ed.; Verlag Helvetica Chimica Acta: Zürich, 2010; Vol. 26, pp 53–92. (b) Carlier, P. R.; Sun, Y.-S.; Hsu, D. C.; Chen, Q.-H. *J. Org. Chem.* **2010**, *75*, 6588–6594.
- Seebach, D.; Wasmuth, D. *Angew. Chem., Int. Ed.* **1981**, *20*, 971.

- (15) Fletcher, S. P.; Solà, J.; Holt, D.; Brown, R. A.; Clayden, J. *Belstein J. Org. Chem.* **2011**, *7*, 1304–1309.
- (16) Mondal, S.; Nechab, M.; Vanthuyne, N.; Bertrand, M. P. *Chem. Commun.* **2012**, *48*, 2549–2551.
- (17) For a theoretical support to the origin of memory of chirality in Norrish–Yang cyclization, see: (a) Giese, B.; Wettstein, P.; Stähelin, C.; Barbosa, F.; Neuburger, M.; Zehnder, M.; Wessig, P. *Angew. Chem., Int. Ed.* **1999**, *38*, 2586–2587. (b) Sinicropi, A.; Barbosa, F.; Basosi, R.; Giese, B.; Olivucci, M. *Angew. Chem., Int. Ed.* **2005**, *44*, 2390–2393.
- (18) (a) Schmittel, M.; Strittmatter, M.; Kiau, S. *Tetrahedron Lett.* **1995**, *36*, 4975–4978. (b) Schmittel, M.; Kiau, S.; Siebert, T.; Strittmatter, M. *Tetrahedron Lett.* **1996**, *37*, 7691–7694. (c) Schreiner, P. R.; Prall, M. *J. Am. Chem. Soc.* **1999**, *121*, 8615–8627.
- (19) For general reviews, see: (a) Mohamed, R. K.; Peterson, P. W.; Alabugin, I. V. *Chem. Rev.* **2013**, *113*, 7089–7129. (b) Peterson, P. W.; Mohamed, R. K.; Alabugin, I. V. *Eur. J. Org. Chem.* **2013**, *13*, 2505–2527. (c) Navarro-Vazquez, A.; Prall, M.; Schreiner, P. R. *Org. Lett.* **2004**, *6*, 2981–2984. (d) Alabugin, I. V.; Breiner, B.; Manoharan, M. *Adv. Phys. Org. Chem.* **2008**, *42*, 1–33.
- (20) (a) De Visser, S. P.; Filatov, M.; Shaik, S. *Phys. Chem. Chem. Phys.* **2001**, *3*, 1242–1245. (b) Prall, M.; Wittkopp, A.; Schreiner, P. R. *J. Phys. Chem. A* **2001**, *105*, 9265–9274. (c) Sakai, S.; Nishitani, M. *J. Phys. Chem. A* **2010**, *114*, 11807–11813.
- (21) Logan, C. F.; Ma, J. C.; Chen, P. *J. Am. Chem. Soc.* **1994**, *116*, 2137–2138.
- (22) (a) Wenthold, P. G.; Wierschke, S. G.; Nash, J. J.; Squires, R. J. *Am. Chem. Soc.* **1993**, *115*, 12611–12612. (b) Wenthold, P. G.; Wierschke, S. G.; Nash, J. J.; Squires, R. J. *Am. Chem. Soc.* **1994**, *116*, 7378–7392.
- (23) For a recent application to Bergman cyclization, see: Greer, E. M.; Cosgriff, C. V.; Doubleday, C. *J. Am. Chem. Soc.* **2013**, *135*, 10194–10197.
- (24) (a) Kobayashi, R.; Handy, N. C.; Amos, R. D.; Trucks, G. W.; Frisch, M. J.; Pople, J. A. *J. Chem. Phys.* **1991**, *95*, 6723–6733. (b) Crawford, T. D.; Lee, T. J.; Handy, N. C.; Schaefer, H. F., III. *J. Chem. Phys.* **1997**, *107*, 9980–9984. (c) Lindgren, I.; Salomonson, S. *Int. J. Quantum Chem.* **2002**, *90*, 294–316.
- (25) (a) Purvis, G. D., III; Bartlett, R. J. *J. Chem. Phys.* **1982**, *76*, 1910–1918. (b) Čížek, J. In *Advances in Chemical Physics: Correlation Effects in Atoms and Molecules*; LeFebvre, R., Moser, C., Eds.; John Wiley & Sons, Inc.: Hoboken, NJ, 2007; Vol. 14, pp 35–89.
- (26) (a) Ess, D. H.; Johnson, E. R.; Hu, X.; Yang, W. *J. Phys. Chem. A* **2011**, *115*, 76–83. (b) Lim, M. H.; Worthington, S. E.; Dulles, F. J.; Cramer, C. J. In *Chemical Applications of Density-Functional Theory*; Laird, B. B.; Ross, R. B.; Ziegler, T., Eds.; American Chemical Society: Washington, DC, 1996; Chapter 27, pp 402–422.
- (27) (a) Baroudi, A.; Mauldin, J.; Alabugin, I. V. *J. Am. Chem. Soc.* **2010**, *132*, 967–979. (b) Zeidan, T. A.; Manoharan, M.; Alabugin, I. V. *J. Org. Chem.* **2006**, *71*, 954–961. (c) Zeidan, T. A.; Kovalenko, S. V.; Manoharan, M.; Alabugin, I. V. *J. Org. Chem.* **2006**, *71*, 962–975. (d) Alabugin, I. V.; Manoharan, M.; Kovalenko, S. V. *Org. Lett.* **2002**, *4*, 1119–1122. (e) Kraka, E.; Cremer, D. *J. Am. Chem. Soc.* **2000**, *122*, 8245–8264. (f) Gräfenstein, J.; Hjerpe, A. M.; Kraka, E.; Cremer, D. *J. Phys. Chem. A* **2000**, *104*, 1748–1761.
- (28) (a) Basak, A.; Das, S.; Mallick, D.; Jemmis, E. D. *J. Am. Chem. Soc.* **2009**, *131*, 15695–15704. (b) Bekele, T.; Christian, C. F.; Lipton, M. A.; Singleton, D. A. *J. Am. Chem. Soc.* **2005**, *127*, 9216–9223. (c) Alabugin, I. V.; Manoharan, M. *J. Am. Chem. Soc.* **2003**, *125*, 4495–4509. (d) Chen, W.-C.; Zou, J.-W.; Yu, C.-H. *J. Org. Chem.* **2003**, *68*, 3663–3672.
- (29) Zhao, Y.; Truhlar, D. *Acc. Chem. Res.* **2008**, *41*, 157–167.
- (30) Frisch, M. J.; Trucks, G. W.; Schlegel, H. B.; Scuseria, G. E.; Robb, M. A.; Cheeseman, J. R.; Scalmani, G.; Barone, V.; Mennucci, B.; Petersson, G. A.; Nakatsuji, H.; Caricato, M.; Li, X.; Hratchian, H. P.; Izmaylov, A. F.; Bloino, J.; Zheng, G.; Sonnenberg, J. L.; Hada, M.; Ehara, M.; Toyota, K.; Fukuda, R.; Hasegawa, J.; Ishida, M.; Nakajima, T.; Honda, Y.; Kitao, O.; Nakai, H.; Vreven, T.; Montgomery, J. A., Jr.; Peralta, J. E.; Ogliaro, F.; Bearpark, M.; Heyd, J. J.; Brothers, E.; Kudin, K. N.; Staroverov, V. N.; Kobayashi, R.; Normand, J.; Raghavachari, K.; Rendell, A.; Burant, J. C.; Iyengar, S. S.; Tomasi, J.; Cossi, M.; Rega, N.; Millam, N. J.; Klene, M.; Knox, J. E.; Cross, J. B.; Bakken, V.; Adamo, C.; Jaramillo, J.; Gomperts, R.; Stratmann, R. E.; Yazyev, O.; Austin, A. J.; Cammi, R.; Pomelli, C.; Ochterski, J. W.; Martin, R. L.; Morokuma, K.; Zakrzewski, V. G.; Voth, G. A.; Salvador, P.; Dannenberg, J. J.; Dapprich, S.; Daniels, A. D.; Farkas, Ö.; Foresman, J. B.; Ortiz, J. V.; Cioslowski, J.; Fox, D. J. *Gaussian 09, Revision D.01*, Gaussian, Inc., Wallingford, CT, 2009.
- (31) (a) Roos, B. O. In *Advances in Chemical Physics: Ab Initio Methods in Quantum Chemistry Part 2*; Lawley, K. P., Eds.; John Wiley & Sons, Inc.: Hoboken, NJ, 2007; Vol. 69, pp 399–445. (b) Yamamoto, N.; Vreven, T.; Robb, M. A.; Frisch, M. J.; Schlegel, H. B. *Chem. Phys. Lett.* **1996**, *250*, 373–378.
- (32) Schmidt, M. W.; Baldrige, K. K.; Boatz, J. A.; Elbert, S. T.; Gordon, M. S.; Jensen, J. H.; Kosecki, S.; Matsunaga, N.; Nguyen, K. A.; Su, S. J.; Windus, T. L.; Dupuis, M.; Montgomery, J. A. *J. Comput. Chem.* **1993**, *14*, 1347–1363.
- (33) Nakano, H. *J. Chem. Phys.* **1993**, *99*, 7983–7992.
- (34) Myers, A. G.; Dragovich, P. S.; Kuo, E. Y. *J. Am. Chem. Soc.* **1992**, *114*, 9369–9386.
- (35) For a more detailed comparison of computed values using various methodologies, see refs 6a, 6b, 14a, 14c, and references cited therein.
- (36) Kamada, K.; Ohta, K.; Shimizu, A.; Kubo, T.; Kishi, R.; Takahashi, H.; Botek, E.; Champagne, B.; Nakano, M. *J. Phys. Chem. Lett.* **2010**, *1*, 937–940.
- (37) The four transition states corresponding to the clockwise and counterclockwise rotations around bonds α and β were located at the UM06-2X/6-31G(d) level of calculation in their triplet configuration. Single point energy calculations at the UBS-M06-2X/6-31G(d) level of calculation provided the energy of the spin-contaminated singlet transition states ($\langle S^2 \rangle$ value close to 1). Both are highly energetic for clockwise/counterclockwise rotations around bond α (40.0/23.5 kJ·mol⁻¹ above (π,π) diradical intermediate **6**, respectively), as compared to those corresponding to clockwise/counterclockwise rotations around bond β (2.5/6.6 kJ·mol⁻¹ above intermediate **6** at this level of calculation, respectively).
- (38) The rotation around bond α was investigated starting from structure **6b**. Both transition states in triplet configuration for the clockwise and counterclockwise rotations around the C–N bond α were located at the UM06-2X/6-31G(d) level of calculation. Single point energy calculations at the UBS-M06-2X/6-31G(d) level of calculation provided the energy of the spin-contaminated singlet transition states ($\langle S^2 \rangle$ value close to 1). Free energy values are 33.7/44.7 kJ·mol⁻¹ above (π,π) diradical intermediate **6b** for clockwise/counterclockwise rotations respectively. It must be noted that this methodology allowed the location of a transition state for the coupling leading to (**R**)-**7**. The free energy value of this stationary point was found only 23.2 kJ·mol⁻¹ above **6b** at this level of calculation.
- (39) According to Hine, J. *Adv. Phys. Org. Chem.* **1978**, *15*, 1–61. “The principle of least motion is the hypothesis that when multiple species with different nuclear structures could theoretically form as products of a given chemical reaction, *the more likely to form tends to be the one requiring the least amount of change in nuclear structure or the smallest change in nuclear positions*”.

4.4 Application à l'organocatalyse

Dans le cadre du projet ANR OEREKA, l'étude théorique de l'addition de Michael organocatalysée de β -cétoamides a été menée. Ces travaux ont fait l'objet d'une publication préliminaire dans le journal *Organic Letters*, démontrant l'influence du pKa de l'hydrogène amidique des β -cétoamides sur le rendement de la réaction. Elle est reportée ci-après. La publication finale classée "Hot Paper" dans le journal *Chem. Eur. J.* est reportée à la suite. Une communication orale et une communication par affiche ont également porté sur ce sujet.

A Cooperative Participation of the Amido Group in the Organocatalytic Construction of All-Carbon Quaternary Stereocenters by Michael Addition with β -Ketoamides

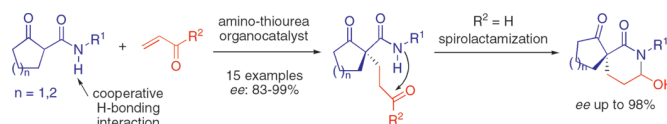
Maria del Mar Sanchez Duque,[†] Olivier Baslé,[†] Nicolas Isambert,[†] Anouk Gaudel-Siri,[†] Yves Génisson,[‡] Jean-Christophe Plaquevent,[‡] Jean Rodriguez,^{*,†} and Thierry Constantieux^{*,†}

Aix-Marseille Université, iSm2, UMR CNRS 6263, Centre St Jérôme, service 531, 13397 Marseille Cedex 20, France, and Université Paul Sabatier Toulouse III, LSPCMIB, UMR CNRS 5068, 31062 Toulouse 9, France

thierry.constantieux@univ-cezanne.fr; jean.rodriguez@univ-cezanne.fr

Received April 8, 2011

ABSTRACT



The secondary amido group of α -substituted β -ketoamides plays a crucial role in the control of the reactivity and spatial arrangement (selectivity) in the organocatalyzed Michael addition to unsaturated carbonyls. This results in an unprecedented activation mode of substrates through H-bonding interactions allowing the construction of enantiomerically enriched functionalized all-carbon quaternary centers and spiroaminals of high synthetic potential.

The enantioselective construction of quaternary centers is one of the most demanding key steps in the stereocontrolled synthesis of complex natural and/or pharmaceuticals products.¹ In this context, the asymmetric conjugate addition represents a powerful tool for the elaboration of these particular stereocenters. Despite well-established transition-metal-based catalytic methods,² the generation of all-carbon quaternary stereocenters via Michael addition still constitutes a formidable challenge owing to additional steric hindrance considerations.³ In the past decade, extensive studies have been devoted to the development of organocatalytic systems performing with

excellent enantioselectivities,⁴ employing simple substrates. In this way, a wide variety of α -substituted-1,3-dicarbonyls or synthetic equivalents such as β -diketones, β -ketoesters⁵ or α -cyanoesters and ketones⁶ have been extensively and successfully used. On the other hand, asymmetric conjugate addition with simple β -ketoamides, of broad

[†] Aix-Marseille Université.

[‡] Université Paul Sabatier Toulouse III.

(1) Steven, A.; Overman, L. E. *Angew. Chem., Int. Ed.* **2007**, *46*, 5488.

(2) Douglas, C. J.; Overman, L. E. *Proc. Natl. Acad. Sci. U.S.A.* **2004**, *101*, 5363. Trost, B. M.; Jiang, C. *Synthesis* **2006**, 369. Alexakis, A.; Vuagnoux d'Augustin, M.; Martin, D.; Kehrl, S.; Palais, L.; Henon, H.; Hawner, C. *Chimia* **2008**, *62*, 461.

(3) Hamashima, Y.; Hotta, D.; Sodeoka, M. *J. Am. Chem. Soc.* **2002**, *124*, 11240. Christoffers, J.; Baro, A. *Angew. Chem., Int. Ed.* **2003**, *42*, 1688. Ogawa, C.; Kizu, K.; Shimizu, H.; Takeuchi, M.; Kobayashi, S. *Chem.—Asian J.* **2006**, *1–2*, 121.

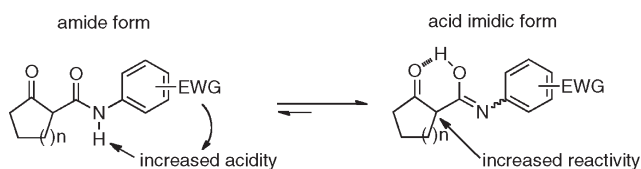
(4) Tsogoeva, S. B. *Eur. J. Org. Chem.* **2007**, 1701. Erkkilä, A.; Majander, I.; Pihko, P. M. *Chem. Rev.* **2007**, *107*, 5416. Dondoni, A.; Massi, A. *Angew. Chem., Int. Ed.* **2008**, *47*, 4638. Melchiorre, P.; Marigo, M.; Carlone, A.; Bartoli, G. *Angew. Chem., Int. Ed.* **2008**, *47*, 6138. Palomo, C.; Oiarbide, M.; López, R. *Chem. Soc. Rev.* **2009**, *38*, 632. Bertelsen, S.; Jorgensen, K. A. *Chem. Soc. Rev.* **2009**, *38*, 2178. Gruttadauria, M.; Giacalone, F.; Noto, R. *Adv. Synth. Catal.* **2009**, *351*, 33. Bella, M.; Gasperi, T. *Synthesis* **2009**, 1583. For a recent example, see: Zhu, Q.; Lu, Y. *Angew. Chem., Int. Ed.* **2010**, *49*, 7753.

(5) Capuzzi, M.; Perdicchia, D.; Jorgensen, K. A. *Chem.—Eur. J.* **2008**, *14*, 128. Rigby, C. L.; Dixon, D. J. *Chem. Commun.* **2008**, 3798. Yu, Z.; Liu, X.; Zhou, L.; Lin, L.; Feng, X. *Angew. Chem., Int. Ed.* **2009**, *48*, 5195. Akiyama, T.; Katoh, T.; Mori, K. *Angew. Chem., Int. Ed.* **2009**, *48*, 4226. Boddaert, T.; Coquerel, Y.; Rodriguez, J. *Adv. Synth. Catal.* **2009**, *351*, 1744. Yang, J.; Li, W.; Jin, Z.; Liang, X.; Ye, J. *Org. Lett.* **2010**, *12*, 5218.

(6) Jautze, S.; Peters, R. *Synthesis* **2010**, 365 and references cited therein. See also: Kawato, Y.; Takahashi, N.; Kumagai, N.; Shibasaki, M. *Org. Lett.* **2010**, *12*, 1484.

synthetic value by post-transformations involving the amido functionality,^{7,8} remained unsolved. This limitation is due to the lack of efficient activation modes of these peculiar substrates. According to mechanistic studies on proton exchange in amides and related compounds,⁹ β -ketoamides are better represented under their imidic acid form that could constitute a new activation mode of these unexplored potential pronucleophiles in Michael addition (Scheme 1).

Scheme 1. Equilibrium between Amide and Acid Imidic Forms



Moreover, based on the seminal works from Miller's group,¹⁰ the presence of the amido moiety will result in a favorable cooperative effect in the organization of the transition state for efficient enantiocontrol of the reaction. Based on our precedent developments in ketoamide reactivity¹¹ and organocatalytic conjugate additions,¹² we present these unprecedented achievements under thiourea-based bifunctional catalysis,¹³ for the enantioselective construction of functionalized all-carbon quaternary stereocenters from α -substituted β -ketoamides as pronucleophiles.¹⁴ Also, the synthetic advantage of the additional amide function is illustrated through an efficient enantioselective domino Michael/spirolactamization sequence leading to chiral scaffolds of high synthetic interest.

To initiate our study, we selected the conjugate addition of β -ketoamide **1a** to methylvinylketone (**2a**) in the presence of 10 mol % of various organocatalysts **3a–h**, as a test experiment (Table 1).

(7) Pilling, A. W.; Boehmer, J.; Dixon, D. J. *Angew. Chem., Int. Ed.* **2007**, *46*, 5428. Yang, T.; Campbell, L.; Dixon, D. J. *J. Am. Chem. Soc.* **2007**, *129*, 12070. Pilling, A. W.; Böhrer, J.; Dixon, D. J. *Chem. Commun.* **2008**, 832.

(8) Very recently, α -unsubstituted β -amidoesters have been proposed as pronucleophiles leading to the creation of a tertiary stereogenic center: Franzén, J.; Fisher, A. *Angew. Chem., Int. Ed.* **2009**, *48*, 787. Zhang, W.; Franzén, J. *Adv. Synth. Catal.* **2010**, *352*, 499. Valero, G.; Schimer, J.; Cisarova, I.; Vesely, J.; Moyano, A.; Rios, R. *Tetrahedron Lett.* **2009**, *50*, 1943. Jin, Z.; Wang, X.; Huang, H.; Liang, X.; Ye, J. *Org. Lett.* **2011**, *13*, 564.

(9) Perrin, C. L.; Dwyer, T. M.; Rebek, J., Jr.; Duff, R. J. *J. Am. Chem. Soc.* **1990**, *112*, 3122 and references therein.

(10) Horstmann, T. E.; Guerin, D. J.; Miller, S. J. *Angew. Chem., Int. Ed.* **2000**, *39*, 3635. Vasbinder, M. M.; Jarvo, E. R.; Miller, S. J. *Angew. Chem., Int. Ed.* **2001**, *40*, 2824. Jakobsche, C. E.; Peris, G.; Miller, S. J. *Angew. Chem., Int. Ed.* **2008**, *47*, 6707.

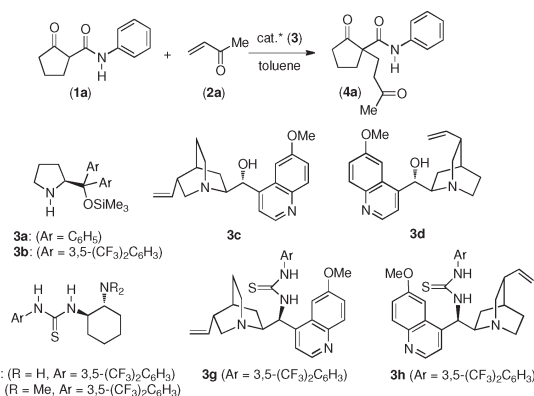
(11) Sanchez Duque, M. M.; Allais, C.; Isambert, N.; Constantieux, T.; Rodriguez, J. *Top. Heterocycl. Chem.* **2010**, *23*, 227 and references cited there in.

(12) Bonne, D.; Salat, L.; Dulcère, J.-P.; Rodriguez, J. *Org. Lett.* **2008**, *10*, 5409. Raimondi, W.; Lettieri, G.; Dulcère, J.-P.; Bonne, D.; Rodriguez, J. *Chem. Commun.* **2010**, *46*, 7247.

(13) Connon, S. J. *Chem. Commun.* **2008**, 2499. Zhang, Z.; Schreiner, P. R. *Chem. Soc. Rev.* **2009**, *38*, 1187. Connon, S. J. *Synlett* **2009**, 354.

(14) For isolated examples of enantioselective addition of an α -substituted- β -amidoester to a nitroolefin, see: Jakubec, P.; Helliwell, M.; Dixon, D. J. *Org. Lett.* **2008**, *10*, 4267. Jakubec, P.; Cockfield, D. M.; Dixon, D. J. *J. Am. Chem. Soc.* **2009**, *131*, 16632.

Table 1. Screening of Catalysts for the Organocatalytic Conjugate Addition of β -Ketoamide **1a** to Methylvinylketone (**2a**)^a



entry	catalyst	time (h)	temp (°C)	conversion ^b (%)	ee (%) ^c
1	3a ^d	96	20	20 ^e	0
2	3b ^d	144	20	No reaction	—
3	3c	20	20	100	35
4	3d	24	20	100	73
5	3e	168	20	100	32
6	3f	48	20	100	87
7	3f	48	0	100	83
8	3f	48	−20	100	79
9	3g	48	20	100	75
10	3h	48	20	100	80

^a A solution of **1a** (1 equiv), **2a** (2 equiv), and catalyst **3** (10 mol %) in toluene (0.05 M) was stirred until full conversion. ^b Determined by TLC analysis. ^c Determined by HPLC on a chiral stationary phase. ^d Catalyst loading 20 mol %. ^e Determined by ¹H NMR.

Efficient in the case of α -unsubstituted β -amidoesters,⁸ the (*S*)-proline derivatives **3a** and **3b** either gave a very low conversion with no enantioselection or failed in producing the desired Michael adduct (entries 1 and 2), ruling out a possible mechanism involving enamine or iminium intermediates.¹⁵ On the contrary, H-bonding activation with bifunctional catalysts **3c–h** led to complete conversion and moderate to good ee's (entries 3–10). The Takemoto ThioUrea Catalyst¹⁶ (TUC, **3f**) proved to be the most promising, giving the adduct with 87% ee after 48 h at rt (entry 6). It is noteworthy that the presence of a tertiary amine in the structure of the catalyst is crucial, since **3e** with a less basic appended primary amine provided the desired product with decreased efficiency and selectivity (entry 5). Unfortunately, lowering the temperature to 0 or −20 °C did not improve the enantioselectivity of the reaction (entries 7 and 8), and cinchona alkaloids **3c** and **3d** or their more elaborated thiourea derivatives¹⁷ **3g** and **3h** revealed to be less efficient than the TUC **3f** (entries 3, 4, 9, and 10).

(15) Bartoli, G.; Melchiorre, P. *Synlett* **2008**, 1759.

(16) Okino, T.; Hoashi, Y.; Furukawa, T.; Xu, X.; Takemoto, Y. *J. Am. Chem. Soc.* **2005**, *127*, 119. Hamza, A.; Schubert, G.; Soós, T.; Pápai, I. *J. Am. Chem. Soc.* **2006**, *128*, 13151.

(17) *Cinchona Alkaloids in Synthesis and Catalysis*; Song, C. E., Ed.; Wiley-VCH: Weinheim, 2009. Marcelli, T.; Hiemstra, H. *Synthesis* **2010**, 1229.

Finally, several solvents have been investigated in combination with **3f**, and toluene was selected as the best one.

We next decided to explore the effect of the amide functionality on reactivity and selectivity and try to identify its role in the activation process. We postulated that simple modification of the secondary amide substituent would impact its H-bonding character and potentially increase the reaction selectivity. Thus, various cyclic aromatic β -ketoamides **1b–g** were reacted with methylvinylketone (**2a**) under the optimized conditions to afford the corresponding Michael adducts with good to high yields and high ee values (Table 2).

Table 2. Effect of the Amide Nature on the Enantioselectivity^a

entry	R	4	time (h)	yield (%) ^b	ee (%) ^c
1	1-naphthyl (1b)	(-)- 4b	48	90	91
2	1-anthracenyl (1c)	(-)- 4c	96	98	90
3	<i>p</i> -NO ₂ C ₆ H ₄ (1d)	(-)- 4d	72	62	97
4	<i>p</i> -MeOC ₆ H ₄ (1e)	(-)- 4e	40	98	83
5	<i>m</i> -MeOC ₆ H ₄ (1f)	(-)- 4f	48	64	83
6	Tosyl (1g)	(-)- 4g	72	88	98
7	Tosyl (1g)	(+)- 4g	72	90	99 ^d

^a A solution of **1** (1 equiv), **2a** (2 equiv), and catalyst (*R,R*)-**3f** (10 mol %) in toluene (0.05 M) was stirred until full conversion. ^b Isolated yield after purification by column chromatography on silica gel. ^c Determined by HPLC on a chiral stationary phase. ^d In this case, catalyst (*S,S*)-**3f** was used, vide infra.

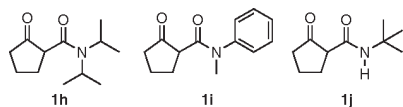
As expected, the modifications that operated on the amide function had a significant impact on the reaction selectivity. Indeed, substrates with polyaromatic substituents **1b** (entry 1) and **1c** (entry 2) or electron-withdrawing group-substituted aniline **1d** (entry 3) led to high ee's, whereas aniline derivatives **1e** (entry 4) and **1f** (entry 5) bearing an electron-donating substituent on the aromatic ring were revealed to be less efficient.

From these experimental data, we surmised that the observed ee's might be correlated to the acidity of the proton of the amide function. Although this is a simplistic hypothesis,¹⁸ we intended to verify it with substrate **1g** derived from tosylamide.¹⁹ To our delight, the TUC-**3f** catalyst efficiently activated this substrate providing the desired Michael adduct **4g** with the highest ee (Table 2, entry 6). Then, to confirm the importance of the presence

(18) For a complete study on the p*K*_a slide rule, see: Gilli, P.; Pretto, L.; Bertolasi, V.; Gilli, G. *Acc. Chem. Res.* **2009**, *42*, 33.

(19) Presset, M.; Coquerel, Y.; Rodriguez, J. *J. Org. Chem.* **2009**, *74*, 415.

(20) See Supporting Information for experimental details. Unreactive substrates **1h–j**.



of a proton on the amide function, we ran additional experiments with various substrates under the standard conditions.²⁰ First, we were pleased to note that neither aliphatic **1h** nor aromatic tertiary amides **1i** showed any significant reactivity even after a long reaction time. Also, the sterically crowded and electron-rich aliphatic secondary β -ketoamide **1j** (R = *t*-Bu), with a less acidic amide proton, remained totally unreactive, highlighting the crucial role of the proton in the activation of the substrate.²¹

To lend further credence to the hypothesis of a proposed correlation between ee and the acidity of the N–H proton, we performed theoretical calculations,²⁰ to determine the N–H p*K*_a values of ketoamides **1a**, **1d**, **1g**, and **1j**. As depicted in Figure 1, a direct correlation has been evidenced, clearly indicating that the ee increased with the acidity of the amide proton. This theoretical study also revealed that the N–H p*K*_a value of the amide **1j** bearing a *tert*-butyl substituent is much higher than that of aromatic amides, preventing its participation in activating H-bonding interactions.

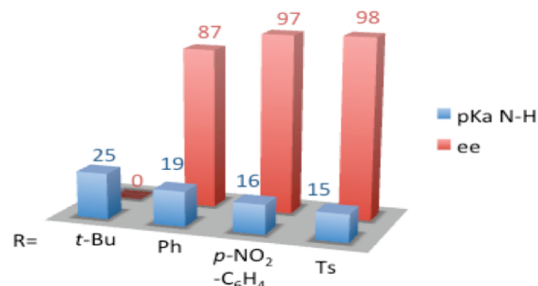


Figure 1. Correlation between ee and p*K*_a (NH).

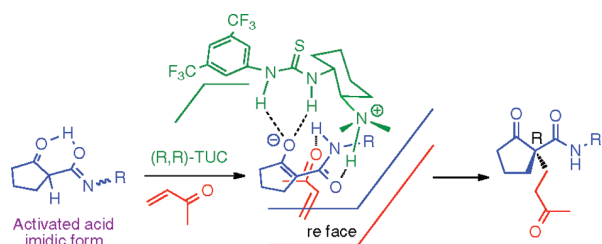
To understand the enantioselective outcome of this transformation, it was of main interest to assess the absolute configuration of the newly created stereogenic center. This was made possible by single crystal X-ray analysis of adduct **4d**.^{20,22} In addition, the (+)-(*S*)-enantiomer of **4g** has been also obtained with a very high ee, using catalyst *S,S*-**3f** (Table 1, entry 7). The absolute configurations of the stereogenic centers of both enantiomers of adduct **4g** were determined by comparison of experimental and calculated Vibrational Circular Dichroism (VCD) spectra.²⁰

At this early stage of the study, the mode of action of the catalyst is not known with certitude, but the stereochemical data combined with our experimental observations concerning the decisive role of the amide N–H moiety prompted us to propose a transition-state model (Scheme 2). In the presence of the bifunctional catalyst, the activated acid imidic form would favor the base-catalyzed abstraction of the

(21) We observed a similar effect with α -ketoamides in organocatalyzed conjugate addition to nitroolefins: Baslé, O.; Raimondi, W.; Sanchez Duque, M. M.; Bonne, D.; Constantieux, T.; Rodriguez, J. *Org. Lett.* **2010**, *12*, 5246.

(22) CCDC 798318 contains the supplementary crystallographic data for this paper which can be obtained free of charge from The Cambridge Crystallographic Data Centre (www.ccdc.cam.ac.uk/data_request/cif).

Scheme 2. Transition-State Model for the Michael Addition of β -Ketoamides



exposed methine proton to generate a reactive enolate intermediate stabilized by the thiourea function. Subsequently, the resulting protonated tertiary amine would coordinate the basic oxygen atom of the tautomeric amide form, resulting in the formation of an ion pair complex in which only the *re* face of the enolate is accessible. As a consequence, the acidic amide N–H would be free to activate the carbonyl of the acceptor, according to Miller's model.¹⁰ This proposed double activation of both the substrate and acceptor by the (*R,R*)-TUC catalyst may account for the observed *R* absolute configuration and highlights the crucial cooperative role of the N–H proton in the activation.

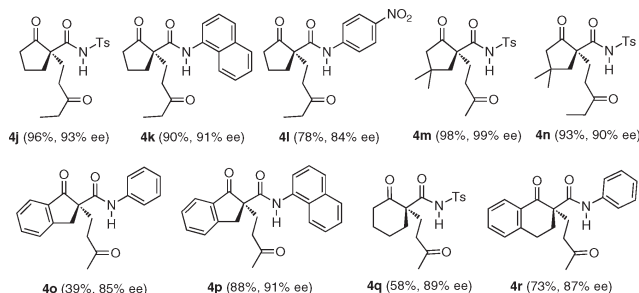


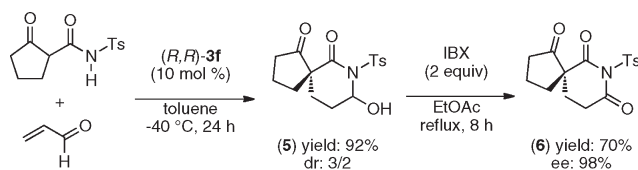
Figure 2. Scope of the enantioselective Michael addition.

The next step was the investigation of the scope of the process compiled in Figure 2. Various cyclic substrates were reacted with either methyl- or ethylvinylketone to afford the corresponding adducts **4j–r** in good yields and high ee's up to 99%. This methodology works well with five- and six-membered cyclic compounds, and tosyl and naphthyl derivatives generally give the best results. Substituted indanones and tetralones proved also to be suitable substrates, allowing this methodology to generate complex structure diversity **4o,p,r** without altering the enantioselective potential of the process.

We then investigated the use of enals in place of enones (Scheme 3). To our delight, the (*R,R*)-**3f**-catalyzed reaction

(23) The ee of **5** was not determined because of its instability under chiral HPLC analysis conditions.

Scheme 3. Synthesis and Oxidation of Hemi-aminal **5**



between β -ketoamide **1g** and acrolein, in toluene at $-40\text{ }^{\circ}\text{C}$, produced the spiro-hemiaminal **5** as a 3/2 mixture of two diastereomers according to a domino Michael addition–spiro-hemiacetalization sequence.²³ Oxidation of **5** afforded the corresponding spiroimide **6** isolated with an excellent ee of 98%. This methodology opens the way to a general access to various aza-spiro compounds²⁴ under an optically active form,²⁵ which is of prime importance since biological activities are frequently associated with the asymmetric spiro-carbon atom.²⁶

In summary, we have developed the first organocatalytic enantioselective conjugate addition of α -substituted β -ketoamides to unsaturated carbonyls by bifunctional catalysts, involving an unprecedented cooperative effect of the amide function in the activation of these pronucleophiles. The corresponding adducts containing a highly functionalized all-carbon quaternary stereocenter are obtained in good yields and high to excellent ee's. The synthetic potential of the products bearing the extra amide function was highlighted using acrolein through a new domino spiroannulation leading to a synthetically valuable intermediate precursor of highly enantioenriched spiro-heterocycles of biological and synthetic interest.


Acknowledgment. This work was supported by the Agence Nationale de la Recherche (ANR-07-CP2D-06), the Université Paul Cézanne, the CNRS, and the Centre Régional de Compétences en Modélisation Moléculaire de Marseille (CR-CMM). Dr. Nicolas Vanthuyne (*ee* measurements), Dr. J.-V. Naubron (VCD analysis), and Dr. M. Giorgi (X-ray analysis) are gratefully acknowledged.

Supporting Information Available. Experimental procedures, NMR spectra, chiral HPLC chromatograms, and cif file of **4d**. This material is available free of charge via the Internet at <http://pubs.acs.org>.

(24) Zhou, C.-Y.; Che, C.-M. *J. Am. Chem. Soc.* **2007**, *129*, 5828. Adam, A. W.; Boehmer, J.; Dixon, D. J. *Angew. Chem., Int. Ed.* **2007**, *46*, 5428. Habib-Zahmani, H.; Viala, J.; Hacini, S.; Rodriguez, J. *Synlett* **2007**, 1037. Boddaert, T.; Coquerel, Y.; Rodriguez, J. *Adv. Synth. Catal.* **2009**, *351*, 1744. Li, M.; Dixon, D. J. *Org. Lett.* **2010**, *12*, 3784. Presset, M.; Coquerel, Y.; Rodriguez, J. *Org. Lett.* **2010**, *12*, 4212.

(25) To our knowledge, there is only one isolated example of an optically pure spiro-lactam of this type reported in the literature: Hilmey, D. G.; Paquette, L. A. *Org. Lett.* **2005**, *7*, 2067.

(26) Meng, X.; Maggs, J. L.; Pryde, D. C.; Planken, S.; Jenkins, R. E.; Peakman, T. M.; Beaumont, K.; Kohl, C.; Park, B. K.; Stachulski, A. V. *J. Med. Chem.* **2007**, *50*, 6165. Nakagawa, A.; Uno, S.; Makishima, M.; Miyachi, H.; Hashimoto, Y. *Bioorg. Med. Chem.* **2008**, *16*, 7046.

Organocatalysis | *Hot Paper* **Origin of the Enantioselectivity in Organocatalytic Michael Additions of β -Ketoamides to α,β -Unsaturated Carbonyls: A Combined Experimental, Spectroscopic and Theoretical Study**

Adrien Quintard,^[a] Diana Cheshmedzhieva,^[b, e] Maria del Mar Sanchez Duque,^[a]
Anouk Gaudel-Siri,^[b] Jean-Valère Naubron,^[c] Yves Génisson,^[d] Jean-Christophe Plaquevent,^[d]
Xavier Bugaut,^[a] Jean Rodriguez,^{*[a]} and Thierry Constantieux^{*[a]}

Abstract: The organocatalytic enantioselective conjugate addition of secondary β -ketoamides to α,β -unsaturated carbonyl compounds is reported. Use of bifunctional Takemoto's thiourea catalyst allows enantiocontrol of the reaction leading either to simple Michael adducts or spirocyclic aminals in up to 99% ee. The origin of the enantioselectivity has

been rationalised based on combined DFT calculations and kinetic analysis. This study provides a deeper understanding of the reaction mechanism, which involves a predominant role of the secondary amide proton, and clarifies the complex interactions occurring between substrates and the catalyst.

Introduction

Recent years have witnessed an explosive growth in the field of asymmetric organocatalysis, which is now considered as one of the three pillars of enantioselective synthesis, together with biocatalysis and organometallic catalysis.^[1] Compared to these last two well-established modes of activation, organocatalysis can deliver complementary or orthogonal selectivities. Although still in its adolescence,^[2] this hot research topic has already demonstrated its high potential for the enantioselective

formation of carbon–carbon or carbon–heteroatom bonds, and is being increasingly applied in multiple bond-forming transformations^[3] such as one-pot,^[4] domino^[5] and multicomponent procedures,^[6] including in the total synthesis of complex molecules.^[7] Current developments mainly focus on the design of new catalysts and the identification of new modes of activation for the discovery of original reactivities. However, to convert these scientific advances into synthetically useful organic transformations, especially for the implementation of an academic process to industry,^[8] a clear understanding of the mechanism of a new organocatalysed reaction is fundamental and will help to define its scope and limitations.^[9] In this sense, recent significant advances have blossomed from experimental investigations combined with computational explorations,^[10] resulting in an enrichment of the modern toolbox of asymmetric synthesis with environmentally-friendly methods.

In the context of our ongoing efforts in the development of domino and multicomponent reactions from 1,2- and 1,3-dicarbonyl derivatives to reach polyfunctionalised heterocycles in a regio- and/or stereoselective manner,^[11,12] we recently turned our attention to the use of 1,3-ketoamides as substrates.^[13] Compared with the corresponding intensively studied 1,2- and 1,3-ketoesters, these pronucleophiles have received considerably less attention in such processes. Nevertheless, they possess an additional aza-nucleophilic function that can be used to tune their reactivity and is of great synthetic value for subsequent derivatisation reactions or domino cascades.^[14] As an illustration of this high but still unexplored synthetic potential, we pioneered in 2005 the use of β -ketoamides in multicomponent reactions by reporting a molecular sieves-promoted diastereoselective three-component reaction that leads to original bicyclic compounds with a 2,6-DABCO (diazabicyclo[2.2.2]octane) type core.^[15] In this Michael addition-initiated se-


[a] Dr. A. Quintard, Dr. M. M. Sanchez Duque, Dr. X. Bugaut, Prof. J. Rodriguez, Prof. T. Constantieux
Aix Marseille Université
Centrale Marseille
CNRS, iSm2 UMR 7313
13397, Marseille (France).
Fax: (+ 33)491-289-187
E-mail: jean.rodriguez@univ-amu.fr
thierry.constantieux@univ-amu.fr

[b] Dr. D. Cheshmedzhieva, Dr. A. Gaudel-Siri
Aix Marseille Université - CNRS
Institut de Chimie Radicale (UMR-7273)
Marseille (France).

[c] Dr. J.-V. Naubron
Spectropole - Aix Marseille Université
13397, Marseille (France).

[d] Dr. Y. Génisson, Dr. J.-C. Plaquevent
Université Paul Sabatier - Toulouse III, CNRS
UMR 5068 LSPCMIB
Toulouse (France).

[e] Dr. D. Cheshmedzhieva
Present address : Faculty of Chemistry and Pharmacy
University of Sofia
1164 Sofia (Bulgaria).

 Supporting information for this article is available on the WWW under <http://dx.doi.org/10.1002/chem.201404481>.

quence, the β -ketoamide acts as a dual C,N bis-nucleophile. However, when we turned our attention to the development of an organocatalysed enantioselective version of this reaction,^[16] we realised that the activation of simple β -ketoamides by small chiral organic molecules had not been previously reported. This fact prompted us to develop our own methodology for the organocatalysed enantioselective Michael addition of β -ketoamides to enals and enones. Thus, in a preliminary communication,^[17] we identified bifunctional tertiary amine-thiourea derivatives as excellent catalysts for the activation of secondary α -substituted- β -ketoamides¹⁸ leading enantioselectively to Michael adducts containing an all-carbon quaternary stereogenic centre (Figure 1).^[19] These products constitute valuable synthetic platforms from which to access more complex chiral building blocks by cascade sequences or post-functionalisation. Moreover, this study highlighted a crucial role played by the hydrogen atom of the amide moiety, allowing us to disclose an unprecedented activation mode for these pronucleophiles.

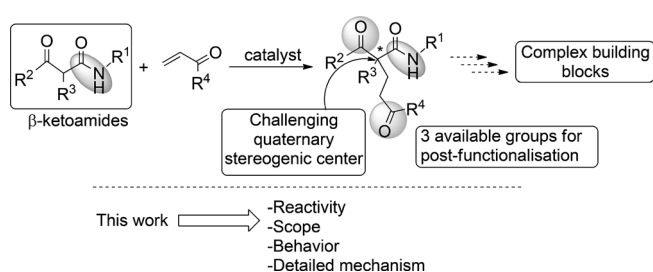


Figure 1. Interest and challenges associated with the asymmetric Michael addition of β -ketoamides to α,β -unsaturated carbonyls.

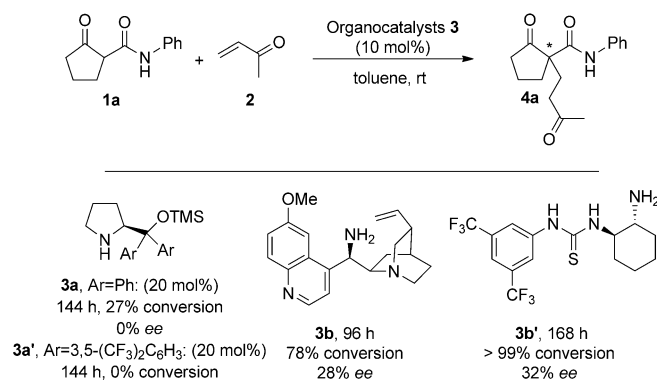
The aim of this article is to shed light on the unique role of the hydrogen atom of the amide in determining both the reactivity and the enantiocontrol in Michael addition reactions of secondary β -ketoamides to enones and enals. Based on the X-ray determination of the absolute configuration of the newly created all-carbon quaternary centre, combined with a kinetic study and a detailed theoretical investigation, a mechanism is proposed that correlates with the observed enantioselectivities, arising from the predominant role of the secondary amide proton, and the complex interactions occurring between substrates and the catalyst. With this rationale in hand, the scope of the conjugate addition and some synthetically useful post-functionalisation reactions of the adducts are also presented.

Results and Discussion

Optimisation and scope

When we started our study, the organocatalysed activation of β -ketoamides toward nucleophilic addition was unknown. However, in parallel to our investigations, some efficient asymmetric cascade reactions involving Michael addition of related β -amidoesters to α,β -unsaturated aldehydes were reported.^[17b-h] In these studies, the strategy was based not on

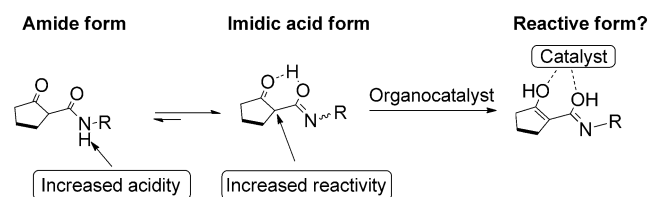
the activation of the pronucleophile by an organocatalyst, but on the activation of the electrophile through the formation of an iminium intermediate by reaction with chiral secondary amines.^[20] In all cases, the corresponding adducts evolve through the formation of a cyclic hemiaminal. To avoid this type of cascade reaction, that is, to stop the reaction at the formation of the adduct, and to control its enantioselective formation, we decided first to focus on the conjugate addition of α -substituted β -ketoamides to α,β -unsaturated ketones. Thus, we started our study by exploring the application of structurally different catalysts in the addition of β -ketoamide **1a**^[21] to methyl vinyl ketone (**2**) (Scheme 1).^[22] At the outset, as de-



Scheme 1. Iminium catalysts screening in the organocatalytic conjugate addition of **1a** to **2**.

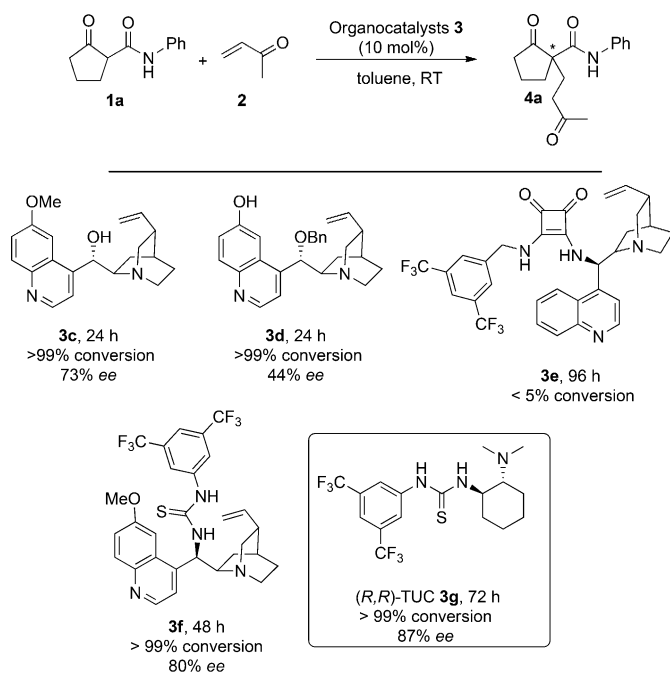
scribed for the organocatalytic conjugate addition of β -amidoesters to enals, we tested a strategy based on simple activation of the electrophile through potential iminium ion formation. Unfortunately, by using secondary amine catalysts **3a** or **3a'**, almost no reaction was observed. Alternatively, the use of primary amines **3b** and **3b'**, which are known to be good catalysts for the activation of unsaturated ketones,^[23] only provided the Michael adduct with moderate levels of enantiocontrol (28 and 32% ee) and at low reaction rate.

These disappointing results showed that simple activation of the electrophile was insufficient in the case of β -ketoamides to promote both good reactivity and enantiocontrol, but strongly suggested that bifunctional entities might be appropriate catalysts for our purpose. Indeed, literature studies on proton exchanges indicated that NH-containing β -ketoamides can be in equilibrium with their imidic acid form (Scheme 2).^[24]



Scheme 2. Specific behaviour of β -ketoamides and potential activation.

This particular behaviour with an apparent acidic proton, indicated a potential for applying bifunctional thiourea-based catalysts.^[19d,25] Notably, this unexplored acid imidic form should increase the reactivity of the starting material by favouring the equilibrium toward a more reactive enol/enolate with the aid of an appropriate catalyst. The bifunctional character of the catalyst should also activate the acceptor, leading to a highly defined transition state and thus achieving good enantiocontrol. To validate this hypothesis, different bifunctional organocatalysts were screened in the test reaction (Scheme 3).



Scheme 3. Selected bifunctional catalysts screening in the organocatalytic conjugate addition of **1a** to MVK **2**.

It rapidly became clear that the presence on the catalyst of a tertiary amine together with at least one acidic hydrogen atom was beneficial for both reactivity and enantiocontrol, confirming our dual activation hypothesis. As a result of this dual activation, cinchona derivatives **3c** and **3d**, possessing both tertiary amines and free OH, led to excellent reactivity (full conversion in 24 h) and promising levels of enantiocontrol (44–73% ee).^[26] Inserting a thiourea in catalyst **3f** slightly increased the enantioselectivity to 80% ee, whereas the squaramide catalyst **3e**, totally shut down the reactivity. Finally, the best result was obtained by applying the Takemoto thiourea catalyst *(R,R)*-TUC **3g**,^[26c] leading to the creation of the quaternary stereogenic centre with full conversion and 87% ee. Attempts to improve these preliminary results were then undertaken by optimising the reaction conditions. These efforts are summarised in Table 1. Unfortunately, although good reactivity was obtained in all cases, deviations from the original conditions (entry 1, 10 mol% **3g**, toluene, RT) led to a decrease in the enantioselectivity. It must be pointed out that the presence of water, which is a solvent that can potentially limit H-bonding interactions between the catalyst and the substrates,

Table 1. Screening of conditions for the organocatalytic conjugate addition of **1a** to MVK **2**.^[a]

Entry	3g [equiv]	Solvent	<i>t</i> [h]	<i>T</i> [°C]	ee [%] ^[b]
1	0.1	toluene	72	RT	87
2	0.1	CH ₂ Cl ₂	48	RT	86
3	0.1	H ₂ O	96	RT	11
4	0.1	toluene	40	0	83
5	0.1	CH ₂ Cl ₂	72	0	82
6	0.1	toluene	40	50	70
7	0.05	toluene	48	RT	79

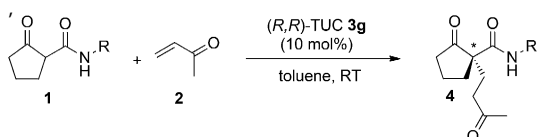
[a] A solution of **1a** (1 equiv), **2** (2 equiv), and catalyst **3g** (10 mol%) in toluene (0.05 M) was stirred until full conversion. [b] Determined by HPLC analysis on a chiral stationary phase.

dramatically reduced the enantioselectivity (11% ee; entry 3), supporting the proposed mode of activation. Finally, either changing the temperature (entries 4–6) or decreasing the catalyst loading to 5 mol% (entry 7) were also detrimental to the enantioselectivity.

Based on the postulated mechanistic importance of the amide proton on the reactivity of the β-ketoamide, we wondered whether a slight modification on the nitrogen substituent would impact the reaction profile. By appropriately designing the Michael donor, it should thus be possible to modulate both reactivity and enantiocontrol by favouring the H-bonding character of the donor (β-ketoamide). When a phenyl group is present on the nitrogen, modifying the steric bulk by including *ortho*-substituents on the ring hampered the reaction and reduced the stereoselectivity (Table 2, entries 1 and 2). Substrates bearing an N-substituent with extended aromatic system performed efficiently (Table 2, entries 3–5). Highly sterically demanding substrate **1b** significantly decreased the ee to 79% (entry 2), suggesting a possible repulsion with the catalyst. In contrast, 1-naphthyl or 1-anthracenyl substituent **1c** or **1e** were tolerated well, leading to the products in 91 and 90% ee, respectively (entries 3 and 5). Quite surprisingly, 2-naphthyl β-ketoamide **1d** gave slightly reduced levels of enantiocontrol (82% ee, entry 4). Alternatively, when placing a benzylic chain on the nitrogen, a dramatic drop in both reactivity and enantioselectivity was observed (46% ee, entries 6–7) whereas the inclusion of a *tert*-butyl group completely inhibited the reaction (entry 8). At first glance, these results suggested that a possible π-stacking was involved between the aromatic substituent on the nitrogen and that of the catalyst. To investigate this first hypothesis, the electronic nature of the substituent on the aromatic ring was then modulated (Table 3).

As expected, modification of the R group strongly impacted the enantioselectivity (54–99% ee). Unfortunately, attempts to favour possible π-stacking by the introduction of an electron-rich aromatic ring (entries 2–5), did not lead to any improvement in the enantioselectivity (65–83% ee) and, as expected,

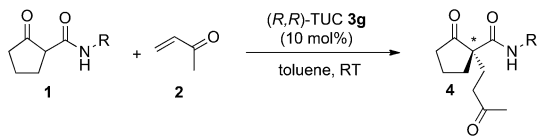
Table 2. Effect of the nature of the nitrogen substituent on substrates **1**.^[a]



Entry	R	4	t [h]	Yield [%] ^[b]	ee [%] ^[c]
1		4a	72	> 99	87
2		4b	72	70	79
3		4c	48	90	91
4		4d	72	95	82
5		4e	96	98	90
6		4f	48	26	46
7		4g	168	73	46
8		4h	168	0	–

[a] A solution of **1** (1 equiv), MVK **2** (2 equiv), and catalyst (10 mol%) in toluene (0.05 M) was stirred until full conversion. [b] Isolated after silica gel column chromatography. [c] Determined by HPLC analysis on a chiral stationary phase.

Table 3. Effect of the electronic nature of the nitrogen substituent on substrates **1**.^[a]



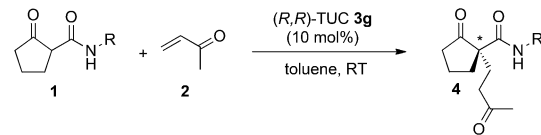
Entry	R	4	t [h]	Yield [%] ^[b]	ee [%] ^[c]
1	<i>p</i> -MeOC ₆ H ₄	4i	40	98	83
2	<i>m</i> -MeOC ₆ H ₄	4j	48	64	83
3	<i>o</i> -MeOC ₆ H ₄	4k	72	75	65
4	<i>m,m'</i> -(MeO) ₂ C ₆ H ₃	4l	20	nd	82
5	<i>p</i> -FC ₆ H ₄	4m	96	82	80
6	<i>p</i> -(CF ₃) ₂ C ₆ H ₄	4n	96	87	82
7	<i>p</i> -(CN) ₂ C ₆ H ₄	4o	24	96	78
8	<i>p</i> -(NO ₂) ₂ C ₆ H ₄	4p	72	62	97
9	<i>m,m'</i> -(CF ₃) ₂ C ₆ H ₃	4q	48	87	54
10	<i>m,m'</i> -(NO ₂) ₂ C ₆ H ₃	4r	48	81	82

[a] A solution of **1** (1 equiv), MVK **2** (2 equiv), and catalyst (10 mol%) in toluene (0.05 M) was stirred until full conversion. [b] Isolated after silica gel column chromatography. [c] Determined by HPLC analysis on a chiral stationary phase.

the inclusion of a substituent in the sterically demanding *ortho*-position worsened the situation (entry 4). These results suggested that a π -stacking of this group with the catalyst was not the most important factor controlling the enantioselectivity. Placing an inductively attractive substituent in the *para* position had a moderate impact on the enantiocontrol (entries 5 and 6), whereas the mesomeric attractive *para*-nitro substituent, impressively increased the *ee* to 97% with compound **4p** (entry 8). Finally, increasing the steric demand by the introduction of a second group on the aromatic ring dramatically reduced the selectivity (54–82% *ee*; entries 9 and 10). Even though these variations could be the result of several parameters, the best enantioselectivity, found for **4p**, might be due to the higher acidity of the proton in the starting β -ketoamide. To verify this second hypothesis, we studied the influence of other electron-withdrawing groups on the nitrogen atom (Table 4).

Benzoyl substituents were found to strongly enhance the reactivity of the substrates, resulting in fast transformations even at -10°C (entries 1–3). Under these conditions, full conversion was observed in 5 min to 24 h, without any notable difference in the enantioselectivity (85–86% *ee*). Alternatively, insertion of methyl- or *p*-anisyl-sulfonyl groups did not produce a notable increase of the reactivity and conserved the same level of enantiocontrol (entries 4 and 5). To our delight, tosylamide **1x**, provided the Michael adduct in a perfect 99% *ee* and 88% yield, validating our hypothesis (entry 6). This result indicates

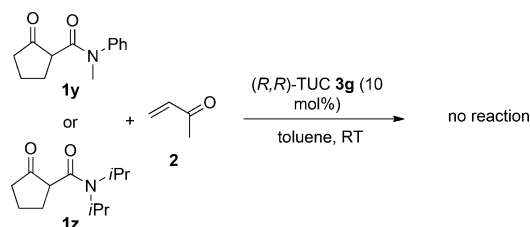
Table 4. Effect of the nature of the nitrogen substituent on substrates **1**.^[a]



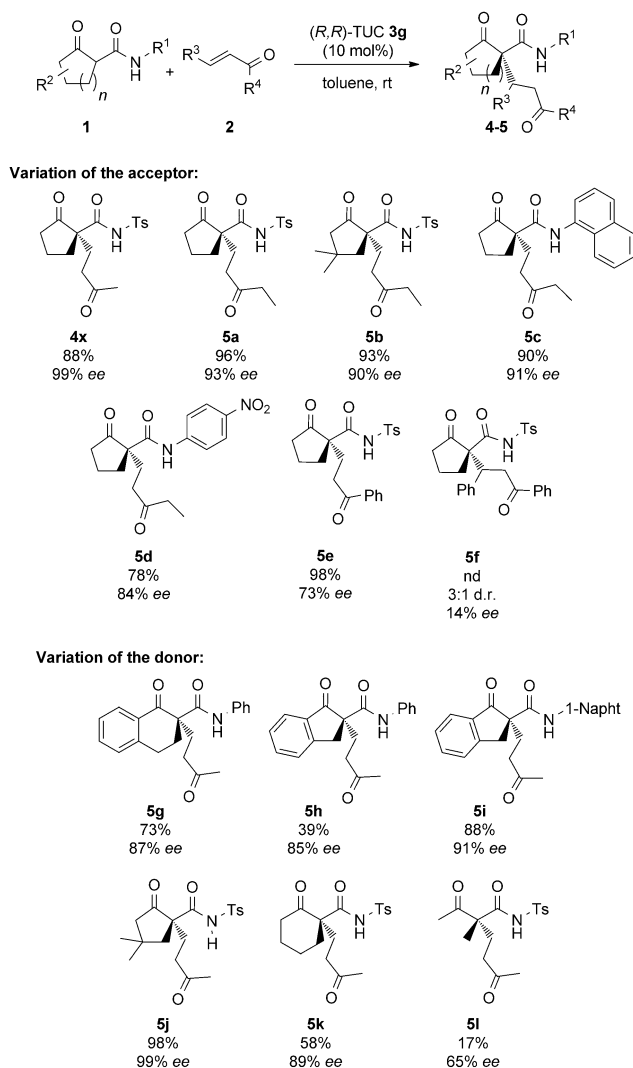
Entry	R	T [°C]	4	t [h]	Yield [%] ^[b]	ee [%] ^[c]
1		RT	4s	5 min	94	85
2		-10°C	4t	20	86	85
3		-10°C	4u	24	99	86
4		-10°C	4v	120	94	85
5		RT	4w	72	40	89
6		RT	4x	72	88	99

[a] A solution of **1** (1 equiv), MVK **2** (2 equiv), and catalyst (10 mol%) in toluene (0.05 M) was stirred until full conversion. [b] Isolated after silica gel column chromatography. [c] Determined by HPLC analysis on a chiral stationary phase.

the crucial importance of the secondary amide proton on the enantioselectivity of the reaction. To confirm this role, we tested two substrates **1y** and **1z**, possessing a tertiary amide motif (Scheme 4). In full agreement with our expectation, absolutely no reaction was observed in either case, highlighting the crucial role of the secondary amide proton for the substrate activation.^[27]



Scheme 4. Michael addition in the presence of a tertiary amide.



Scheme 5. Scope of acceptors and donors in the enantioselective Michael addition.

With this accumulated knowledge on the role of the amide substituent, we then decided to investigate the scope of this process by focusing on the partner structures. First modifications were performed on the Michael acceptor (enones, Scheme 5). Besides methyl vinyl ketone (MVK; **2**), the parent ethyl vinyl ketone was also well tolerated, leading to Michael adducts **5a–d** in 84–93% ee. Phenyl vinyl ketone also reacted well with the β -ketoamide **1x**, giving adduct **5e** in 98% yield, albeit with decreased enantiocontrol (73% ee). Finally, increasing the substitution at the β -position of the enone considerably decreased the stereoselectivity, and **5f** was obtained with a 3:1 d.r. and 14% ee, indicating a poor tolerance for this type of compound.^[28]

Concerning the Michael donor, various β -ketoamides could also be efficiently applied in this transformation (Scheme 5). Totally different backbones were well tolerated in this process: Various cyclic five- and six-membered β -ketoamides could be applied, generating structurally diverse compounds **5g–k** in usually good enantioselectivities (85–99% ee). In the case of **5g–i**, difficulties in preparing the starting *N*-tosylamides forced us to use the parent *N*-phenyl or *N*-naphthyl substrates, however preserving a good level of enantioselectivity (85–91% ee). In contrast, with an acyclic β -ketoamide, both reactivity and stereocontrol were considerably decreased (**5l**; 17% yield, 65% ee). This suggests that a greater level of rotational freedom is not tolerated on the β -ketoamide and that conformational rigidity is a prerequisite for better efficiency.

Mechanistic study and determination of the activation mode

Experimental Study

Having pointed out the broad substrate scope of this new transformation, we then focused on its particular mechanism. Notably, given the bifunctional character of the catalyst and the unusual structure of the Michael donor, the question of the possible interactions and activation modes occurring during the process remains open.

At first, to better understand this transformation, the absolute configurations of the obtained products were determined. As previously reported in our preliminary communication,^[17a] single-crystal X-ray analysis of **4p** indicated an *R* absolute configuration on the Michael adduct. VCD spectroscopy was also used to determine the absolute configurations of **4p**, **4x** and **4c**. Thus, based on the vibrational excitonic coupling model proposed by Taniguchi et al.,^[29] we have confirmed the absolute configuration *R* of **4p** and established that **4x**^[17a] and **4c** are also *R* enantiomers.^[30] A complete study of the VCD analyses will be published later in full details.

To shed light on the potential activation mode of the substrate with the catalyst, we undertook several other mechanistic experiments. First we investigated the change in the NMR spectra recorded with a stoichiometric mixture of starting β -ketoamide **1x** and catalyst **3g** (Figure 2). A clear and instantaneous modification was observed in CD₃CN whereas several days were required in [D₆]-toluene (see the Supporting Information). First, the persistence of a triplet for proton 2 at 2.95 ppm

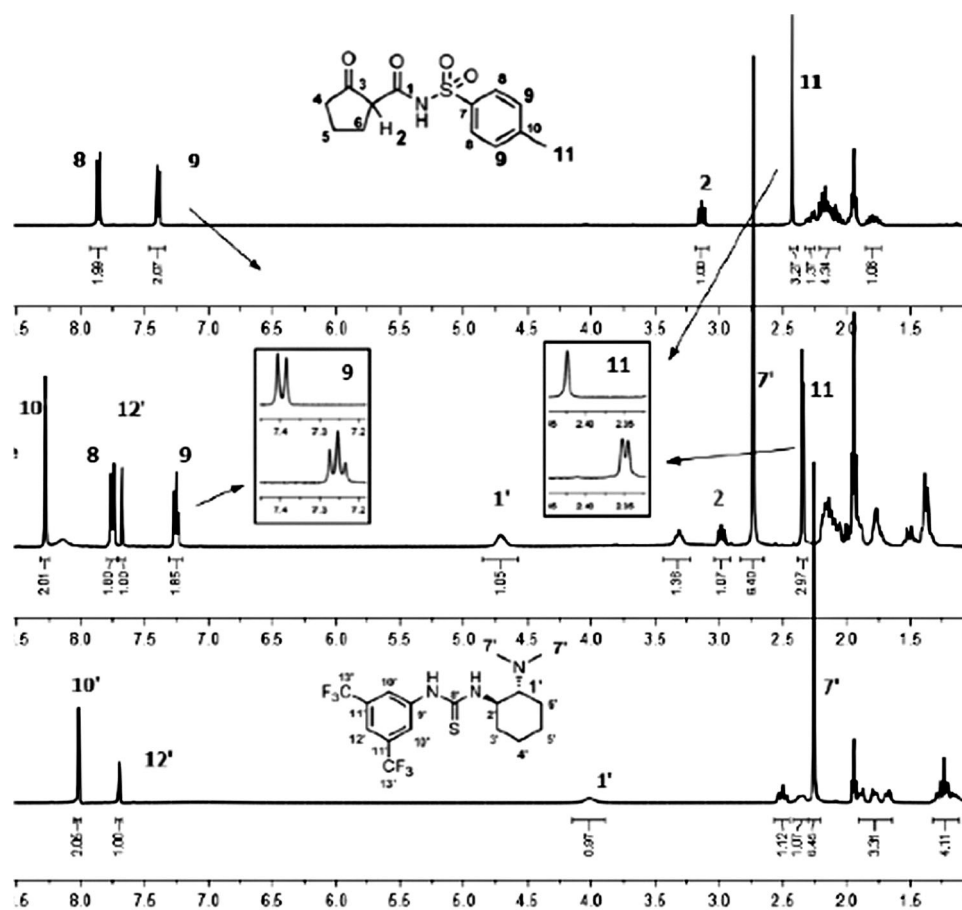


Figure 2. ^1H NMR spectroscopic study of a mixture of β -ketoamide **1x** and **3g** in CD_3CN . (Top) β -ketoamide **1x**; (centre) 1:1 mixture; (bottom) **3g**.

(Figure 2, centre) indicates that the enol form of the substrate was not present. Consistent with this finding, a strong downfield shift operating on proton $1'$ ($\Delta = 0.5$ ppm) together with a strong downfield shift on protons $7'$ of the dimethyl amino substituent of the catalyst ($\Delta = 0.7$ ppm) indicates the presence of a hydrogen bond. Finally, it must be pointed out that aromatic protons **8** and **9**, and protons $10'$ and $12'$ from the substrate and catalyst, respectively, are also significantly shifted, indicating a probable interaction between these two groups. Although we cannot draw direct conclusions for the structure, this simple NMR experiment clearly indicates the presence of a relatively strong interaction between the catalyst **3g** and β -ketoamide **1x**.

With these preliminary NMR experiments, we then decided to undertake a kinetic analysis of the described transformation. First, the reaction profile was determined by following the conversion by ^1H NMR spectroscopic analysis in $[\text{D}_8]$ -toluene (Figure 3). The obtained curve indicates a fast initial rate without any induction period. The decrease in reactivity observed after a relatively short period of time is characteristic of either catalyst decomposition or inhibition by the product, but can also be attributed to the reversibility of the reaction. However, mixing back the Michael adduct with 10 mol% of catalyst did

not lead to any evolution, suggesting a poor reaction reversibility.

To identify the potential inhibition pathway and the kinetically significant steps in this transformation, the order in each component was determined by independently varying their respective concentration. Given the reaction profile, the initial rate was chosen at 60 min and conversions were determined by ^1H NMR spectroscopic analysis after acidic treatment of the mixture; the results are summarised in Figure 4. As expected, a positive rate order was observed for both MVK and the catalyst (Figure 4a,c). In contrast, a zero rate order was observed for the β -ketoamide (Figure 4b).^[31] Finally, increasing the initial concentration in final Michael adduct, clearly reduced the initial reaction rate (Figure 4d). The absence of a significant primary kinetic isotopic effect ($K_{\text{H/D}} = 1.15$) when starting from $> 80\%$ deuterated β -ketoamide is also consistent with a rapid deprotonation leading to the active form (Scheme 6).

Theoretical study

With these experimental data in hand, we then attempted to complete the study with a detailed computational investiga-

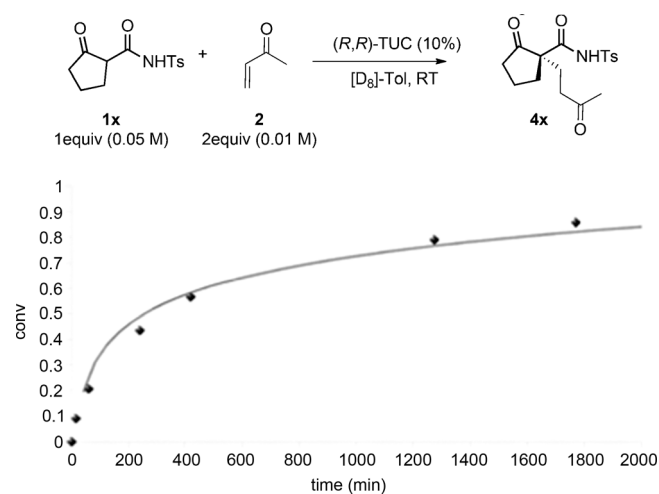


Figure 3. Kinetic profile of the reaction at 16°C .

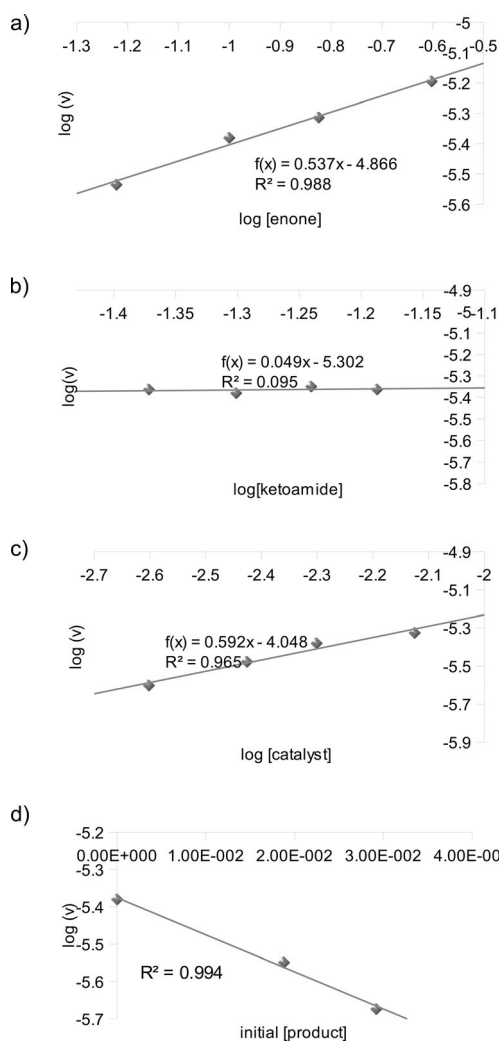
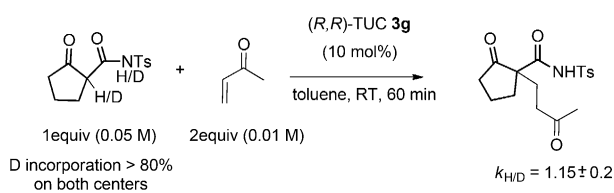


Figure 4. Initial rate dependence on the concentration of the different components: a) [enone], b) [β-ketoamide], c) [catalyst], d) [product].



Scheme 6. Deuterium kinetic isotope effect experiment.

tion. We anticipated that the calculations would help to clarify the mechanism mainly by improving our understanding of the interactions present with the bifunctional catalyst.

Tautomeric equilibrium: Computational calculations on the nature of the starting β-ketoamide have been performed with the hybrid *meta*-GGA DFT functional M06-2X^[32] with the 6-31 + G(d,p) basis set implemented in Gaussian 09.^[33] Vibrational frequencies were calculated at the same level to determine the nature of the located stationary points; zero point energies and thermodynamic data were calculated by using the specified scaling factor (0.940).^[34] The theoretical calculations on the

substrates showed that the most stable form in all the substituted β-ketoamides is the keto form. The difference between the keto and enol forms is in the range of 0.5–3.0 kcal mol⁻¹ depending on the substitution of the nitrogen atom (for **1a**, **1c**, **1i**, **1k**, **1p** and **1x**). The imidic acid form is very unstable in comparison to the keto form. For the tosyl substituted β-ketoamide **1x** (Figure 5), the imidic acid form **Ax** is 9.03 kcal mol⁻¹

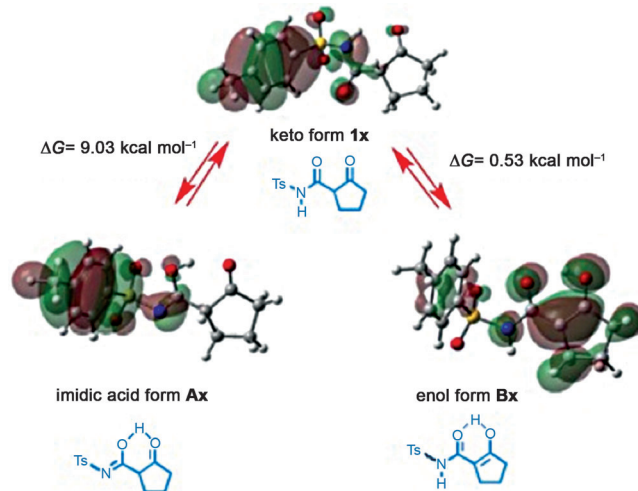


Figure 5. The HOMO orbitals for keto form **1x**, imidic acid form **Ax** and enol form **Bx**.

higher in energy. Both **Ax** and **Bx** have an intramolecular H-bond, but the observed relative higher stability of **Bx** can be attributed to the extension of conjugation. The HOMO orbitals in amide, enol and imidic acid forms are represented in Figure 5.

Reaction mechanism: With these preliminary indications on the β-ketoamide behaviour, a detailed study on the reaction mechanism has been carried out. The computations have been performed with the hybrid *meta*-GGA DFT functional M06-2X,34 with the 6-31G(d) basis set. The functional was chosen based on a model calibration carried out for the prediction of keto-enol tautomeric equilibrium and literature data.^[34,35] Full geometry optimisations in toluene were carried out for all the stationary points along the reaction path by using IEFPCM formalism.^[36] There was no significant difference found between the transition-state structures in the gas phase and in solvent. Vibrational frequencies were calculated at the same level to determine the nature of the located stationary points; zero point energies and thermodynamic data were calculated by using the specified scaling factor (0.947).^[37] All transition-state geometries were confirmed by intrinsic reaction coordinate (IRC) calculations. Stabilisation energies of the complexes in all stationary points are BSSE-corrected (Figure 6).

To analyse the proposed transformations, we focused on three distinct parts, namely deprotonation of the β-ketoamide, the C–C bond-formation event and liberation of the catalyst. The reaction mechanism was studied for the tosyl substituted β-ketoamide **1x**, which shows the highest *ee* values in the

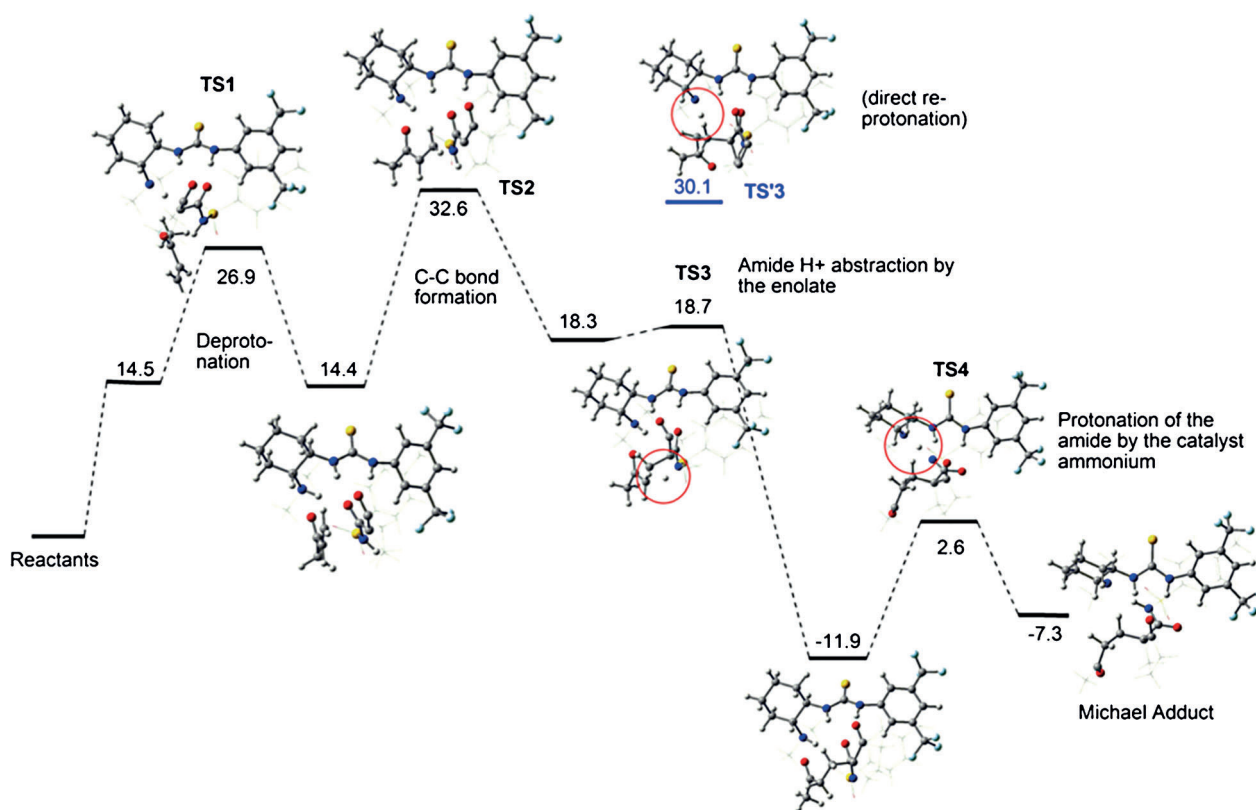


Figure 6. Relative Gibbs free energies (in kcal mol⁻¹) along the reaction coordinate.

studied series (Figure 6). The first stage of the reaction is the deprotonation of the substrate and the formation of the nucleophile (TS1). Two possible paths for the production of the reactive enolate form have been studied. Between the two acidic hydrogen atoms present on **1 x**, the more acidic is the methine proton ($pK_a=7.1$ vs. 15.4 for the NH). Even though the CH is more acidic, the energy barrier for the direct NH deprotonation (Table 5) by **3 g** is much lower than for CH deprotonation (Table 5, $\Delta G^\ddagger = 16.7$ kcal mol⁻¹). The relatively low energy barrier observed for the direct NH deprotonation (Table 5, $\Delta G^\ddagger = 1.1$ kcal mol⁻¹) is in complete agreement with the fast deprotonation observed by ¹H NMR spectroscopic analysis, mixing ketoamide and TUC only. The deprotonation of the amide hydrogen is an equilibrium process with a low barrier for the forward and reverse reaction. Even though the energy barrier is lower for the N deprotonation, it does not lead directly to a reactive form. Indeed, from this N-deprotonated intermediate, the possibility for an intramolecular hydrogen transfer and formation of the reactive enolate form were studied. All the obtained paths were very high in energy (> 46 kcal mol⁻¹), disfavouring such a process.^[38] Finally, direct enolate formation from the corresponding enol form also re-

quired a proton transfer event that was higher in energy.^[38] Based on these calculations and on the experimental observation of a fast deprotonation, it seems that the most probable path involves abstraction of the amide hydrogen of **1 x** by the organocatalyst **3 g**. This leads reversibly to an off-cycle unreactive form.

For the reaction to proceed forward, equilibrium back to the starting β -ketoamide and subsequent enolate methine hydrogen abstraction would be the preferred path (Figure 6). Subsequent coordination of the MVK to the amide hydrogen leads to the direct formation of the most stable enolate intermediate (Figure 6; $\Delta G = 14.4$ kcal mol⁻¹).

The second stage of the reaction is nucleophilic addition to the MVK, creating the new stereogenic centre (C–C bond-forming event, TS2). First, it should be noted that the C–C bond-forming step is not thermodynamically favoured because the resulting intermediate lies higher in energy than the ternary complex deprotonated β -ketoamide-protonated catalyst-MVK ($\Delta\Delta G = 3.9$ kcal mol⁻¹). Various addition possibilities leading to the formation of *R* and *S* products have been studied. The transition states differ in the enolate coordination to the catalyst and/or the approaching site of the ketone.^[38] As already described by Pápai,^[39] coordination of the β -ketoamide to the thiourea part of the Takemoto catalyst is energetically preferred, with a lower energy barrier for this C–C bond formation of 18.2 kcal mol⁻¹ ($\Delta G = 32.6$ kcal mol⁻¹). In the most favoured transition states, the β -ketoamide (pronucleophile) has an orientation that is perpendicular with the thiourea (Figure 7). Gratifyingly, the structure leading to the formation

Table 5. Energy barriers for the β -ketoamide **1 x** deprotonation.

	ΔG^\ddagger [kcal mol ⁻¹]
deprotonation from C*	16.7
deprotonation from N*	1.1

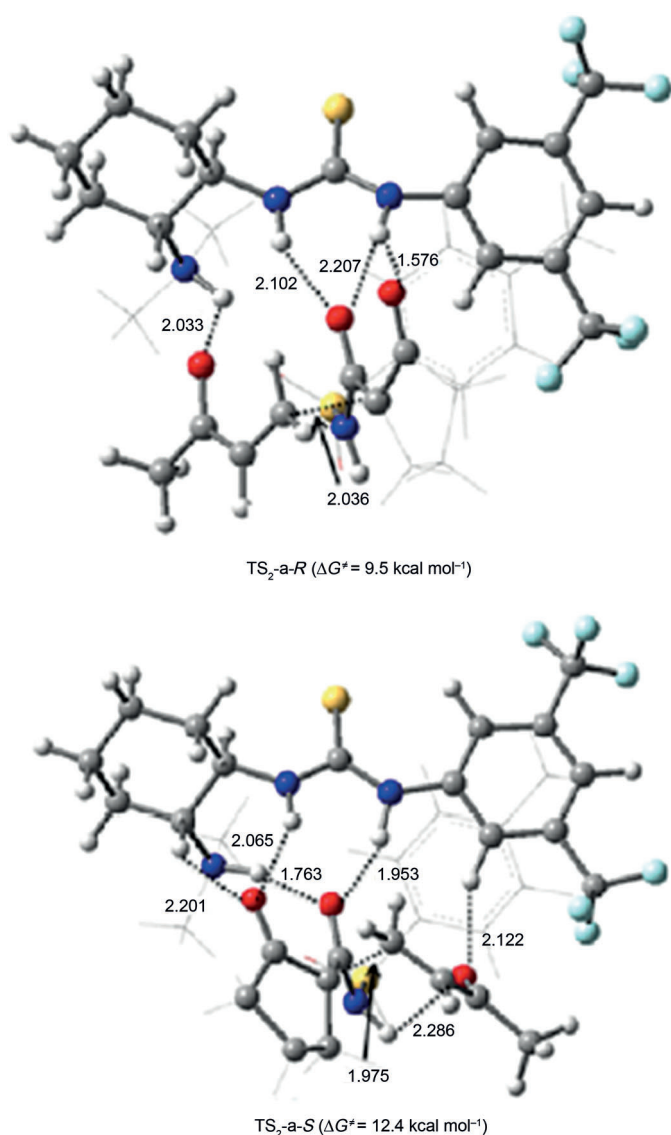


Figure 7. Optimised geometries for the preferred transition-state structures calculated for the C–C bond formation.

of the *R* adducts (Figure 7; TS₂-a-*R*) is lower in energy by 2.9 kcal mol⁻¹ over the structure leading to the formation of the *S* adducts (Figure 7; TS₂-a-*S*). This is in complete agreement with the experimentally observed 99% *ee* at room temperature using **3g**. It must be pointed out that these transition-state structures are very ordered. A network of hydrogen bonds between the catalyst and the substrate stabilises the transition state. Additional stabilisation is gained due to the π -stacking between the aromatic rings. The thiourea N–H bonds position the enolate C–O bonds with the help of a network of hydrogen bonds. At this stage, the enolate generated during the C–C bond formation must be reprotonated. Direct abstraction of the proton of the catalyst by the enolate has a barrier of 11.8 kcal mol⁻¹ (TS'3; Figure 6). Alternatively, a relay by prior abstraction of the amide proton by the enolate followed by a proton transfer from the ammonium to the amide is a greatly favoured pathway: the first of these steps is nearly barrierless (0.4 kcal mol⁻¹), whereas the second step has reasonable acti-

vation energy of $\Delta G^\ddagger = 14.5 \text{ kcal mol}^{-1}$ (TS3–TS4; Figure 6). The ease of proton transfer from the amide to the enolate, combined with the high stability of the resulting intermediate probably helps to displace the equilibrium of the thermodynamically unfavourable C–C bond-formation step. This phenomenon probably explains the experimental observation that the acidity of the amide proton is crucial for the success of the reaction. What is also notable here is that the deprotonated amide–ammonium complex is thermodynamically more stable than the separated products ($\Delta\Delta G = 4.6 \text{ kcal mol}^{-1}$; Figure 6), in complete agreement with the experimentally observed inhibition of the catalyst by the product. With both energy diagram and experimental study in hand, a complete catalytic mechanism can be drawn for the conjugate addition (Scheme 7).

Direct abstraction of the amide proton is fast and reversible (off cycle). Deprotonation from the acidic CH gives a productive ammonium enolate that can then add to MVK. This rate-determining step is highly enantioselective and gives the *R* adduct with 99% *ee*. Subsequent intramolecular proton transfer from the amide to the enolate leads to the thermodynamic ammonium salt intermediate, from which the liberation of the catalyst occurs by protonation of the amide anion. Given this mechanism, it appears that the thermodynamically demanding liberation of the catalyst can be a limitation of this reaction. We surmised that the formation of a cyclic hemiaminal inter-

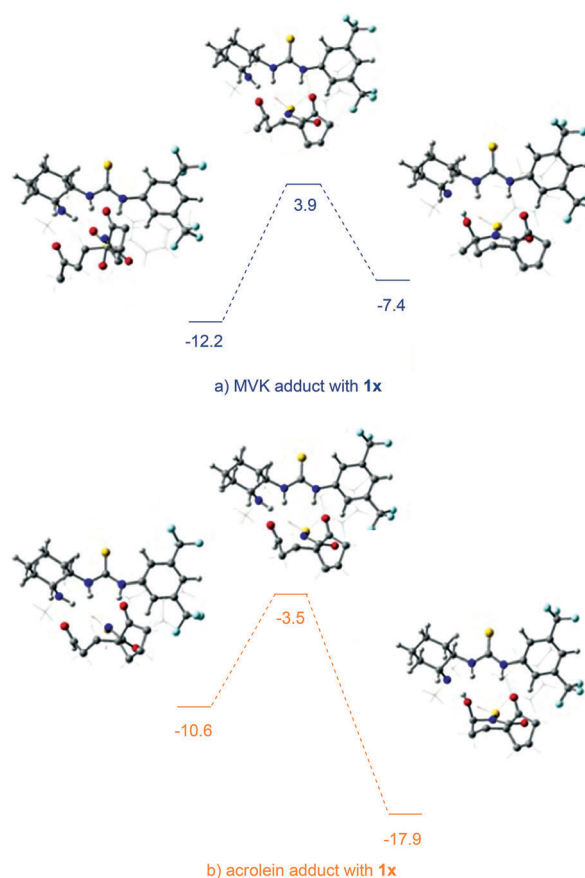
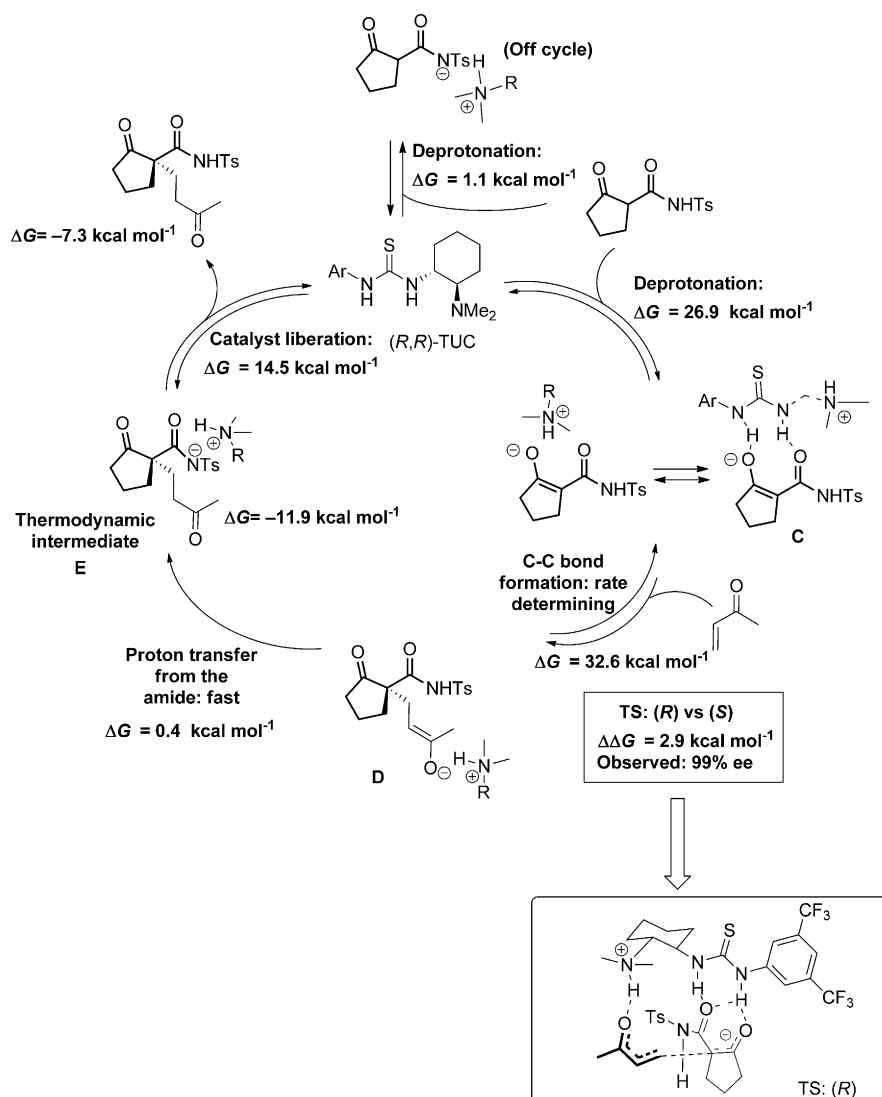


Figure 8. Gibbs free energies (kcal mol⁻¹) for the formation of the hemiaminal for a) MVK adduct with **1x**, or b) acrolein adduct with **1x**.



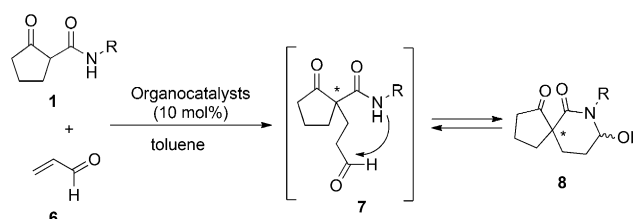
Scheme 7. Detailed catalytic cycle of the conjugate addition of substituted β -ketoamides to MVK catalysed by **3g**.

mediate, by intramolecular addition of the amide to the electrophilic carbonyl, should displace the equilibrium toward catalyst release (Figure 8). Calculations performed on the MVK adduct with **1x** confirmed that this cyclisation is kinetically demanding ($\Delta G^\ddagger = 16.1 \text{ kcal mol}^{-1}$; Figure 8a) and thermodynamically disfavoured in the case of ketones ($\Delta\Delta G = 4.8 \text{ kcal mol}^{-1}$; Figure 8a). In contrast, calculations performed on the corresponding acrolein adduct indicate a kinetically affordable ($\Delta G^\ddagger = 7.1 \text{ kcal mol}^{-1}$; Figure 8b) and thermodynamically favoured process ($\Delta\Delta G = -7.3 \text{ kcal mol}^{-1}$; Figure 8b). This intramolecular trapping strategy, already applied for the addition of unsubstituted β -ketoamide should help liberate the catalyst and possibly increase the reaction rate.^[18]

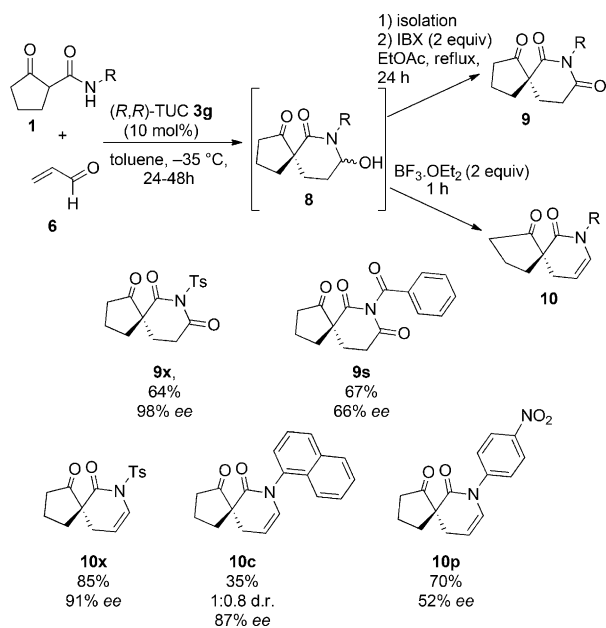
Michael addition to α,β -unsaturated aldehydes

With this clear understanding of the complete reaction mechanism and in particular of catalyst liberation, we considered ways to take advantage of the intrinsic aldehyde reactivity to

favour the catalyst turnover by pushing the formation of spiro-hemiaminals **8** (Scheme 8). Given the prevalence of this spiro skeleton in natural products and the challenge associated with its synthesis, a modular enantioselective access would be of high synthetic interest. Gratifyingly, when the addition of various β -ketoamides to acrolein was performed at low temperature (-35°C), exclusive formation of the expected spiro compounds **8** was observed (Scheme 9). As expected, the reaction was much faster than in the case of MVK, probably due to easier catalyst liberation, and full conversion was observed after 24–48 h even at this low temperature. To simplify isolation and to determine the enantioselectivity of the reactions, spiro compounds **8** were directly derivatised to the corresponding enantioenriched glutarimides **9** or dihydropyridones **10** by oxidation or dehydration, respectively. Moderate to good enantiocontrol (52–98% ee) was observed, depending on the nature of the R substituent present on the nitrogen atom. As already indicated in our preliminary study,^[17a] the enantiopurities of compounds **8** were not determined because of their instability under HPLC conditions, but we may assume that oxidised compounds **9** and their precursors **8** have the same enantiomeric excess. However, the partial racemisation observed upon dehydration (**9x** vs. **10x**, for example) may be due to the formation of an iminium intermediate under acidic conditions, for which a racemisation pathway through a retro-Michael and uncatalysed intramolecular Michael addition sequence can be envisioned.^[40] Although both heterocyclic scaffolds are important structural motives that are found in many bioactive natural products,^[41,42] to our



Scheme 8. Proposed spirocyclisation of the Michael adducts with acrolein.

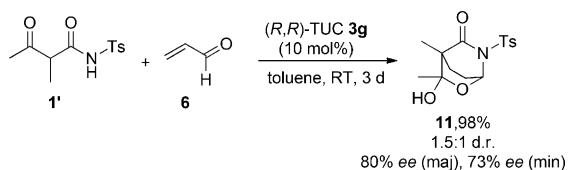


Scheme 9. Spirocyclisation by Michael addition of β -ketoamides to acrolein.

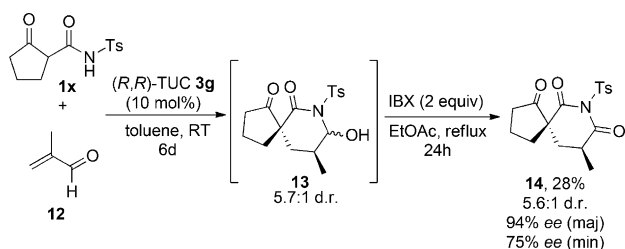
knowledge there is only one report on the direct enantioselective synthesis of glutarimides.^[43] It must be pointed out that compound **10c** is formed as a 1:0.8 mixture of two atropoisomers that could not be separated. HPLC analysis indicated a rotation energy barrier of 23 kcal mol⁻¹.^[44]

By using acyclic β -ketoamide **1'**, unexpectedly, the formation of the transient hemiaminal was followed by a hemiacetalisation, leading to the stable bicyclic compound **11** as a mixture of two diastereomers in a 1.5:1 ratio (Scheme 10). This reactivity must be due to a better freedom of the acyclic species, allowing the second cyclisation to occur. It is interesting to note that even though an acyclic β -ketoamide was used, a promising 80% ee was obtained for the major diastereomer.

Finally, substitution on the α,β -unsaturated aldehyde was then tested in this spirocyclisation (Scheme 11). Increasing the



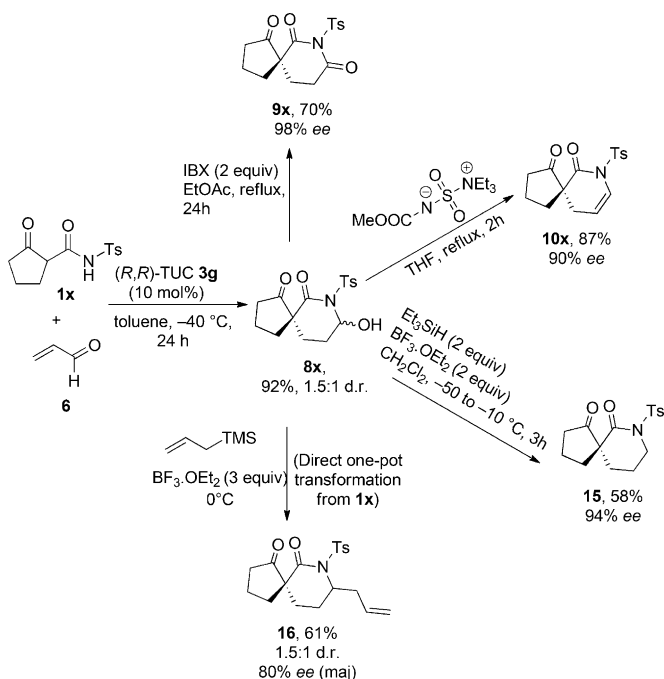
Scheme 10. Double cyclisation with acyclic β -ketoamide **11** and acrolein.



Scheme 11. Michael addition to methacrolein catalysed by (R,R) -TUC.

level of substitution on the acceptor by using methacrolein **12** considerably decreased the reaction rate (6 days for full conversion).^[45] Despite this limitation, excellent stereocontrol was obtained in this reaction, giving rise to the major diastereomer of glutarimide **14** in a 5.6:1 ratio and 94% ee after oxidation of the corresponding hemiaminal **13**.

With this straightforward access to different spiro structures, and given the potential of such scaffold in natural product synthesis, different derivatisation reactions were then undertaken with the ultimate goal of maintaining the stereochemistry of the generated stereocentres. Thus, starting from the isolated spiro compound **8x**, diverse post-functionalisation reactions could be successfully performed with good retention of the stereochemical information (Scheme 12).^[46] The corresponding



Scheme 12. Post-functionalisation reactions of spirocyclic compound **8x**.

glutarimide **9x**, dihydropyridone **10x** and 2-piperidone **15** could be obtained in 90–98% ee by using a range of oxidation/reduction methods. Finally, direct one-pot Lewis acid *N*-acyliminium formation and subsequent trapping with allyl trimethylsilane allowed the efficient introduction of another functional group in structure **16** with 80% ee and 1.5:1 d.r. on the newly formed stereocentre.

Conclusions

An asymmetric catalysed Michael addition of α -substituted β -ketoamides to various unsaturated carbonyl compounds has been developed. A complete and detailed mechanistic study has allowed us to demonstrate for the first time the unique role of the hydrogen atom of the amide in controlling both the reactivity and the enantioselectivity. With the accumulated

detailed knowledge of the reaction process, a large panel of attractive structurally different skeletons possessing a quaternary stereogenic centre have been obtained with usually high levels of enantiocontrol (up to 99% ee). Additional reactions were successfully designed leading to original spiro hemiaminals by taking advantage of the reactivity of the Michael adducts with acroleins. The utility of the obtained scaffolds was further demonstrated by several post-functionalisation reactions leading to valuable enantioenriched glutarimides and pyridones.

Given the reaction efficiency, simple protocols, wide scope and detailed mechanistic understanding, we are convinced that this study will serve as a stepping stone for the development of related transformations and should readily find applications in drug and natural products synthesis.

Experimental Section

General procedure for the enantioselective organocatalytic Michael addition of β -ketoamides to enones: α,β -Unsaturated ketone **2** (0.4 mmol, 2.0 equiv) was added at RT to a stirred solution of β -ketoamide **1** (0.2 mmol, 1.0 equiv) and *R,R*-TUC **3g** (0.02 mmol, 0.1 equiv) in anhydrous toluene (4 mL). The progress of the reaction was monitored by TLC analysis. Upon full conversion, the reaction mixture was concentrated in vacuo and the product was purified by flash column chromatography on silica gel (EtOAc/petroleum ether) to afford the desired Michael adduct. The enantiomeric excess was determined by HPLC analysis on a chiral stationary phase.

Representative description of product (4a): By following the general procedure, **4a** (99% yield) was afforded as a white solid; m.p. 66.2–69.3 °C; HPLC: ee = 87% (Chiralpak AD-H; hexane/ethanol = 90/10; flow rate = 1.0 mL min⁻¹; λ = 254 nm): t_R = 25.45 (major), 35.60 min (minor); $[\alpha]_D^{30}$ = -60.97 (c = 1.23 in CHCl₃); R_f = 0.13 (EtOAc/PE, 1:4); ¹H NMR (400 MHz, CDCl₃): δ = 8.71 (brs, 1H; NH), 7.53 (d, J = 7.7 Hz, 2H; H-8), 7.33 (t, J = 7.7 Hz, 2H; H-9), 7.11 (t, J = 7.7 Hz, 1H; H-10), 2.70–2.60 (m, 1H; H-6), 2.52 (t, J = 7.7 Hz, 2H; H-12), 2.49–2.35 (m, 2H; H-4), 2.17–2.09 (m, 1H; H-6'), 2.12 (s, 3H; H-14), 2.02–1.89 ppm (m, 4H; H-5,11); ¹³C NMR (75 MHz, CDCl₃): δ = 220.56 (C3), 206.91 (C13), 167.09 (C1), 137.53 (C7), 128.96 (2CH), 124.42 (CH10), 119.75 (2CH), 59.86 (C2), 38.69 (CH₂(4)), 38.46 (CH₂(12)), 31.54 (CH₂(6)), 30.31 (CH₂(11)), 30.04 (CH₃(14)), 18.63 ppm (CH₂(5)); HRMS (ESI): m/z calcd for [C₁₆H₁₉NO₃+H]⁺: 274.1438; found: 274.1434.

Acknowledgements

The Agence Nationale pour la Recherche (ANR-07-CP2D-06 and ANR-11-BS07-0014), the COST ORCA (CM0905), the Centre National de la Recherche Scientifique (CNRS) and the Aix-Marseille Université are gratefully acknowledged for financial support. We also thank Dr. N. Vanthuyne and M. Jean (ee measurements) and Dr. M. Giorgi (X-ray diffraction analysis). This work was supported by the computing facilities of the CRCMM, "Centre Régional de Compétences en Modélisation Moléculaire de Marseille".

Keywords: density functional calculations · enantioselectivity · Michael addition · organocatalysis · reaction mechanisms

- [1] For some recent selected reviews on asymmetric organocatalysis, see: a) A. G. Doyle, E. N. Jacobsen, *Chem. Rev.* **2007**, *107*, 5713; b) S. Mukherjee, J. W. Yang, S. Hoffmann, B. List, *Chem. Rev.* **2007**, *107*, 5471; c) S. Bertelsen, K. A. Jørgensen, *Chem. Soc. Rev.* **2009**, *38*, 2178; d) M. Bella, T. Gasperi, *Synthesis* **2009**, 1583; e) R. C. Wende, P. R. Schreiner, *Green Chem.* **2012**, *14*, 1821; f) L. Bernardi, M. Fochi, M. C. Franchini, A. Ricci, *Org. Biomol. Chem.* **2012**, *10*, 2911.
- [2] A. Dondoni, A. Massi, *Angew. Chem. Int. Ed.* **2008**, *47*, 4638; *Angew. Chem.* **2008**, *120*, 4716.
- [3] For a recent concept article from our group, see: a) D. Bonne, T. Constantieux, Y. Coquerel, J. Rodriguez, *Chem. Eur. J.* **2013**, *19*, 2218. See also: b) N. J. Green, M. S. Sherburn, *Aust. J. Chem.* **2013**, *66*, 267.
- [4] L. Albrecht, K. Jiang, K. A. Jørgensen, *Angew. Chem. Int. Ed.* **2011**, *50*, 8492; *Angew. Chem.* **2011**, *123*, 8642.
- [5] H. Pellissier, *Adv. Synth. Catal.* **2012**, *354*, 237.
- [6] For selected recent reviews, see: a) J. Yu, F. Shi, L.-Z. Gong, *Acc. Chem. Res.* **2011**, *44*, 1156; b) A. Moyano, R. Rios, *Chem. Rev.* **2011**, *111*, 4703; c) C. M. Marson, *Chem. Soc. Rev.* **2012**, *41*, 7712; d) C. de Graaff, E. Ruijter, R. V. A. Orru, *Chem. Soc. Rev.* **2012**, *41*, 3969; e) S. S. van Berkel, B. G. M. Bögels, M. A. Wijdeven, B. Westermann, F. P. J. T. Rutjes, *Eur. J. Org. Chem.* **2012**, 3543.
- [7] For selected reviews on the application of asymmetric organocatalysis to total synthesis, see: a) R. M. de Figueiredo, M. Christmann, *Eur. J. Org. Chem.* **2007**, 2575; b) E. Marqués-López, R. P. Herrera, M. Christmann, *Nat. Prod. Rep.* **2010**, *27*, 1138; c) C. Grondal, M. Jeanty, D. Enders, *Nature Chem.* **2010**, *2*, 167.
- [8] For an interesting recent highlight on the necessary factors for the application of an academic reaction to industry, see: T. W. J. Cooper, I. B. Campbell, S. J. F. MacDonald, *Angew. Chem. Int. Ed.* **2010**, *49*, 8082; *Angew. Chem.* **2010**, *122*, 8258.
- [9] For a recent review dealing with mechanistic studies in aminocatalysis, see: N. Nielsen, D. Worgull, T. Zweifel, B. Gschwend, S. Bertelsen, K. A. Jørgensen, *Chem. Commun.* **2011**, 47, 632.
- [10] P. H.-Y. Cheong, C. Y. Legault, J. M. Um, N. Celebi-Olcüm, K. N. Houk, *Chem. Rev.* **2011**, *111*, 5042.
- [11] For some recent reviews from our group, see: a) D. Bonne, Y. Coquerel, T. Constantieux, J. Rodriguez, *Tetrahedron: Asymmetry* **2010**, *21*, 1085; b) N. Isambert, M. M. Sanchez Duque, J.-C. Plaquevent, Y. Génisson, J. Rodriguez, T. Constantieux, *Chem. Soc. Rev.* **2011**, *40*, 1347; c) D. Bonne, T. Constantieux, Y. Coquerel, J. Rodriguez, *Org. Biomol. Chem.* **2012**, *10*, 3969; d) S. Gouedranche, W. Raimondi, X. Bugaut, T. Constantieux, D. Bonne, J. Rodriguez, *Synthesis* **2013**, *45*, 1909; e) X. Bugaut, D. Bonne, Y. Coquerel, J. Rodriguez, T. Constantieux, *Curr. Org. Chem.* **2013**, *17*, 1920.
- [12] Selected recent contributions from our group: a) W. Raimondi, D. Dauzonne, T. Constantieux, D. Bonne, J. Rodriguez, *Eur. J. Org. Chem.* **2012**, 6119; b) W. Raimondi, O. Baslé, T. Constantieux, D. Bonne, J. Rodriguez, *Adv. Synth. Catal.* **2012**, *354*, 563; c) A. Quintard, T. Constantieux, J. Rodriguez, *Angew. Chem. Int. Ed.* **2013**, *52*, 12883; *Angew. Chem.* **2013**, *125*, 13121.
- [13] Selected recent contributions from our group: a) C. Allais, O. Baslé, J.-M. Grassot, M. Fontaine, S. Anguille, J. Rodriguez, T. Constantieux, *Adv. Synth. Catal.* **2012**, *354*, 2084; b) D. Mailhol, M. M. Sanchez Duque, W. Raimondi, D. Bonne, T. Constantieux, Y. Coquerel, J. Rodriguez, *Adv. Synth. Catal.* **2012**, *354*, 3523; c) W. Raimondi, M. M. Sanchez Duque, S. Gouedranche, A. Quintard, T. Constantieux, X. Bugaut, D. Bonne, J. Rodriguez, *Synthesis* **2013**, *45*, 1659; d) S. Gouedranche, X. Bugaut, T. Constantieux, D. Bonne, J. Rodriguez, *Chem. Eur. J.* **2014**, *20*, 410.
- [14] For pioneering racemic cascade reaction from β -amidoesters, see: a) A. W. Pilling, J. Boehmer, D. J. Dixon, *Angew. Chem. Int. Ed.* **2007**, *46*, 5428; *Angew. Chem.* **2007**, *119*, 5524; b) A. W. Pilling, J. Böhmer, D. J. Dixon, *Chem. Commun.* **2008**, 832; c) K. M. Bogle, D. J. Hirst, D. J. Dixon, *Org. Lett.* **2010**, *12*, 1252.
- [15] a) F. Liéby-Muller, T. Constantieux, J. Rodriguez, *J. Am. Chem. Soc.* **2005**, *127*, 17176; See also: b) Z. El Asri, Y. Génisson, F. Guillen, O. Baslé, N. Isambert, M. M. Sanchez Duque, S. Ladeira, J. Rodriguez, T. Constantieux, J.-C. Plaquevent, *Green Chem.* **2011**, *13*, 2549.

- [16] We recently succeeded in the development of the enantioselective version of this reaction, see: M. M. Sanchez Duque, O. Baslé, Y. Génisson, J.-C. Plaquevent, X. Bugaut, T. Constantieux, J. Rodriguez, *Angew. Chem. Int. Ed.* **2013**, *52*, 14143; *Angew. Chem.* **2013**, *125*, 14393.
- [17] For our preliminary report on this Michael addition, see: a) M. M. Sanchez Duque, O. Baslé, N. Isambert, A. Gaudel-Siri, Y. Génisson, J.-C. Plaquevent, J. Rodriguez, T. Constantieux, *Org. Lett.* **2011**, *13*, 3296; During our investigations involving simple β -ketoamides, some work on the activation of more reactive β -amidoesters by chiral organocatalysts, and its application to enantioselective cascades have also been published, see: b) P. Jakubec, M. Helliwell, D. J. Dixon, *Org. Lett.* **2008**, *10*, 4267; c) P. Jakubec, D. M. Cockfield, D. J. Dixon, *J. Am. Chem. Soc.* **2009**, *131*, 16632; d) G. Valero, J. Schimer, I. Cisarova, J. Vesely, A. Moyano, R. Rios, *Tetrahedron Lett.* **2009**, *50*, 1943; e) J. Franzén, A. Fisher, *Angew. Chem. Int. Ed.* **2009**, *48*, 787; *Angew. Chem.* **2009**, *121*, 801; f) Z. Jin, X. Wang, H. Huang, X. Liang, J. Ye, *Org. Lett.* **2011**, *13*, 564; g) Z. Jin, F. Yu, X. Wang, H. Huang, X. Luo, X. Liang, J. Ye, *Org. Biomol. Chem.* **2011**, *9*, 1809; h) Z. Jin, H. Huang, W. Li, X. Luo, X. Liang, J. Ye, *Adv. Synth. Catal.* **2011**, *353*, 343.
- [18] More recently, proline derivatives also proved to be efficient catalysts for the activation of β -ketoamides in conjugated addition processes, see: a) W. Zhang, J. Bah, A. Wohlfarth, J. Franzén, *Chem. Eur. J.* **2011**, *17*, 13814; b) X. Wu, Q. Liu, H. Fang, J. Chen, W. Cao, G. Zhao, *Chem. Eur. J.* **2012**, *18*, 12196.
- [19] The generation of all-carbon quaternary stereocentres still constitutes a formidable challenge because of the additional steric hindrance considerations. For recent reviews highlighting works based on conjugate addition strategies to achieve this goal, see: a) S. B. Tsogoeva, *Eur. J. Org. Chem.* **2007**, 1701; b) A. Erkkilä, I. Majander, P. M. Pihko, *Chem. Rev.* **2007**, *107*, 5416; c) P. Melchiorre, M. Marigo, A. Carlone, G. Bartoli, *Angew. Chem. Int. Ed.* **2008**, *47*, 6138; *Angew. Chem.* **2008**, *120*, 6232; d) C. Palomo, M. Oiarbide, R. Lopez, *Chem. Soc. Rev.* **2009**, *38*, 632.
- [20] K. L. Jensen, G. Dickmeiss, H. Jiang, L. Albrecht, K. A. Jørgensen, *Acc. Chem. Res.* **2012**, *45*, 248.
- [21] All the β -ketoamides used in this study were prepared according to our Wolff rearrangement methodology under microwaves, see: a) M. Presset, Y. Coquerel, J. Rodriguez, *J. Org. Chem.* **2009**, *74*, 415; b) M. Presset, D. Mailhol, Y. Coquerel, J. Rodriguez, *Synthesis* **2011**, 2549.
- [22] The results of a detailed screening of 34 different catalysts is provided in the Supporting Information.
- [23] P. Melchiorre, *Angew. Chem. Int. Ed.* **2012**, *51*, 9748; *Angew. Chem.* **2012**, *124*, 9886.
- [24] a) C. L. Perrin, T. M. Dwyer, J. Rebeck Jr, R. J. Duff, *J. Am. Chem. Soc.* **1990**, *112*, 3122 and references cited herein; b) T. E. Horstmann, D. J. Guerin, S. J. Miller, *Angew. Chem. Int. Ed.* **2000**, *39*, 3635; *Angew. Chem.* **2000**, *112*, 3781; c) M. M. Vasbinder, E. R. Jarvo, S. J. Miller, *Angew. Chem. Int. Ed.* **2001**, *40*, 2824; *Angew. Chem.* **2001**, *113*, 2906; d) C. E. Jakobsche, G. Paris, S. J. Miller, *Angew. Chem. Int. Ed.* **2008**, *47*, 6707; *Angew. Chem.* **2008**, *120*, 6809.
- [25] For a general review, see: S. J. Connon, *Chem. Commun.* **2008**, 2499.
- [26] a) B. Vakulya, S. Varga, A. Csampai, T. Soos, *Org. Lett.* **2005**, *7*, 1967; b) H. Li, Y. Wang, L. Tang, F. Wu, X. Liu, C. Guo, B. M. Foxman, L. Deng, *Angew. Chem. Int. Ed.* **2005**, *44*, 105; *Angew. Chem.* **2005**, *117*, 107; c) T. Okino, Y. Hoashi, Y. Takemoto, *J. Am. Chem. Soc.* **2003**, *125*, 12672.
- [27] Such an effect was also observed in our organocatalysed addition of α -ketoamides to nitroolefins, see: O. Baslé, W. Raimondi, M. M. Sanchez Duque, D. Bonne, T. Constantieux, J. Rodriguez, *Org. Lett.* **2010**, *12*, 5246.
- [28] Neither 3-penten-2-one nor cyclohexenone reacted at all in this process.
- [29] a) T. Taniguchi, K. Monde, *J. Am. Chem. Soc.* **2012**, *134*, 3695; b) T. Asai, T. Taniguchi, T. Yamamoto, K. Monde, Y. Oshima, *Org. Lett.* **2013**, *15*, 4320.
- [30] Comparison of measured and calculated IR and VCD spectra has also been used to establish the absolute configuration of **4p**. Calculations were performed by using DFT with the B3LYP functional and the 6-311+G (d,p) basis set. Solvent effects (CH₂Cl₂) were introduced by using the polarisable continuum model IEF-PCM combined with cavities parameters SMD. Solutions with concentrations of 0.06 mol L⁻¹ (**4p**, **4x**) and 0.08 mol L⁻¹ (**4c**) in CD₂Cl₂ were used for measurements.
- [31] The low correlation observed on this slope ($R^2=0.095$) is not significant and the measured differences (less than 0.001 m on the product formed) are within the experimental error. See the Supporting Information for details.
- [32] Y. Zhao, D. Truhlar, *Acc. Chem. Res.* **2008**, *41*, 157.
- [33] Gaussian 09, Revision A.02, M. J. Frisch, G. W. Trucks, H. B. Schlegel, G. E. Scuseria, M. A. Robb, J. R. Cheeseman, G. Scalmani, V. Barone, B. Menucci, G. A. Petersson, H. Nakatsuji, M. Caricato, X. Li, H. P. Hratchian, A. F. Izmaylov, J. Bloino, G. Zheng, J. L. Sonnenberg, M. Hada, M. Ehara, K. Toyota, R. Fukuda, J. Hasegawa, M. Ishida, T. Nakajima, Y. Honda, O. Kitao, H. Nakai, T. Vreven, J. A. Montgomery, Jr., J. E. Peralta, F. Ogliaro, M. Bearpark, J. J. Heyd, E. Brothers, K. N. Kudin, V. N. Staroverov, R. Kobayashi, J. Normand, K. Raghavachari, A. Rendell, J. C. Burant, S. S. Iyengar, J. Tomasi, M. Cossi, N. Rega, J. M. Millam, M. Klene, J. E. Knox, J. B. Cross, V. Bakken, C. Adamo, J. Jaramillo, R. Gomperts, R. E. Stratmann, O. Yazyev, A. J. Austin, R. Cammi, C. Pomelli, J. W. Ochterski, R. L. Martin, K. Morokuma, V. G. Zakrzewski, G. A. Voth, P. Salvador, J. J. Dannenberg, S. Dapprich, A. D. Daniels, Ö. Farkas, J. B. Foresman, J. V. Ortiz, J. Cioslowski, D. J. Fox, Gaussian, Inc., Wallingford CT, **2009**.
- [34] I. M. Alecu, J. Zheng, Y. Zhao, D. G. Truhlar, *J. Chem. Theory Comput.* **2010**, *6*, 2872.
- [35] a) S. Steinmann, C. Corminboeuf, *J. Chem. Theory Comput.* **2011**, *7*, 3567; b) S. Ilieva, D. Cheshmedzhieva, D. Tashveva, *Tetrahedron* **2010**, *66*, 5168; c) B. Cho, C.-H. Tan, M. W. Wong, *Org. Biomol. Chem.* **2011**, *9*, 4550; d) H. Yang, M. W. Wong, *Org. Biomol. Chem.* **2012**, *10*, 3229; e) Y.-H. Lam, K. N. Houk, U. Scheffler, R. Mahrwald, *J. Am. Chem. Soc.* **2012**, *134*, 6286.
- [36] J. Tomasi, B. Mennucci, R. Cammi, *Chem. Rev.* **2005**, *105*, 2999.
- [37] <http://cccbdb.nist.gov/vibscalejust.asp>.
- [38] Full theoretical calculations can be found in the Supporting Information.
- [39] a) A. Hamza, G. Schubert, T. Soos, I. Pápai, *J. Am. Chem. Soc.* **2006**, *128*, 13151; b) T. Azuma, Y. Kobayashi, K. Sakata, T. Sasamori, N. Tokitoh, Y. Takemoto, *J. Org. Chem.* **2014**, *79*, 1805–1817. For a theoretical study on squaramide-thiourea catalysts, see also: c) B. Kótai, G. Kardos, A. Hamza, V. Farkas, I. Pápai, T. Soós, *Chem. Eur. J.* **2014**, *20*, 5631.
- [40] a) For a similar discussion, see Scheme 1 and its related paragraph in ref. [16]; b) For a similar erosion of enantiomeric excess upon dehydration of a six-membered hemiaminal, see: J.-P. Wan, C. C. J. Loh, F. Pan, D. Enders, *Chem. Commun.* **2012**, *48*, 10049.
- [41] A. Pepe, M. Pamment, Y. S. Kim, S. Lee, M.-J. Lee, K. Beebe, A. Filikov, L. Neckers, J. B. Trepel, S. V. Malhotra, *J. Med. Chem.* **2013**, *56*, 8280.
- [42] For selected examples of glutarimide-containing natural products, see: a) R. G. Powell, C. R. Smith Jr., D. Weisleder, D. A. Muthard, J. Clardy, *J. Am. Chem. Soc.* **1979**, *101*, 2784; b) T. Kagata, S. Saito, H. Shigemori, A. Ohsaki, H. Ishiyama, T. Kubota, J. Kobayashi, *J. Nat. Prod.* **2006**, *69*, 1517; c) L. L. Silva, A. C. Joussef, *J. Nat. Prod.* **2011**, *74*, 1531; d) G.-B. Xu, L.-M. Li, T. Yang, G.-L. Zhang, G.-Y. Li, *Org. Lett.* **2012**, *14*, 6052.
- [43] For a recent enantioselective approach from our group, see ref. [13e]. For efficient methodologies for the construction of glutarimides in the racemic series, see: a) H. Takaya, K. Yoshida, K. Isozaki, H. Terai, S.-I. Murahashi, *Angew. Chem. Int. Ed.* **2003**, *42*, 3302; *Angew. Chem.* **2003**, *115*, 3424; b) H.-W. Chen, R.-T. Hsu, M.-Y. Chang, N.-C. Chang, *Org. Lett.* **2006**, *8*, 3033; c) J. Zhang, M. Senthilkumar, S. C. Ghosh, S. H. Hong, *Angew. Chem. Int. Ed.* **2010**, *49*, 6391; *Angew. Chem.* **2010**, *122*, 6535.
- [44] O. Trapp, V. Schurig, *J. Chromatogr. A* **2001**, *911*, 167.
- [45] When using crotonaldehyde under the same conditions, only 50% conversion was obtained, indicating a poor tolerance for a β -substitution on the enal.
- [46] All the post-functionalisation reactions depicted in Scheme 12 were conducted from the same batch of precursor **8x**, highlighting once again the fact that these cyclic hemiaminals can be obtained with high enantiomeric excesses but promptly epimerise slightly under acidic conditions.

Received: July 20, 2014

Revised: September 18, 2014

Published online on November 7, 2014

5 Conclusions et perspectives

Les travaux rassemblés dans ce manuscrit ont permis de mettre en évidence les différents domaines de la modélisation moléculaire (méthodes classiques et quantiques) que j'ai abordés au cours de ma carrière universitaire. Mes travaux de recherche futurs s'inscriront dans la continuité des projets entrepris depuis mon doctorat et seront essentiellement centrés sur les espèces radicalaires. Mes compétences dans les différents domaines de la modélisation moléculaire me permettront d'entretenir des collaborations avec différents équipes d'expérimentateurs. Mon activité se concentrera principalement sur les sujets suivants :

- étude de la structure et de la réactivité d'espèces radicalaires à l'aide de méthodes quantiques
- étude des interactions d'espèces radicalaires avec des molécules-hôtes à l'aide de la dynamique moléculaire

5.1 Réactivité des espèces radicalaires

5.1.1 Etude théorique de la décomposition des adduits de spin de radicaux oxygénés

En collaboration avec l'équipe SREP (Structure et Réactivité des Espèces Paramagnétiques) de l'ICR, j'ai tout d'abord effectué par mécanique moléculaire l'analyse conformationnelle des adduits de spin obtenus en spin-trapping (travaux de thèse et publications jusqu'en 2006). Cette étude a été poursuivie au sein de l'équipe Chimie Théorique à l'aide de simulations de dynamique moléculaire en champ de force polarisable, suivies de calculs de constantes de couplage (thèse de Céline Houriez, 2009) Depuis octobre 2012, nous avons commencé l'étude théorique de la décomposition des adduits de spin de radicaux oxygénés (thèse de Sergiu Lescic).

Le radical anion superoxyde ou un radical alkylperoxyde est piégé par addition sur une nitroène cyclique. L'adduit persistant est alors observable par Résonance Paramagnétique Electronique. Cependant, en fonction des substituants R^1 , R^2 présents sur la nitroène, l'adduit de spin est plus ou moins persistant (temps de demi-vie variant de moins d'une minute à environ 1h en milieu aqueux). Les produits de décomposition ont clairement été identifiés et résultent a priori de la rupture des liaisons O-O et C-N (Figure 5.1).

En plus de l'effet de substituant, d'autres facteurs sont à prendre en compte en milieu aqueux :

- Le milieu contient des espèces fortement réductrices telles que le radical anion superoxyde $O_2^{\cdot-}$ ($E_0(O_2/O_2^{\cdot-}) = -0,563V$) et la dégradation de l'adduit est plus rapide quand le flux d'anion superoxyde augmente.
- Le dégradation est plus lente en milieu organique que dans le tampon phosphate ($pH = 7,4$) ce qui implique peut-être l'intervention des ions H^+ dans le processus de dégradation.
- Le mécanisme de dégradation peut être différent pour l'adduit de $O_2^{\cdot-}$ et l'adduit de radicaux alkylperoxyde.

Dans un premier temps, nous avons émis plusieurs hypothèses pour expliquer la formation des produits de dégradation (Figures 5.1 à 5.4).

FIGURE 5.1 – a) Spin-trapping pour le piégeage de radicaux O_2^- ou alkylperoxyde par une nitrone cyclique. b) Produits de dégradation identifiés.

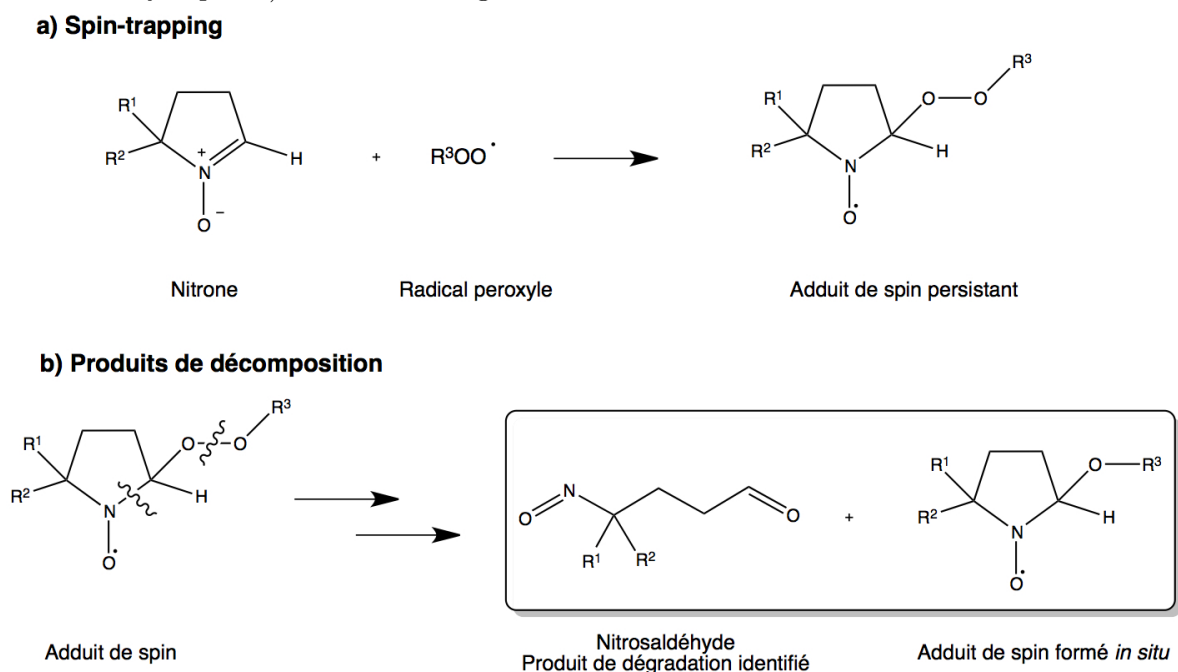
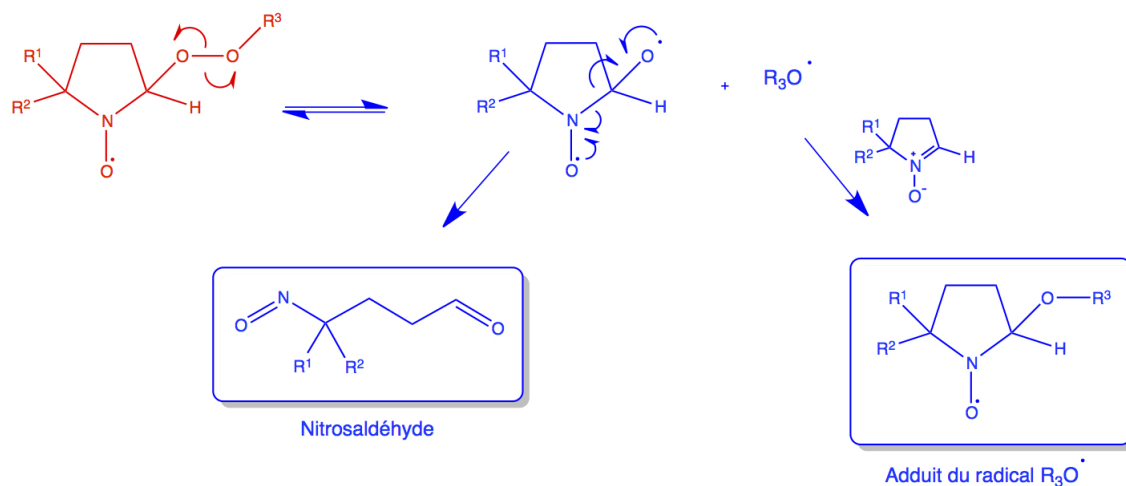


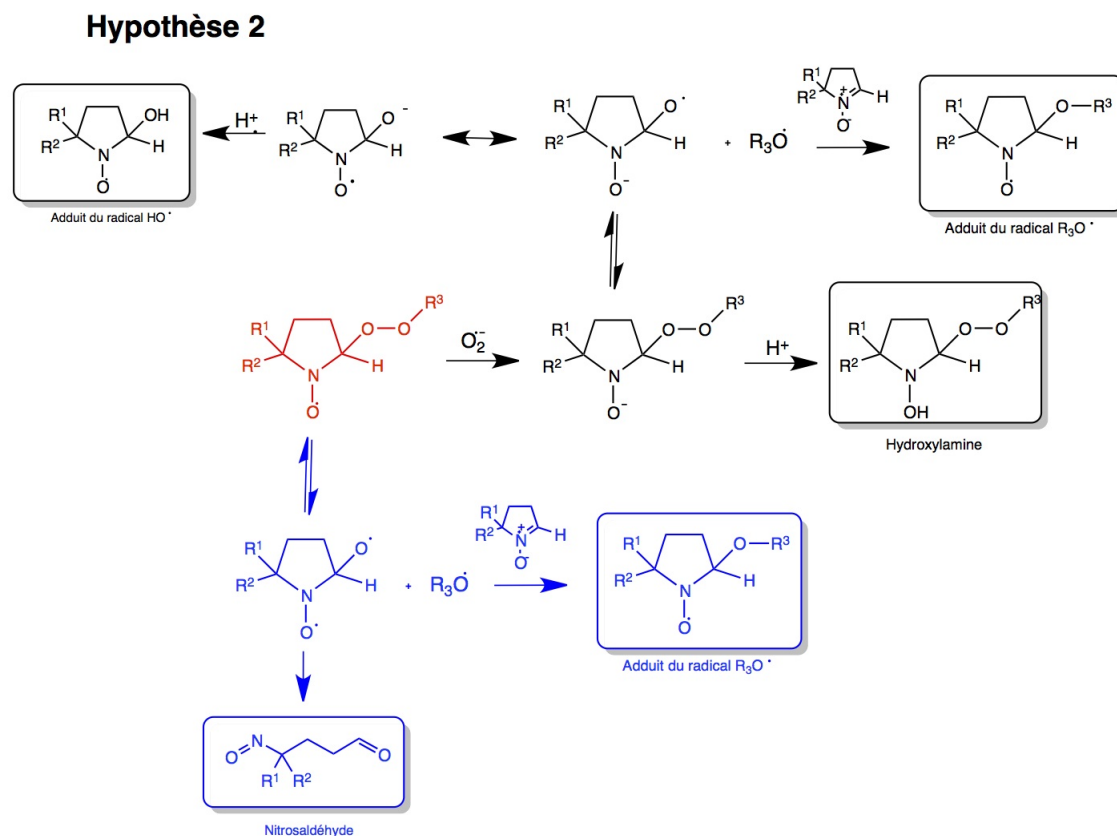
FIGURE 5.2 – Première hypothèse purement radicalaire.

Hypothèse 1



Le premier mécanisme serait le seul mis en jeu en milieu organique. Dans un tampon phosphate, les mécanismes 1-3 pourraient se superposer et expliquer la dégradation plus rapide des adduits de spin ainsi que la formation d'autres produits de dégradation tels que l'hydroxylamine et l'adduit du radical RO^\bullet/HO^\bullet . Dans le mécanisme 1, le système subit une réorganisation électronique profonde au cours de la décomposition, le cycle passant d'un état doublet puis à un état de biradical singulet et enfin l'ouverture du cycle conduit à une molécule à couche fermée. Afin de décrire au mieux la rupture homolytique des deux liaisons, nous avons choisi la méthode post-Hartree-Fock CASSCF pour explorer la surface d'énergie potentielle de ces systèmes. Les valeurs d'énergie sont corrigées a posteriori par un calcul CASPT2. Plusieurs bases et plusieurs espaces actifs sont testés. L'espace actif varie en fonction de la nature des substituants R^1 et R^2 . D'après les résultats actuels de M^r S. Lescic, la rupture homolytique de la liaison peroxydique s'effectue sans état de transition sur la surface d'énergie

FIGURE 5.3 – Deuxième hypothèse en milieu aqueux.



électronique et les enthalpies libres de réaction sont comprises entre 50 et 60 kcal.mol⁻¹. La localisation de l'état de transition pour la rupture de la liaison C-N s'avère difficile : pour l'instant, aucun état de transition n'est localisé. On note cependant une augmentation de l'énergie nécessaire à la rupture des liaisons quand le substituant devient plus électro-négatif. L'étude porte sur les adduits du radical $\bullet\text{OOME}$ et $\bullet\text{OotBu}$ ayant les substituants : R¹=R²=Me (adduit de la DMPO), R¹=Me, R²=CO₂Me (adduit de l'EMPO), R¹=Me, R²=CF₃ (adduit du TFMPO) et R¹=Me, R²=P(O)(OMe)₂ (adduit de la DEPMPO). Parallèlement à l'étude théorique, de nouvelles mesures de temps de demi-vie en milieu organique dégazé ont été effectuées par l'équipe SREP et nous avons pu montrer une très bonne corrélation entre ces valeurs et les enthalpies libres de rupture homolytique de la liaison O-O.

5.1.2 Etude théorique de la fragmentation des radicaux en spectrométrie de masse

Dans le cadre d'une collaboration avec l'équipe SACS (Spectrométries Appliquées à la Caractérisation Structurale) de notre UMR, nous avons commencé l'étude des profils réactionnels de fragmentation de radicaux nitroxyle au cours de leur analyse par spectrométrie de masse. Cette étude a pour objectif de confirmer/infirmer les hypothèses formulées à l'issue de l'analyse des spectres de masse. Pour l'instant, notre étude porte sur le TEMPO et le SG1 (Figure 5.5). Nous utilisons la méthode DFT B3LYP/6-31G(d) dans un premier temps. Les enthalpies libres sont ensuite calculées au niveau B3LYP/6-311++G(3df,3pd).

L'étude simultanée de systèmes radicalaires par spectrométrie de masse et modélisation moléculaire, grâce à la collaboration enrichissante entre ces deux équipes, va se développer et permettre une analyse fine des structures d'espèces persistantes ou à faible durée de vie. Une telle étude a été menée sur l'adduit DEPMPO-OotBu en collaboration avec l'équipe SREP.

FIGURE 5.4 – Troisième hypothèse concernant l'adduit du radical anion superoxyde.

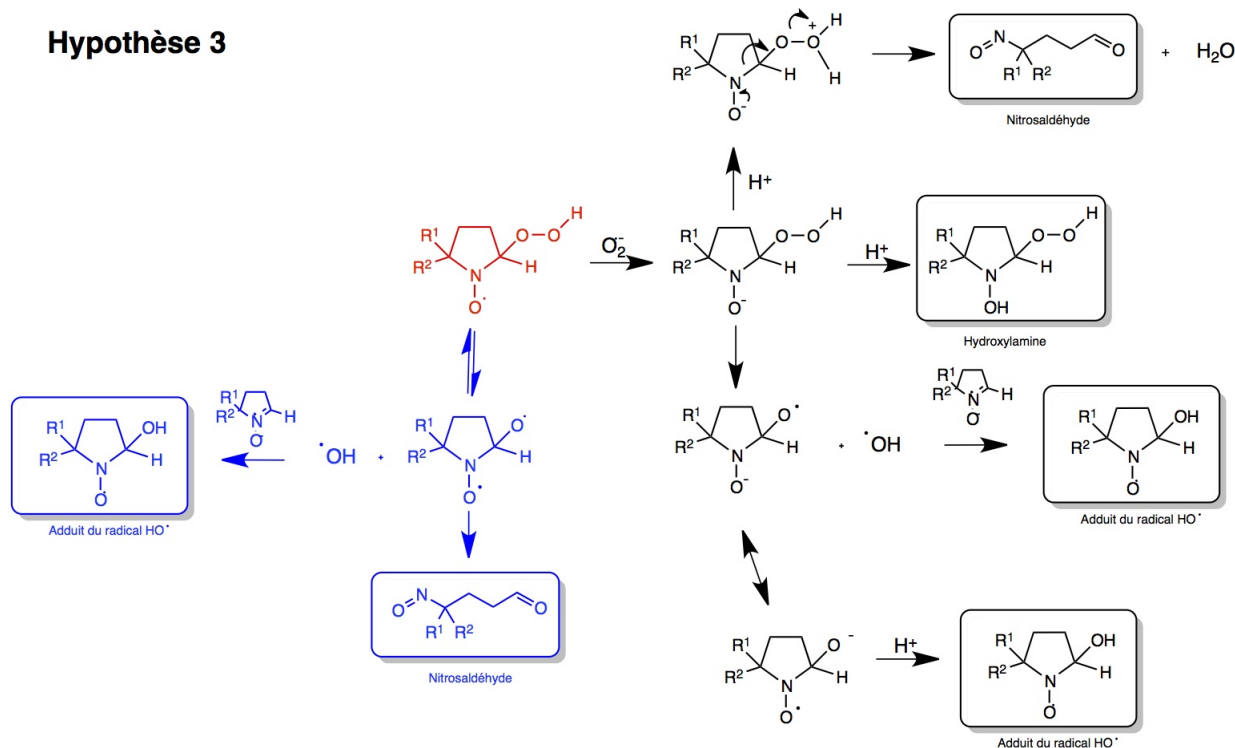
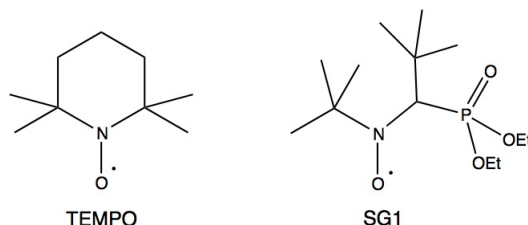


FIGURE 5.5 – Structures du TEMPO et du SG1.

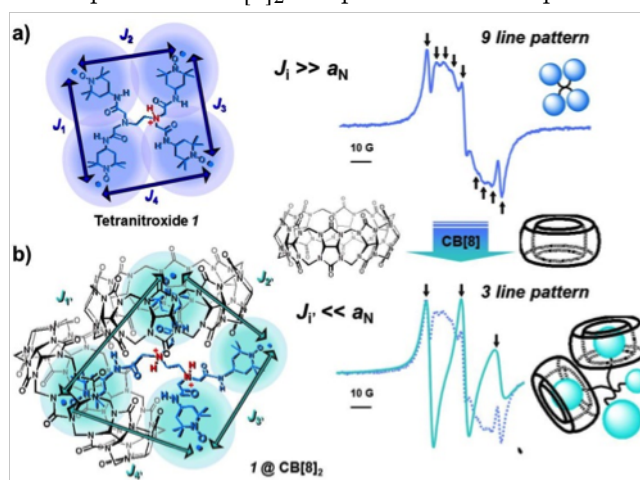


5.2 Etude d'espèces radicalaires par dynamique moléculaire

Dans le cas de polyradicaux, si les N centres radicalaires $X\cdot$ sont proches, la constante d'échange J entre les centres radicalaires devient de l'ordre de grandeur de la constante de couplage $a_{X\text{voire}}$ nettement supérieure. Dans ce cas, le spectre expérimental est assez complexe car il comporte un plus grand nombre de raies $(2N+1)$ (Figure 5.6). Des systèmes supramoléculaires constitués de polyradicaux et de molécules-hôtes permettent de moduler l'aspect du spectre RPE des polyradicaux en fonction de la proximité des centres radicalaires. L'ajout d'une molécule-hôte présentant une forte affinité pour les polyradicaux simplifie les spectres RPE des polyradicaux en éloignant les centres radicalaires et en rendant négligeable la constante d'échange J . La famille des cucurbituriles (CB) présente une grande affinité pour les nitroxydes grâce à la formation d'un réseau de liaisons hydrogène entre le polynitroxyde et l'hôte. La molécule-hôte CB[8] est particulièrement intéressante du fait du rayon de sa cavité.

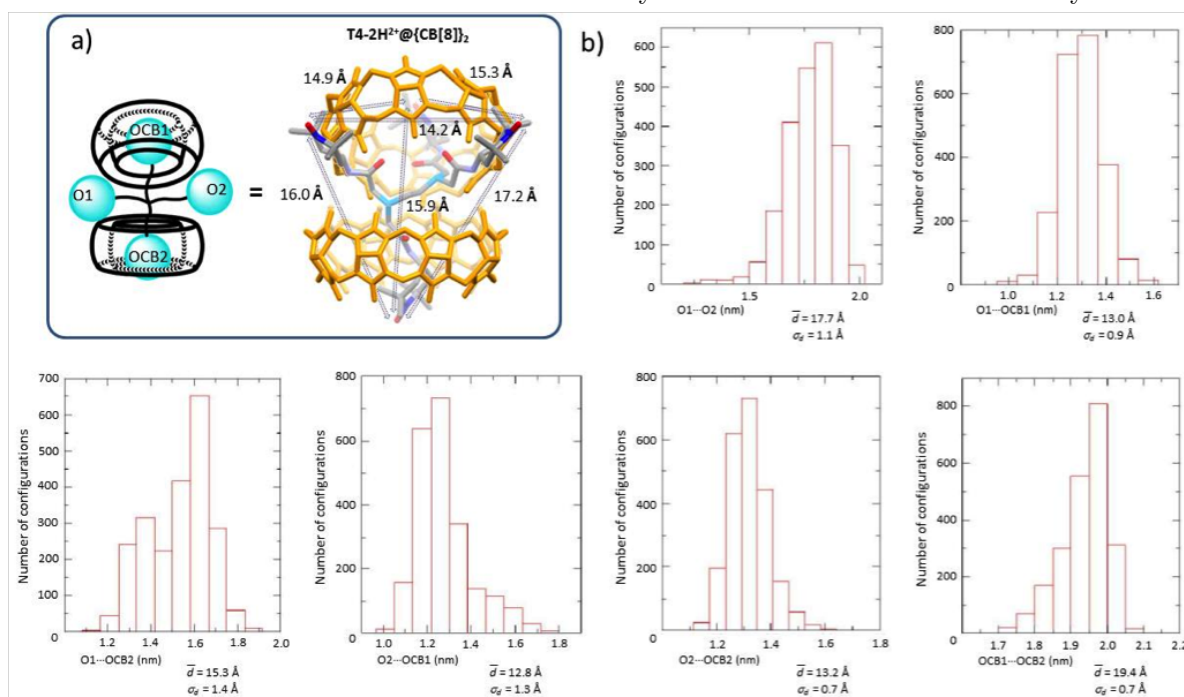
L'étude de tels systèmes complexes en milieu solvato n'est envisageable que par dynamique moléculaire. Des simulations de plusieurs nanosecondes ont été entreprises à l'aide du logiciel Gromacs en utilisant plusieurs champs de force pour traiter les différents composants du système : le champ de

FIGURE 5.6 – a) Structure du tétranitroxyde 1 et spectre RPE expérimental comportant 9 raies. b) Structure du complexe 1@CB[8]₂ et spectre RPE simplifié à 3 raies.



force développé par V. Barone et al.¹ pour le tétranitroxyde, GAFF² pour le CB[8] et TIP3P³ pour les molécules d'eau. Les distances moyennes entre les centres radicalaires sont calculées sur la durée de la simulation et permettent de confirmer la présence ou non du phénomène d'échange de spin. Une distance supérieure à 11-12 Å est suffisante pour éliminer tout échange de spin. Les résultats sur le système 1@CB[8]₂ confirment les résultats expérimentaux (Figure 5.7) et ont été acceptés au *J. Am. Chem. Soc.* La publication est reportée ci-après.

FIGURE 5.7 – Distribution des distances moyennes entre les 4 fonctions nitroxyles.



1. E. Stendardo, A. Pedone, P. Cimino, M. C. Menziani, O. Crescenzi, V. Barone *Phys. Chem. Chem. Phys.* 2010, 12, 11697-11709.
2. J. Wang, R. Wolf, J. Caldwell, P. Kollman, D. Case *J. Comput. Chem.* 2004, 34, 1157-1174.
3. W. L. Jorgensen, J. D. Madura, *J. Am. Chem. Soc.* 1983, 105, 1407-1473.

Spin Exchange Monitoring of the Strong Positive Homotropic Allosteric Binding of a Tetraradical by a Synthetic Receptor in Water

David Bardelang,^{*,†} Gilles Casano,[†] Florent Poulhès,[†] Hakim Karoui,[†] Jessica Filippini,[†] Antal Rockenbauer,[‡] Roselyne Rosas,[§] Valérie Monnier,[§] Didier Siri,[†] Anouk Gaudel-Siri,[†] Olivier Ouari,^{*,†} and Paul Tordo^{*,†}

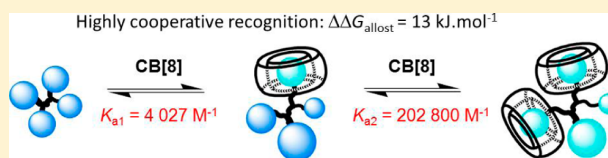
[†]Aix-Marseille Université, CNRS, Institut de Chimie Radicalaire, UMR 7273, 13397 Marseille, France

[‡]Department of Physics, Budapest University of Technology and Economics and MTA-BME Condensed Matter Research Group, Budafoki út 8, 1111 Budapest, Hungary

[§]Aix-Marseille Université, CNRS, Spectropole, FR 1739, 13013 Marseille, France

Supporting Information

ABSTRACT: The flexible tetranitroxide 4T has been prepared and was shown to exhibit a nine line EPR spectrum in water, characteristic of significant through space spin exchange (J_{ij}) between four electron spins interacting with four nitrogen nuclei ($J_{ij} \gg a_N$). Addition of CB[8] to 4T decreases dramatically all the J_{ij} couplings, and the nine line spectrum is replaced by the characteristic three line spectrum of a mononitroxide. The supramolecular association between 4T and CB[8] involves a highly cooperative asymmetric complexation by two CB[8] ($K_1 = 4027 \text{ M}^{-1}$; $K_2 = 202\,800 \text{ M}^{-1}$; $\alpha = 201$) leading to a rigid complex with remote nitroxide moieties. The remarkable enhancement for the affinity of the second CB[8] corresponds to an allosteric interaction energy of $\approx 13 \text{ kJ mol}^{-1}$, which is comparable to that of the binding of oxygen by hemoglobin. These results are confirmed by competition and reduction experiments, DFT and molecular dynamics calculations, mass spectrometry, and liquid state NMR of the corresponding reduced complex bearing hydroxylamine moieties. This study shows that suitably designed molecules can generate allosteric complexation with CB[8]. The molecule must (i) carry several recognizable groups for CB[8] and (ii) be folded so that the first binding event *reorganizes* the molecule (unfold) for a better subsequent recognition. The presence of accessible protonable amines and H-bond donors to fit with the second point are also further stabilizing groups of CB[8] complexation. In these conditions, the spin exchange coupling between four radicals has been efficiently and finely tuned and the resulting allosteric complexation induced a dramatic stabilization enhancement of the included paramagnetic moieties in highly reducing conditions through the formation of the supramolecular 4T@CB[8]₂ complex.



INTRODUCTION

Allostery is a collective property of some unusual chemical or biological systems occurring when this ensemble behaves differently with respect to expected interactions based on isolated, individual molecular components.¹ This property is usually closely related to positive cooperativity found when, for successive supramolecular events, the binding of a first component enhances the following binding events.² Allostery has been shown to play crucial roles in biology where subtle interaction-induced conformational changes are pivotal for new biological functions to occur.³ This concept has then been relayed to chemists⁴ that used it to prepare efficient catalysts⁵ and advanced molecular architectures⁶ even though the design of efficient allosteric systems is still challenging. Among allosteric systems, organic assemblies working in water remain rare,⁷ but several interesting studies based on cucurbiturils have been reported.⁸ However, quantification of the allosteric binding involving cucurbiturils has only been realized in two instances and for heterotropic systems.^{8b,c} Nitroxides are routinely used as paramagnetic probes,⁹ and in recent years,

various reports described the preparation of supramolecular assemblies containing nitroxide free radicals.¹⁰ One of the motivations for their use is related to the property of nitroxides to report subtle changes in their local environment and dynamic features induced by complexation or self-assembly phenomena. In the macrocyclic host/guest chemistry, nitroxides have been shown to be very useful to study the binding properties of cyclodextrins¹¹ and cucurbiturils¹² by electron paramagnetic resonance (EPR) spectroscopy. For instance, in mononitroxides, the nitrogen hyperfine coupling constant (a_N) changes as a function of its direct surrounding and the EPR line shape is a good reporter of the dynamics of the system.¹³ For polynitroxides, additional magnetic interactions, i.e., electron–electron dipolar and electron spin exchange, are present in the molecule.

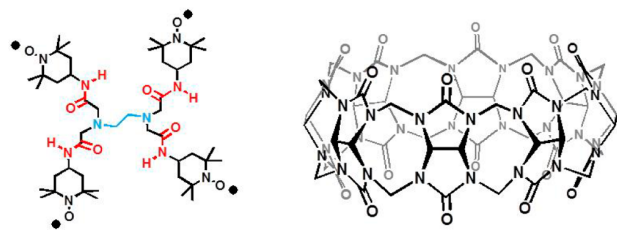
Because the spin exchange interaction is distance dependent, variations of the conformation of the molecule can be visualized

Received: September 23, 2014

Published: November 22, 2014

by EPR.¹⁴ Recently, several authors have reported the modulation of this interaction in dinitroxides using different strategies. For example, Feringa used light as the stimulus to control the cis/trans isomerization of an alkene bearing two TEMPO nitroxides.¹⁵ Using host/guest complexation or self-assembly, Chechik,¹⁶ Kaifer,¹⁷ Lucarini,¹⁸ and Ramamurthy and Ottaviani¹⁹ controlled the distance separating the unpaired electrons by adding CB[*n*], CDs, octaacid, and resorcinarene capsules to the system, or by guanosine quadruplex formation. In our investigation at the interface between free radicals and macrocyclic hosts,²⁰ we recently reported the occurrence of a supratiradical based on 4-methoxy-TEMPO (4M) and cucurbit[8]uril (CB[8])²¹ of composition {4M@CB[8]}₃, giving an EPR signature corresponding to a triangular assembly (seven line pattern).^{22,23} Herein, we report the dramatic and reversible modulation of the spin exchange interaction in a tetranitroxide controlled by the allosteric complexation of CB[8] (Scheme 1). The EDTA core structure of the

Scheme 1. Structures of Tetranitroxide 4T and of CB[8]



tetradical offers a promising scaffold: (i) carrying four TEMPO units to monitor the allosteric complexation by subtle changes of the spin exchange interaction and (ii) presenting two protonable amine groups amenable for the attraction and complexation of CB[8] macrocycles and four additional amide groups as hydrogen bond donors. We also discuss structural requisites that are responsible for this allosteric behavior.

RESULTS AND DISCUSSION

Synthesis of Tetranitroxide EDTA4T. The tetranitroxide EDTA4T (hereafter referred to as 4T) based on the EDTA skeleton was synthesized in two steps starting from 4-aminoTEMPO (Supporting Information Figure S1). First, the amine function was acetylated using 2-bromoacetyl bromide under argon at room temperature for 24 h. The purified product was then reacted with ethylenediamine in acetonitrile at 50 °C during 5 days, and 4T was obtained with a global yield of 56% after purification.

EPR Spectroscopy. At 363 K, the aqueous solution EPR spectrum of 4T (Figure 1) is composed of nine lines, the line spacing corresponding to about 1/4 of the nitrogen hyperfine splitting (a_N) for TEMPO in water.

These EPR features are characteristic of strong exchange couplings ($J_{ij} \gg a_N$) between the unpaired electrons, each electron interacting equally with the four equivalent nitrogen nuclei.²⁴ Neglecting the nonsecular terms of the equivalent nitrogen hyperfine couplings, the spin Hamiltonian for a polynitroxide bearing equivalent nitroxide moieties is written as

$$\sum_i g\beta_e B \hat{S}_{iz} + a_N \sum_i \hat{S}_{iz} \hat{I}_{iz} + \sum_{ij} J_{ij} \hat{S}_i \hat{S}_j$$

The first component is the Zeeman coupling between the unpaired electron spins and the magnetic field, the second

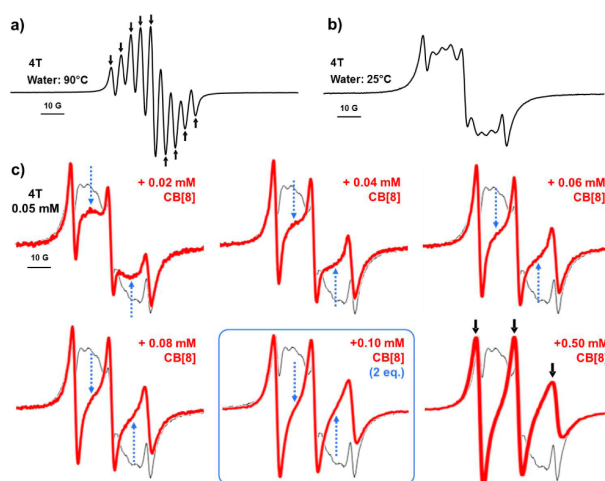


Figure 1. EPR spectra in water solution of (a) 4T at 363 K, (b) 4T at 298 K, and (c) 4T in the presence of increasing amounts of CB[8] highlighting the absence of noticeable changes above 2 equiv of CB[8].

component is the hyperfine coupling between the unpaired electron spin and the nitrogen nuclear spin of a nitroxide moiety, and the third component is the spin exchange between the unpaired electron spins. For a flexible molecule like 4T, the exchange couplings have time dependence ($J_{ij}(t)$), and the shape of the EPR spectrum depends dramatically on the ratio between the magnitudes of the average exchange coupling (\bar{J}) and a_N .^{24–26} When \bar{J} is small compared to a_N ($\bar{J} \ll a_N$), each nitroxide moiety separately contributes to the EPR signal, which is therefore constituted of a 1:1:1 triplet. On the other hand, when $\bar{J} \gg a_N$, each unpaired electron interacts equally with the nitrogen nuclei and the number of lines depends on the number of nitrogen nuclei. With four nitrogen nuclei, a spectrum composed of nine lines separated by $a_N/4$ and with relative intensities of 1:4:10:16:19:16:10:4:1 is expected.^{24–26} In water solution at 363 K the EPR spectrum of 4T is indeed composed of nine lines (Figure 1a), with a line spacing (4.2 G) corresponding to $\sim 1/4$ of the a_N value observed for TEMPO in water solution. However, at 363 K, the limit of very rapid exchange is not yet achieved, and the spectral lines do not exhibit the expected intensity ratios. In water at 298 K, a dramatic change of the EPR spectrum was observed (Figure 1b).

Nine lines are still observable, but the spectrum, while remaining symmetric, looks like the superimposition of a sharp triplet and six broad lines. This change is a consequence of the major contribution of the J modulation to the transverse electron relaxation time in polynitroxides.²⁷ The lines of the EPR spectrum arising from polyradicals in which all ^{14}N nuclei have the same spin state (i.e., $m_I = 1$, $m_I = -1$, or $m_I = 0$ for all I , where m_I is the ^{14}N spin quantum number for the i th nitroxide) do not have hyperfine fluctuations and are not broadened by the J modulation.²⁷ Thus, for 4T, as shown in Figure 1b, the two extreme spectral lines ($M_I = \pm 4$) and one component of the central line ($M_I = 0$) remain relatively sharp, while the other lines are broadened to varying degrees. The influence of temperature on the 4T EPR spectrum shape brings to light the high flexibility of the molecule and the dramatic influence of the J modulation. We thus aimed to study the effect on the spin exchange, of CB[8] that has (i) a suitable size to complex TEMPO moieties with respect to CB[7] and (ii)

carbonyl fringed portals which can stabilize the protonated forms of the two amine sites of 4T. It rapidly appeared that very low concentrations of CB[8] dramatically changed the shape of the EPR signal of 4T (Figure 1c). To determine the binding model and the association constants between 4T and CB[8], we performed EPR titrations which were analyzed by the 2D_EPR program we have developed²⁸ (Table 1 and

Table 1. EPR Parameters and Stepwise Binding Constants of All Species Considered in the Titration of Tetranitroxide 4T by CB[8] in Water

species	<i>g</i>	<i>a_N</i> /mT	<i>K</i> /M ⁻¹
4T (BS ^{<i>a</i>} + T ^{<i>b</i>})			
4T-CB[8]	2.0060	1.638	4 027
4T-(CB[8]) ₂	2.0057	1.641	202 800
4T-(CB[8]) ₃	2.0058	1.597	157

^aFictive nitrogen coupling constant, see Supporting Information. ^b*g* = 2.0058, *a_N* = 16.99 G.

Supporting Information Figures S2–S4). Here, the crucial point of this approach is to precisely determine the variation, with respect to the CB[8] concentration, of the relative concentration of species contributing to the EPR signal. We considered four contributing species: the free 4T and three 4T@CB[8]_{*n*} complexes with *n* = 1, 2, and 3. A curve fitting nicely the EPR signal of the free 4T was obtained through the superimposition of a broad signal (BS, obtained with a hyperfine pattern using effective nitrogen splitting constants, Supporting Information Figure S4) to a 1.1.1 triplet identical to the TEMPO triplet (*g* = 2.0058, *a_N* = 16.99 G). Following the concentration variation in a broad range, we determined association constants for the three 4T@CB[8]_{*n*} complexes.

The spectra of the four components used to fit the calculated spectra are shown in the Supporting Information (Figure S4). The use of an artificial spectrum for the free 4T does not affect the reliability of association constants, but the hfs couplings have no significance. After decomposing all the spectra into the five species, their EPR parameters (*g*, *a_N*, *α*, *β*, *γ*) and the association constants *K_n* were determined (29 parameters altogether) (Table 1, Figure 2, and the Supporting Information). The increase of relaxation parameters (Supporting Information Table S1) and the decrease of *a_N* are clear signs of binding events. However, it should be noted that the apparent *a_N* value is an average of the four hyperfine couplings (between included and free TEMPO moieties). A striking

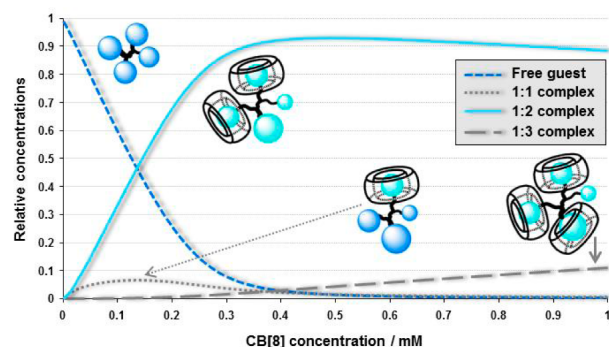


Figure 2. Product distribution for the binding of tetranitroxide 4T (0.05 mM) with CB[8] in water.

result is the propensity of CB[8] to rapidly form a 1:2 complex (Figure 2). A moderate binding constant was found for the first binding event ($K_1 \approx 4027 \text{ M}^{-1}$), however, the association for the second event is exceedingly high ($K_2 \approx 202\,800 \text{ M}^{-1}$), indicating a strong cooperativity. To the best of our knowledge, this is one of the highest cooperative systems reported for synthetic complexes so far.^{7,8} This 50-fold enhancement in CB[8] binding after the first complexation corresponds to an allosteric interaction energy of $\approx 13 \text{ kJ mol}^{-1}$, which is similar to the difference between the first and the last binding steps of oxygen by hemoglobin ($\Delta\Delta G_{\text{allost}} \approx 15 \text{ kJ mol}^{-1}$).^{6b,29} The cooperativity factor ($\alpha = 4K_2/K_1 \approx 201$)^{2b,30} is large and reflects that the association of a second cucurbit[8]uril is promoted if already one CB[8] is associated. In essence, it means that the first binding event greatly enhances (by a factor of ≈ 200) the binding of a second CB[8]. The possible driving forces for this process are most likely a preorganization of the tetranitroxide in the 1:1 complex, where a suitable second TEMPO unit is favorably included in an additional CB[8] but also a large set of available C–H and N–H hydrogen bonds between the tetranitroxide skeleton toward the incoming oxygen rich cucurbituril rim of the second CB[8] molecule. As will be seen later (NMR, DFT), additional hydrogen bonds between the two cucurbiturils are also very likely to strengthen the assembly in a manner reminding of what is seen in crystal structures of cucurbiturils (partial self-closing of the cavities)³¹ and in the CB[8] triangles.^{21–23} Although this phenomenon is quite common in biology with systems displaying high α values,³² it remains relatively rare for organic systems. If a third CB[8] was to be considered for binding, its association was found to be much less promoted than the second ($K_3 \approx 157 \text{ M}^{-1}$) reflecting some hindrance or energy penalty for the binding event leading to the 1:3 complex (negative cooperativity). Figure 2 shows the species distribution over a small range of CB[8] concentrations. It shows that, at 0.3 mM, around 85% of the tetranitroxide is in the form of the 1:2 complex and, after 0.4 mM, there hardly remains free tetranitroxide in solution. Finally, electrospray mass spectrometry also supported these results^{33,34} with the observation of all three complexes with guest:host stoichiometries from 1:1 to 1:3 (Supporting Information). The entire set of properties of this system (spin probes, EPR monitoring, high affinity cucurbituril hosts, tendency of CBs aggregation, protonable guest) is at the origin of the observed results.

NMR Spectroscopy. NMR study of the inclusion complexes was performed by reducing the paramagnetic nitroxides to diamagnetic hydroxylamines using ascorbic acid.³⁵ In these conditions, the ¹H NMR spectrum of 4T exhibits a set of two well-resolved singlets occurring for the methyl groups around 1.5 ppm (Supporting Information Figure S6). However, when CB[8] is added to the solution, the two singlets become broader and less resolved and two new sets of broad signals are observed which are shifted upfield. These additional signals are in a slow exchange regime with regard to the NMR time scale. The values of the complexation induced chemical shift changes ($\Delta\delta$) are large (-0.60 and -0.65 ppm), in line with previous work for TEMPO diamagnetic analogues in the presence of CB[8] (≈ 0.70 ppm upfield shift).²³ The ratio between the integrals of the signals assigned to free and complexed species roughly correspond to a 1:2 complex. Interestingly, the NMR signals of CB[8] are modified upon mixing, displaying multiple unresolved peaks (Figure 3). For instance, the CB[8] equatorial methine protons display 7 peaks

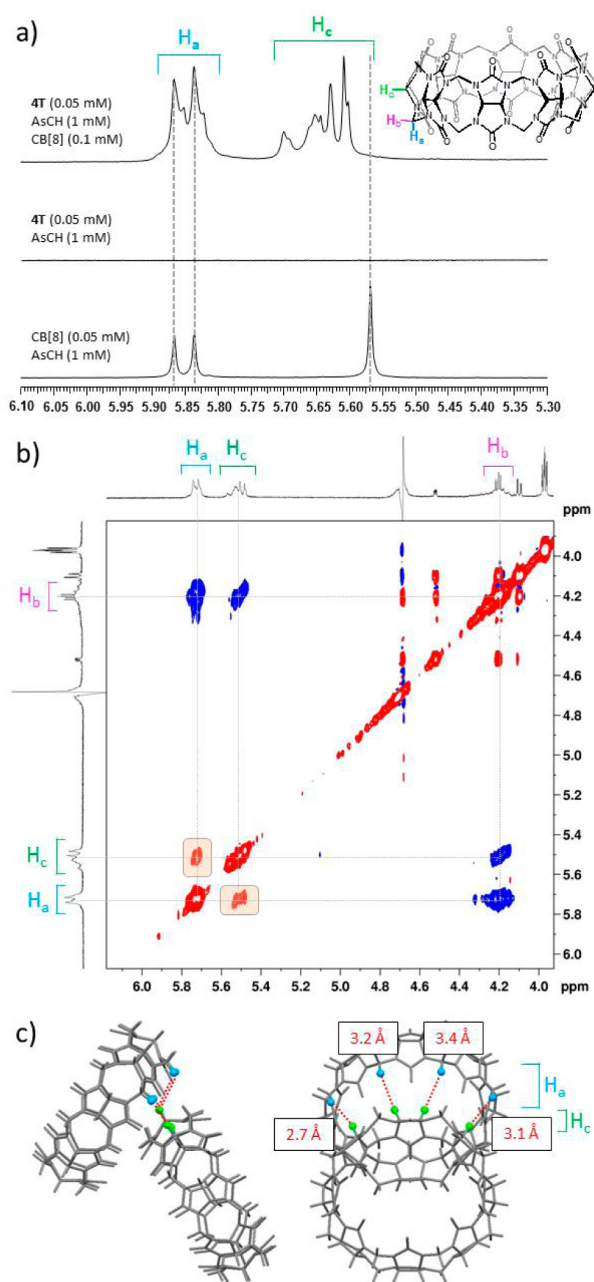
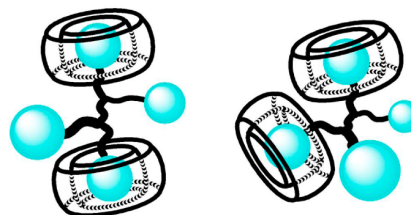


Figure 3. (a) Excerpts of the 600 MHz ^1H NMR spectra of the reduced form of 4T (hydroxylamines) in the absence and in the presence of CB[8] in water showing the splitting of the singlet of the methine protons of CB[8]. (b) Part of the 2D-ROESY spectrum of a mixture of 4T (0.05 mM) and CB[8] (0.1 mM) with ascorbic acid (1 mM, 300 K, mixing time: 800 ms). (c) Part of the CB[8] supramolecular triangle (X-ray structure of ref 21) featuring two CB[8] interacting by multiple C–H \cdots O interactions as a means to measure H \cdots H contacts between $\text{H}_a(\text{CB}[8])_{\text{TOP}}$ and $\text{H}_c(\text{CB}[8])_{\text{BOTTOM}}$.

(Figure 3a) instead of a singlet for free CB[8]. This change reflects the break of the D_{8h} symmetry of CB[8] (H_c), which is not compatible with the occurrence of a 1:1 complex or with a symmetric 1:2 complex (Scheme 2 left).

Therefore, instead of a C_8 symmetry sandwich complex in which the two cucurbiturils would be maintained relatively far

Scheme 2. Two Possible Modes of Inclusion for the Complex $4\text{T}@\text{CB}[8]_2$



from one another, it seems more plausible that the complex tends to be folded in a way in which the two CB[8] can be close to each other (Scheme 2 right). It is well-known that cucurbiturils tend to self-associate by means of multiple weak CH \cdots O hydrogen bonds so that they self-close their cavities.³¹ The inclusion of two TEMPO groups in two CB[8] may have brought two macrocycles close enough to interact as seen in crystals of CB[8]. Another explanation may be the occurrence of several conformers of the 1:2 complex exchanging slowly with respect to the NMR time scale. But the absence of noticeable changes in these NMR patterns with increasing temperature (283–343 K) does not favor this hypothesis.

In order to gain further insights on the complex structure, 2D NMR experiments were performed. The 2D-ROESY spectrum shows cross correlations due to H_b – H_a and H_b – H_c interactions that are most likely intramolecular (Figure 3b in blue). Indeed, these cross peaks have opposite signs with respect to diagonal peaks and suggest the occurrence of ROE contacts. However, the detection of a positive H_a – H_c cross peak (orange highlighted, Figure 3b) which is absent when 4T is not present in the sample (i.e., for CB[8] alone at the same concentration) is in line with cucurbituril aggregates.^{34,36} This observation is in good agreement with the splitting pattern observed for H_c in the 1D ^1H NMR spectrum highlighting asymmetric 4T complexation by two CB[8] molecules (Figure 3a). The sign of the cross peak was intriguing, and after the recording of TOCSY, ROESY, and NOESY spectra at different mixing times, the building curves (volume integrals of the cross peak as a function of the mixing time) indicate that this correlation is most probably due to spin diffusion instead of direct dipolar coupling (NOE effect).³⁷

This correlation indicates that there must be some protons acting as relays between H_a and H_c but also that the distance between these two kinds of protons must be rather short. All these data are in line with a tetranitroxide 4T complexed by a V-shaped dimer of CB[8] (Figure 3c) reminding of the case of the supramolecular triangles for which one CB[8] is missing.²¹

These results are further supported by molecular dynamics simulations and DFT calculations of tetranitroxide 4T (neutral, singly charged, and doubly charged), the 1:1 complexes (singly and doubly charged) and the 1:2 complex (doubly charged). The pK_a values of 4T were measured by pH-metry in pure water. The titration curve allowed determination of two very close jumps corresponding to the two pK_a values 6.45 and 7.35 reflecting a very rapid transition from the unprotonated (4T) to the mono- (4T-H^+) and diprotonated (4T-2H^{2+}) forms.

Theoretical Calculations. Molecular dynamics (MD) simulations in water using Gromacs 4.6³⁸ package over a period of 5 ns allowed determination of the interspin distances between the four TEMPO units for 1:1 and 1:2 complexes (doubly charged form). Computational details are given in the

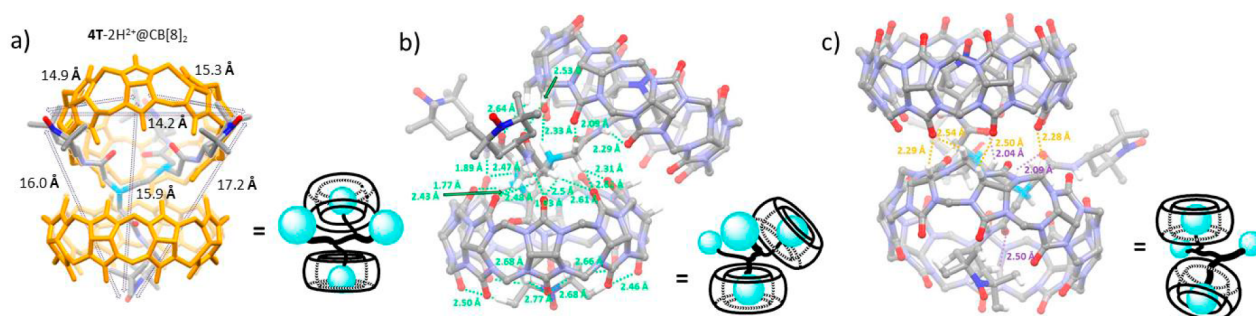


Figure 4. (a) Calculated structure (B3LYP/6-31G(d)) of the most stable conformer of the 1:2 complex of tetranitroxide **4T** in its doubly charged state with CB[8]. The large interspin distances (>14 Å) correlate well with experimental data (EPR). Host–guest (b) and host–host (c) hydrogen bonds and weak interactions found in the 1:2 complex of **4T** with CB[8] (see text and Supporting Information for details).

Supporting Information. For the 1:1 CB[8] inclusion complex, the tetranitroxide stayed included with one TEMPO unit in the CB[8] cavity. Average $O^{\bullet}-O^{\bullet}$ distances and complete range of $O^{\bullet}-O^{\bullet}$ distances are in a large window of ~ 9 Å ($6-7 < d_{O^{\bullet}-O^{\bullet}} < 15$ Å, Supporting Information Figure S7). For the 1:1 complex, while four of the six interspin distances are above 11 Å, some conformations are found with distances $O^{\bullet}_1-O^{\bullet}_3$ and $O^{\bullet}_2-O^{\bullet}_3$ of 9 Å and 6–7 Å, respectively. These conformations correspond to a regime where the spin exchange interactions are large with regard to the hyperfine coupling, leading to an EPR spectrum exhibiting a number of lines >3 (not experimentally observed, see Figure 1c, 3 lines). Thus, geometrical considerations regarding the 1:1 complex are not sufficient to account for the observed EPR results. However, for the 1:2 complex, the two CB[8] molecules repelled the TEMPO units away from each other. The interspin distances are all above 11–12 Å, with averaged distances between 13 and 19 Å (Supporting Information Figure S8), which is in agreement with the observed three line EPR spectrum. Interestingly, the CB–CB distance (between the center of mass of the two closest oxygen crowns) is ~ 10 Å and the angle between the two planes defined by these crowns is $25 \pm 14^{\circ}$, which compares favorably with the DFT minimized structure (33° , Figure 4a).

Quantum mechanics calculations have been performed to determine the geometries of the free and complexed (1:1 and 1:2) molecules.³⁹ DFT calculations were performed at the B3LYP/6-31G(d) level with a continuum of water (PCM method) using Gaussian 09 D.01.⁴⁰ For the tetranitroxide alone, at pH 6.8, at which the EPR experiments were performed, a mixture of **4T-H⁺** and **4T-2H²⁺** should be considered with a substantial population of **4T**. These three species were then considered for the DFT calculations. Because of the pK_a shift effect of cucurbiturils (supramolecular charge stabilization),⁴¹ we only considered charged states for the CB[8] complexes. Thus, **4T-H⁺** and **4T-2H²⁺** were considered for the complexes (**4T-H⁺@CB[8]**), **4T-2H²⁺@CB[8]**, **4T-2H²⁺@CB[8]₂**). The simulations for **4T** alone (neutral, singly charged, and doubly charged forms) indicate that for the vast majority of the 10 most stable conformations (Supporting Information Figure S9), the four TEMPO moieties tend to magnetically interact (folded conformations) with interspin distances in the range 8–13.8 Å, which is compatible with the EPR spectrum of **4T** in water (Figure 1b). In the four most stable conformers of the 1:1 complex (Supporting Information Figure S10), three uncomplexed TEMPO moieties are placed relatively close (8.3–13.5 Å) while the last TEMPO is pushed

away from the others once included in the CB[8] cavity ($d > 17$ Å except for the monoammonium form). Thus, the first binding event reorganizes the molecule **4T** favoring the approach of a further CB[8]. Interestingly, the proximity of one of the two carbonyl crowns of the complexed CB[8] to the two amine functions of **4T** likely shifts their pK_a and this may be an additional driving force for the binding of the second CB[8]. For the 1:2 complex, the two included TEMPO moieties are far from all others and the two remaining are also pushed away at distances >14.2 Å (Figure 4a). In this conformation, the spin exchange interactions are expected to be small, in agreement with the observed three line spectrum of Figure 1c.

Whereas free tetranitroxide **4T** is shown to have at least three intramolecular hydrogen bonds (number independent of protonation states, Supporting Information Figure S9), the 1:1 complex shows one TEMPO moiety included in CB[8] with the tetradical skeleton multiply hydrogen bonded for the three conformers of the bisammonium form (Supporting Information Figure S10). Besides the hydrophobic effect (TEMPO inclusion), a strong charge stabilization is likely to direct the structure of the 1:1 complex as reflected by the large number (12 for **4T-1H⁺@CB[8]** and 17 for **4T-2H²⁺@CB[8]**) of intramolecular and intermolecular $CH\cdots O$ and $NH\cdots O$ interactions featuring activated (amide, α -amine, or α -ammonium) or nonactivated (TEMPO) hydrogen atoms. The three strongest H bonds (1 $N^+-H\cdots O=C$ and 2 $N-H\cdots O=C$) appear to anchor the tetradical near the entrance of one rim of CB[8]. In addition to these stabilizing interactions, there are a number of $CH\cdots O$ close contacts, ranging from close (2.1 Å, 159.8°) to some near the limit of the sum of van der Waals radii (~ 2.8 Å, 165.0°). The $N-H\cdots O=C$ hydrogen bonds occur to orientate two of the three remaining TEMPO units at opposite directions in the plane perpendicular to the C_8 axis of CB[8]. Thus, one TEMPO moiety is isolated from the three other moieties with distances ranging from 9.5 to 13.5 Å contrary to 7.0–12.4 Å for the free tetradical. The inclusion process likely benefits from (i) the hydrophobic effect due to the encapsulation of one TEMPO unit and (ii) additional stabilizing interactions, mainly host–guest hydrogen bonds plus one charge-assisted hydrogen bond due to the presence of the ammonium cation.

However, the addition of a second CB[8] to produce the 1:2 complex resulted in TEMPO moieties being further separated from one another. As a consequence, the interspin distance is now between 14.2 and 17.2 Å, precluding the occurrence of any strong spin exchange interaction (Figure 4a).⁴² In this

geometry, the two cationic charges are stabilized by ion–dipole interactions and there are numerous host–guest hydrogen bonds (21) plus 3 intramolecular hydrogen bonds and 4 host–host C–H⋯O=C hydrogen bonds further stabilizing the architecture and reflecting the very strong binding between the guest and the two hosts (Figures 4b and 4c). The observed host–host multiple weak interactions (Figure 4c) also support the asymmetric binding model deduced from NMR experiments (Scheme 2 right and Figure 3c).

The first inclusion promotes the isolation of one TEMPO unit from the other spin carrying units, but the carbonyl fringe complexing the ammonium cation is still highly hydrogen bond demanding and thus entails two other TEMPO moieties to position perpendicular to the CB[8] D_{8h} symmetry axis by means of amide hydrogen bonds. In our opinion, the first inclusion followed by the positioning of the three other TEMPOs causes the second CB[8] to bind to the 1:1 complex tightly. The presence of the first carbonyl crown is also believed to shift the pK_a of the two amines (protonated form) to further promote the second binding event. This new structure thus offers an ideal means for a second CB[8] to complex a pendant TEMPO moiety benefiting extra energy stabilization by a preorganized skeleton which is multiply hydrogen bond donating. Therefore, theoretical calculations showed how the first binding event reorganized the molecule to propose a more favorable issue for the second binding in accord with the Monod–Wyman–Changeux model.⁴³ Finally, the second CB[8] can be anchored after the first binding event with the aid of the first CB[8] (host–host interactions, Figure 4c) further strengthening the 4T@CB[8]₂ assembly. Taken altogether, these considerations are likely to explain the experimentally observed very high cooperativity.

Competition and Reduction Experiments. The initial nine line pattern of the EPR spectrum is restored after addition of a competitor (benzylamine or adamantylamine) to the solution of 4T and CB[8] (Figure 5a and Supporting Information Figure S11).

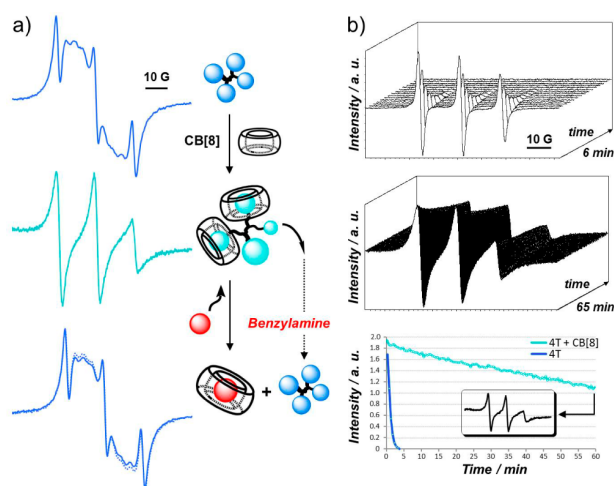


Figure 5. (a) EPR spectra of tetranitroxide 4T in water (0.1 mM) and the observed three line spectrum after addition of CB[8] (1 mM) before coming back to the nine line pattern after the addition of a competitor (dashed line: initial spectrum). (b) Kinetics of the signal decay before (top) and after (middle) addition of CB[8] (1 mM) with ascorbic acid (5 mM) to a solution of tetranitroxide 4T (0.1 mM) in water.

The DFT calculations indicate that even though one TEMPO nitroxide protrudes well from CB[8] (bisammonium 1:1 complex), this is not the case for the other 1:1 and the highly favored 1:2 complex. In these cases, the N–O oxygen atoms of the included TEMPOs stay near the carbonyl crown of the bulk exposed rim. In order to have a more detailed indication of the position of the nitroxide inside the cavity, EPR experiments were performed in the presence of ascorbate as reductant. The ascorbate anion is known to be a strong reductant for nitroxides,³⁵ and monitoring the reduction can be a good assay to probe the deepness of inclusion or accessibility of the nitroxides once complexed with CB[8]. Ascorbic acid (5 mM) was added to a solution of 4T (0.1 mM) and CB[8] (0.4 mM; >92% 1:2 complex, see Figure 2). Whereas all the nitroxides are reduced within 2.5 min ($t_{1/2} \approx 20$ s) in the absence of CB[8] (Figure 5b and Supporting Information Figure S12), an EPR signal can be detected after 1 h if CB[8] was added to the mixture (Figure 5b). This result indicates that most of the nitroxides are protected against the reduction reaction. Without CB[8], the half-lifetime of the 4T EPR signal is around 22 s. In the presence of CB[8], the decay curve is more flat and cannot be fitted according to a first order process. Two half-lifetime values were obtained assuming two sets of kinetics for the nitroxide reduction (Supporting Information Figure S13). The first component is approximately as fast as the reduction of 4T without CB[8] ($t_{1/2} \approx 136$ s). The second component is longer, indicating a strong protection due to the inclusion of the two remaining TEMPO units in the two CB[8] cavities ($t_{1/2} \approx 31$ min) which represents an 85-fold decrease of the nitroxide reduction rate (Supporting Information Table S3). Moreover, after ≈ 200 s, half of the signal disappeared (two nitroxides over four have been reduced) and the remaining three line spectrum remains for more than 1 h. The monitoring of the nitrogen coupling constant (Supporting Information Figure S14) and the line width (Supporting Information Figure S15) shows significant variations during the first 200–250 s (a_N decrease and line width increase) before it reached plateau values corresponding to included radicals. This observation indicates that the remaining species hold the two nitroxides deeply immersed and immobilized in the CB[8] cavities. If the nitroxides would have protruded from the cavities or if a rapid exchange process had occurred (high k_{out}), a rapid loss of the EPR signal would have been observed. If a higher concentration of CB[8] was used (until 1 mM), a larger protection was obtained ($t_{1/2} \approx 75$ min for the second component) corresponding to a 210-fold decrease in nitroxide reduction. The competition and reduction experiments further confirm the stoichiometry and the strength of the complex formed when the tetranitroxide 4T and CB[8] are mixed in water.

CONCLUSION

Overall, these results report the modulation of the through space spin exchange interaction in a tetranitroxide (4T) upon complexation by the synthetic host CB[8] in water. The affinity of CB[8] for the tetranitroxide is very high, as shown by the need of only three equivalents (Figure 1) to entirely change the conformation of 4T and so the mean distance between each radical center. This property of communication of magnetic information between several spin centers was used to finely investigate the allosteric binding of two CB[8] molecules. The binding of a first CB[8] induces a profound conformational change of the molecule which highly favors binding of a second CB[8]. The well-known capacity of cucurbiturils to shift pK_a of

amines to higher means may also be a further driving force explaining this surprisingly effective positive cooperativity. The inclusion process resulted in a complete suppression of electron–electron spin exchange interaction between all four nitroxides, and this phenomenon could be restored by adding a suitable CB[8] competitor. The extent of allosteric interaction energy is surprisingly high ($\Delta\Delta G_{\text{allos}} 4\text{T/CB}[8]_2 \approx 13 \text{ kJ mol}^{-1}$) but can be rationalized by the conformational properties of *folded vs unfolded*, and information stored in *hydrogen bonds and protonable sites*, the tetra-radical and the binding properties of CB[8]. Previously, peptides⁴⁴ and molecules carrying amide bonds⁴⁵ have been shown to display new and exciting properties in the context of supramolecular chemistry. The possibility to tune magnetic spin exchange interaction on demand in the present report is particularly attractive for molecular scale information processing and the production of memory devices. More generally, we believe that the assignment of the role of each subcomponent (amide functions, protonated amines, hydrophobic spin centers, size, and flexibility of the scaffold) in the reported strong cooperativity will contribute to the design and preparation of efficient allosteric systems based on cucurbiturils.

■ ASSOCIATED CONTENT

● Supporting Information

Details of chemical syntheses and additional EPR and NMR spectra. Additional molecular dynamics and DFT results, especially absolute energies and the coordinates of the atoms for all the molecules whose geometries have been optimized. Competition and kinetic results of radical decay in reducing conditions. This material is available free of charge via the Internet at <http://pubs.acs.org>.

■ AUTHOR INFORMATION

Corresponding Authors

david.bardelang@univ-amu.fr
olivier.ouari@univ-amu.fr
paul.tordo@univ-amu.fr

Notes

The authors declare no competing financial interest.

■ ACKNOWLEDGMENTS

The CNRS and the Aix-Marseille Université are acknowledged for financial support. This work was supported by the computing facilities of the CRCMM, “Centre Régional de Compétences en Modélisation Moléculaire de Marseille”.

■ REFERENCES

- (1) (a) Hunter, C. A.; Anderson, H. L. *Angew. Chem., Int. Ed.* **2009**, *48*, 7488–7499. (b) Takeuchi, M.; Ikeda, M.; Sugasaki, A.; Shinkai, S. *Acc. Chem. Res.* **2001**, *34*, 865–873.
- (2) (a) Ercolani, G.; Schiaffino, L. *Angew. Chem., Int. Ed.* **2011**, *50*, 1762–1768. (b) Shinkai, S.; Ikeda, M.; Sugasaki, A.; Takeuchi, M. *Acc. Chem. Res.* **2001**, *34*, 494–503. (c) Rebek, J., Jr.; Costello, T.; Marshall, L.; Wattle, R.; Gadwood, R. C.; Onan, K. *J. Am. Chem. Soc.* **1985**, *107*, 7481–7487. (d) Badjic, J. D.; Nelson, A.; Cantrill, S. J.; Turnbull, W. B.; Stoddart, J. F. *Acc. Chem. Res.* **2005**, *38*, 723–732.
- (3) (a) Goodey, N. M.; Benkovic, S. J. *Nat. Chem. Biol.* **2008**, *4*, 474–482. (b) Stefan, M. I.; Le Novère, N. *PLoS One* **2013**, *9*, e1003106. (c) Williams, D. H.; Stephens, E.; O'Brien, D. P.; Zhou, M. *Angew. Chem., Int. Ed.* **2004**, *43*, 6596–6616.
- (4) A large part of the literature is devoted to artificial allosteric systems working in organic solvents and mainly related to cation or anion binding. For a recent, comprehensive review, see: Kremer, C.; Lützen, A. *Chem.—Eur. J.* **2013**, *19*, 6162–6196.
- (5) (a) Yoon, H. J.; Kuwabara, J.; Kim, J.-H.; Mirkin, C. A. *Science* **2010**, *330*, 66–69. (b) Kovbasyuk, L.; Kramer, R. *Chem. Rev.* **2004**, *104*, 3161–3187. (c) Zhu, L.; Anslyn, E. V. *Angew. Chem., Int. Ed.* **2006**, *45*, 1190–1196. (d) Rebek, J., Jr. *Acc. Chem. Res.* **1984**, *17*, 258–264. (e) Lu, X.; Masson, E. *Org. Lett.* **2010**, *12*, 2310–2313.
- (6) (a) Mendez-Arroyo, J.; Barroso-Flores, J.; Lifschitz, A. M.; Sarjeant, A. A.; Stern, C. L.; Mirkin, C. A. *J. Am. Chem. Soc.* **2014**, *136*, 10340–10348. (b) Khvostichenko, D.; Yang, Q.-Z.; Boulatov, R. *Angew. Chem., Int. Ed.* **2007**, *46*, 8368–8370. (c) Sessler, J. L.; Tomat, E.; Lynch, V. M. *J. Am. Chem. Soc.* **2006**, *128*, 4184–4185. (d) Le Gac, S.; Marrot, J.; Reinaud, O.; Jabin, I. *Angew. Chem., Int. Ed.* **2006**, *45*, 3123–3126. (e) Marlin, D. S.; Cabrera, D. G.; Leigh, D. A.; Slawin, A. M. Z. *Angew. Chem., Int. Ed.* **2006**, *45*, 1385–1390. (f) Ikeda, T.; Sada, K.; Shinkai, S.; Takeuchi, M. *Supramol. Chem.* **2011**, *23*, 59–64. (g) Setsune, J.-i.; Watanabe, K. *J. Am. Chem. Soc.* **2008**, *130*, 2404–2405. (h) Sprafke, J. K.; Odell, B.; Claridge, T. D. W.; Anderson, H. L. *Angew. Chem., Int. Ed.* **2011**, *50*, 5572–5575.
- (7) (a) Bistri, O.; Colasson, B.; Reinaud, O. *Chem. Sci.* **2012**, *3*, 811–818. (b) Kumar, M.; George, S. J. *Chem. Sci.* **2014**, *5*, 3025–3030. (c) Jose, D. A.; Elstner, M.; Schiller, A. *Chem.—Eur. J.* **2013**, *19*, 14451–14457. (d) Raker, J.; Glass, T. E. *J. Org. Chem.* **2002**, *67*, 6113–6116. (e) Harada, A.; Nozakura, S.-i. *Polymer Bull.* **1982**, *8*, 141–146. (f) Liu, Y.; Chen, Y. *Acc. Chem. Res.* **2006**, *39*, 681–691. (g) Hugues, A. D.; Anslyn, E. V. *Proc. Natl. Acad. Sci. U.S.A.* **2007**, *104*, 6538–6543.
- (8) (a) Huang, W.-H.; Liu, S.; Zavalij, P. Y.; Isaacs, L. *J. Am. Chem. Soc.* **2006**, *128*, 14744–14745. (b) Rekharsky, M. V.; Yamamura, H.; Kawai, M.; Osaka, I.; Arakawa, R.; Sato, A.; Ko, Y. H.; Selvamalam, N.; Kim, K.; Inoue, Y. *Org. Lett.* **2006**, *8*, 815–818. (c) Chernikova, E.; Berdnikova, D.; Fedorov, Y.; Fedorova, O.; Peregodov, A.; Isaacs, L. *Chem. Commun.* **2012**, *48*, 7256–7258. (d) Bhasikuttan, A. C.; Mohanty, J.; Nau, W. M.; Pal, H. *Angew. Chem., Int. Ed.* **2007**, *46*, 4120–4122. (e) Leclercq, L.; Noujeim, N.; Sanon, S. H.; Schmitzer, A. R. *J. Phys. Chem. B* **2008**, *112*, 14176–14184. (f) Choudhury, S. D.; Mohanty, J.; Pal, H.; Bhasikuttan, A. C. *J. Am. Chem. Soc.* **2010**, *132*, 1395–1401. (g) Lemaure, V.; Carroy, G.; Poussiguet, F.; Chiro, F.; De Winter, J.; Isaacs, L.; Dugourd, P.; Cornil, J.; Gerbaux, P. *ChemPlusChem* **2013**, *78*, 959–969. (h) Pemberton, B. C.; Barooah, N.; Srivatsava, D. K.; Sivaguru, J. *Chem. Commun.* **2010**, *46*, 225–227.
- (9) (a) Mileo, E.; Yi, S.; Bhattacharya, P.; Kaifer, A. E. *Angew. Chem., Int. Ed.* **2009**, *48*, 5337–5340. (b) Manoni, R.; Neviani, P.; Franchi, P.; Mezzina, E.; Lucarini, M. *Eur. J. Org. Chem.* **2014**, *1*, 147–151.
- (10) (a) Manoni, R.; Romano, F.; Casati, C.; Franchi, P.; Mezzina, E.; Lucarini, M. *Org. Chem. Front.* **2014**, *1*, 477–483. (b) Lucarini, M. In *Supramolecular Radical Chemistry, Basic Concepts and Methodologies*; Encyclopedia of Radicals in Chemistry, Biology and Materials; Wiley: 2012, Vol. 2, p 229. (c) Nakabayashi, K.; Kawano, M.; Kato, T.; Furukawa, K.; Ohkoshi, S.-i.; Hozumi, T.; Fujita, M. *Chem.—Asian J.* **2007**, *2*, 164–170. (d) Bardelang, D.; Giorgi, M.; Pardauna, C.; Hornebecq, V.; Rizzato, E.; Tordo, P.; Ouari, O. *Chem. Commun.* **2013**, *49*, 3519–3521.
- (11) (a) Michon, J.; Rassat, A. *J. Am. Chem. Soc.* **1979**, *101*, 995–996. (b) Kotake, Y.; Janzen, E. G. *J. Am. Chem. Soc.* **1989**, *111*, 5138–5140. (c) Rossi, S.; Bonini, M.; Lo Nostro, P.; Baglioni, P. *Langmuir* **2007**, *23*, 10959–10967.
- (12) (a) Mezzina, E.; Cruciani, F.; Pedulli, G. F.; Lucarini, M. *Chem.—Eur. J.* **2007**, *13*, 7223–7233. (b) Kirilyuk, I.; Polovyanenko, D.; Semenov, S.; Grigorev, I.; Gerasko, O.; Fedin, V.; Bagryanskaya, E. *J. Phys. Chem. B* **2010**, *114*, 1719–1728. (c) Yi, S.; Captain, B.; Kaifer, A. E. *Chem. Commun.* **2011**, *47*, 5500–5502. (d) Vostrikova, K. E.; Peresyphkina, E. V.; Drebuschak, V. A.; Nadolinny, V. A. *Polyhedron* **2011**, *30*, 3083–3087.
- (13) (a) Karoui, H.; Le Moigne, F.; Ouari, O.; Tordo, P. *Stable Radicals*; Hicks, R. G., Ed.; Wiley: 2010; pp 173–229. (b) Likhtenstein, G. I.; et al. *Nitroxides*; Wiley: 2008; pp 205–237. (c) Borbat, P. P.; Costa-Filho, A. J.; Earle, K. A.; Mosciacki, J. K.; Freed, J. H. *Science*

- 2001, 291, 266–269. (d) Jeschke, G. *Prog. Nucl. Magn. Reson. Spectrosc.* **2013**, 72, 42–60.
- (14) In the following papers, the allostery concept was used to illustrate how cations or thiourea reorganize the conformations of a polyradical and as a consequence the extent of spin coupling: (a) Ulrich, G.; Turek, P.; Ziessel, R. *Tetrahedron Lett.* **1996**, 37, 8755–8758. (b) Gagnaire, G.; Jeunet, A.; Pierre, J. L. *Tetrahedron Lett.* **1991**, 32, 2021–2024.
- (15) Wang, J.; Hou, L.; Browne, W. R.; Feringa, B. L. *J. Am. Chem. Soc.* **2011**, 133, 8162–8164.
- (16) (a) Ionita, G.; Chechik, V. *Chem. Commun.* **2010**, 46, 8255–8257. (b) Ionita, G.; Meltzer, V.; Pincu, E.; Chechik, V. *Org. Biomol. Chem.* **2007**, 5, 1910–1914.
- (17) Yi, S.; Captain, B.; Ottaviani, M. F.; Kaifer, A. E. *Langmuir* **2011**, 27, 5624–5632.
- (18) (a) Casati, C.; Franchi, P.; Pievo, R.; Mezzina, E.; Lucarini, M. J. *Am. Chem. Soc.* **2012**, 134, 19108–19117. (b) Mileo, E.; Casati, C.; Franchi, P.; Mezzina, E.; Lucarini, M. *Org. Biomol. Chem.* **2011**, 9, 2920–2924. (c) Graziano, C.; Masiero, S.; Pieraccini, S.; Lucarini, M.; Spada, G. P. *Org. Lett.* **2008**, 10, 1739–1742. (d) Mezzina, E.; Fani, M.; Ferroni, F.; Franchi, P.; Menna, M.; Lucarini, M. *J. Org. Chem.* **2006**, 71, 3773–3777.
- (19) (a) Chen, J. Y.-C.; Jayaraj, N.; Jockusch, S.; Ottaviani, M. F.; Ramamurthy, V.; Turro, N. J. *J. Am. Chem. Soc.* **2008**, 130, 7206–7207. (b) Porel, M.; Ottaviani, M. F.; Jockusch, S.; Turro, N. J.; Ramamurthy, V. *RSC Adv.* **2013**, 3, 427–431. (c) Porel, M.; Ottaviani, M. F.; Jockusch, S.; Jayaraj, N.; Turro, N. J.; Ramamurthy, V. *Chem. Commun.* **2010**, 46, 7736–7738. (d) Jockusch, S.; Zeika, O.; Jayaraj, N.; Ramamurthy, V.; Turro, N. J. *J. Phys. Chem. Lett.* **2010**, 1, 2628–2632.
- (20) (a) Hardy, M.; Bardelang, D.; Karoui, H.; Rockenbauer, A.; Finet, J.-P.; Jicsinszky, L.; Rosas, R.; Ouari, O.; Tordo, P. *Chem.—Eur. J.* **2009**, 15, 11114–11118. (b) Bardelang, D.; Finet, J.-P.; Jicsinszky, L.; Karoui, H.; Marque, S. R. A.; Rockenbauer, A.; Rosas, R.; Charles, L.; Monnier, V.; Tordo, P. *Chem.—Eur. J.* **2007**, 13, 9344–9354. (c) Bardelang, D.; Rockenbauer, A.; Finet, J.-P.; Karoui, H.; Tordo, P. *J. Phys. Chem. B* **2005**, 109, 10521–10530.
- (21) Bardelang, D.; Banaszak, K.; Karoui, H.; Rockenbauer, A.; Waite, M.; Udachin, K.; Ripmeester, J. A.; Ratcliffe, C. I.; Ouari, O.; Tordo, P. *J. Am. Chem. Soc.* **2009**, 131, 5402–5404.
- (22) Mileo, E.; Mezzina, E.; Grepioni, F.; Pedulli, G. F.; Lucarini, M. *Chem.—Eur. J.* **2009**, 15, 7859–7862.
- (23) Jayaraj, N.; Porel, M.; Ottaviani, M. F.; Maddipati, M. V. S. N.; Modelli, A.; Da Silva, J. P.; Bhogala, B. R.; Captain, B.; Jockusch, S.; Turro, N. J.; Ramamurthy, V. *Langmuir* **2009**, 25, 13820–13832.
- (24) (a) Brière, R.; Dupeyre, R.; Lemaire, H.; Morat, C.; Rassat, A.; Rey, P. *Bull. Soc. Chim. Fr.* **1965**, 3290–3297. (b) Ottaviana, M. F.; Modelli, A.; Zeika, O.; Jockusch, S.; Moscatelli, A.; Turro, N. J. *J. Phys. Chem. A* **2012**, 116, 174–184.
- (25) (a) Shinomiya, M.; Higashiguchi, K.; Matsuda, K. *J. Org. Chem.* **2013**, 78, 9282–9290. (b) Kröck, L.; Shivanyuk, A.; Goodin, D. B.; Rebek, J., Jr. *Chem. Commun.* **2004**, 272–273.
- (26) Rieger, P. H. *Electron Spin Resonance: Analysis and Interpretation*; Royal Society of Chemistry: 2007.
- (27) (a) Luckhurst, G. R. *Mol. Phys.* **1966**, 10, 543–550. (b) Luckhurst, G. R.; Pedulli, G. F. *J. Am. Chem. Soc.* **1970**, 92, 4738–4739.
- (28) Rockenbauer, A.; Szabo-Planka, T.; Arkosi, Sz.; Korecz, L. *J. Am. Chem. Soc.* **2001**, 123, 7646–7654.
- (29) (a) Ackers, G. K.; Doyle, M. L.; Myers, D.; Daugherty, M. A. *Science* **1992**, 255, 54–63. (b) Thordarson, P.; Bijsterveld, E. J. A.; Elemans, J. A. A. W.; Kasak, P.; Nolte, R. J. M.; Rowan, A. E. *J. Am. Chem. Soc.* **2003**, 125, 1186–1187.
- (30) (a) Taylor, P. N.; Anderson, H. L. *J. Am. Chem. Soc.* **1999**, 121, 11538–11545. (b) Niu, Z.; Slobodnick, C.; Gibson, H. W. *Org. Lett.* **2011**, 13, 4616–4619. (c) Connors, K. A. *Binding Constants*; J. Wiley and Sons: New York, 1987; pp 78–86.
- (31) (a) Bardelang, D.; Udachin, K. A.; Leek, D. M.; Margeson, J.; Chan, G.; Ratcliffe, C. I.; Ripmeester, J. A. *Cryst. Growth Des.* **2011**, 11, 5598–5614. (b) Bardelang, D.; Udachin, K. A.; Anedda, R.; Moudrakovski, I.; Leek, D. M.; Ripmeester, J. A.; Ratcliffe, C. I. *Chem. Commun.* **2008**, 4927–4929.
- (32) (a) Terwilliger, T. C. *Biochemistry* **1996**, 35, 16652–16664. (b) Kohlstaedt, L. A.; Cole, R. D. *Biochemistry* **1994**, 33, 12702–12707. (c) Amiriky, B. R.; Vologodskii, A. V.; Lyubchenko, Y. L. *Nucleic Acids Res.* **1981**, 9, 5469–5482.
- (33) (a) Lee, T.-C.; Kalenius, E.; Lazar, A. I.; Assaf, K. I.; Kuhnert, N.; Gruen, C. H.; Jaenis, J.; Scherman, O. A.; Nau, W. M. *Nat. Chem.* **2013**, 5, 376–382. (b) Rauwald, U.; Biedermann, F.; Deroo, S.; Robinson, C. V.; Scherman, O. A. *J. Phys. Chem. B* **2010**, 114, 8606–8615. (c) Lee, S. J. C.; Lee, J. W.; Lee, H. H.; Seo, J.; Noh, D. H.; Ko, Y. H.; Kim, K.; Kim, H. I. *J. Phys. Chem. B* **2013**, 117, 8855–8864.
- (34) Da Silva, J. P.; Jayaraj, N.; Jockusch, S.; Turro, N. J.; Ramamurthy, V. *Org. Lett.* **2011**, 13, 2410–2413.
- (35) (a) Emoto, M.; Mito, F.; Yamasaki, T.; Yamada, K.-i.; Sato-Akaba, H.; Hirata, H.; Fujii, H. *Free Radical Res.* **2011**, 45, 1325–1332. (b) Martinie, J.; Michon, J.; Rassat, A. *J. Am. Chem. Soc.* **1975**, 97, 1818–1823. (c) Jeunet, A.; Nickel, B.; Rassat, A. *Nouv. J. Chim.* **1986**, 10, 123–132. (d) Ebel, C.; Ingold, K. U.; Michon, J.; Rassat, A. *Tetrahedron Lett.* **1985**, 26, 741–744.
- (36) (a) Wheate, N. J.; Anil Kumar, P. G.; Torres, A. M.; Aldrich-Wright, J. R.; Price, W. S. *J. Phys. Chem. B* **2008**, 112, 2311–2314. (b) Grant, M. P.; Wheate, N. J.; Aldrich-Wright, J. R. *J. Chem. Eng. Data* **2009**, 54, 323–326.
- (37) (a) Neuhaus, D.; Williamson, M. P. *The Nuclear Overhauser Effect in Structural and Conformational Analysis*, 2nd ed.; 2000; Chapter 3, pp 74–77. (b) Keepers, J. W.; James, T. L. *J. Magn. Reson.* **1984**, 57, 404–426.
- (38) Hess, B.; Kutzner, C.; van der Spoel, D.; Lindahl, E. *J. Chem. Theory Comput.* **2008**, 4, 435–447.
- (39) Rinkevicius, Z.; Frecus, B.; Murugan, N. A.; Vahtras, O.; Kongsted, J.; Agren, H. *J. Chem. Theory Comput.* **2012**, 8, 257–263.
- (40) Frisch, M. J.; Trucks, G. W.; Schlegel, H. B.; Scuseria, G. E.; Robb, M. A.; Cheeseman, J. R.; Scalmani, G.; Barone, V.; Mennucci, B.; Petersson, G. A.; Nakatsuji, H.; Caricato, M.; Li, X.; Hratchian, H. P.; Izmaylov, A. F.; Bloino, J.; Zheng, G.; Sonnenberg, J. L.; Hada, M.; Ehara, M.; Toyota, K.; Fukuda, R.; Hasegawa, J.; Ishida, M.; Nakajima, T.; Honda, Y.; Kitao, O.; Nakai, H.; Vreven, T.; Montgomery, J. A., Jr.; Peralta, J. E.; Ogliaro, F.; Bearpark, M.; Heyd, J. J.; Brothers, E.; Kudin, K. N.; Staroverov, V. N.; Kobayashi, R.; Normand, J.; Raghavachari, K.; Rendell, A.; Burant, J. C.; Iyengar, S. S.; Tomasi, J.; Cossi, M.; Rega, N.; Millam, J. M.; Klene, M.; Knox, J. E.; Cross, J. B.; Bakken, V.; Adamo, C.; Jaramillo, J.; Gomperts, R.; Stratmann, R. E.; Yazyev, O.; Austin, A. J.; Cammi, R.; Pomelli, C.; Ochterski, J. W.; Martin, R. L.; Morokuma, K.; Zakrzewski, V. G.; Voth, G. A.; Salvador, P.; Dannenberg, J. J.; Dapprich, S.; Daniels, A. D.; Farkas, Ö.; Foresman, J. B.; Ortiz, J. V.; Cioslowski, J.; Fox, D. J. *Gaussian 09, Revision D.01*; Gaussian, Inc.: Wallingford, CT, 2009.
- (41) Saleh, N.; Koner, A. L.; Nau, W. N. *Angew. Chem., Int. Ed.* **2008**, 47, 5398–5401.
- (42) Liu, Y.; Villamena, F. A.; Rockenbauer, A.; Song, Y.; Zweier, J. L. *J. Am. Chem. Soc.* **2013**, 135, 2350–2356.
- (43) (a) Monod, J.; Wyman, J.; Changeux, J.-P. *J. Mol. Biol.* **1965**, 12, 88–118. (b) Kawai, H.; Katoono, R.; Nishimura, K.; Matsuda, S.; Fujiwara, K.; Tsuji, T.; Suzuki, T. *J. Am. Chem. Soc.* **2004**, 126, 5034–5035.
- (44) (a) Logsdon, L. A.; Schardon, C. L.; Ramalingam, V.; Kwee, S. K.; Urbach, A. R. *J. Am. Chem. Soc.* **2011**, 133, 17087–17092. (b) Reczek, J. J.; Kennedy, A. A.; Halbert, B. T.; Urbach, A. R. *J. Am. Chem. Soc.* **2009**, 131, 2408–2415. (c) Rekharsky, M. V.; Yamamura, H.; Inoue, C.; Kawai, M.; Osaka, I.; Arakawa, R.; Shiba, K.; Sato, A.; Ko, Y. H.; Selvapalam, N.; Kim, K.; Inoue, Y. *J. Am. Chem. Soc.* **2006**, 128, 14871–14880.
- (45) (a) Ferrand, Y.; Chandramouli, N.; Kendhale, A. M.; Aube, C.; Kauffmann, B.; Grélard, A.; Laguerre, M.; Dubreuil, D.; Huc, I. *J. Am. Chem. Soc.* **2012**, 134, 11282–11288. (b) Gan, Q.; Ferrand, Y.; Chandramouli, N.; Kauffmann, B.; Aube, C.; Dubreuil, D.; Huc, I. *J. Am. Chem. Soc.* **2012**, 134, 15656–15659.

5.3 Etude de la réactivité de systèmes complexes

Jusqu'à présent, mes études de réactivité ont porté sur des systèmes relativement petits, dont l'ensemble a été traité par des méthodes quantiques. L'étude de la réactivité de systèmes plus importants nécessiterait l'utilisation de méthodes mixtes MQ/MM dans lesquels le centre réactif est traité au niveau quantique tandis que les groupements plus éloignés sont traités par mécanique moléculaire. Une partie de la difficulté réside dans le choix de la frontière entre les deux modélisations du système :

- la partie quantique doit être suffisamment étendue pour rendre compte de la réactivité du système (effets électroniques) sans alourdir exagérément le temps de calcul
- la partie classique et le solvant agissent sur le centre réactif par leurs effets stérique et électrostatique